Alma Mater Studiorum – Università di Bologna

DOTTORATO DI RICERCA IN

Scienze e tecnologie della salute

Ciclo XXXIV

Settore Concorsuale: 03/C2 – CHIMICA INDUSTRIALE

Settore Scientifico Disciplinare: CHIM/04 – CHIMICA INDUSTRIALE

3D BIOPRINTED ORGAN MODELS FOR DRUG SCREENING

Presentata da: Giorgia Pagnotta

Coordinatore Dottorato	**Supervisore**
Prof. Marco Viceconti	Prof. Maria Letizia Focarete

Co-supervisore

Prof. Claudio Borghi
Prof. Stefania Rapino
Prof. Arrigo Francesco Giuseppe Cicero

Esame finale anno 2022

Index

Abstract

The culture of cells on two-dimensional (2D) surfaces represents the ‘gold-method’ to culture cells and proven fundamentals in cell biology, cancer research and drugs development. In fact, 2D cell cultures play a crucial role in the early stages of drug screening pipeline since they represent the *in vitro* models of the target to be replicated and they act as a tool to predict behaviour and effects on humans, by limiting the number of failures during animal testing. However, most physiologic parameters of organs, such as tissue architecture, cell-to-cell and cell-to-matrix interactions, mechanical properties, and biochemical networks are lost under these simplified conditions. Cells naturally grown in three-dimensional (3D) environment and the extra cellular matrix (ECM) play a central role both from a biological and mechanical point of view. In particular, each human tissue displays well distinct characteristics and properties in terms of matrix stiffness, chemical composition and cellular components which are fundamental aspects to reproduce a physiological-like *in vitro* model. Cellular behaviour, pathways, proliferation, morphology, gene and protein expressions are strictly correlated with the ECM features, especially in presence of tissue inflammation or diseases. In this context, the development of 3D in vitro models, in which cells are embedded inside a matrix, are strongly needed to produce more physiologically relevant tissue~~s~~ models. The evaluation of cell-matrix interaction and the corresponding cellular response allows to evaluate the mechanobiology of specific tissues. Furthermore, the possibility to have tailored physical and chemical properties of the matrix might improve the physiological-like conditions of the models even in altered state of the tissues. In this way, both the prediction of drug effects in humans and the selection of more bioavailable and safe drugs to be clinically developed might be improved, leading to a reduction of the use of animal models and of under or overestimation of drug response.

In recent years, 3D bioprinting has emerged as an innovative and versatile technology able to produce complex 3D constructs that resemble the native spatial organization of organ tissues. A 3D bioprinter employs one or more bioinks composed of various types of cells suspended in a hydrogel that provides a three-dimensional structure in which cells can grow and proliferate. The hydrogel not only provide mechanical support and stability to the cells but also allows to tailor protein composition, nutrition, chemical and spatial gradients to match the native extracellular matrix. Natural-based hydrogels, such as gelatin, collagen, alginate or blend of them, and semi-synthetic hydrogels, such as alginate-methacrylate (AlgMa) and gelatin-methacrylate (GelMa), are extensively used for 3D bioprinting models since they mimic the natural composition of the tissues, they are biocompatible and bioactive with customizable mechanical properties, allowing to support cell growth. Moreover, considering that in several disease conditions the microenvironment surrounding cells changes in terms of mechanical properties, the possibility to tailor hydrogels mechanical properties by modifying the chemical structures to obtain photo-crosslinkable materials, while maintaining their biocompatibility and biomimicry, make their use versatile and suitable to simulate a broad spectrum of physiological features. Finally, since 3D bioprinting allows to precise position in a layered manner, several bioinks, differing in terms of cells or hydrogels composition, it can be exploited at the same time to produce complex and multi-components tissues containing different type of cells, proteins, matrices and gradients in the z-axis.

In this PhD Thesis, 3D bioprinted *in vitro* models with tailored mechanical properties and physiologically-like features were fabricated. In particular, AlgMa bioinks were employed to produce living 'fortune-cookie' platform with gradient stiffness, with the aim to create an easy to handle and accessible biological tool to evaluate both cell-to-matrix interaction and the resulting mechanobiology. In addition, GelMa, collagen and IPN of GelMa and collagen were used as bioinks to fabricate a proof-of-concept of 3D intestinal barrier, which include multiple cell components and multi-layered structure.

The use of rheology to evaluate both printability of the bioinks and mechanical properties of the printed models was deeply explained and proposed as useful method to (i) produce reliable and reproducible *in vitro* models, (ii) correlate rheological parameters with the bioprinting process and (iii) screen for the bioinks which can undergo bioprinting.

Natural-based bioinks were firstly formulated starting from the chemical functionalization of natural polymers, such as alginate and gelatin, in order to get photo-crosslinkable hydrogels with controllable crosslinking process, tuneable gelation and tailored mechanical properties. Here, an affordable alginate methacrylation process based on green synthetic approach was accomplished. Furthermore, in order to provide a more physiological nature to the models, collagen-based bioink was developed in cooperation with Typeone Biomaterials s.r.l. company, since collagen is an ECM-derived component and it is the most abundant protein of the human extracellular matrix. HeLa cells were selected to produce the AlgMa-based living 'fortune cookie' platform since they are easy to culture in 2D conditions and they represent the 'gold-standard' model to reproduce cancer tissue, while human intestinal fibroblast, human skin fibroblast and human epithelial colonic cells were used to propose the fabrication of the proof-of-concept of intestinal barrier model. The 3D bioprinting process was optimized in order to evaluate the feasibility of the fabrication of both 'fortune-cookie' platform and multi-structured 3D intestinal models, by correlating rheological analysis and 3D bioprinting tests.

Bioprinting was performed with the aim to obtain a continuous filament extrusion, by avoiding any clogging of the nozzle and preserving as much as possible cell viability and functionalities, and to generate 3D structures with consistent shape fidelity. Post-printing crosslinking processes were performed and optimized in order to increase the mechanical stability of the models, in incubation conditions during time, and to sustain cell growth and proliferation. Furthermore, the tuneable crosslinking processes aim to tailor the mechanical properties of the models in the same range of stiffness of the tissues to be replicated, while preserving, at the same time, cell survival. Therefore, the final models are capable to describe the native tissue condition both in terms of spatial 3D environment, chemical nature and stiffness. A dual post-printing crosslinking process was proposed as a method to fine tuning the 'fortune-cookie' platform mechanical properties in the desired range of stiffness. In particular, both photo-crosslinking and ionic-crosslinking were carried out after bioprinting to stabilize the platform from a mechanical point of view by reducing UV light exposure which can irreversibly damages cell functionalities. Three regions with different stiffness properties were obtained by exposing the 'fortune-cookie' to the UV light through a photo-protecting hand-made mask. In this way, a 3D bioprinted platform with gradient stiffness was obtained. On the contrary, single post-printing crosslinking process was carried out on the 3D bioprinted intestinal models through UV irradiation, in the presence of photo-initiator, by ensuring the suitable mechanical stability and cells safety. Finally, 'fortune-cookie' platform and 3D intestinal barrier were cultured up to 14 days and 21 days, respectively, in incubation conditions.

Proton nuclear magnetic resonance (^{1}H-NMR), Fourier transform infrared spectroscopy (FT-IR), thermogravimetric analysis (TGA), Matrix Assisted Laser Desorption Ionization - Time of Flight (MALDI-TOF) and titration with TNBS were carried out to assess the chemical functionalization of the methacrylic group onto the polymer backbone chains and the degree of substitution (DS). AlgMa chemical characterization demonstrates that the green and affordable synthetic approach proposed in this Thesis was successfully achieved, leading to the formation of photocrosslinkable alginate methacrylate. Both ^{1}H-NMR and FT-IR confirm the chemical substitution, while the MALDI-TOF analysis reports a quantitative substitution (DS) of 63 %. Finally, TGA analyses show that methacrylation does not significantly affect the thermal stability of the material. In the case of GelMa synthesis, ^{1}H-NMR and FT-IR analyses confirm the chemical substitution, while the titration with TNBS provides a quantitative degree of substitution (DS) of 80 %. Even in this case, TGA analyses show that methacrylation does not significantly affect the thermal stability of the pristine gelatin.

Bioinks formulations were optimized in order to get biocompatible and printable materials able to support cell growth and proliferation during time. A deep rheological characterization was performed on all the bioinks before and after bioprinting and after the crosslinking processes, in order to predict their printability, shape fidelity, recovery behaviour and stiffness. In particular, amplitude sweep analyses were performed to evaluate both storage and loss moduli before and after printing process and to quantify how the crosslinking process affect the mechanical moduli of the models. Flow curves were obtained to assess the printability of the bioinks and their shear-thinning behaviour. Recovery tests were carried out to demonstrate the ability of the bioinks to recover their internal structure and initial mechanical properties after they experienced high shear-rate simulating the extrusion moment, which is strictly linked with the shape-fidelity of the structures. Furthermore, the effect of the cells inside the bioinks on the final mechanical properties of the scaffolds was also evaluated through rheology. Amplitude sweep and flow curve analyses carried out on AlgMa-based bioinks demonstrates their shear thinning behaviour, good printability properties and ability to recover in the proper manner the initial mechanical properties after they experienced extrusion. The 'fortune-cookie' 3D bioprinting process was optimized in order to get in one shot of printing a gradient stiffness with a recognizable geometry which makes distinguishable the different regions with specific mechanical properties. Rheological measurements were carried out on the final printed and crosslinked platform to evaluate the different stiffness of each area in the 3D model. Results show that the dual crosslinking process here proposed provides the suitable mechanical properties to replicate the stiffness of different tissues (0.05 kPa – 2 KPa): from a healthy one, softer with low stiffness, to one displaying pathological alterations or inflammation state, which usually presents stiffer matrices. Furthermore, amplitude sweep analysis performed on the cell-embedded structures after printing and crosslinking processes demonstrates that the presence of the cells strongly affects mechanical properties of the models, by decreasing of one order of magnitude the storage moduli.

Finally, biological characterizations were carried out on both 'fortune-cookie' platform and 3D bioprinted intestinal models in order to evaluate their biocompatibility, bioactivity, ability to sustain cell growth and reproduce the 3D native environment of the tissue, and to assess the functionalities of the models. In particular, the correlation between mechanical properties and HeLa cells inside the 'fortune-cookie' platform was evaluated through live/dead assays and confocal images, while, in the case of 3D bioprinted intestinal barrier, the biological assessment of the models was provided through live/dead assays, confocal images, cell proliferation, immunofluorescence and immunohistochemistry analysis.

Biological assay such as live/dead staining was carried out on the final printed constructs, in order to assess cells viability and to evaluate cellular morphology into the polymeric matrices. The platform maintains good mechanical stability and provides support to HeLa growth up to 14 days. Live/dead results show that there is a strong correlation between mechanical properties and cell behaviour, since by moving from the lowest stiffness region of the platform to the highest one, cell viabilities decrease (from 80 % to 30 %). For what concerns the 3D intestinal models, the 3D bioprinting process was successfully optimized to obtain the layered structure with personalized and different bioinks (GelMa, collagen and IPN of GelMa and collagen) for the desired layer. All the models displayed the suitable mechanical stability to replicate the intestinal tissue and maintained the proper stiffness during the whole experiment in incubation condition (21 days).

Live/dead assay highlight that human skin fibroblast and epithelial colonic cells display the highest cell viability (> 90%), a good cell proliferation and a clear change in morphology up to 21 days. For these reasons, these cell types were selected to fabricate the final 3D models. Alamar blue assays confirm the high cell proliferation into all the matrices, by showing the highest value of proliferation in the IPN-based bioinks, and the immunofluorescence images clearly show the formation of an epithelial monolayer characterized by intermembranes proteins and tight-junctions. Finally, a new biological procedure for the inclusion of 3D bioprinted constructs for immunohistochemistry analyses was optimized, in order to carry out histological tests by preserving as much as possible the integrity of the samples, which is usually affected by the strong stiffening of the matrix occurring after several required treatments.

In conclusion, natural-based bioinks formulations were successfully synthetized and optimized for the fabrication of 3D bioprinted organ/tissue models. The use of rheology has proven to be a great tool for the characterization and prediction of both bioinks printability and 3D bioprinting process, respectively, and of the mechanical properties of the final models. A useful rheological guide to drive users to the selection of the suitable bioinks for 3D bioprinting and to correlate the model's mechanical stability after crosslinking is proposed. In addition, a platform capable to reproduce models with gradient stiffness, as in the case of pathologically-like tissue, was developed. Finally, the fabrication of 3D bioprinted intestinal models displaying a good hierarchical structure and cells composition was fully reported and successfully achieved. The good biological results obtained demonstrated that 3D bioprinting can be used for the fabrications of 3D intestinal barrier and that the mechanical properties of the external environment plays a key role on the cell pathways, viability and morphology

1. Introduction

1.1. 2D vs 3D in vitro models

2D in vitro models, known also as monolayer cell culture, has provided groundbreaking insights into basic cell biology becoming an indispensable tool for the understanding of all those mechanisms that underlie *in vivo* cell behavior such as cell differentiation, migration, growth and proliferation, which are mainly affected by biochemical stimuli, biomechanical microenvironment, injuries and inflammation processes [1–3]. Furthermore, the employment of monolayer culture has become increasingly important to predict and assess drug behavior and its organ toxicity-response, with aim to minimize the unethical and non-responsible use of animal models along with avoiding costly failures of drugs later in development of drug candidates. In drug discovery, the conventional procedure of screening drug compounds starts with 2D cell culture tests, followed by animal model tests and finally clinical trials. In particular, in the early stages of drug development, *in vitro* strategy intends to support the determination of drug uptake, metabolism, and excretion, as well as the detection of potential undesired effects on the human health. Regulatory agency, such as FDA, asks for specific and standardized assays including AMES, hepatic tolerance, teratogenic potential or the activation of drug metabolism, which allow to select the suitable clinical candidates to be tested in the second stage of pre-clinical trials. In particular, in the early stages of drug development, *in vitro* strategy intends to support the determination of drug uptake, metabolism, and excretion, as well as the detection of potential undesired effects on the human health [4]. Regulatory agency, such as FDA, asks for specific and standardized assays including AMES, hepatic tolerance, teratogenic potential or the activation of drug metabolism, which allow to select the suitable clinical candidates to be tested in the second stage of pre-clinical trials [5]. In this way, considerably efforts are made to mechanistically understand any side-effects occurring during pre-clinical stages, especially during animal experiments which more resemble *in vivo* conditions and provide an estimate of the human relevance of the observed effect in relation with the administered dose.

2D cell culture relies on adherence to a flat surface, typically a petri dish of glass or polystyrene, to provide mechanical support for the cells. Cell growth in monolayers allows for access to a suitable amount of nutrients and growth factors present in the culture medium, which results in homogenous proliferation during time easy to access and ready to be use for drug screening and experiments in a high throughput manner. This characteristic makes 2D platforms attractive to biologists and clinical users due to its simplicity, efficiency and high scalability. However, most of these *in vitro* methods do not provide control of cell morphology, which determines biophysical cues affecting cell bioactivities *in vivo*. To improve and customize 2D cell culture morphology, micro-patterned substrates [6], such as cell-adhesive islands [7-8], microwells [9], and micropillars [10-11] have been created allowing to study the effects of cell shape on bioactivities. Furthermore, to improve safety prediction of drug candidates in the early stage of the testing, genomics, proteomics, metabolomics, and high content imaging have been explored to clarify and better understand the entire biological processes rather than just at the single endpoint level, thanks to technologies improvement occurred in the last decade [12-13]. The advantage of these technologies lies in the ability to generate a global screening without prior focus on a limited set of potential targets of drugs [12-13]. However, not only better readouts and improved technologies are required to improve prediction of drug behavior based on *in vitro* data, but also the models themselves used to generate those data need reviewing.

Disadvantages of 2D in vitro models

Despite all the advantages of the current 2D models, the mechanical properties of polystyrene and glass differ largely from those of the extra-cellular environment. Polystyrene, for instance, displays a stiffness in the range of 1–3 GPa, which is about six orders of magnitude higher than that of the majority of native tissues. In many studies the effect of substrate stiffness on different cell types and mechanism has already been proven, including drug sensitivity, proliferation, gene expression and differentiation [14-22]. Anyway, even if recently surface coatings enriched with ECM molecules [16-17] or synthetic materials [18-19] were developed to produce 2D substrate that more resemble native stiffness of the target tissue, the cells still experience a non-physiologic spatial environment lacking most of the interactions occurring in the native 3D tissue, which play a key role in the cell pathway, phenotypes and genotypes expression. In particular, most physiologic parameters of organs, such as tissue architecture, cell-to-cell and cell-to-matrix interaction, 3D cellular aggregation in spheroids-like shape, mechanical properties, and biochemical networks are lost under these simplified conditions [20,1]. Furthermore, also chemical and physical parameters are different from the native situation. In fact, in the 2D models, cells have a direct and uncontrolled access to nutrients and metabolites contained in the culture medium and their overexposure to the atmospheric oxygen can affect cellular behaviors [20]. The absence of oxygen, nutrients gradients and the permeability of the surrounding ECM, increase the need to move one step forward in the creation of improved 3D models [2,21].

Another unreproducible *in vivo* situation with these standard models, is the niche-tumor or cancer environment, which displays usually increased mechanical properties in terms of stiffness and rigidity of the ECM with respect to the healthy tissue, which affect cell pathways, biochemical and drug response during the drug screening [22-27].

Importance of the ECM

What's the role and the importance to replicate ECM in the *in vitro* models? In the native tissue, cells connect not only to each other, but also to a support structure so called extracellular matrix (ECM). This contains proteins, such as collagen, elastin and laminin, that conferee to the tissue specific mechanical properties, depending on the type of tissue and cells, and help to organize communication between cells embedded within the matrix. Receptors on the surface of the cells, known as integrins, anchor their bearers to the ECM, and also determine how the cells interpret biochemical cues from their immediate surroundings. ECM is made of an intricate network of proteins and polysaccharides secreted mostly by a special family of cells, the fibroblasts. Two large classes of macromolecules can be distinguished as main components of the ECM: the large polysaccharides, the so-called glycosaminoglycans (GAGs) which form highly hydrated gels, in which the second class of macromolecules, fibrous proteins such as collagen and fibronectin, can be embedded in. These proteins provide robustness and strength to the hydrogels and support cell growth within the ECM. All of these components, contained in specific proportions and concentrations inside the matrix tissues, are organized in a variety of way able to build different structures, ranging from rigid or hard ECM in bone, tension-resistant structure of tendons to the extreme elasticity of blood vessels [29-31]. Besides strong tensile mechanical properties, many tissues display high flexibility, such as blood vessels, lungs and skin, which is mainly provided by an extensive network of elastic fibers. Finally, fibronectin and RGD moieties play a central role for cell attachment and proliferation into the matrix [32,33].

ECM viscosity and its mechanical forces strictly influences both CO_2 and nutrients permeability along with oxygen concentration along the z-axis. Furthermore, external mechanical forces on the cells such as compression, tension, bending, torsion, hydrostatic pressure and shear stress, function as source of environmental stimulus which drive cells differentiation, migration and adhesion [34,35].

For all the reasons highlighted above, the development of 3D cell culture models that more replicate physiological conditions are strongly needed both to improve prediction of drug effects in humans, in order to plan more targeted clinical trials, and to improve the selection of more bioavailable and safe drugs to be clinical developed.

From 2D to 3D conditions

By providing a reproducible and customized microenvironment that mimics *in vivo* conditions, 3D cell cultures have become a valid tool to overcome the limitations of the standard 2D culture and, in addiction, to reduce the use of animal models. Thank to this improvement, 3D cell cultures have accelerated our understanding of organogenesis and cancerogenesis by leading to more advanced approaches in drug testing and personalized medicine.

Despite these cultures still remain a simplification of the native conditions, they incorporate the most relevant physiologically interactions such as cell-cell and cell-matrix interactions, which provide several critical features present in tissues, including morphology, differentiation, polarity, proliferation rate, gene expression and genomic profiles, nutrient and oxygen gradients [36-38]. At the same time, they still being easy to handle as 2D models and practical to being adapt to standard biochemical assay, imaging and technologies.

In order to fill the gap between 3D culture and *in vivo* environment, many fields of science have contributed to improve, manipulate and control the chemistry, geometry and mechanical properties of the cellular microenvironment, such as bioengineered materials, nanotechnology, microfluidics, and 3D bioprinting. These contributions have led to creation of several 3D cell culture systems designed according to specific scientific needs.

1.2. Type of 3D cell cultures

3D in vitro models can be divided in function of their shape, geometry, type of tissue, technology, presence or absence of external matrix to simulate ECM. In this section, 3D models are classified based on the role of the external matrix, which acts as an artificial ECM, and can be divided in (i) non-scaffold-based cultures, (ii) scaffold-based cultures and (iii) specialized 3D platforms.

1.2.1. Non-scaffold-based 3D cultures

An example of 3D cell culture system is represented by non-scaffold 3D cultures, or 3D scaffold-free, which rely on the self-aggregation of a high number of cells, or tissue strands, by means of specialized techniques such as hanging drop microplates, magnetic levitation and low adhesion plates that promotes multicellular aggregation in a spheroids-like shape [21]. These aggregates recapitulate physiological characteristics of some tissues, especially the soft tissue founded in the tumor environment, since they are characterized by strong cell-cell interaction and, when they synthesize their own ECM, also cell-matrix interactions take place [21,39]. Spheroid size mainly depends on the initial number of cells seeded and they can reach specific dimensions displaying oxygen and nutrient gradients similar to the tissue of interest. The scaffold-free techniques can always be applied if cells autonomously create a strong intercellular connection, that lead to a self-organized cell structure without the use of external forces.

In order to replicate a higher number of tissues, in term of their mechanical properties and characteristics, from the hardest tissues to the softest one by differentiating them considering possible issues such as tumor or inflammation, the combination of spheroids models with an external matrix, might represent a valid solution. In this way, the presence of the matrix provides the suitable network to replicate *in vivo* conditions [21]. For instance, mammary glands tissue [40], intestinal barrier [41] or skin tissue [42,43], cannot be strictly replicate without the presence of an external matrix, since they develop highly organised structure in the native condition especially by interacting with neighboring cells and with their ECM, including the basement membrane to which they are attached.

1.2.2. Scaffold-based cultures

As ECM affects cellular organisation and cell functions, scaffold-based 3D cultures have gained great attention since the cells are embedded inside a matrix whose chemical, physical and mechanical property can be customized to better mimic native conditions of the tissues. In this situation, cells basically grow to form spheroids, organoids or multi-layered structures inside or onto a matrix which can be based on decellularized ECM (dECM), synthetic or engineered polymer-based scaffolds. When synthetic scaffolds are used, in order to better mimic key properties of ECM enhancing the recognition between cells and matrix, they can be modified or customized by adding growth factors, biologically active molecules and proteins [21]. Depending on the type of tissue to replicate, a variety of scaffolds and materials combination have been employed in the last decade to accomplish this goal, from soft or hard hydrogels to highly tough polymers [21]. Firstly, the most important aspect to consider is the understanding of the native mechanical and chemical properties of the tissue that must be replicated. For example, cells of skin, intestine, peripheral nerve tissues are surrounded by a soft and hydrated ECM, thus hydrogel polymers, such as collagen, elastin, fibrin, alginate or blend of these, might the best choice to host the suitable type of cells for the specific tissue [44]. Another widely used materials for soft tissue replication are both commercial acellular matrices, such as Biotek, Alvetex and AlgiMatrix [45-48] and commercial hydrogel, such as Matrigel, Cellendes, Glycosan Biosystems, QGel [45,47,49]. Another typical scaffold material used is the synthetic polymer polyethylene glycol (PEG) thanks to its flexibility, tunable mechanical properties, biocompatibility and easily functionalization with biological cellular binding sites, such as RGD and MMP moieties [50,51], which make it more biomimicry. In the case of tissues characterized by strong and rigid mechanical properties, such as bone or cartilage, the scaffold selection is oriented on hard and stiff polymers, such as PCL, PLA or a combination of PCL-collagen and PLA-gelatin [52-55].

Scaffolds are characterized by different shape, structure and morphology, such as electrospun nanofiber, which show nanostructured features and porosity, or freezed dry sponge [56]. However, the use of these systems does not allow for ultimate control of the microstructural features positioning which, in many cases, is fundamental to replicate the extracellular matrix.

Among the most used materials in this field, polymer hydrogels are the suitable candidates since they can be adapted and customized to reproduce different type of tissues. The advantages to use hydrogels to mimic ECM is the high biocompatibility, the possibility to exploit both their physical and chemical cross-linking strategies, in order to obtain the most suitable stiffness matrix and network for a specific tissue formation. Another important parameter to take into account with these cultures, is the presence of a porosity network inside the scaffolds, in order to ensure the suitable exchange of nutrients, gases and waste metabolites into the whole spheroids, especially when aggregates reach 1-2 mm in thickness [57,58]. Inside these scaffolds-based cultures category, cells can assume different shape, structural and cellular morphology, complexity and organization leading to three main type of models: (i) **spheroids**, (ii) **organoids** and (iii) **3D bioprinted models.**

Spheroids and organoids are mainly employed to replicate tumor tissue, as anti-cancer models, due to their high cell-cell interactions, chemical and physical gradients, which typically characterize tumor or neoplastic tissues [59,60]. Despite spheroids simplify tumor environment, they are widely employed in drug screening stages since they are easy to obtain, capable to undergo High Throughput Screening (HTS), closely resemble non-vascularized or poorly vascularized tumors and portray metabolic gradients when grown larger than 500 µm by displaying an outer layer of proliferating cells, a middle layer of quiescent cells and an inner layer of hypoxic and necrotic cells [26,27]. However, there are several practical challenges associated with spheroid cultures, including the development and maintenance of spheroids of uniform size, the formation of spheroids from a small number of seeded cells and the precise control of specific ratios of different cell types in spheroids of co-cultures.

Organoids have gained major attention thanks to their capability to form highly complex structural units with a well-defined *in vivo*-like morphology that partially resemble the unit of an organ, in structure, cell organization, function, histologically and genetically [61,62]. They can produce self-assembled multi-layered cellular structure that preserve the natural cell morphology of the tissue. An example, is represented by intestinal organoids in which intestinal crypts patient-derived were used to form multi-layered intestinal barrier, displaying villi-like structure in the outermost layer and intestinal lumen in the center which support the oxygen demand [63]. However, since most of organoids are formed starting by undifferentiated stem cells, in some cases, they can retain fetal resemblance when pluripotent stem cells (PSC) are used [64] and in other cases, they are limited in recapitulate only the histological and genetic features of their adult donor tissues when adult stem cells (ASC) are employed [65].

While spheroids can be formed both with or without the presence of an external ECM by self-assembling, as described in the non-scaffold-based cultures, organoids always require an external matrix to develop the level of complexity needed. This mainly depends on the cell source. In particular, since spheroids formation is triggered by spontaneous self-assembly of cell lines, multicellular mixtures, primary cells or tumor cells, they do not need external signals of the ECM to develope organized tumor structures. On the contrary, organoids are mainly based on embryonic stem cells, adult stem cells, or induced pluripotent cells, which cellular self-organization and self-assembly into a specific final differentiated cellular model, require a differentiation stage of the cells stimulated in response to external physical and chemical cues provided from the ECM.

For what concern **3D bioprinted scaffolds**, they are produced through 3D bioprinting technologies, which allow the deposition of the cells loaded inside hydrogels in a controlled manner by following a CAD design. In this way, native tissue architecture, cellular composition and vasculature can be recapitulated in vitro to create biomimetic tissue models, which can be used for studying disease mechanisms, screening drugs and other clinical applications. These models can reproduce both healthy or illness tissues, including the hardest ones (i.e. cartilage, bone) and the softest ones (i.e. brain, gut, skin), composed by different cells sources, types of matrices, in terms of both stiffness and chemical properties, degree of porosity and spatial and cellular organizations, with the aim to provide realistic features to the models [66,67]. In particular, these models, allow to reproduce in a personalized, customized and precise manner, units of organ or tissue, since they take into account the heterogeneity of the tissue and the geometry, providing a realistic physical, chemical and cellular gradient in the z-axis, which should improve *in vitro* model for the drug testing and the consistency of the readouts. 3D bioprinting allows to create multi-layered structures, with different shape and complexity, in which cells are embedded inside an artificial ECM, usually composed by synthetic (i.e. PEG, pluronic) or natural (i.e. hyaluronic acid, collagen, alginate, gelatin) hydrogels, that provide mechanical support, biological activities, cell growth, cell proliferation and cell orientation and oxygen gradient. Furthermore, 3D bioprinted models can combine different materials, such as hard PCL, PLLA, with hydrogels to produce composite scaffolds, with the aim to exploit the chemical, mechanical and bioactive properties of all the materials to promote cell growth, differentiation and proliferation [68-70]. In this way, cells can arrange themselves inside the hydrogels in different shape, such as spheroids, aligned, randomly, reproducing the native structure of the *in vivo* condition thanks to mechanical and chemical signal provided by the matrices. In order to enhance the bioactivity of the artificial ECM, it is also possible to combine hydrogels with growth factor, proteins or bioactive molecule [71-73]. Different type of cells can be loaded in the hydrogels and can be deposited in a patterned way, in order to create a high level of cellular complexity for all those tissues which displays multi-layered cell types, such as skin [74-76], lung [75,76] and intestinal barrier [77].The selection of the materials and cell types depends on the type of tissue to be replicate and on the technique used to produce the models.

Many 3D bioprinted models have been produced for drug screening such as liver, heart and muscle, cancers and vascularized tissues [78], which will be discussed in detail in the paragraph 1.8.

1.2.3. Specialized 3D culture platforms

An important consideration when moving from 2D cultures to 3D constructs is the maintenance of mass transport and dynamic flux. With the improving in fabrication technologies, (i) **microfluidic devices** and (ii) **organ-on-a-chip model** integrated with 3D culture systems, have become a central tool to reproduce dynamic *in vivo* environment.

Microfluidic devices are designed for cell cultures under perfusion conditions, suppling oxygen and nutrients and, at the same time, removing waste. The devices are usually simple and mainly consist of microchannels and microchamber which host cells spheroids. Microfluidic devices can be built to mimic cells shear forces found *in vivo* such as that one produced by blood flow to endothelial cells [79]. Furthermore, microfluidic devices allow for the continue application of drugs or other soluble molecules such as growth factors, or the exchange of fluid between different compartments that may harbor different types of cells. In these systems, fluids are confined in devices that have a significant dimension on the micrometer scale. Due to this extreme confinement, the volumes used for drug assays and similar studies are tiny (milliliters to femtoliters), and special physics apply. In a microfluidic device there are only laminar flows and no turbulences, which grants an extremely high control over the fluids employed, diffusion of drugs and the progress of reactions. In order to guarantee cell growth in 3D morphology, PDMS can be functionalized with biological molecule and the flow can be tuned to obtain the suitable size of spheroid [80].

A limited number of cells can be introduced inside microfluidic devices mainly via hanging drop. Cells can flow through the microchannels reaching the microchamber in which the spheroid is formed during time. One of the best in vitro models for cancer is a tumor spheroid, which comprises a gel-free system. A microfluidic device was developed by incorporating microwells that induced the seeded human carcinoma cells HT-29 to aggregate and create spheroids spontaneously. Subsequently, the formed spheroids were exposed to multiple doses of 5-fluorouracil, and cell viability was investigated by measuring spheroid size. The created spheroids showed high viability for 10-12 days, which suggests this culture system is a promising platform to study drug effects in the long-term analysis [81].

In other cases, considering the importance of the presence of an ECM to provide oxygen gradient and mechanical strength, several gel-supported 3D cell cultures in microfluidic devices have been designed using native ECMs such as agarose, collagen, hyaluronic acid, fibronectin, and fibrin [82-84]. In one study, a combination of collagen and hyaluronic acid in a microfluidic channel was used to mimic angiogenesis *in vitro,* to study endothelial cell sprouting and migration. The use of both hydrogels improved adhesion, migration, and proliferation of human umbilical vein endothelial cells (HUVECs) in response to the vascular endothelial growth factor (VEGF) [85]. On the other hand, doxorubicin was perfused through a microfluidic channel containing breast cancer cells encapsulated within an alginate hydrogel and cultured into a 3D tumor spheroid. Compared to 2D cell culture, doxorubicin had lower effectiveness on cell viability and proliferation [86].

However, these systems still suffer from some limitations, such as the restricted simulation of the complex cell-cell and cell-matrix interactions to investigate cell behavior.

For this reason, **organ-on-a-chip** platforms were developed starting from microfluidic devices in order to incorporate functional units with a minimal number of living components of an organ that sufficiently retains the tissue- and organ-level interactions. They refer to an artificial, miniature model of a human organ on a microfluidic cell culture chip. The chip usually consists of a series of well-defined structures, patterns, or scaffolds. Therefore, the position, shape, function, and chemical and physical microenvironments of the cells in culture can be controlled with high spatiotemporal precision using microfluidics. They have been described for a variety of organs including heart [87,88], liver [89,90], neural tissue [91-93] and gut [94,95]. An example, is the heart-on-chip system which allows the investigation of contractility and electrophysiological behaviors under *in vitro* conditions along with the quantification of cardiac tissue contractility under various conditions of health, disease, and exposure to chemical agents [96]. Another example, is represented by a human gut-on-a-chip model which consists of two micro-channels separated by a porous flexible membrane coated with ECM and lined by human intestinal epithelial cells (Caco-2) [95]. A slow fluid flow generated low shear stress over the channels, and a cyclic strain was exerted to mimic physiological peristaltic motions. The developed model allowed spontaneous growth of 3D villi-like structures and quantified the trans-epithelial electrical resistance (TEER), which was three to four-fold higher than that of static Transwell cultures.

With the advancement of these 3D culture technologies, organs-on-a-chip are poised to provide advanced tools for drug development and high-throughput screening in the future.

1.3. 3D cell cultures techniques

Scaffold-based cultures, non-scaffold-based cultures and specialized 3D cultures can be formed through different methods and technologies. The generation of non-scaffold-based cultures, such as cellular aggregates or spheroids, is realized by exploiting the inherent cell self-organization process which can be produced through simple methods such as (i) **hanging drop methods**, (ii) **low attachment plate** and (iii) **magnetic levitation**. Scaffold-based 3D cultures, which include spheroids, organoids and 3D bioprinted scaffolds, can be formed through various methods, based on more or less complex technologies, such as (i) **porous and fibrous-scaffolds supporting growth**, (ii) **bioreactor** and (iii) **3D bioprinting** technologies. 3D specialized cultures are mainly fabricated by means of **soft lithography**, a low-cost, easy to use and high-resolution technology that allow the fabrication of customized and ultra-precise pattern that can range from nanometer to micrometer precision, depending on the needs and application.

1.3.1. Hanging drop, low attachment plate, magnetic levitation

Hanging drop methods is a well-known 3D culture technology which exploit self-aggregation of cells into spheroids when a surface is not available for cell attachment. Spheroids can be created in specialized plates with open, bottom-less wells that are designed for the formation of a small droplet of media. The droplet is big enough for cells suspended in the medium to aggregate but small enough to prevent it from being dislodged during manipulation. Cultured for several days, cells in hanging drop plate (HDP) can form spheres that may represent tumor layers in the vicinity of a capillary, a peripheral layer with proliferating cells due to the closeness to the supply of oxygen and nutrients, underlaid by an intermediate layer with quiescent cells and an inner necrotic core [97]. These spheres can form oxygen and nutrient gradients and provide a reservoir for the accumulation of waste, accompanied by low pH. Hanging drop cultures have found applications in cancer research [98,99], in toxicity testing in hepatocytes [100] or in engineering cardiac spheroids [101].

Similar to hanging drop method, **microplates** with round, tapered or v-shaped bottoms, take advantage of the lack of cell attachment surfaces to promote aggregation of cells and spheroid formation. This method is one of the oldest techniques to generate self-assembled cellular structures in media for 3D cell culture. This system inhibits the attachment of cells to the surface of the culture plate, resulting in force floating of cells. Force floating improves cell-to-cell interactions, enabling multicellular aggregation. To provide attachment-resistant cell surfaces, cell culture plates or surfaces are coated with polymers that possess low cell-binding properties, such as 2-hydroxyethyl methacrylate (poly-HEMA) [102], polyethylene glycol [102], chitosan [102], agar [102], and agarose [102].

In **magnetic levitation** technique, cells are preloaded with magnetic nanoparticles and then, using an externally applied magnetic field, are floated toward the air/liquid interface within a low adhesion plate to promote cell-cell aggregation and spheroid formation. Magnetic levitation has been used to generate spheroids from cells of various tissue, to form cellular or multicellular spheroids for tissue engineering [103], regenerative medicine [104] and tumor modeling for drug screening [105,106].

1.3.2. Bioreactors

Bioreactors enable the precise and reproducible control over many environmental conditions required for cell culture, such as temperature, pH, suitable flow rate of culture media, oxygen, nutrient supply, and waste metabolite removal. In addition, complex system of bioreactors can be designed to apply of external forces on the scaffolds to encourage differentiation and maturation when it is required. Thanks to the ability to provide dynamic mass transport, bioreactors are really useful to control and accelerate cell seeding and to fine tune drug administration in a scaffold. In the last case, 3D models are not constantly in direct contact with the drugs, at the same concentration in a static environment, but they experience a drug transport mechanism which more resemble the physiological scenario.

Bioreactors can be mainly grouped into (i) **rotating wall vessels** [107], (ii) **hollow fibres** [107], (iii) **spinner flasks** [107], (iv) **mechanical force systems** [107] and (v) **direct perfusion systems** [107].

Rotating wall vessels provide continuously moving culture conditions where cell constructs are grown under low shear stress forces and enable high rates of mass transfer. In this situation, the speed of rotation ensure that constructs are in continuous free-flow [108].

Hollow fibre systems are used for cells that have a high metabolic rate. Cells are usually seeded within a matrix or scaffold contained porous fibres. The medium is then perfused externally over the fibres to increase mass transfer [109].

Spinner flasks can be used to seed cells into constructs and also culture them thereafter. Seeding is conducted by the introduction of cells into the medium and their perturbation by the spinner, generating convection currents. Mass transfer for subsequent culture is maintained by the spinner mechanism [110-112].

Mechanical force systems exploit the mechanism by which tissues respond to force during growth. Cells such as osteoblasts are known to be mechanoreceptive and respond to force with the activation of intracellular signal transduction pathways [113]. Secondary messenger signals arising can control gene expression and determine the expression of differentiation genes thereafter, and consequently enhance conditions for 3D construct maturation [113].

Direct perfusion systems allow the culture medium, drugs or other external substances to pass through the construct with a controlled rate and path [114,115]. A major advantage here is the ability to seed cells directly into the scaffold under flow conditions which usually allows for a high seeding efficiency [114,116]. The control of medium flow enables cell adhesion and growth, where a high mass transfer rate is typically achieved throughout the entire construct [115,116].

1.3.3. Soft lithography

Scaffold-based microfluidic and organ-on-a-chip culture systems can be produced by etching silicon wafers, using traditional electronics manufacturing principles [117]. Since silicon is expensive and opaque, which is a critical limitation with respect to designing biological experiments, the soft elastomer polydimethylsiloxane (PDMS) was employed, due to its prized for its optical transparency, elastic features, biocompatibility, and permeability to gases. The process of PDMS systems production usually involves several steps. First, a mold is created. The layout of the channels within this mold is printed directly onto a mask via a high-resolution printer. This mold is then used to outline the channel positions on photoresistant material on a silicon wafer, using a photolithographic process. The cured material is left protruding off the silicon. This is called the “master.” The PDMS system is thereafter cast using the master and cured for 2 h at 60 °C [117]. After the curing process is complete, the PDMS stamp is removed. The PDMS system now has the channel structures etched at the bottom and can be adhered to another flat sheet of PDMS, glass, or other materials, in order to seal the channels.

1.3.4. 3D bioprinting

In recent years, three-dimensional (3D) bioprinting has occupied a prominent place among all other methods for producing tissue scaffolds [118].

3D Bioprinting is a rapid layer-by-layer additive manufacturing process based on the classic 3D printing technology, in which biomaterials and/or cell-embedded hydrogels (bioink) are deposited from the bottom to the top, to create well-designed and precise three-dimensional structures by using computer-aided software (CAD). Besides, it is a rapid and inexpensive method to generate geometrically precise scaffolds and offers precise control over the composition of cells and biomaterials, associated with spatial distribution, and architectural accuracy. Moreover, its ability for precise placement of high-density cells in the desired location by using multiple types of cells and bioinks in an orderly fashion, mimics heterogeneous architectures of native tissues. It also allows the formation of vascular structures capable of recapitulating the structural features of human tissues.

The precision of the final printed constructs not only depends on the technology resolution but also on customizable parameters, such as bioink selection, cell-type, nozzle-type, printing rate, 2D and 3D imaging of the CAD modeling, thus on the type of bioprinter [118].

The entire biofabrication process could be divided into three steps:

(a) pre-bioprinting (modeling/design),
(b) bioprinting,
(c) post-bioprinting (maturation and assessment of the models).

In the pre-bioprinting process, the CAD model has to be designed to represent the desired features of the targeted tissues or organs and the appropriate bioink has to be selected considering its printable capacity and its chemical/mechanical properties that should replicate the ECM environment.

The bioprinting process can be divided into two categories: (i) acellular bioprinting and (ii) cellular printing processes. In the first case, one or more biomaterials are deposited without being mixed with cells prior the printing process; on the contrary, in the second case, the biomaterials, which are specifically hydrogels, are intimate mixed with one or more cell types prior printing process, to form the so called bioink. It is stated that it is also possible to combine both processes in one stage of bioprinting, whether the bioprinter provides of multiple bionks holders, in order to exploit the potentiality of the materials in terms of their mechanical, chemical and biological properties. Anyway, independently on the type of bioprinting process, the material chosen to be printed is directly loaded into the bioprinter and deposited layer-by-layer inside standard multiwell or bioreactors to form a model, which might represent a functional organ unit, a tissue or an ECM niche, by following the software command which generally convert the CAD model in G-code or STL file format.

Finally, the post-printing stage involves the maturation and the assessment of the model. The model's maturation includes (i) cell proliferation and maturation, (ii) cell morphological changes, (iii) ECM remodeling and (iv) genes and proteins expression. These processes can be detected and followed through standardized biological assays along with optical/confocal images, which are helpful to assess the biological model's functionalities. Furthermore, when the printing process is performed inside the bioreactors (direct perfusion bioreactor) the provided dynamic *in vitro* environment ensures a more realistic maturation process and, consequently, more consistent biological activities and functionalities with respect to the static 3D bioprinted models (i.e. models printed inside standard multiwells).

1.4. 3D bioprinting technologies

As mentioned in the previous paragraph, the structure, shape, resolution, composition and precision of the final 3D printed models, strictly depend on the type and technology of bioprinter, which differ for specific features such as resolution, mechanism, speed, volume, stability, type of bioinks, cell density, and cost effectiveness. Three different bioprinting technologies can be identified: (i) inkjet-based bioprinting, (ii) laser-assisted bioprinting and (iii) extrusion-based bioprinting (Figure 1.).

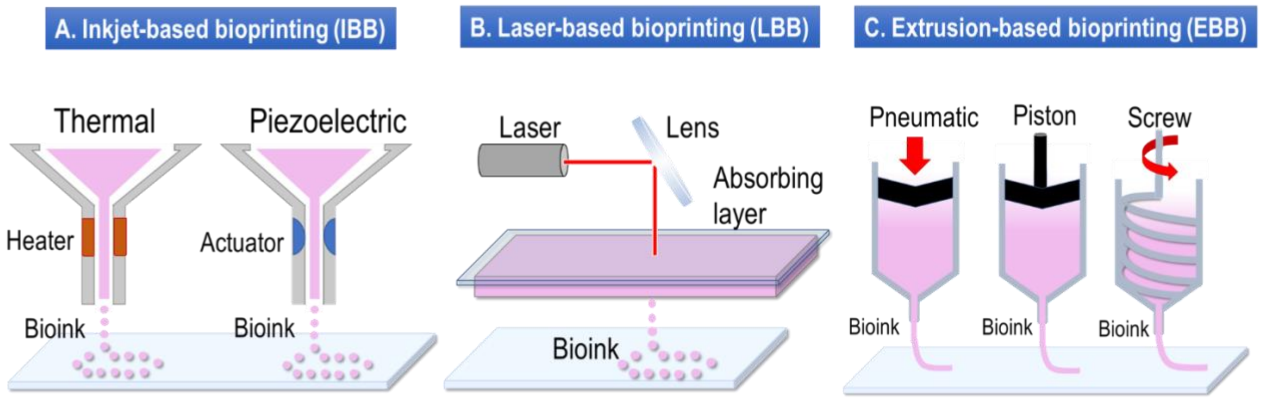

Figure 1. Representation of different bioprinting technologies: (a) Inkjet-Based Bioprinting (IBB), (b) Laser-Based Bioprinting and (c) Extrusion-Based Bioprinting.

1.4.1. Inkjet-based bioprinting

Inkjet bioprinting (IBB) or drop-on-demand bioprinting was initially used for 2D ink-based printing and it was later modified by replacing the ink in the cartridge with bioinks, and the paper with an electronically controlled elevator stage.

Currently, inkjet bioprinting can be performed on bioprinters that are custom-designed to handle and print biological materials with high precision, speed, and resolution.

Inkjet bioprinting is based on the ejection of drops of liquid onto a substrate by exploiting thermal or acoustic forces. In the case of acoustic inkjet technology, a piezoelectric crystal is employed to create acoustic waves inside the print head to break the liquid into droplets. When a voltage is applied to a piezoelectric substance, a rapid change in shape is induced. This, in turn, generates pressure required to force droplets out of the nozzle (Figure1a). Regarding the heat inkjet bioprinting, this technology can be achieved by electrically heating the print head to generate pressure that causes the release of droplets from the nozzle. The droplet formation process can be affected by two types of factors: (1) bioink properties and (2) process parameters. The bioink properties include cell type, cell density, and polymer concentration. The bioprinting process parameters include excitation waveform (e.g., excitation voltage, rise time, dwell time, fall time, echo time, and frequency), nozzle speed, nozzle diameter, and air gap. Both bioink properties and process parameters have a significant impact on the droplet formation processes, thereby affecting droplet velocity and volume. Since bioinks should display low viscosity to properly form droplets. It is possible to use different cross-linking methods after droplet formation and deposition to improve the mechanical properties of the materials and stabilized the final 3D printed construct, such as (i) ionic cross-linking method, where a liquid contained a crosslinking agent (usually ionically-based water solution) is placed inside a reservoir platform which instantly cross-linked the bioink droplet [119] (Figure 2 a) or (ii) sprayed on the top of the printed structures [120] (Figure 2 b); (iii) UV light cross-linking method, where the bioink droplet deposition is followed by UV light exposure [83] (Figure 2 c).

The advantages of inkjet printing include high spatial resolution (50-300 µm) [71], high printing speeds (up to 10000 drops /s) [121], and also its low cost. In addition, the modification of commercially available inkjet printers into 3D bioprinters is a cost-effective adaptation utilized in many labs to fabricate tissue constructs. However, inkjet bioprinting presents many challenges. These include the ejection of liquid phase bioinks within a limited range of viscosity (3.5-12 mPa) and the inability to print thick constructs due to a discretized flow. In a thermal inkjet bioprinter, the applied heat which causes evaporation can cause transient pores in the cell membrane, as the temperature in the nozzle could reach ~ 300 °C or even higher [121]. The excessive thermal stress may negatively impact the functionality of cells and cell viability. There is also a risk of cell lysis in the high frequency range of piezoelectric pulse. Additionally, in order to maintain a high cell viability in a printed construct and avoid nozzle clogging, bioinks for the inkjet bioprinting usually have to be prepared with a reduced cell density (less than 10^6 cells/ mL) compared to natural tissues. In conclusion, inkjet printing is not an ideal choice if one intends to print larger, more complex and clinically relevant sizes of constructs for bio-fabrication, because this technology can only generate continuous small droplets.

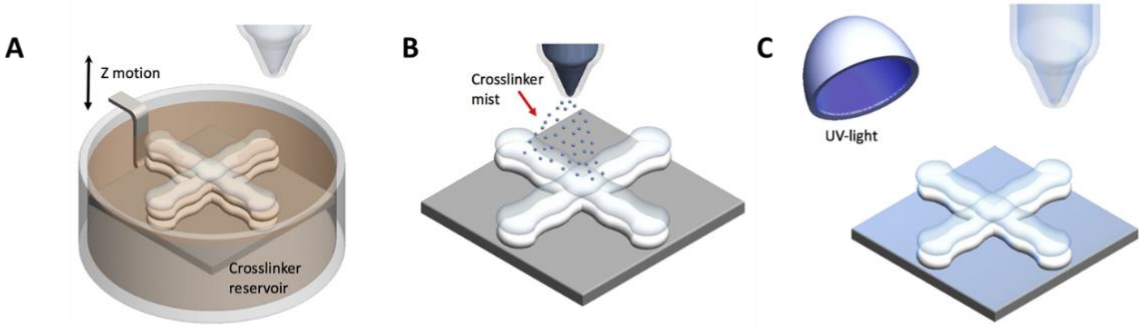

Figure 2. Schematic representation of different cross-linking methods after LBB droplet formation: ionic-crosslinking methods through (a)cross-linker reservoir or (b) cross-linker spraying on the top of the printed structure; (c) UV-light crosslinking methods. Figure re-adapted from [122].

1.4.2. Laser-assisted bioprinting

The laser-assisted bioprinting (LAB) process is direct writing based on laser-induced forward transfer (LIFT) technology initially developed for high-resolution patterning of metals for computer chip fabrication. It consists of three main parts: (i) a pulsed laser source, (ii) a ribbon, and (iii) a receiving substrate, as represented in Figure 3. Nanosecond lasers with UV wavelength such as excimer laser 193 nm, 248 nm, or near UV wavelength such as 1064 nm are usually used as energy sources to obtain a pulse energy deposition with 1-20 μJ/pulse. The ribbon is a multilayer component comprised of transparent glass, a thin layer of laser absorbing metal, such as gold or titanium, and a suspended layer of the bioink that is composed of cells, hydrogels, and bioactive factors. When the laser beam pulses at a specified time duration that focuses on the ribbon, the metal layer on top of the hydrogel is vaporized, which will create a high-pressure bubble that ejects the bioink droplets onto the receiving substrate. The receiving substrate contains culture media to support growth after the cell droplets are transferred from the ribbon to the substrate. The resolution is defined as cells are printed successively in a continuous manner at desired coordinates.

The resolution of LAB varies from picometer to micrometer in size and it is influenced by many factors, including the laser fluence (energy delivered per unit area), the surface tension, the wettability of the substrate, the air gap between the ribbon and the substrate, and the thickness and viscosity of the biological layer. Because LAB is nozzle-free, the problem of clogging with cells or materials that plague other bioprinting technologies is avoided. LAB is compatible with a range of viscosities (1–300 mPa/s) and can print mammalian cells with negligible effect on cell viability and function [122,123]. LAB can deposit cells at a density of up to 10^8 cells/ml with microscale resolution (20-80 μm) of a single cell per drop using a laser pulse repetition rate of 5 kHz, with speeds up to 1,600 mm/s [124]. This non-contact bioprinting approach has several advantages. Firstly, there is no contact between the bioinks and the dispenser, which leads to a decreased chance of contamination as compared to in-contact printing methods. Moreover, a highly viscous bioink can be used while at the same time, maintaining high viability of cells (>95%) because no mechanical forces are directly applied on the cells [125,126]. Additionally, this technology can generate high resolution droplets [124].

Despite these advantages, only a relatively narrow range of printable viscosities (1-300 mPa*s) are allowed for using in laser-assisted bioprinting. Furthermore, this method is not commonly employed in the most labs due to the complexity of laser pulse control and the high cost of laser sources. Furthermore, the high resolution of LAB requires rapid gelation kinetics to achieve high shape fidelity, which results in a relatively low overall flow rate, and the preparation of each individual ribbon is time-consuming. Because of the nature of the ribbon cell coating, it can be difficult to accurately target and position cells [127].

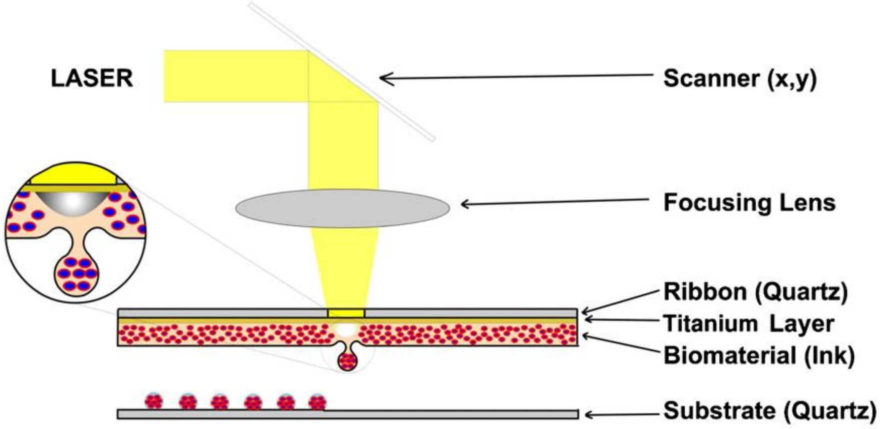

Figure 3. Laser-assistAd Bioprinting (LBB) schematic setup [128].

1.4.3. Extrusion-based bioprinting

Extrusion-based bioprinting (EBB), also known as direct writing, has been widely engaged in biofabrication and tissue engineering in recent years [129]. The bioinks extrusion takes place based on two main mechanisms: pneumatical force (gas or pressurized air) and mechanical force (screw and piston). For all the extrusion mechanisms, the bioink is loaded into the syringe and placed on the printer header. Then, in the case of the pneumatic mechanism, a continuous air or gas pressure is applied to the surface of the bioinks, while the mechanical one applies mechanical force to the surface of the bioink using a piston or a screw-based movement, which provides rotational force to continuously extrude the bioink through nozzles with different diameters.

These methods are compatible with a wide range of biomaterial's fluid properties which display viscosities ranging from 30 mPa/s to 6 × 10^7 mPa/s [130] and possess shear-thinning properties (non-

Newtonian behavior), thus meaning that they are able to flow through a nozzle, decreasing their viscosity, by applying an external force.

The extrusion bioprinting process involves three main steps, as reported in Figure 4: (i) a pre-printing step, in which the bioink is in a static temporary condition inside the syringe; (ii) a printing step, in which the materials undergo an high shear stress at the nozzle level that allow the formation of continuous filament; (iii) a post printing step, in which the shear rate decreases and the filament is deposited onto the printer plate, causing a sharp increase in viscosity.

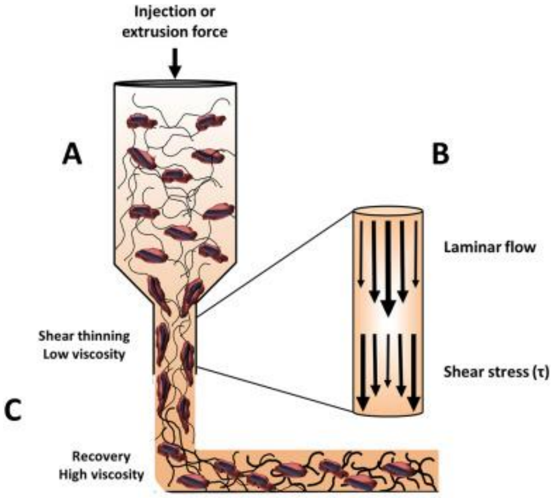

Figure 4. Schematic representation of the entire extruded-based bioprinting process of a bioink (composed by a hydrogel, represented by the chain, and cells, represented by the corpuscles) inside a syringe. (a) pre-printing process (bioink is in static condition showing high viscosity), (b) printing process (bioink undergoes shear-stress displaying shear-thinning behavior) and (c) post-printing process (shear rate decreases and the bioink recovers its initial viscosity) [131].

Shear-thinning property not only depends on the chemical nature of the bioink but also on the temperature of the printing process. In fact, several hydrogels that show unsuitable parameters to be printed, such as high viscosity, at higher temperature or pressure with respect to RT or atmospheric pressure, display lower viscosity along with shear-thinning behavior. For this reason, it is possible to customize the printing process by choosing the proper printing temperature and pressure, in order to extend the number of printable bioinks.

Despite the possibility of nozzle clogging and low printing resolution (typically greater than 100 μm), the ability to print high, biologically relevant, highly viscous bioinks and hydrogels in a controlled manner, along with the economic aspects and commercial availability have made EBB the most popular technique amongst all the bioprinting technologies. Furthermore, EBB compared to other 3D printing methods enables to (i) producing tissue scaffolds using a wide variety of biomaterials and cell types, (ii) obtaining successful layer-by-layer bioink deposition with physiological cell density in a designed way, (iii) controlling structure porosity, shape, dimension of the filament by changing the nozzle size and diameters and the printable pattern, (iv) building oriented and aligned structures, useful especially to replicate muscles tissues models [132], (v) inducing relatively low cell damages, (vi) regulating, conducting stem cell growth and differentiation for many applications and (v) printing multi-bioinks at the same time, or the combination of bioinks and not cell-laden hydrogels or biomaterials [133], by using multiple printheads bioprinter [134], in order to exploit chemical, biological and mechanical properties of all the printed materials, to obtain high complex and multi-component layered structures and to obtain high control over cells distribution on the fabricated models.

In the Askari et al. review, the most recently reported scaffolds produced through EBB, i.e., skin, bone, cartilage, vascular, neural, and muscular tissues, are systematically discussed with an emphasis on the advanced extrusion-based fabrication techniques and on the importance of the selection of the suitable bioinks and printing process parameters, to get complicate, precise, heterogeneous and functional 3D models [129]. A summary of the differences between the most common printing techniques, ECC, IBB and LAB, in terms of viscosity of the bioinks, cell density, resolution and ability to form complex structures is reported in Table 1.

Table 1. Summary of the most common bioprinting techniques.

Technique	Extrusion-based bioprinting (EBB)	Inkjet-based bioprinting (IBB)	Laser-Assisted Bioprinting (LAB)
Viscosity (mPa×s)	High value 30-6×10^7	Very low value 3.5-12	Low value 1-300
Cell density (Cell/mln)	High cell spheroids	Low (< 10^6)	Medium (~ 10^8)
Resolution (μm)	>100	50-300	20-80
Structure	Thick, complex	Very thin	Thin

1.5. Hydrogels for 3D bioprinting

In 3D bioprinting, hydrogels are used as bioink materials, in combination with cells, or as cell delivery vehicles. As mentioned in the previous paragraph, the selection of the appropriate hydrogel, along with suitable cells type, plays a crucial role for the effective fabrication of the targeted model.

Hydrogels are three-dimensional network structures permeable to oxygen and nutrients and capable of taking on large amounts of water, which make them attractive for use in biological applications.

They consist of polymer chains which can form chemical or physical crosslinks and/or chain entanglements that typically prevents the hydrogel from dissolving, therefore retaining structure and stiffness. When used for 3D cell culture application, the hydrogel properties can be adapted to match the specific use and tissues, since they are biocompatible, typically biodegradable, and a majority of them possess specific cell binding sites that are desirable for cell attachment, spreading, growth, and differentiation. Furthermore, thanks to their ‘gelling’ consistency and ability to flow under applied shear force, hydrogels, in combination with cells, are widely employed for 3D bioprinting applications.

The successfulness of the fabrication process mainly depends upon properties of the bioink and, in particular, on the properties of the hydrogel component such as chemical, physical and recovering kinetics properties, which are correlated with the ability of the polymer to recover their mechanical properties and mechanically support the fabricated models after printing process. Furthermore, a suitable bioink should provide the growth factors, adhesion factors, signaling proteins, and mechanical and structural properties of ECM, in order to promote a suitable environment for cell survival, viability, and differentiation.

Hydrogels can be classified in function of their source (i.e. natural, semi-synthetic and synthetic), structural composition (i.e. homopolymers, copolymers, IPN), cross-linking methods (i.e. UV light and ionic) and responsiveness to stimuli (i.e. temperature and pH).

1.5.1. Hydrogels classification

1) *Source of hydrogel*

Natural hydrogels. Many polymers used for 3D bioprinting comes from nature source including alginate, collagen, fibrin, chitosan, gelatin, hyaluronic acid and nanofibrillar cellulose, which is extracted from wood. Among these natural hydrogels, some of them are also natural constituents of the ECM such as collagen, fibrin, and hyaluronic acid, thus can strictly replicate the *in vivo* ECM environment.

These polymers have advantages of inherent biocompatibility, are abundant in source and present natural binding sites, which provide the interaction between cells and matrix [135]. However, low stability, poor mechanical properties and rapid degradation rate are major disadvantages of the natural-based hydrogels.

Alginate

Alginate is a polysaccharide extracted from brown algae, which is a natural anionic polymer electrolyte. It is a strictly linear copolymer that composed of two monosaccharides of a-L-guluronic acid (G) and b-D-mannuronic acid (M) respectively. Because of its abundance, inexpensiveness and biocompatibility, it is widely employed in the biofabrication field, especially for 3D bioprinting applications [136]. When alginate interacts with divalent ions, such as Ca^{++}, Sr^{++}, a dense 3D structure called an "egg box" is formed, which improves its mechanical properties. However, it may be hard to control the degradation rate and the instantaneous crosslinking process, as it is a considerable challenge for cationic polymers. The major disadvantages of alginate are the poor not tunable mechanical properties as well as poor cell adhesion [136]. To overcome these limitations, hybrid hydrogels can be formed by combining alginate with other type of polymers, which could be synthetic or natural ones. For example, the combination of alginate and polyethyleneglycol diacrylate (PEGDA) is useful to achieve toughness greater than natural cartilage due to a PEG network with a high elasticity and reversible crosslinking quality under deformation of alginate [137][138]. On the other hand, because of the poor adhesive property of alginate-based hydrogel, RGD sequences peptides are used to improve cell adhesion [139,140]. Mooney group successfully developed a model where GRGDY-modified alginate hydrogel showed cellular interaction between the hydrogel and mouse skeletal myoblasts [141]. Another solution to improve alginate mechanical properties, regards the possibility to chemically modify alginate functional group with methacrylate group, in order to obtain a semi synthetic polymer with photo-curable and tunable mechanical properties [136].

Collagen

Collagen is one of the major components of ECM protein existing in mammalian tissue. Collagen contains unique helix structure where three left handed polypeptide helices intertwine together into a right-handed triple helix, and at the ends of each helix peptide bonds are crosslink adjacent helices. Even though collagen can be extracted from almost every living animal, the source for tissue engineering applications includes porcine skin, bovine skin and tendons, and rat tail among others. Collagen types I, II, III, V, and XI are only known for making collagen fibers out of 29 distinct collagen types up to date. Among all the collagen types, type I collagen (Col-I) is the most studied in 3D bioprinting due to its ability to undergo self-assembly to form fibrous hydrogels [142]. Type I collagen stays in liquid or low viscous form at low temperatures while, increasing temperature (37 °C) or remaining at neutral pH, forms fibrous hydrogels. However, Col-I has an intrinsic limitation due to the slow gelation, since it takes half an hour to form gel at 37 °C. Because of this slow gelation, the required structural stability cannot be achieved after bioprinting. Also, the slow gelation reduces homogeneity of the cells in the hydrogel, since the cells move downwards and stabilize in the bottom due to the gravity. Thus, the use of only collagen in 3D bioprinting field is challenging and, due to its weaker mechanical properties and slow gelation rates, it is usually employed with a supporting material, such as alginate and gelatin [143] or mixed with other natural polymer and then crosslinked with physical or chemical crosslinking methods [144].

Gelatin

Gelatin is one of most essential biopolymers, which is a soluble protein obtained by the irreversible process of partial hydrolysis of collagen [145]. It can be derived from fish, insects and the skin of land animals. Unlike its progenitor collagen I, which is weakly acid soluble, gelatin is a water-soluble natural polymer that can absorb 5-10 times the equivalent weight of water. When the temperature is increased, the dissolution speed can be accelerated to certain degree. Gelatin solution has an amphoteric behavior because of the presence of alkaline amino acids and acid functional groups.

Gelatin is a polydisperse peptide with high molecular weight and because of its gelling, thickening characteristics, biocompatible and thermo-responsive properties, it is a popular material for biomedical use and for 3D bioprinting application [146]. Gelatin hydrogels can be formed via chemically [147-151] and physically crosslinking methods [152-155]. However, chemical crosslinking usually involves genipin which might affect cell viability and it is not easy to handle during 3D bioprinting while physical crosslinking is a reversible process and does not provide stable mechanical properties at 37 °C during incubation time. In fact, a typical property of the gelatin solution is the capability to be gelled at low temperature (about 20-30 °C) by cooling to form hydrogels. This process is known as sol-gel transition process, in which locally ordered regions among the gelatin molecules take place, that are subsequently joined by non-specific bonds, such as hydrogen, electrostatic and hydrophobic bonds. The resultant hydrogel has a unique thermo-reversible character, since the non-specific bonds can be easily broken by heating.

Since gelatin show short degradation rates, poor mechanical properties and lack of thermal stability, it is possible to overcome these limitations by modifying its molecular chains by adding methacrylate groups, which make the gelatin methacrylate a new semi synthetic photo-crosslinkable polymer with tunable mechanical properties [156].

Synthetic hydrogels. Differently from natural polymers, the chemistry of synthetic polymers is tunable, so that physicochemical and mechanical properties of synthetic hydrogels can be optimized. Additionally, different molecular weights, block structures and degradable linkages can lead to tunable mechanical properties and degradation rate. Lack of adhesion sites, biocompatibility, and degradation products are some disadvantages of synthetic based hydrogels.

Among the most used synthetic polymers, which display high compatibility with cellular system, are: poly(ethylene glycol) (PEG), poly(acrylic acid) (PAA), poly(ethylene oxide) (PEO), poly(vinyl alcohol) (PVA), poly(hydroxyethyl methacrylate) (PHEMA), and poly(methacrylic acid) (PMMA) [142]. Synthetic structures of such hydrogels offer no biological information to cells, but can be easily tuned according to the mechanical (viscoelastic) requirements and have high uniform quality as well as defined structure. The choice of the hydrogel is dependent on the experimental setup (i.e., required stiffness, optical properties, conductive properties), material availability, and cost.

Semi-synthetic hydrogels. This class of hydrogels combine the best properties of both the abovementioned hydrogels. The resulting hydrogels have highly predictable and tunable mechanical properties and, at the same time, offer biological information and support to cells. Semi-synthetic hydrogels are often produced in co-polymerization reactions between the polymer precursor and the biological conjugate. Some examples of such combinations are hydrogels which consist of PEG, which is inert to cells, modified with peptide sequences (i.e., RGD) for cell adhesion [157,158] or PEG modified with fibrinogen [159].

Alginate methacrylate (AlgMa) and gelatin methacrylate (GelMa) are the most common examples of semy-synthetic hydrogels used for 3D bioprinting [160] since they are highly biocompatible and cell friendly, and they display high shape fidelity and stability at physiological temperature by means of photo-crosslinking with UV light and in presence of a photo-initiator. One of the most popular polymer functionalization methods is to incorporate covalent crosslinking by modifying the polymer backbone using methacrylate groups [160]. The advantages of these functionalized materials are that they are able to maintain their bioactivity, biocompatibility, cell supporting spreading and growing along with improved mechanical properties [161-165]. Furthermore, both GelMa and AlgMa maintain the characteristics of the corresponding unmodified species, such as thermo-responsive ability and physical crosslinking, respectively. In conclusion, this polymer functionalization can introduce new crosslinking methods and incorporate new biological activity into bioinks.

Hydrogels fabricated from synthetic polymers are usually covalently crosslinked networks, while hydrogels from natural polymers are physically crosslinked through conformation changes and physical interactions. By chemically modifying natural polymer chain with methacrylate groups, it is possible to exploit the dual crosslinking, in which single networks that are crosslinked in more than one way, e.g., covalently and ionically in the same network. The permanence and increased bond energy of covalent crosslinks over physical interactions has driven research into incorporating covalent functionalization into natural hydrogels to increase their strength and durability after 3D printing.

2) Structural composition

Classification by structural composition divides hydrogels into **homopolymeric** (derived from the single monomer species), **copolymeric** (derived from two or more monomer species), **interpenetrating polymer networks** or IPN.

The most widely used **homopolymer** hydrogels in 3D mammalian cell culture are collagen, fibrin, nanocellulose, gelatin methacrylate (GelMA) and alginate methacrylate (AlgMa) [141].

Copolymeric hydrogels suitable for 3D cell culture are represented by alginates, hyaluronic acid and poly(N-isopropolyacrylamide) hydrogels PEG-based copolymers (PEGMEMA–MEO2MA–PEGDA), and synthetic saccharidepeptide hydrogels.

Some examples of **interpenetrating polymer networks** are networks of dextran and gelatin, gelatin and silk fibroin or alginate and reconstituted basement membrane matrix hydrogels.

IPNs derive from two independent crosslinked polymers, where at least one of them being synthesized and/or crosslinked within the immediate presence of the other and without any covalent bonds between them. Since they are held together only by permanent topological interlocking interactions without covalent bonds in between, it is impossible to separate them from each other without breaking their own cross-linked networks. This structural composition allows to improve and enhance mechanical stability of such polymer (i.e. collagen) which alone are too fragile with low mechanical performance. Example of IPN widely employed in 3D bioprinting field are (i) gelatin-methacrylate and collagen [145,167-170], (ii) alginate and collagen [171,172] and alginate and gelatin methacrylate [173-175].

3) *Cross-linking methods*

The crosslinks between individual polymer molecules maintain the entire 3D structure of the hydrogel after swelling in water. For use in 3D cell culture (especially in the case of cell encapsulation prior polymerization) not only the polymer material, but also crosslinking reaction must be cell-friendly, which means that reaction conditions and products should not affect cell viability. Crosslinking methods can be divided into two categories: (i) physical crosslinking methods, which include thermal crosslinking, molecular self-assembly and ionic crosslinking and (ii) chemical crosslinking method, which include photo-crosslinking.

Thermal crosslinking

Most of the seaweed-derived natural polysaccharides, including agarose, and some animal-derived protein, including gelatin, elastin, and collagen, make the thermally driven hydrogels. Thermal gelation occurs at either increasing temperature or decreasing temperature, in which the transition temperatures are defined as the upper critical solution temperature (UCST), where above this temperature water and polymer are miscible, and lower critical solution temperature (LCST), where below this temperature water and polymer are miscible [165]. Three types of possible interactions are taken place when a polymer is dissolved in water, namely polymer-polymer, polymer-water, and water-water. For example, polymer exhibiting an LCST, temperature increase makes polymer-water interaction unfavourable, making the other two interactions more favourable, which results in negative free energy (G) [165]. In this type of system, water-water interaction is the “driving force” and hence the entropy of water is increased. This phenomenon is known as the “hydrophobic effect”. It is noteworthy to mention that LCST is an “entropy driven” effect while UCST is an “enthalpy driven” effect, which is the opposite to previous one.

Molecular self-assembly

Molecular self-assembly is the other form of physical gelation process. Self-assembly is driven by the noncovalent, weak bonding mechanisms such as hydrogen bonds, hydrophobic interactions, electrostatic interactions, and it is mainly dominated by the peptide and protein-based hydrogels. These hydrogels have two distinct properties which are essential for 3D bioprinted hydrogels: (i) they are shear thinning, thus show low viscosity under applied shear stress, and (ii) self-healing, ability to recover when the stress is removed. However, the major challenge in this type of system is the prolonged time for self-healing, which adversely affects the cell encapsulation [175]. Despite this, several biomimetic supramolecular systems have been developed by using host-guest structures [176].

Ionic crosslinking

The hydrogel can also be formed either chelation or electrostatic interaction, facilitating spontaneous physical gelation due to the presence of electrically charged species. These polymers are known as polyelectrolytes, which contain net charged along the polymer backbone, and crosslink to form insoluble complexes when combined with multi-valent cations or anions according to the charge of the polymer. The reason for the insolubility of these polyelectrolyte complexes in the water is the scarcity of the charged groups of the polymer, which are mutually shielded by the complex formation. Most of the natural polymers are negatively charged, such as alginate and hyaluronic acid due to the presence of carboxyl or sulfate groups. However, the presence of the amino groups in the polymer backbone make positively charged polymers like chitosan and gelatin. Calcium alginate is a prominent example for ionotropic hydrogel. Alginate is composed of guluronic acid (G units) and mannuronic acid (M units) monomers, which vary in amount and depending on the source of alginate. The presence of divalent cations such as Ca^{++} and Ba^{++} facilitate binding between the G-units of the adjacent alginate chains in an "egg-box" form. In contrast to the natural polymers, polyelectrolytes from synthetic polymers offer a wide range of controllable electrostatic properties. The most common example for the synthetic ionotropic hydrogel is the poly (l-lysine) (PLL) [177] and poly (acrylic acid) (PAA) [178].

Photo-crosslinking

The most stable and tunable hydrogels can be obtained through the formation of covalently bound hydrogels as compared to the physical cross-linking. One of the widely used strategies is crosslinking with visible or UV light through photopolymerization of sensitive to light polymers, usually those one which contain acrylate or methacrylate-modified chains.

To make this crosslinking process cell compatible, it is important to select the suitable photo-initiator to trigger the radical reaction which is responsible to the formation of crosslinks between polymer chains. In particular, the photoinitiator should be efficient in free radical generation and, at the same time, must be cell friendly, which mean that the radical process produced after UV light exposure must preserve cell viability and functionalities.

Photoinitiators can be separated into two categories (in relationship with the radical generation mechanisms): (1) Type-I photoinitiators (cleavable photoinitiators) and (2) Type-II (bimolecular photoinitiating). Type-I photoinitiators generate two radicals while the process of Type-II (e.g., benzophenone/tertiary amine) presents more complexity. For example, benzophenone is excited and promotes fast electron transfer (from the lone pair of tertiary amine), which is followed by the proton transfer process; this process provides the radical (H-donor) that initiates photopolymerization. In some cases, to avoid the UV light damaging effects, including DNA damage and cancer effects [179], some visible light photoinitiators have been investigated and demonstrated to be useful for bioprinting with cells [180].

For the reproducing of living tissues, UV sensitive photoinitiators are the most used. In particular, 2,2′-Azobis[2-methyl-n-(2-hydroxyethyl)propionamide] (VA-086), Lithium phenyl-2,4,6-trimethylbenzoylphosphinate (LAP) and 1-[4–(2-Hydroxyethoxy)-phenyl]-2-hydroxy-2-methyl-1-propanone (Irgacure 2959) have been widely employed for the fabrication of 3D bioprinted models [181] since their low toxicity and high photopolymerization efficiency have been demonstrated.

1.5.2. Mechanical and physical requirements

Mechanical requirements

The ECM surrounds most cells in tissues of complex organisms, protecting them from stress and regulating cellular functions such as spreading, migration, proliferation, and stem cell differentiation. Stiffness of the ECM is considered to have implications for development, differentiation, disease, and regeneration [31].

In physiological condition, there is a large variation in the ECM environment in terms of stiffness, starting from the neural cells, as the softer, to the cartilage and bone cells, as the stiffer. Studies have shown that by adjusting the stiffness of the matrix rather than making changes just to the biochemical environment (i.e., use of growth factors or defined media) a directed differentiation can be achieved [31].

Matching the stiffness of the hydrogel to the tissue is of interest particularly when targeting MSC (Mesenchymal Stem Cells) fates, since MSCs (and numerous other cell types) can convert external mechanical cues to intracellular biochemical signals. This ability to sense mechanical microenvironment called mechano-sensing is described in several studies and reviews [182][183][184]. Those MSCs cultured in lower stiffness hydrogel (2 kPa) show a tendency to differentiate toward cells expressing neural markers; those cultured in hydrogel with a kPa of 10 formed myocytes and those cultured on rigid substrates (40 kPa) become osteoblasts [185].

There are many examples of studies where matrix stiffness has been shown to play a role in cell development, migration or differentiation, for example, neural cells, MSC differentiation, muscle cells, breast cancer cells, and bone [186]. Some of them are relative to the anchorage-dependent mesenchymal stem cells which are highly responsive to hydrogel properties, in particular to the stiffness and pore structure, and once printed cells into the gelatin methacrylate (GelMa), they demonstrate higher spreading in low stiffness hydrogels (24 Pa) and almost no spreading when high stiffness (1537 Pa) is involved [187].

Physical requirements

In all multicellular organisms gradients of different nature (stable, temporary, physiological or pathological) can be found [31] and can be classified as physical, chemical, and biological. For example, stable physiological mechanical gradients characterize different tissues like cartilage, ligaments, tendon, bone, and tooth. Stable chemical physiological gradients such as, oxygen concentrations, pH gradient as a result of catabolite distribution, can be found by increasing the distances from blood vessels [188]. Stable pathological gradients (chemical, physical, and biological) can be found in tumors, in which fast growing cellular mass breaks tissue homeostasis. For these reasons, cellular fate is strongly influenced by the physical composition of the tissue microenvironment and, in addition, cells convert the external stimuli governed by the ECM into intracellular biochemical signals.

The influence of different microenvironmental signals can be reproduced and studied in hydrogel-based 3D models with the aim to recapitulate *in vivo* gradients and help to find an optimal niche for different cell types and co-cultures. In this context, to achieve this, it is possible to manipulate different hydrogel properties such as (i) mechanical, (ii) biological, and (iii) chemical. Mechanical gradients can be created by tuning hydrogel stiffness and pore architecture through variation of crosslinker concentration or polymerization intensity, which can be correlated with chemical gradient as well, since the oxygen permeability, for instance, is lower in that zone of the gel where the cross-linking density is higher with respect to the area with low degree of crosslinking (and porosity) [189]. For what concern the biological gradient, it is possible to introduce in the polymer backbone chain biological moieties or protein functionalities, or mix them directly within the bioink, and printing different concentration of the desired formulation in a pre-defined manner to obtain a spatial biological gradient [190].

1.6. Cell source

The choice of cells for tissue or organ printing is crucial for the correct functioning of the fabricated construct. Tissues and organs comprise multiple cell types with specific and essential biological functions that must be recapitulated in the artificial tissue. In addition to the primary functional cell types, most tissues also contain cell types that provide supportive, structural or barrier functions, are involved in vascularization or provide a niche for stem cell maintenance and differentiation.

Cells chosen for printing should closely mimic the physiological state of cells *in vivo* and are expected to maintain their native functions under optimized conditions. Furthermore, the cells used for bioprinting applications must be robust enough to survive the bioprinting process and withstand physiological stresses once transplanted, including physical forces such as shear stress and pressure as well as biological stressors including presence of toxins, enzymes and non-physiological pH.

Primary cell types are widely employed in 3D bioprinting, especially to reproduce cancer models with a targeted type of tissue, and they are extracted directly from the tissue or organ of interest. These cells are easy to access, to cultivate and to maintain and can be easily adapt to the 3D bioprinting process. However, their lifespan and number of passages are limited and the type of tissue reproducible depends on the origin and the type of the cells.

Stem cells are a promising cell type for 3D bioprinting owing to their ability to proliferate in an undifferentiated way and to generate multiple functional tissue-specific cell phenotypes [191]. Embryonic stem cells and induced pluripotent stem cells are capable of indefinite self-renewal and have demonstrated their longevity by maintaining their undifferentiated state for over 80 passages. The capacity of pluripotent stem cells to generate large numbers of cells highlights the potential of these cells for bioprinting [192]. Other types of stem cells, such as adult stem cells from bone marrow and fat or perinatal stem cells from amniotic fluid or placenta, are thought to have a more limited multipotent differentiation potential but are considered safer for clinical transplantation. With established protocols for the isolation, expansion and differentiation, mesenchymal stromal cells (MSCs) may also be a promising cell source for bioprinted constructs. Clinically relevant numbers of MSCs have been successfully generated *in vitro* for clinical trials, and future advances in cell-culture techniques are likely to make use of other stem cell populations for bioprinting clinical applications a realistic possibility [193-196].

Advances in cell culture techniques as well as in reprogramming and directed differentiation methods will be important for providing highly proliferative, functional, nonimmunogenic and robust cell populations that are suitable for bioprinting applications.

1.7. Correlation between rheological properties and printability

In order to successfully predict the capability of a hydrogel to undergone 3D bioprinting process, is crucial to characterize some fundamental parameters, such as shear-thinning behavior, recovery of mechanical properties after printing process and mechanical stability of the final printed model, which are strictly correlated with rheological parameters such as loss (G’’) and storage (G’) moduli and viscosity. In this paragraph, the specific considerations regarding the importance of rheological properties of a candidate bioink to predict its printability and the generated constructs are discussed.

In 3D extrusion-based processes, a bioink initially present a bulk resting state (pre-printing stage), displaying high value of viscosity, undergoes a transition to a high shear condition while passing through the nozzle (printing process stage), takes a new shape, and finally reaches a new resting state (post printing stage), as mentioned in the paragraph 1.4.3. The key rheological properties describing these transitions are **viscosity**, **viscoelastic shear moduli** and **elastic recovery**.

Viscosity (η) is the resistance of a fluid to flow under the application of stress and has a great influence on both the print fidelity and efficiency of cell encapsulation. Generally, higher viscosities result in higher printing fidelity but also leads to increased shear stress, which can affect cells viability suspended in the bioink. The main factors determining the viscosity of polymers in solution are molecular weight, concentration and presence of entanglements, thus the higher is the concentration, the molecular weight and the number of the entanglements, the higher is the viscosity. Viscosity is also defined as the ratio of the shear stress (τ) to the shear rate ($\dot{\gamma}$). So, when fluids show a linear relationship between shear stress and shear rate are termed Newtonian. On the contrary, fluids exhibiting deviations from linearity, with either decreasing or increasing ratios are defined **non-Newtonian**, which can be further classified into time independent (**shear-thinning** and **shear thickening**) and time-dependent fluids (thixotropic) (Figure 5).

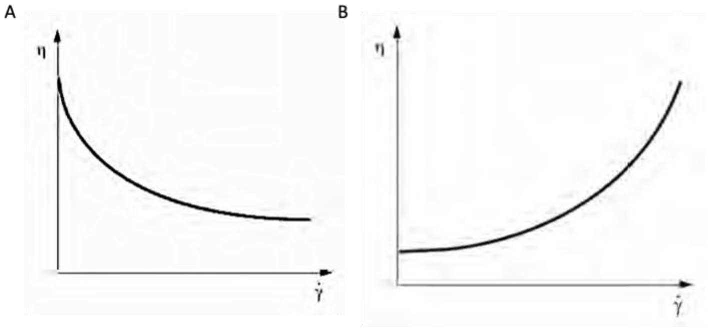

Figure 5. Hydrogel showing (a) shear-thinning behavior and (b) shear-thickening behavior [197].

Shear-thinning behavior is the most common type of time-independent non-Newtonian fluid behavior characterizing printable bioink, in which the increasing shear rates result in a decrease of viscosity that promote filament formation. An ideal bioink produces a continuous and homogenous filament without affecting cell viability. The molecular mechanisms behind shear-thinning, and the physicochemical interactions between molecular chains giving shape retention, mainly depend on polymer disentanglement and macromolecular orientation along the shear flow.

After bioink extrusion, rheological properties should show an opposite trend with respect to those reported in the shear thinning situation, since the polymers chains of the hydrogel starts to build up the internal forces responsible of the elastic shape retention. The property of displaying viscous flow and elastic shape retention is known as **viscoelasticity**. This behavior can be described using two parameters: the **storage modulus** (**G′**) and the **loss modulus** (**G″**). G′ is the measure of the amount of energy elastically stored during deformation and therefore is associated with elastic shape retention of a hydrogel. G″ measures the amount of energy dissipated by the material and therefore is linked to the viscous flow. Viscoelastic properties can be determined via oscillatory rheology, such as amplitude sweep test, whereas viscosity is measured under rotation. G′ and G″ are typically measured as a function of the frequency and amplitude of the oscillation. The G″/G′ ratio is designated as damping factor, loss tangent or tan(δ). When G' > G'', the hydrogel behaves like a 'solid-like' gel, which means the hydrogel has predominately elastic characteristic, like a solid material. On the contrary, when G'' > G' the hydrogel shows 'liquid-like' properties, resembling to a liquid with respect to a gel, as reported in Figure 6**.**

Tan δ is a parameter which identifies a suitable balance between flow and shape retention; In fact, values comprise between 0,4 and 0,5 are related to a good filament formation and high shape fidelity.

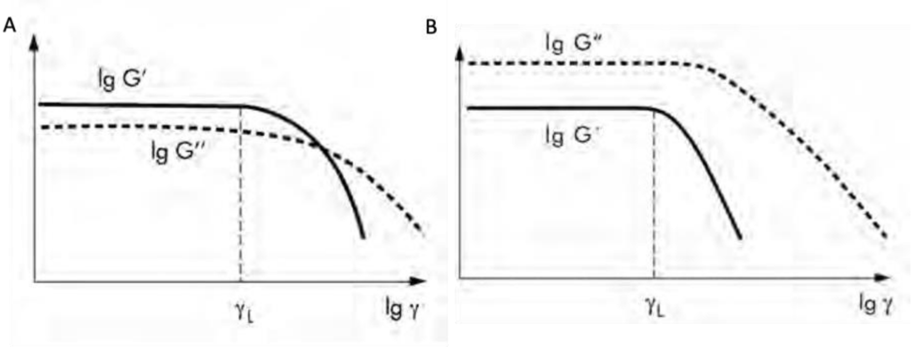

Figure 6. Amplitude sweep of samples showing (a) solid-like character and (b) liquid-like character. Graphic representation of yield point (γ_L) by evaluating storage (G') and loss (G'') moduli through amplitude sweep test (oscillation) [197].

Besides storage modulus, shape retention can also be described in terms of the yield point ($\boldsymbol{\gamma_L}$). The yield point is the shear stress value at which the range of the reversible elastic deformation (LVE) behavior ends and the range of the irreversible deformation behavior begins, as represented in Figure 6 a.

Increased yield stress of a bioink generally improves filament extrusion, reducing at the same time drops formation, and the stiffness of the final construct, but it can also affect cell encapsulation.

Furthermore, shape retention can be correlated with the shape fidelity of the final printed construct with represent the ability of the bioink to preserve and maintain the filament shape and resolution in a multi-layered structure after printing process and during time.

In general, the assessment of printability by means of rheological test can be performed in the following way. A first **oscillation test** (**amplitude sweep**) can be performed to evaluate the rheological properties of a bioink after printing process subjecting the material to increasing shear stress to assess whether the hydrogel exhibits a yield stress behavior and if it displays 'solid-like' (G' > G'') or 'liquid-like' (G'' > G') behaviour. In fact, a hydrogel to be able to form a continuous and stable filament with good shape fidelity, must show a 'solid-like' features where physical entanglements, crosslinks and chain's interactions are able to undergo the extrusion and re-form initial interactions.

The next step is the evaluation of the **shear-thinning property** by measuring the viscosity of the ink as a function of the shear rate. In this case, a hydrogel to be printable must flow under shear force by reducing its viscosity with the increase of the shear rate, as mentioned before.

Finally, **recovery tests** can be performed to analyze the ability of the materials to restore their elastic properties when exposed to alternating high and low shear stress. In fact, with a rheometer, it is possible to provide to the hydrogel an initial high shear rate, in order to reproduce the extrusion process and, after that, decrease the shear rate almost to zero, in order to evaluate how the hydrogel recovers its shape by means of reconstituting internal entanglements. The overall printability assessment process is reported in the figure 7.

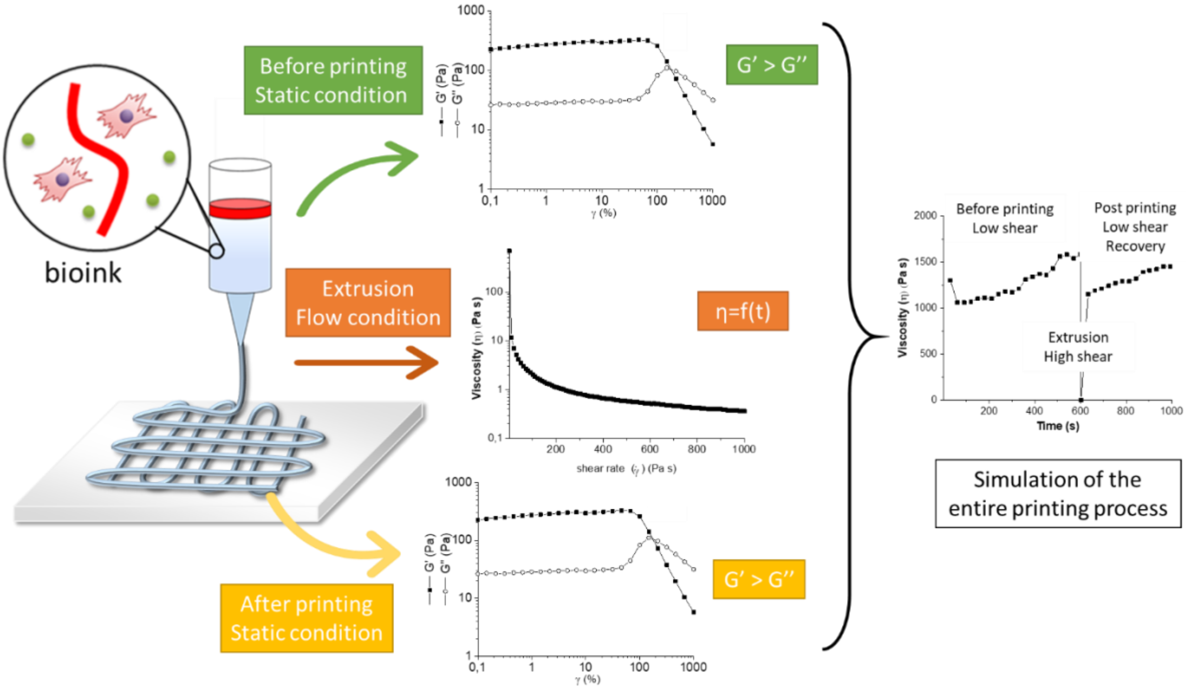

Figure 7. Schematic representation of the correlation between the printing process and the rheological characterization.

1.8. Application of 3D bioprinted models for drug screening

This section discusses the applications of 3D bioprinting technologies to build 3D organ models used for drug toxicity and drug metabolism studies. More specifically, the use of different 3D bioprinting approaches and the performance of current 3D printed tissue constructs, in terms of their drug-metabolizing potentials and drug dose responses are reviewed. Even though many organ models have been reproduced through 3D bioprinting techniques, to be proposed as alternative approaches for drug screening, only few works demonstrated their actual use for this purpose, including liver, tumor, intestine and cardiac tissue models.

Liver models

Drug-induced liver toxicity is one of the most important reasons for the interruption of a possible drug candidate development. Since the liver performs an essential role in drug metabolism, the investigation of hepatotoxicity and drug pharmacokinetics is necessary for preclinical drug studies. The liver displays a complex structure consisting of permeable endothelium surrounded by hepatocytes and several mesenchymal cells. The highly complex structure of this organ makes conventional 2D cultures inadequate for an accurate prediction of drug testing due to their lack of physiological relevance. For this reason, many 3D in vitro models have been fabricated reproducing liver environment into microfluidic systems by using soft-lithography to evaluate drugs responses [198-203]. However, new systems ensuring a better dynamic environment replication, for a more accurate evaluation of drug metabolism and hepatotoxicity, are highly in demand. 3D bioprinting is paving the way to improvement in 3D liver models, thanks to its ability to precise pattern cell-laden hydrogels forming complex 3D structures [204,205]. More specifically, different types of cells and a wide variety of hydrogels can be printed to replicate complex physiological conditions and fabricate models that better mimic 3D cellular architecture while maintaining in vitro liver functions.

Mazzocchi and co-workers fabricated a simple 3D liver microenvironment using 3D extrusion-based bioprinting and studied the hepatocyte functionality under exposure to acetaminophen (APAP) toxicant [206]. In this work, type I methacrylated collagen was prepared with thiolated hyaluronic acid and UV crosslinker. Primary human hepatocytes and liver stellate cells were mixed with the hydrogel to form printable and physiologically relevant bioink that was recognized by the cells as their own ECM. Four-spoke structures of this bioink were then printed without affecting the viability and functionality of the cell (Figure 8a). To assess the overall functionality of liver organoids, urea, albumin, α-GST- a detoxification protein, lactic acid dehydrogenase (LDH), a marker of liver damage, were measured over time by adding APAP and the results were compared with the non-treated model. A significant decrease in urea and albumin levels was observed for the APAP treated conditions, compared with the stable levels in the untreated constructs (Figure 8 b,c). Furthermore, treated constructs displayed a decrease in LDH and α-GST activities due to the toxicity-related cells death. At the same time, untreated models maintain steady LDH and a high level of α-GST (Figure 8 d,e). Considering these results, this simple 3D bioprinted liver demonstrates to be able to maintain hepatocytes viability and to support physiologic response to a well-known liver toxin. Bhise et al. reported developing a liver-on-a-chip platform for long-term culture of 3D human HepG2/C3A spheroids for drug toxicity assessment [207]. Firstly, HepG2/C3A spheroids, previously fabricated using micromolds, were mixed with photocrosslinkable gelatin-methacrylate (GelMa) hydrogel to form a printable bioink. Then a perfusable bioreactor composed of the main chamber and an inlet and outlet fluidic ports was fabricated to host 3D printed construct and to ensure to the cells physiological flow conditions (Figure 8f). Finally, the cell-laden hydrogel was directly printed within the bioreactor's culture chamber and was incubated under continuous perfusion (Figure 8g). Cellular functionality was assessed for four weeks by monitoring the concentration of four biomarkers (albumin, A1AT, transferrin, and ceruloplasmin) secreted by the hepatic construct. Moreover, cellular metabolic activity was evaluated after acute APAP drug exposure in dynamic and physiological conditions as a model for predictive drug toxicity. Aqueous media's minimum flow rate was ensured to provide sufficient oxygen and nutrient within the cell culture, representing a more realistic system with respect to static in vitro conditions. The results show that the printing process does not affect spheroids viability for all the incubation period. The liver model was able to well sustain the biomarker production for four weeks. The acute hepatotoxic dose of APAP administered to the liver construct causes HepG2 apoptosis and leads to a decrease in the biomarkers secretion levels in the bioreactor system over time, as observed in other in vitro studies [208][209]. Furthermore, while the metabolic activity increased in the bioreactor condition without APAP treatment, there was a significant decrease in metabolic activity in the bioreactor cultures treated with APAP (Figure 8 b). This metabolic response had a reasonably good correlation with in vivo APAP toxicity data [48]. Utilizing physiologically relevant dynamic models, which provide appropriate mass transport for gas and metabolite waste, becomes imperative for drug toxicity studies. Furthermore, the great challenge to developing an in vitro liver model lies in the existing limitations in recapitulating the liver microenvironment based on a complex microarchitecture and different cell combinations. In this context, Li and co-workers fabricated an in vitro hepatoma model containing highly uniform 3D tumor spheroids based on 3D co-culture cell printing to study the pharmacodynamic of a new monoclonal antibody drug known as Metuzumab [210]. Firstly, human hepatocellular carcinoma cell line and human umbilical vein endothelial cells (HUVEC) were mixed with thermo-sensitive hydroxypropyl chitin (HPCH) hydrogel and Matrigel to form a bioink, which was printed using an extrusion-based 3D bioplotter. In a second time, the printed construct was located in a microfluidic system that provided a biomimetic extracellular microenvironment to the commonly used 3D printed models and improve the pharmacodynamic test's accuracy (Figure 8h). Human peripheral blood (PBMC) was used to vehicle Metuzumab drug through the 3D printed construct inside the microfluidic system. The presence of the HUVEC printed layer provides liver filtration function for the model. In contrast, PBMC allows the whole model to serve as a platform for the antibody-dependent cell-mediated cytotoxicity (ADCC) tests. 2D and 3D co-culture printed models that are not inserted in the microfluidic system were used to compare cytotoxicity and pharmacodynamic response to Metuzumab treatment. In cytotoxicity (Figure 8 i) and pharmacodynamic (Figure 8 l) results, 3D printed liver showed a stronger resistance to Metuzumab than 2D cultures but stronger sensitivity to drug concentrations to the normal 3D printed model. These results are more similar to those obtained from animal experiments with similar mouse monoclonal antibody drugs with respect to those one obtained in 2D condition [208][209], mainly due to the more biomimetic drug transport and the 3D microenvironment.

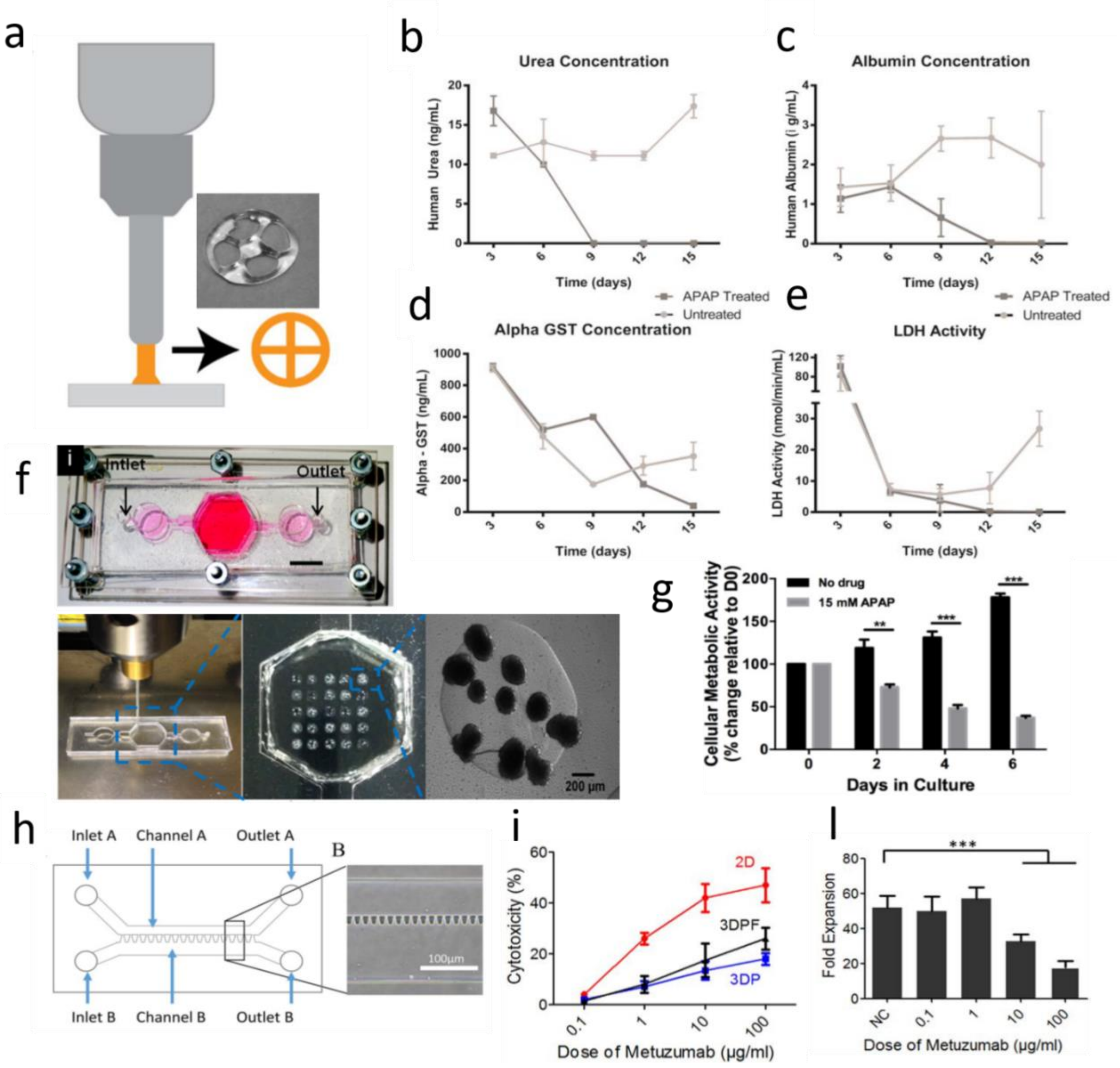

Figure 8. (a) Schematic illustration of methacrylated collagen type I printed structure combined with thiolated hyaluronic acid to obtain a liver organoid. (b,c,d,e) Evaluation of urea, albumin, α-GST, lactic acid

dehydrogenase (LDH) production with and without APAP treatment to assess the overall functionality of liver organoid. (f) Bioprinting of photocross-linkable GelMA hydrogel-based hepatic construct within the microfluidic system. (g) Cellular metabolic activity of GelMA hydrogel-based hepatic construct in the bioreactor after APAP treatment detected by Presto Blue assay. (h) Schematic diagram of the microfluidic system containing 3D printed cell-laden construct. (i) Cytotoxicity result obtained from antibody-dependent cell-mediated (ADCC) test on 3D printed cell-laden construct after Metuzumab treatment. (l) Pharmacodynamic result obtained by the following proliferation of 3D printed hepatoma cells in the microfluidic system after Metuzumab treatment [206, 207, 210].

Tumor models

Anti-cancer drug toxicity, along with drug-induced liver toxicity, is one of the reasons for the increase in the number of clinical trials failures due to the inaccurate in vitro preclinical models and the limited availability of animal models. The tumor microenvironment consists of a complex and heterogeneous tissue with various types of cells embedded in ECM. Their properties change in terms of matrix stiffening, protein composition and degrees of vascularization [211]. For this reason, printed cell-laden hydrogels can provide both suitable mechanical properties and the presence of different types of cells, thanks to the tunable rheological properties of the hydrogels and to the possibility of printing different cell sources at the same time. Here, some examples of 3D bioprinted cervical, brain and breast tumors were discussed. Zhao et al. reported a method to construct in vitro cervical tumor models by extrusion printing of Hela cells embedded in gelatin/alginate/fibrinogen hydrogels to study paclitaxel drug effects (Figure 9 a) [212]. The anti-cancer drug was administered to 3D and 2D cultures by simply adding paclitaxel in the culture media. Cell proliferation and metabolic activity were evaluated before and after drug treatment and were compared with conventional 2D culture. According to experimental data, authors observed the formation of cellular spheroids in the printed construct with a higher proliferation rate than monolayer cell sheets growth in 2D culture. Spheroids showed higher metabolic activity before and after drug exposure (Figure 9 b), which was evaluated considering matrix metalloproteinase (MMP) expression, and higher chemoresistance than those obtained in 2D culture drug (Figure 9 c). It demonstrated the importance of three-dimensionality on the effectiveness of anti-cancer treatment. In another work, Wang and co-workers developed 3D-bioprinted mini-brains consisting of glioblastoma cells and macrophages. They screened different anti-cancer drugs that target the interaction between these two cell types, which plays a crucial role in glioblastoma cell progression [213]. A two-step extrusion printing process was proposed in this work to fabricate a tumor model. Firstly, the mouse macrophages cell line (RAW264.7) was printed, conferring a spherical shape with an empty cavity to the construct. In the second printing step, the cavity was filled with mouse glioblastoma cells (GL261) embedded into photocrosslinkable GelMa, to incorporate a mass of glioblastoma tumor into brain tissue containing macrophages (Figure 9 d).

Data demonstrated that the low stiffness and the high cell-cell interaction provided from this 3D microenvironment increase the production of glioblastoma biomarkers and allow an effective cross-talk between the different cell types, with respect to 2D cultures on stiff plastic, as shown in physiological conditions. Furthermore, tumor cells can attract macrophages to their site and educate them to support their survival and fast growth. Lastly, the Authors demonstrated the suitability of this co-culture model to be used for the screening of different types of drugs by following the metabolic activity of the cells after drug treatment (Figure 9 f,g). Results highlighted that tumor isolated from 3D co-culture had a higher growth rate compared to monoculture and 2D models and that, after anti-cancer (BCNU) treatment, the growth of the tumor isolated from the 3D co-culture (Figure 9 f) is strongly inhibited compared to the other models (Figure 9 e). It is established that chemotherapy works more efficiently in rapidly growing cells [214] and co-culture with macrophages significantly enhanced the tumor cell growth, which can be significantly inhibited by chemotherapy.

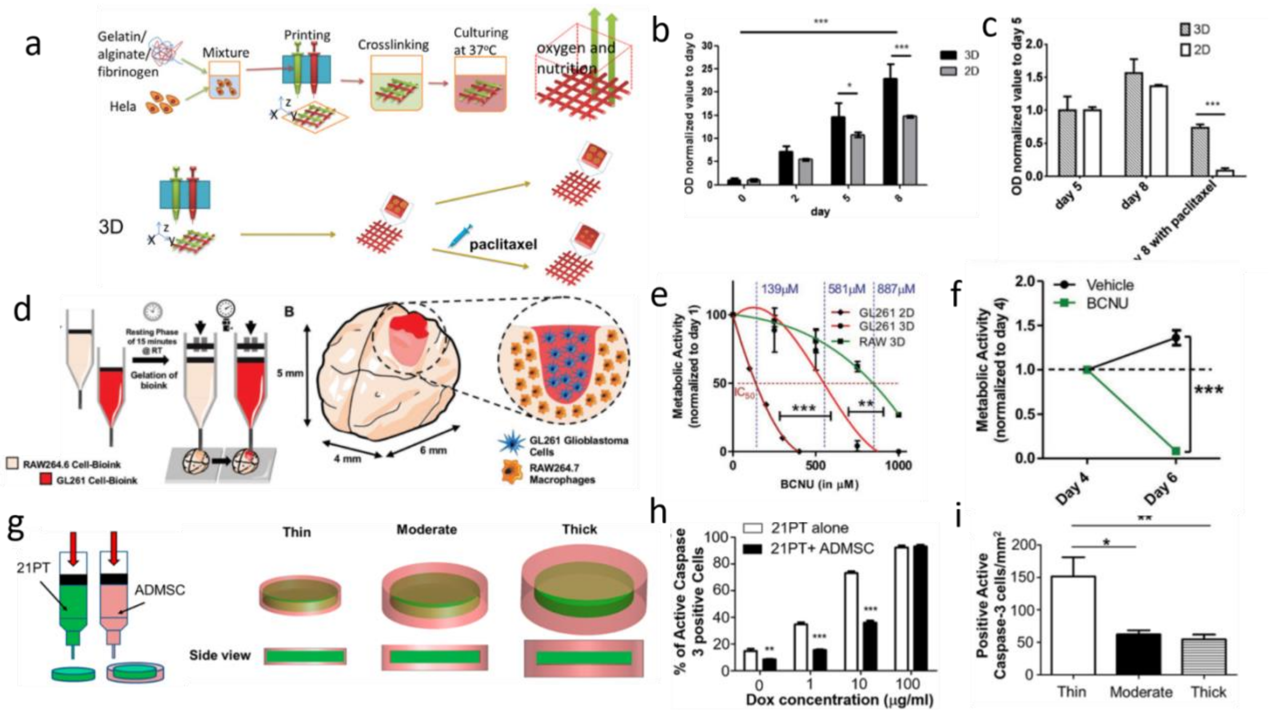

Figure 9. (a) Schematic illustration of the 3D cell printing process (up) and design of the 3D Hela/hydrogel constructs (down). (b) Cellular metabolic change in 2D planar culture and 3D Hela/hydrogel constructs. (c) Cellular metabolic activity after paclitaxel treatment in 2D planar culture and 3D Hela/hydrogel constructs. (d) Schematic representation of the cell-laden GelMA-gelatin bioinks preparation for the bioprinted mini-brains. (e) Concentration-dependent metabolic activity of GL261 cells in 2D monolayer and GL261 and RAW264.7 3D monocultures after treatment with BCNU. (f) Metabolic activity of GL261 after co-culture with RAW264.7 after treatment with vehicle or BCNU. (g) Schematic of breast cancer bioprinting process using dual cell laden bioinks (left) and schematic of bioprinted constructs with thin, moderate, and thick ADMSC layers (right). (h) Percentage of cells that were stained positive to cleaved Caspase-3 based on IF staining analysis. (i) Positive cleaved Caspase-3 cell density in the middle region in the bioprinted constructs with different ADMSC layer thicknesses [212, 213, 215].

In another work, 3D breast cancer in vitro model was fabricated by Wang et al. by using extrusion-based bioprinting to study doxorubicin (DOX) drug resistance [215]. Photocrosslinkable methacrylated hyaluronic acid (Me-HA) and GelMa hydrogels were used in the vehicle printing process of breast tumor cell line (21PT) and primary human ADMSC, the most common stromal cells found in the breast cancer microenvironment. More specifically, 21PT was printed with a disk-like shape and ADMSC was printed as a crown around the disk (Figure 9 g). Drug treatment was administered to the 3D model by simply adding DOX to the culture media. The cellular metabolic activity was evaluated by following capsase-3 protein expression, which plays a central role in the execution phase of cell apoptosis. 21PT monoculture was used as a control to understand how the concentric co-culture architecture affects DOX efficacy. In the 3D co-culture system, 21PT cells were not directly exposed to DOX treatment which first penetrate the ADMSC layers and had an apoptotic effect on the 21PT cells. In comparison, monoculture showed higher capsase-3 production since 21PT are in direct contact with DOX dose, demonstrating to be more sensitive to DOX dose (Figure 9 h). The thickness of the ADMSC layers to mimic the status of obesity was further tuned (Figure 9 g). In the moderate and thick layer groups, significantly less cleaved Caspase-3 staining was observed, indicating a lower apoptosis rate (Figure 9 i). Moreover, the matrix remodeling process produced from ADMSC and 21PT was observed by evaluating the hydrogel stiffness after 21 days of culture. The stiffnesses in both regions significantly increased, demonstrating matrix remodeling and stiffening.

Cardiac tissue models

Cardiovascular diseases are one of the leading causes of global deaths. Heart donors are not readily available, so there is a great need to focus on new cardiac regenerative medicines. 3D bioprinting technology has a great potential for engineering 3D tissue models for cardiovascular regeneration [216]. 3D cardiac tissue models can better recapitulate the 3D microenvironment and its impact on the cardiac cells. Millet et al. [217] created a cardiac micro-tissue with microscale alignment cues in a hydrogel scaffold consisted of a mixture of alginate, gelatin methacryloyl and photoinitiator Irgacure 2959. They validated these cardiac tissues against isoproterenol and verapamil drugs and observed measurable beating frequency and displacement changes. The developed bioprinted cardiac micro-tissues have excellent potential for high-throughput screening in drug discovery. In vitro replication of cardiac tissues remains a significant challenge due to the hierarchical structure and the strong cellular directionality of the native myocardium. The lack of vascularization brings additional complexity and limits currently available models, improving the fabrication of integrated cardiovascular organoids. Zhang et al. [218] proposed a novel strategy based on 3D bioprinting to fabricate microfibrous scaffold encapsulating endothelial cells (HUVEC) to form a layer of confluent endothelium that can support cardiomyocytes (CMs) growth in a relevant physiological tissue. The improvement of these models with respect to other 3D printed cardiac tissue consists of the combination with a microfluidic perfusion bioreactor adopted to screen pharmaceutical compounds for their cardiovascular toxicity. Firstly, a mixture of alginate and photocrosslinkable GelMa loaded with HUVEC was printed to form a multilayer grid that sustained scaffold endothelialization and vascularization (Figure 10 a1,2). Then, CMs were seeded onto the printed construct following the formation of a confluent endothelium layer (Figure 10 a3). The printed scaffold was placed in a pre-fabricated bioreactor consisting of two hemi-chambers that provide all the nutrients and allow the study of drug effect in dynamic conditions. The results showed that assembling endothelial cells within the bioprinted scaffold resembled a blood vessel structure (Figure 10 a4). Dose-dependent response of both cardiomyocytes and endothelial cells was observed in perfusion conditions. The human-derived myocardial organoids seemed to have slightly lower endurance than those of rat origin (Figure 10 b,c,d,e).

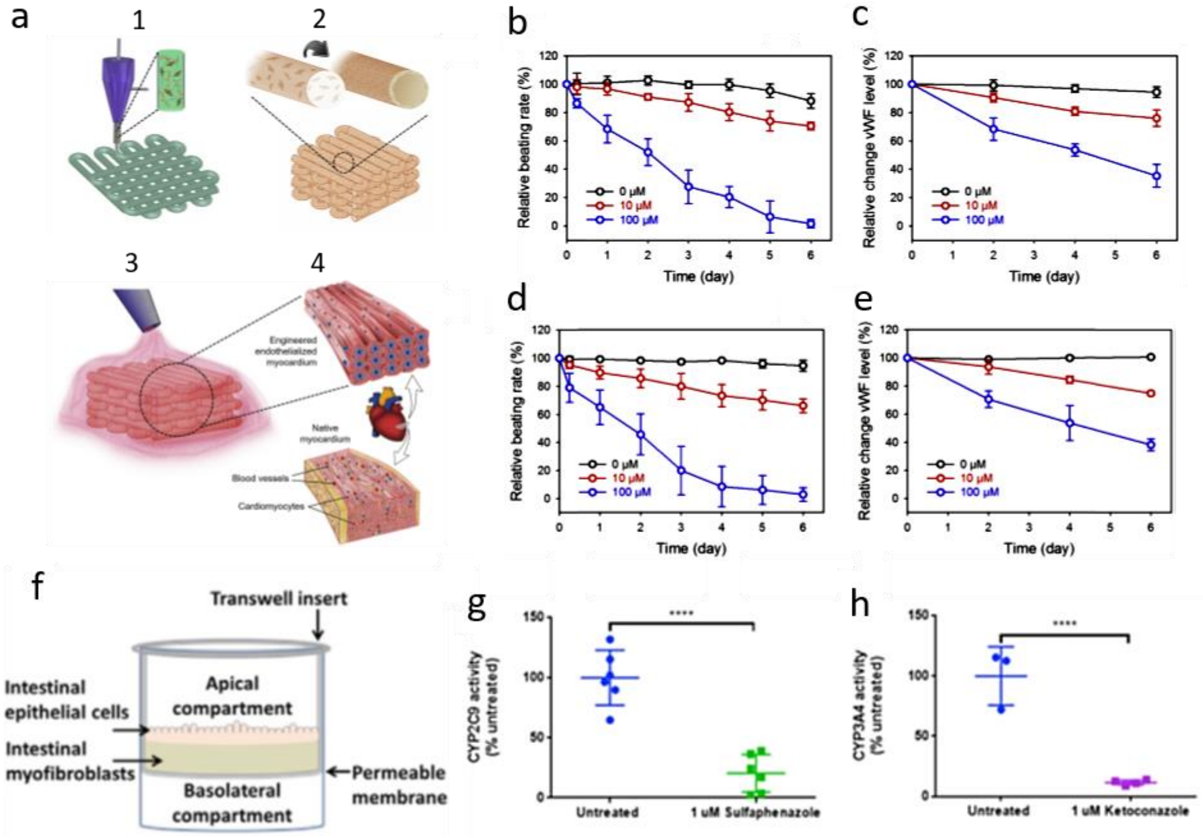

Figure 10. (a) Schematic representation of fabricating endothelialized myocardium using the 3D bioprinting strategy. (1) Bioprinting of a microfibrous scaffold encapsulating endothelial cells. (2) Formation of the vascular bed through migration of HUVECs to the peripheries of the microfibers. (3) Seeding of cardiomyocytes into the endothelialized scaffold. (4) Formation of engineered endothelialized myocardium.

(b) Relative beating of the endothelialized myocardial tissues and (c) the levels of vWF expression by the endothelial cells, respectively, upon treatment with different dosages of doxorubicin. (d) Relative beating of the endothelialized human myocardial tissues and (e) the levels of vWF expression by the endothelial cells, respectively, upon treatment with different dosages of doxorubicin. (f) Schematic representation of interstitial layer containing 3D printed adult human intestinal myofibroblasts (IMF) and adult human intestinal epithelial cells (hIEC). Evaluation of 3D intestinal tissue metabolic activity considering CYP2C9 (g) and CYP3A4 (h) enzymes activity [218, 219].

Intestine models

The human intestinal mucosa plays a crucial role in the drugs absorption, distribution, metabolism, and excretion (ADME) process, which can be altered by undesirable side effects involving drug-induced toxicity. This phenomenon contributes to attrition in drug development and points out the need for better preclinical intestinal models. Many developments were made to mimic the intestinal barrier's phenotypic composition and hierarchical architecture, mainly achieved by using soft-lithography or photo-lithography techniques [219]. Recapitulation of intestinal tissue structure through 3D bioprinting remains challenging due to the highly complex structure of intestinal villus and cellular arrangement. Recently, Madden et al. generated a 3D printed intestinal tissue comprising of human primary intestinal epithelial cells (IMF) and myofibroblasts, whose cellular architecture and function mimic the native intestine [219]. Different 3D intestine models were printed into transwell culture inserts composed of a permeable membrane placed over a basolateral compartment (Figure 10 f) [219]. The developed polarized epithelium with columnar epithelial morphology, tight junctions, and villus-like shape formation, maintained its stability for more than two weeks, as reported from the histological characterization. Furthermore, the evidence of mucus production and mucin-2-expressing goblet cells and lysozyme-expressing Paneth cells obtained from the immunohistochemistry suggests this system's potential ability to model mucosal barrier function. In particular, mucin-2 expression confirmed the presence of goblet cells and mucous secretion, a feature similar to that one observed in the native tissue and an indication of normal intestinal function [220]. In addition to goblet cells, other specialized cell types present in the intestinal epithelium included lysozyme-positive Paneth cells and chromogranin-expressing enteroendocrine cells. Patterning of 3D intestinal tissues was similar to that observed in native intestinal tissue and consistent between multiple donors [219]. Moreover, the tissue architecture of the 3D intestinal model was also compared with that of standard Caco-2 monolayer culture [219]. Caco-2 monolayers achieved a polarized epithelial phenotype with tight junction formation, although epithelial morphology appeared less columnar and lacked secondary structure formation. Different compounds were tested to assess drug toxicity and intestine metabolism. More specifically, the metabolic function of 3D intestinal tissue was assessed by evaluating the expression of two major intestinal Phase I cytochrome P450 metabolic enzymes (CYP2C9 and CYP3A4) after exposure to sulfaphenazole and ketoconazole. Results demonstrated the expression of key enzymes involved in xenobiotic metabolism, including CYP3A4 (Figure 10 g,h), an enzyme known to be absent in 2D models [220]. Drug toxicity was evaluated in response to indomethacin, a known toxicant, and the tumor necrosis factor-alpha (TNF-a) [219]. Indomethacin treatment seemed to inhibit prostaglandin E2 secretion, confirming the known mechanism of activity as previously reported *in vitro* by Tomisato et al. [221] and *in vivo* by Boelsterli et al. [222]. Histological analysis further illustrated dose-dependent disruption of epithelial morphology with decreased E-cadherin expression, consistent with the loss of barrier function [219]. Furthermore, since the release of inflammatory cytokines may also damage the intestine, and TNF-α is a major contributor to disease-related inflammation and intestinal toxicity [223,224], to evaluate the susceptibility of the model to pro-inflammatory cytokines, tissues were dosed with TNF-α for 24 hr and evaluated for changes in morphology, LDH release, and gene expression [219]. Results showed that TNF-α altered the epithelial morphology leading to the dissociation of cells from the interstitial layer accompanied by a significant increase in LDH release, suggesting a cytotoxic response and enterocyte death. Finally, as a general consideration, this work [219] suggested that the human intestinal tissue proposed combined with the 3D bioprinting platform makes this system a practical and useful *in vitro* tool for ADME/Tox drug testing, thanks to its compatibility with standard assay approaches.

Conclusions and critical outlooks

3D cell culturing methods provide an excellent alternative to traditional 2D cell cultures and animal testing, for the assessment of drugs' effectiveness and side effects, even though they are still in their beginning stages. These methods have the unique potential of bridging the gap between 2D culture and native tissue and for this reason they are increasingly used in medical research for tissue regeneration and, more importantly, for disease modeling, and drug discovery [223,225]. 3D tissue models are especially promising to better understand and treat human diseases [224] and to obtain more physiologically relevant information for both basic and translational sciences.

Although 3D bioprinting represents an automated technique, easily adaptable to the high-throughput screening, it must overcome several technological challenges. For instance, inkjet technology is limited to a range of viscosity from 3.5 mPa s to 12 mPa s, the thermal inkjet bioprinter may reach certain temperature which can negatively impact cells functionalities and the piezoelectric inkjet bioprinter could induce cell lysis in the high frequency range of piezoelectric pulse [226]. Additionally, in order to maintain high cell viability after the printing process and avoid nozzle clogging, bioinks for the inkjet bioprinting are usually prepared with a reduced cell density with respect to those contained in the natural tissues [226]. Similar consideration can be applied to laser-based bioprinting since only a narrow range of viscosities (1-300 mPa s), which requires rapid gelation kinetics to achieve high shape fidelity, can be printed [128]. Furthermore, this technology is not commonly used as bioprinting technique due to the complexity of the laser system control and its high cost of maintenance, although it can achieve a wide range of resolution from the highest of 20 µm to the lowest of 300 µm [128]. Finally, extrusion-based bioprinting is the most employed technique in the labs since it is easy to manage at an affordable cost and it allow to obtain thick and complex 3D structures even by using different bioink viscosities ranging from 30 mPa s to 6×10^7 mPa s [129]. Despite these advantages, this technology is limited by frequent nozzle clogging, low printing resolution (typically greater than 100 µm) [129], and the bioink not always fulfil specific mechanical requirements.

Furthermore, 3D bioprinted models for drug testing must overcome several technological, regulatory and ethical challenges prior to inclusion in the drug screening pipeline. Firstly, these models lack of key physiologically features which, at the moment, are fully recognized only by the animal models, such as the reproduction of tissue vasculature and incorporation of multi-cellular components which cooperate each other's in a synergic way during drug-tissue interaction. Strategies involving decellularized matrix in combination with 3D bioprinting have been tested to improve the vascularization of these 3D tissues but development on the ability of these models to sustain long-term vascular integration still remains challenging. Secondly, the reproduction of dynamic physiological conditions plays a crucial role for the evaluation of drug effects since it can improve readouts and reduce the number of failures. As reported in the present paragraph, most of the 3D models are mainly employed in static condition, and only few works evaluate drug effects in dynamic flow by combing 3D printing technologies with bioreactors or microfluidic systems [198][199][200][201][202][203]. Finally, the acceptance of a 3D bioprinted model for drug testing applications still requires a long validation process involving reference drugs based on a large set of well documented and already accepted experiments. The main example of a human-relevant in vitro model is the 3D bioprinted skin currently used in cosmetics field [227]. After validation of the model by testing different compounds with well-known mode of action on the skin, the 3D skin model is now considered as an acceptable *in vitro* system for skin irritation testing, demonstrating to be an excellent model to predict drug effects on humans [227].

2. Experimental section

2.1. Hydrogel synthesis

2.1.1. Materials

Sodium alginate (Mw: 200 kDa) was purchased from Carlo Erba; Sodium alginate protanal LFR 5/60 (Mw: 20-80 kDa) was gifted by DuPont; Gelatin from Porcine skin Type A, Gel strength 300 was purchased from Sigma Aldrich; 2,5% w/v Suspension of Type I Collagen was gently provided by TypeOne Biomaterials s.r.l.; Carbonate Bicarbonate Buffer (CB), Methacrylic Anhydride (MAA) (Sigma Aldrich), NaOH 5 M (Sigma Aldrich) and HCl 37 % (Sigma Aldrich) were used for the methacrylation of both alginate (AlgMa) and gelatin (GelMa) hydrogels. Dialysis Membrane 12-14 kDa (Sigma Aldrich) and ultrapure water (Milli-Q H2O) were used for the product purification. Phosphate Buffered Saline (PBS) (Sigma Aldrich) and Calcium Chloride (Sigma Aldrich) were used for the preparation of GelMa and AlgMa hydrogels, while the initiator 2-Hydroxy-4'-(2-hydroxyethoxy)-2-methylpropiophenone (Irgacure 2959) (Sigma Aldrich) and a solution of calcium chloride 40 mM were used for the crosslinking process.

2.1.2. Alginate-methacrylate synthesis optimization

Alginate methacrylate (AlgMa) was prepared by grafting the methacrylic group of the methacrylic anhydride (MAA) into the alginate backbone chains. Although this mechanism of reaction is well-known and widely reported in the literature to produce photocrosslinkable natural-based hydrogels, such as gelatin-methacrylate [156], collagen-methacrylate [228,229], hyaluronic acid-methacrylate [230] and chitosan-methacrylate [231], it is usually based on a laborious practice, which involve numerous pH adjustments during the whole reaction time, to maintain the suitable pH necessary to promote the substitution of the methacrylic group on the hydroxyl group of the alginate carboxylic functionalities. Furthermore, the high molar excess of MAA usually required to achieve a good degree of substitution, make this traditional approach not affordable and not easy to handle. For this reason, in this Thesis, an affordable alginate methacrylation process was accomplished by adapting for the first time the new gelatin methacryloyl synthesis proposed by Shirahama et al. [156] to the alginate polymer chains, in order to make the AlgMa production easier and more manageable and to reduce the excess of MAA used in the reaction.

Alg (2 % w/v) was dissolved in 0.325 M carbonate (CB) buffer at pH 9. Subsequently, excess of MAA (1 mL/g Alg) was dropped into the alginate solution under magnetic stirring at 500 rpm and 50 °C. Once the reaction starts, methacrylic acid sub product is formed and the pH tends to decrease below pH 6. For this reason, NaOH 5 M was added to the reaction until the solution reaches again pH 9, in order to promote the methacrylation process. The reaction proceeded for both 24 h and 72 h, at 50 °C, and the pH was stable for the entire process between 7.5 and 8. Then the solution was dialyzed for 6 days at room temperature (RT), under gentle stirring and protected from light. Then, the dialyzed solutions were filtered with 0.2 µm sterile filters and freezed at -20 °C prior lyophilization. Finally, the samples were lyophilized overnight at – 45 °C and 0.32 Bar and stored at 4 °C protected from light until further use.

2.1.3. Gelatin-methacrylate synthesis

Gelatin methacrylate was obtained through a methacrylation reaction, as reported for the AlgMa synthesis, between the hydroxyl groups and the primary amino groups of the gelatin chains and the MAA, under suitable conditions of pH, temperature, and initial concentration of reagents. The traditional preparation method of GelMa was originally developed by Van Den Bulcke et al. [156]. Over the years, the synthesis of GelMa has been optimized with the aim to reduce the laborious synthesis timing and the several pH adjustments required to run the reaction. For this reason, to accomplish the gelatin methacrylation in the most effective way, CB buffer was employed with respect to the traditional PB solution, which turns out to be the best solvent to carry out the reaction by yielding a high degree of substitution (ca. 90 %). 10% (w/v) of gelatin type A (10 g) was dissolved under vigorous stirring in a 0,25 M (99ml) CB buffer in a two-neck round-bottom flask (250 ml of capacity), by heating at 50 °C through an oil bath. The pH of the solution after gelatin solubilization reached a value of 8. Thus, in order to overcome the isoelectric point of the gelatin and to ensure the de-protonation of the NH_2 groups, the pH was increased up to 9 by using few drops of NaOH 5M. The reaction started with the addition of MAA (0,1ml/gr of gelatin) at 50°C under a rigorous stirring at 500 rpm. The reaction proceeded for 1h at 50°C and then it was quenched by adding HCl, bringing the pH to 7.4. In order to remove methacrylic acid sub-product produced during the reaction and any traces of unreacted methacrylic anhydride, the mixture was dialyzed through 12-14 kDa MWCO (molecular weight cut-off) dialysis membranes for 5 days against ultrapure water (Milli-Q), at 37°C under a vigorous stirring (500 rpm), changing the Milli-Q water every 3 hours. At this point, the solution was freezed at -20°C overnight and lyophilized at -45°C and 0.32 Bar of pressure. The lyophilized product was stored at -4°C protected from the light until further use.

2.1.4. Collagen synthesis

Collagen extraction and synthesis were completely carried out by Typeone Biomaterials s.r.l. The collagen formulation (from equine tendon) was directly provided by the company as a stable suspension at neutral pH and concentration of 2.5 %. The extraction and synthesis process are protected by patents.

2.2. Cell culture

In this Thesis, HeLa cell line, Human skin fibroblast (HSFs) patient's derived, human colonic fibroblasts CCD-18Co (HIFs), Caco-2 cell line and Human colonic epithelial (HCTs-8) cell line tumour's derived were employed as biological components to reproduce living 3D bioprinted *in vitro* models.

2.2.1. HeLa cell culture

HeLa cells (ATCC, CCL-2) were employed during all experiments. Both bidimensional and three-dimensional cultures were maintained in Dulbecco's Modified Eagle's Medium (Microgem, TL1006) supplemented with 10% Fetal Bovine Serum (South America; Microgem, RM10432), 2 mM L-glutamine, 50 U/mL penicillin, 50 µg/mL streptomycin (Microgem) and cultured at 37°C, 5% CO2. Bidimensional cultures were passed upon trypsin digestion every two or three days; growth medium of 3D constructs was changed every two or three days.

2.2.2. Human fibroblast cell culture

Human skin fibroblasts (HSFs) patient's derived and **human colonic fibroblasts CCD-18Co (HIFs)** (ATCC, CRL-1459) cell line were selected in this Thesis to evaluate their different migration and invasion capability in different 3D models. Both cell types were gently provided by the centre of "Investigación Biomédica" from the University of Granada. HSFs were used after approval by the ethics committee. HFs were isolated from samples of human skin (3 x 3 cm) obtained from donors which were transported from operating room to the laboratory in sterile pots containing a solution of 98.28% Dulbecco's Modified Eagle's Medium (DMEM) high glucose and without phenol red (Sigma Aldrich, St Louis, MO, USA), 0.8% Penicillin Penilevel 600.000 U.I. (ERN Laboratories, Barcelona, Spain), 0.5% Amphotericin B solution 250 µg/mL (Sigma Aldrich), 0.4% Gentamicin GENTA GOBENS 20 mg/mL (Normon Laboratory, Madrid, Spain) and 0.02% Vancomycin 500 mg (Ramón Sala Laboratory, Barcelona, Spain) and they were finally processed in the following 24 h. All human samples used in this study were obtained after informed consent and authorization was provided from the Granada Provincial Ethics Committee (Ministry of Health and Families, Andalusia, Spain, reference: 0467-N-20). Once in the laboratory, tissues were introduced in Air Flow Cabinets Type II (Labconco, Kansas City, MO, USA) and washed in a solution constituted of 98.28% Dulbecco's phosphate-buffered saline (DPBS; Sigma Aldrich), 0.8% Penicillin Penilevel 600 000 U.I. (ERN Laboratories), 0.5% Amphotericin B solution 250 µg/mL (Sigma Aldrich), 0.4% Gentamicin GENTA GOBENS 20 mg/mL (Normon Laboratory) and 0.02% Vancomycin 500 mg (Ramón Sala Laboratory) for 30 min. Then, HFs from dermis were isolated and cultured after a process that combine mechanical and enzymatic disaggregation. Briefly, dermis was mechanically detached and was incubated overnight at 37°C under constant agitation in 10 mL of type I collagenase solution (GIBCO, Thermo Fisher Scientific, Waltham, MA, USA). Detached fibroblasts were collected by centrifugation and expanded in culture flasks containing DMEM supplemented with antibiotics (100 U/ml of penicillin G, 10 mg/ml of streptomycin and 0.025 mg/ml of amphotericin B) and 10% of FBS and then incubated at 37°C in 5% CO_2. The medium was changed every 3 days, and subcultivation of the cells was carried out using a trypsin/EDTA (0.5/0.2 g/l) solution at 37°C for 10 min.

HIFs cells were cultivated in T75 flasks and maintained in Dulbecco's modified Eagle medium (1X) + GlutaMAX (DMEM; Gibco) enriched with 10% (v/v) of Fetal Bovine Serum (FBS; Gibco) and 1% (v/v) of penicillin/streptomycin (Gibco;10,000 U/mL) in a 5% CO_2 incubator at 37 °C. The culture media was changed every 2 days and subcultures were obtained by using 0.25% of trypsin (Gibco) for 10 min at 80%-90% of confluency, in order to allow the detachment of the cells from the flasks.

2.2.3. Human epithelial cell culture

Caco-2 cell line (ATCC, HTB-37) was gently provided from the University of Bologna (Fabit department, Prof. Enzo Spisni's research group). Cells were cultivated in T75 flasks and maintained in Dulbecco's modified Eagle medium (1X) (DMEM; Gibco) supplemented with 10% (v/v) of Fetal Bovine Serum (FBS; Gibco), 1% (v/v) of penicillin/streptomycin (10,000 U/mL; Gibco) in a 5% CO_2 incubator at 37 °C. The culture media was changed every 2 days. Caco-2 cells were subcultured in T75 flasks by using 0.25% of trypsin (Gibco) at 80%-90% of confluency for the detachment from the flasks.

Human colonic epithelial (HCTs-8) cell line (ATCC, CCL-244) tumour's derived was selected in this Thesis thanks to its high migration, proliferation rate and ability to autonomously reproduce villi-like structure. Cell line was provided by the centre of "Instrumentación Cientìfica" from the University of Granada. HCTs-8 cells were cultivated in T75 flasks and maintained in Gibco Roswell

Park Memorial Institute (RPMI 1640; Gibco) supplemented with 2mM Glutamine, 1mM Sodium Pyruvate (NaP), 5% Horse Serum (HS; Gibco) + 5% Fetal Bovine Serum (FBS; Gibco) and 1% (v/v) of penicillin/streptomycin (Gibco;10,000 U/mL) in a 5% CO_2 incubator at 37 °C. The culture media was changed every 2 days. HCTs-8 were subcultured in T75 flasks by using 0.25% of trypsin (Gibco) at 80%-90% of confluency for the detachment from the flasks.

2.3. Hydrogel and bioink preparation

2.3.1. Alginate methacrylate

AlgMa-based hydrogel was prepared by weighing and dissolving lyophilized AlgMa in PBS (1X) at 37 °C through a sterile disposable composed by two syringes of 5 ml attached with a luer lock that close the system allowing the solution mixing in sterile condition by avoiding any leaks. After that, the AlgMa solution 4% (w/v) produced, is mixed with a water-based solution of $CaCl_2$ 60 mM, in a ratio of 25:10 v/v, in order to obtain the hydrogel and confer to it good printability and mechanical stability prior the mixing with the cells. The concentration of the pre-crosslinking $CaCl_2$ solution and the ratio between the AlgMa and calcium chloride solution were selected as the best conditions after several trials with other pre-crosslinking solutions. Then, by starting from this hydrogel formulation, two different AlgMa-based inks were developed, named as **AlgMa ink A (AIA)** and **AlgMa ink B (AIB)**, resulting from the mixing between the pre-crosslinked AlgMa hydrogel formulation and the Irgacure 2959 (I2959) at 0,2 % w/v (AIA) and 0,25 % w/v (AIB), respectively. Finally, 100 µL of HeLa cells (10^6 cells/100 µL of cell culture media) were gently mixed with 1 mL of each ink formulation to form **AlgMa bioink A (ABA)** and **AlgMa bioink B (ABB)**, respectively.

2.3.2. Gelatin methacrylate

GelMa 5 % (w/v) hydrogel was prepared by weighing and dissolving lyophilized GelMa in a sterile disposable composed by two syringes of 5 ml attached with a luer-lock that close the system allowing the solution mixing in sterile condition by avoiding any leaks. This double-syringes system was covered and then immersed in a water bath heated at 37°C, in order to promote GelMa solubilization which is a well know thermo-dependent sol-gel process. In fact, over 32 °C GelMa displays liquid features while under 32 °C starts to become a gel phase, which is the typical behavior of the upper critical solution temperature (UCST) hydrogels. After the hydrogel preparation, Irgacure 2959 was added to get a final concentration of 0,1 % (w/v) to produce **GelMa ink (GI)**. Finally, 100 µL of human skin fibroblast (HSF) (10^6 cells/100 µL of cell culture media) and 100 µL of human intestinal fibroblast (HIF) (10^6 cells/100 µL of cell culture media) were separately and gently mixed with 1 mL of GelMa hydrogel to form the corresponding **GelMa bioink HSF (GB_{HSF})** and **GelMa bioink HIF (GB_{HIF})**, respectively.

2.3.3. Collagen

Collagen suspension hydrogel was provided from Typeone Biomaterials directly ready-to-use at 2.5 % (w/v) and with a neutral pH. In this particular case, collagen suspension hydrogel and **collagen ink (CI**) have the same formulation, since Irgacure 2959 is not employed for the photo-crosslinking process. This formulation was left at room temperature for several minutes and, then, it was mixed with cells suspension to directly form the desired bioink. In particular, 100 µL of human skin fibroblast (HSF) (10^6 cells/100 µL of cell culture media) and 100 µL of human intestinal fibroblast (HIF) (10^6 cells/100 µL of cell culture media) were separately and gently mixed with 1 mL of collagen hydrogel to form the corresponding **Collagen bioink HSF (CB_{HSF})** and **Collagen bioink HIF (CB_{HIF})**, respectively.

2.3.4. Gelatin methacrylate and collagen IPN

IPN hydrogel was prepared starting from GelMa hydrogel at a concentration of 10% (w/v) and collagen suspension at a concentration of 2.5% (w/v), in a ratio of 50:50 (v/v). Firstly, GelMa hydrogel 10 % (w/v) was prepared by following the protocol described above. Then, this formulation was mixed to the collagen ink ready-to-use through the double-syringes mixing system coupled with luer-lock system, in order to get an initial homogenous blend of the hydrogels. Finally, to create the so-called interpenetrating network, two photo-crosslinking steps with UV light were exploited before and after the 3D bioprinting process. The first UV irradiation step, which provide the covalent linkages between the collagen chains and can be formed without the presence of a photo-initiator, was carried out by positioning at 1 cm the UV lamp source at 50 % of its intensity (corresponding at 12 mW/cm^2) above the sterile syringe containing the blend. Then, the photo-initiator Irgacure 2959 was mixed by using the same double-syringes mixing system with the partial cross-linked hydrogel at a concentration of 0,1 % (w/v) of Irgacure 2959 to formed the **semi-IPN ink (SI)**. At this point, 100 µL of human skin fibroblast (HSF) (10^6 cells/100 µL of cell culture media) and 100 µL of human intestinal fibroblast (HIF) (10^6 cells/100 µL of cell culture media) were separately and gently mixed with 1 mL of the semi-IPN ink to form the corresponding **semi-IPN bioink HSF (SB_{HSF})** and **semi-IPN bioink HIF (SB_{HIF})**, respectively.

It is important to notice that, the truly IPN formation occurs after the bioprinting process of both SB_{HSF} and SB_{HIF} bioinks when the second photo-crosslinking process is triggered by the second step of UV irradiation, in which the acrylate moieties branched to the GelMa backbone chains form covalent bonds. This process, will be explained in detail in the crosslinking methods paragraph.

2.4. 3D bioprinting

2.4.1. Bioprinters characteristics

Cellink incredible plus, Regemat 3D V1 and REG4LIFE bioprinters were used for the fabrication of the 3D models discussed in this Thesis. In particular, alginate-based models were obtained through a 3D bioprinting process with the Cellink incredible plus, which consists of an integrated cabinet that ensure sterile environment, while gelatin and collagen-based models were fabricated by means of Regemat's bioprinters, which were placed under a laminar flow hood to ensure the sterile working conditions. All the printing systems have multi-syringes heads which allow to print multiple types of bioinks in a controlled manner. The bioprinters can be controlled by the custom-made software provided by the companies in all the spatial environment (x,y,z axis). Cellink incredible plus is based on extrusion mechanism controlled by a pressure system, while Regemat's bioprinters are based on the same extrusion mechanism equipped with a piston driven system. The other differences between the bioprinters are related (i) to the ability of moving independently each syringe holder containing specific bioink, in order to obtain multi-layered and multi-component scaffolds directly with one bioprinting process, and (ii) to the possibility of controlling syringes and bed temperature. In particular, while Cellink and REG4LIFE display independent syringe movement that can be controlled one by one to deposit different bioinks in the desired portions of the pre-designed scaffolds, Regemat V1 does not allow multiple bioinks deposition during the same printing process, since the syringes are located in a single block holder. Furthermore, Regemat's bioplotters were customized with a refrigerating system to fine control both syringes and bed temperature to improve the printing process by avoiding nozzle clogging and to increase printing resolution, especially when thermo-responsive bioinks are used.

2.4.2. Bioprinting parameters

The choice of the nozzle diameters, pressure, temperature, flow speed and head movements are crucial parameters to consider before the printing process, since they directly influence the quality of the printing, the filament extrusion and the resolution of the final scaffolds. Commonly, nozzle sizes ranging from 0.25 mm to 0.41 mm in diameter are involved when soft materials such as hydrogels are employed. It is pointed out that the smaller is the nozzle diameters the greater is the resolution and accuracy of the scaffold fabrication. However, when bioinks containing cells are extruded through a nozzle with small diameters, cells viability and functionalities might be negatively affected due to the high pressure they are forced to undergone. Furthermore, the resolution of the printing strictly depends even on the bioink ability to maintain the filament shape after the extrusion, which is strictly correlated with the rheological properties of the hydrogel formulation. For this reason, after several optimization of the printing setup and parameters, 0.41 mm of nozzle diameter were selected as the best to print all the bioinks and the corresponding inks not containing cells.

2.4.3. 3D models design and fabrication

3D constructs were designed by using CAD design model integrated in the bioprinter's software. The models were exported as STL file (Standard Triangle Language acronym) to generate the G-Code files containing all the information in machine language. The software allows to set the height of each layer that will compose the final structure, the size of the nozzle used, the printing speed of the extruders expressed in mm/s, and, since the bioprinters operate by first depositing the hydrogel that form the perimeter of the desired shape, it is possible to set the percentage and pattern infilling in the structure. To obtain defined structures and a fluent bioprinting process, numerous tests were carried out before to define the optimal printing parameters. AlgMa-based scaffolds were obtained by a pressure-controlled extrusion process at 10 mm/s of flow speed and 50 Pa of pressure. GelMa and collagen-based models were printed by maintaining the temperature of both syringe and bed at 20 °C, in order to avoid nozzle clogging due to their thermo-responsiveness, and the flow speed of 5 mm/s along with the perimeter speed of 10 mm/s were employed. Finally, all the constructs were printed by following the pre-designed geometry inside petri dishes or inside 24 multiwell.

For what concern, AlgMa-based models, solid circular geometry (infill of 100%) with 10 mm of diameters and 3 mm of thickness were obtained to carry out the preliminary biological tests. In a second moment, a “fortune cookie” shape-like platform was printed as reported in the schematic representation below (Figure 11 (a,b)) in order to get a single platform through which cell behaviour can be evaluated in different mechanical conditions provided by the crosslinking process which were specifically optimized for this model and that will be explained in the section 2.5. As represented in Figure 11 a, the “fortune cookie” platform is 3 mm in thickness and 15 mm in width, with 100 % of infill.

Regarding GelMa, collagen and IPN-based models, two types of bioprinting process were carried out. Firstly, simple multi-layered structures were obtained by printing separately collagen and semi-IPN inks, labelled as CI for collagen ink and SI for semi-IPN ink, to produce 3 layers models with a cylindrical shape (1.5 mm of thickness and 1 cm in width) not containing embedded cells, by following shape (A) model as represented in Figure 11 c. In this case, Regemat 3D V1 was employed for the fabrication of these models, since the structures are formed by the same composition through the entire structure. These models will be seeded with Caco-2 cell lines, as explained in the 3D cell culture section. Secondly, a multiple-step bioprinting process was optimized with both GelMa, collagen and semi-IPN-based inks (GI, CI, SI) and the corresponding bioinks (GB, GC, GI) containing human skin fibroblast (GB_{HSF}, GC_{HSF}, GI_{HSF}), in order to build multi-layered structures characterized by different composition through the z-axis (the bottom layers containing cells and the top layer not containing cells). Human intestinal fibroblasts (HIFs) were used as control only in the pure collagen based-models. In particular, two syringes heads of the REG4LIFE were employed for the 3D models fabrication by following the schematically bioprinting steps reported in Figure 11 d, from which the shape (B) models are obtained. Firstly, one layer of bioink C, G and S, containing human skin fibroblasts (CB_{HSF}, GB_{HSF}, SB_{HSF}) and one layer of bioink C containing human intestinal fibroblasts (CB_{HIF}) were printed in a circular shape with 100 % of infill pattern (layers thickness 1.5 mm), in order to ensure the formation of the desired targeted tissue (submucosa layer of the intestinal tissue). Secondly, a second layer of the corresponding inks not containing cells was printed onto the models, which, at this point, are ready to undergone post-printing crosslinking process and cell seeding of epithelial intestinal layer (HCTs-8 cells line), as described in the following sections. All the bioprinting processes were carried out at 20 °C by preserving cell functionalities.

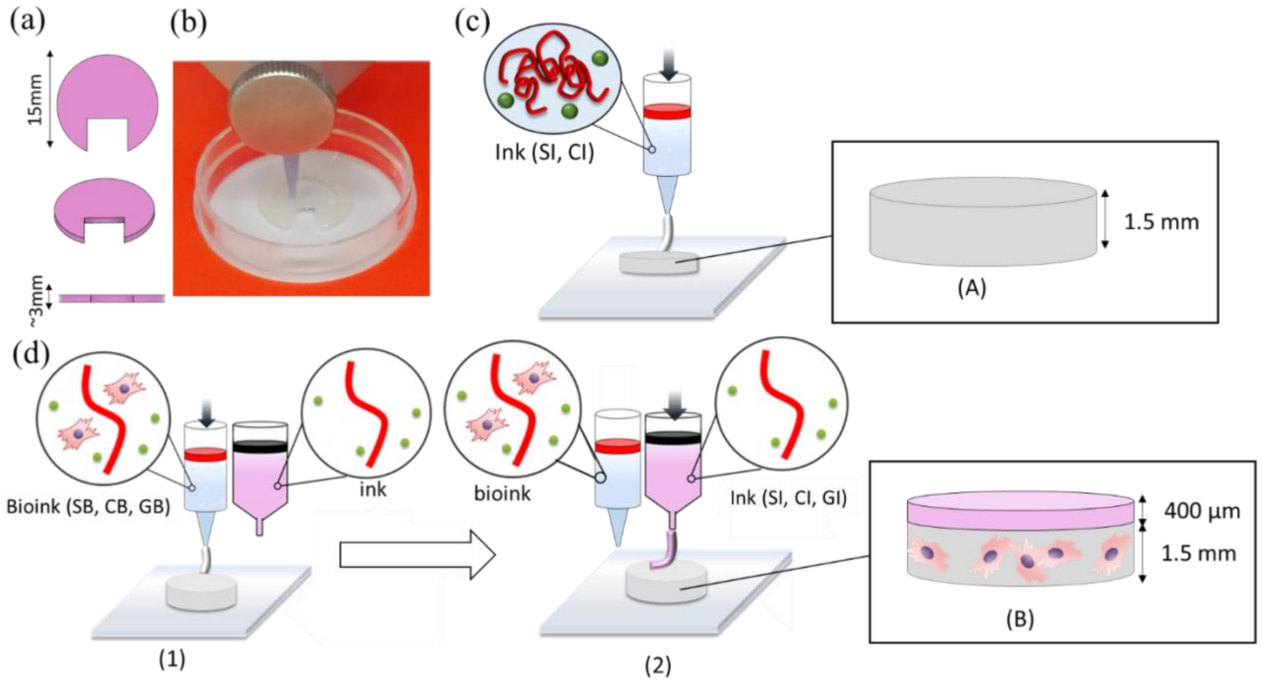

Figure 11. Schematic representation of (a,b) AlgMa-based “fortune cookie” platform; Schematic representation of (c) bioprinting process of semi-IPN and collagen-based models, not containing cells, with shape (A) by using Regemat 3D V1 bioprinter; Schematic representation of (d) bioprinting process of semi-

IPN, collagen and GelMa-based models, containing HIFs and HSFs, with shape (B) by using REG4LIFE bioprinter.

2.5. Crosslinking methods

2.5.1. Alginate methacrylate-based bioinks crosslinking

In order to stabilize the hydrogels against water hydrolysis and obtain tuneable mechanical properties, different post-printing crosslinking processes were carried out on the 3D printed structures. The 3D models obtained with the **AlgMa bioink A** underwent a dual crosslinking process: (1) a first crosslinking step with UV light (intensity: 22-26 mW/cm2, distance from light source: 5 cm, wavelength of UV light: 365 nm) at 60 sec, 90 sec, 120 sec and (2) a second crosslinking step with the $CaCl_2$ solution (40 mM) for 5 min. These three 3D models were labelled as **ABA60Ca**, **ABA90Ca**, **ABA120Ca**. The same protocol was applied to the corresponding models obtained with the ink not containing cells, in order to evaluate whether the presence of the cells affect the ink rheological properties, and the 3D models obtained were labelled as **AIA60Ca**, **AIA90Ca**, **AIA120Ca**. As regards, **AlgMa bioink B** it was used to obtain six 3D models, three of them undergone the same post-printing dual crosslinking process described for bioink A and they were labelled as **ABB60Ca**, **ABB90Ca**, **ABB120Ca**; while the remaining three 3D models, were crosslinked only with UV light for 60 sec, 90 sec and 120 sec after printing process and they were labelled as **ABB60**, **ABB90**, **ABB120**. Same protocol was applied to the corresponding models obtained with ink not containing cells, which were labelled as **AIB60**, **AIB90**, **AIB120**, in the case of models crosslinked only with UV light after printing process and as **AIB60Ca**, **AIB90Ca, AIB120Ca** in the case of models crosslinked with both UV light and $CaCl_2$ solution. In table 2, a summary of the bioinks/inks formulations and the 3D structures obtained after printing process with different crosslinking methods is reported.

Table 2. Summary of AlgMa bioinks formulations and bioprinted models obtained with the dual-crosslinking steps.

Bioink	Step 1: UV light	Step 2: $CaCl_2$	Bioprinted model
ABA (0,2 % I2959)	60 sec	5 min	ABA60Ca
	90 sec	5 min	ABA90Ca
	120 sec	5 min	ABA120Ca
ABB (0,25 % I2959)	60 sec	5 min	ABB60Ca
		/	ABB60
	90 sec	5 min	ABB90Ca
		/	ABB90
	120 sec	5 min	ABB120Ca

		/	ABB120

2.5.2. Gelatin, Collagen and IPN- based bioinks crosslinking

After bioinks formulation and 3D bioprinting process a post-printing crosslinking process was carried out also on the GelMa, collagen and IPN-based 3D constructs, in order stabilize the structures and provide the suitable mechanical resistance during time in incubation condition (37 °C, 5 % of CO_2). For these models, the post-printing crosslinking process involved the same procedure which include the use of only UV light at 3 cm of distance from the UV lamp center to the 3D bioprinted construct at 50 % of its intensity (corresponding at 12 mW/cm^2) for 1 min.

In particular, the constructs obtained from the printing of GelMa-based bioinks, containing both HSF (GB_{HSF}) and HIF (GB_{HIF}) cell types were labelled as **UVGB$_{HSF}$** and **UVGB$_{HIF}$**, respectively. Same protocol was applied to the corresponding models obtained with ink not containing cells, which were labelled as **UVGI**. Thanks to this photo-crosslinking process and the presence of Irgacure 2959, acrylates moieties can form covalent bond by forming permanent crosslinks between GelMa chains. The 3D bioprinted models composed by collagen-based bioinks comprising of both HSF (CB_{HSF}) and HIF (CB_{HIF}) cell types were directly crosslinked after printing process with the same condition used for GelMa-based ones. After this post printing photo-crosslinking, the collagen-based constructs containing HSF and HIF cells were labelled as **UVCB$_{HSF}$** and **UVCB$_{HIF}$**, respectively. Same protocol was applied to the corresponding models obtained with ink not containing cells, which were labelled as **UVCI**. In this case, photo-crosslinking process was carried out without the presence of the photo-initiator, by exploiting the natural radical reaction of the collagen triggered by the UV light exposure. For what concern IPN-based 3D models, Irgacure 2959 was introduced in the semi-IPN bioink and, once the 3D construct is fabricated after the bioprinting process, the second photo-crosslinking process takes place thanks to the presence of the UV light (3 cm, 50 % of intensity, 1 min), which trigger the radical crosslinking of the GelMa hydrogel, in the presence of the already crosslinked collagen. In this way, an interpenetrated network of collagen and GelMa chains is produced.

2.6. 3D cell culture

Before the incubation, Caco-2 cells (400,000 cells/cm^2 of 3D bioprinted model), were manually seeded onto collagen and IPN-based models with shape (A), while HCTs-8 cells were manually seeded onto GelMa, collagen and IPN-based models with shape (B) with and without HIF and HSF cells in the bottom layers (10,000 cells/cm^2). The seeding of both cell lines, ensure the formation of an intestinal epithelial monolayer in the outermost layer of the models, as schematically reported in the Figure 12 (a,b).

Dulbecco's Modified Eagle Medium (1X) (DMEM; Gibco) supplemented with 10% (v/v) of Fetal Bovine Serum (FBS; Gibco) and 1% (v/v) of penicillin/streptomycin (Gibco;10,000 U/mL) was used to grow both AlgMa-based platform with HeLa cell line, collagen and semi-IPN models with Caco-2 seeded in the external layers. The culture media was changed every 2 days up to 72 h.

Gibco Roswell Park Memorial Institute (RPMI 1640; Gibco) supplemented with 2mM Glutamine, 1mM Sodium Pyruvate (NaP), 5% Horse Serum (HS; Gibco) + 5% Fetal Bovine Serum (FBS; Gibco) and 1% (v/v) of penicillin/streptomycin (Gibco;10,000 U/mL) was used to grow collagen, GelMa and blend-based models embedded with HIFs and HSFs seeded with HCTs-8 in the external layers. The culture media was changed every 2 days. All the 3D models obtained were incubated at 37 °C and 5 % of CO_2 up to 72 h for the AlgMa-based models, 72 h for the collagen, GelMa and IPN-based models with Caco-2 and 21 days for GelMa, collagen and IPN-based models containing HSFs or HIFs and HCTs-8.

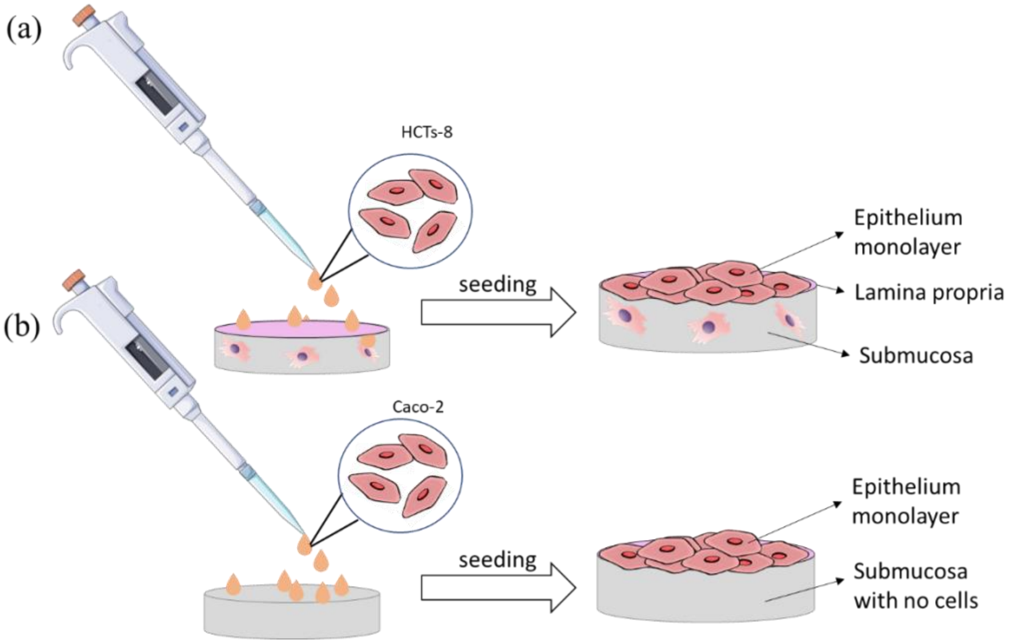

Figure 12. Schematical representation of (a) HCTs-8 cell seeding onto GelMa, collagen and IPN-based 3D models and (b) Caco-2 cell seeding onto collagen and IPN-based 3D models.

2.7. Characterization methods

2.7.1. Chemical characterization

In order to qualitatively assess the chemical substitution of the methacrylate groups onto the sodium alginate and gelatin backbone chains, proton nuclear magnetic resonance (^{1}H-NMR) (NMR Varian model MR400, coupled with ATB PFG probe) and Fourier Transform infrared spectroscopy (FT-IR) (Bruker laser class model ALPHA, equipped with ATR accessory PLATINUM-ATR) were carried out by dissolving the lyophilized hydrogels in D_2O, at a concentration of ca. 50 mg/mL, and by using directly the lyophilized product, respectively. ^{1}H-NMR was carried out at 50 °C, in order to decrease the viscosity of the "gelly-like" solutions by ensuring the suitable resonance with the protons. Moreover, in order to quantitively evaluate the Degree of Functionalization (DoF) for the GelMa and AlgMa products, titration with Trinitrobenzenesulfonic acid (TNBSA) and Matrix-Assisted Laser Desorption/Iionization-Time of Flight coupled with mass spectroscopy (MALDI-MS) were performed, respectively. In particular, the titration was carried out through a calibration curve built by means of TNBSA/glycine reaction at different concertation, in which glycine acts as the standard representing the compound with 100 % of free amino groups when no reaction with TNBS occurs (corresponding to a hypothetically GelMa with free amino groups). When the reaction tale place, an orange-yellow product solution is formed, whose intensity increase by increasing the reducing the number of free amino groups not reacted which is detectable by using UV-vis spectroscopy. The quantitative determination of the number of amines contained within the GelMa can be accomplished through the comparison of the TNBSA/GelMa absorbance and the corresponding absorbance value obtained from the calibration curve. In the case of MALDI-MS analysis, AlgMa sample was firstly subjected to partial acidic hydrolysis using a sample of 2.0 wt% in an acid solution. The partial depolymerization was carried out in trifluoroacetic acid (TFA, 2 M) at a temperature of 90 °C, for 5 h in order to obtain oligosaccharide chains easy to detect by MALDI-MS [232]. 5µL of hydrolyzed sample were added with 5µL of NH4OH solution (15%) and then added with 20µL of MALDI matrix. The best results were obtained using 2,5-Dihydroxybenzoic acid (DHB, 10 mg/mL; H2O/CH3CN, 40:60, v:v; 0.1% TFA) as matrix. Dried droplets method was adopted combined with a fast-drying protocol [233-235]. Then, mass spectrometry analysis was performed on the 5800 MALDI-TOF analyzer (AB SCIEX, Darmstadt, Germany) equipped with an Nd:YLF laser ($\lambda = 345$ nm wavelength, <500 ps pulse length up to 1000 Hz repetition rate). The spectra were acquired in reflectron positive mode (HR), with a mass accuracy of 5 ppm and a mass range of 300−2500 Da. Each spectrum was recorded accumulating at least 5000 laser shots, with a laser pulse rate of 400 Hz. The sample was spotted three times and each spot is measured three times in order to collect nine data points. The spectra were handled using Data Explorer version 4.11 (AB Sciex) to perform theoretically calculated distribution and extract ICA (Isotope Cluster Area) for each ion peak.

2.7.2. Rheological characterization

Rheological properties of GelMa, Collagen, IPN of collagen and GelMa were evaluated with Anton Paar MCR 102 rheometer. It consists of an electronically communicated (EC) permanent magnet synchronous motor-electronically commutated mounted on-air bearings and an optical encoder at high resolution. The optical encoder determines the shear stress and shear rate and allows the measurement and control of angular deflections up to 50 nanoradians. The motor is supported by two air bearings, this system minimizes friction and vibrations caused by physical contacts, improving the accuracy of the measurement. In both lower and upper units of the rheometer, Peltier temperature control element is placed to control the temperature during the measure, which can reach temperature ranging from -10 °C up to +200 °C. In addition, the measuring system is covered by a hood which acts as a trap to avoid solvent evaporation during the measure. Different measurement systems can be mounted inside the instrument. They consist of a fixed part connected to the lower unit of the rheometer and a moving part connected to the rotor through a quick coupling. The choice of the measurement system depends on the type of material to be tested and the type of test chosen. The most common geometries are the plate-plate and the plate-cone one, and the choice of the suitable geometry depends on the type of materials and the information to get, as described in detail below. The setup of the instruments and all the measurements were controlled by the Rheoplus software.

Concerning AlgMa-based hydrogel, inks and 3D bioprinted constructs, amplitude sweep analysis, viscosity and recovery tests were evaluated in a plate–plate geometry with a diameter of 25 mm and a gap of 0.3 mm. Firstly, amplitude sweep analysis, viscosity and recovery tests were carried out on the Alg, AlgMa, both solubilized in PBS (1X), and on the AlgMa hydrogel not containing I2959 (I2959 does not affect rheological properties, thus rheological measures are not shown), in order to evaluate how chemical modification and the presence of the $CaCl_2$ pre-crosslinker solution can affect rheological parameter and hydrogel printability. All the measures were carried out at 25 °C in order to simulate the condition of the pre-printing and printing process. Amplitude sweep tests were carried out in a deformation range (γ) from 0.01 % to 1000 % by using an oscillation mode, by keeping constant the frequency at 1 Hz, in order to characterize G' and G'' moduli as a function of the applied strain (%) of the hydrogels and to have a quick evaluation of their printability. Viscosity tests and flow curves were carried out with a shear rate range (gamma punto) from 0.01 s^{-1} to 1000 s^{-1} by using a rotational mode, in order to assess hydrogels viscosity and shear thinning behaviour. Recovery tests were performed on both AlgMa solution and AlgMa hydrogel pre-crosslinked with $CaCl_2$, in order to understand the ability of the materials to recover their mechanical properties, with and without the presence of the cross-linker, after a high shear-rate, which simulates the shear experienced by the materials during the passage through the nozzle. In this case, low shear-rate (0,1 s^{-1}), high shear-rate (3000 s^{-1}) and again low shear-rate (0,1 s^{-1}) were applied to the materials at 25 °C with the aim to simulate the transition of the materials through the nozzle (high shear), starting from a static situation inside the syringe (low shear), to a second static condition (recovery) represented by the materials deposited onto the printer bed (low shear).

Furthermore, the same amplitude sweep analysis performed on Alg and AlgMa solutions and AlgMa hydrogel , were carried out also on the 3D bioprinted models with and without cells (diameter 5 mm, height 1 mm) after different crosslinking process and after 72 h of incubation, in a deformation range (ɣ) from 0.1 % to 1000 % at 37 °C, in order to simulate the incubation condition and to evaluate how the presence of the cells affect the rheological properties of the final 3D printed models.

As regards GelMa, collagen and IPN-based hydrogel and 3D constructs, amplitude sweep analysis, viscosity, temperature sweep and recovery tests were evaluated in a plate-plate geometry with a diameter of 25 mm and a gap of 0.4 mm. Firstly, amplitude sweep analysis, viscosity and recovery tests were carried out on the GelMa, collagen and IPN-hydrogels formulations, whose preparation has been already described in the section 2.3. All the measures were carried out at 20 °C in order to simulate the condition of the pre-printing and printing process. Amplitude sweep tests were carried out in a deformation range (ɣ) from 0.01 % to 1000 % by using an oscillation mode and by keeping constant the frequency at 1 Hz, in order to characterize G' and G'' moduli as a function of the applied strain (%) of the hydrogels and to have a first evaluation of their printability. Viscosity tests and flow curves were carried out with a shear rate range (gamma punto) from 0.01 s^{-1} to 1000 s^{-1} by using a rotational mode, in order to assess hydrogels viscosity and shear thinning behavior. Recovery tests were performed in order to understand the ability of the materials to recover their mechanical properties after a high shear-rate, which simulates the shear experienced by the materials during the passage through the nozzle. In this case, low shear-rate (0,1 s^{-1}), high shear-rate (3000 s^{-1}) and low shear-rate (0,1 s^{-1}) were applied to the materials at 20 °C with the aim to simulate the extrusion process through the nozzle (high shear), starting from a static situation inside the syringe (low shear), to a second static condition (recovery), represented by the materials deposited onto the printer bed (low shear). Moreover, the same amplitude sweep analysis performed on the hydrogels formulations were carried out also on the corresponding 3D bioprinted models without cells (diameter: 2.5 cm, height: 0.4 mm) after the different crosslinking process customized for each formulations, in a deformation range (ɣ) ranging from 0.1 % to 1000 % at 37 °C, in order to simulate the incubation condition and to evaluate how the crosslinking processes affect the rheological properties of the final 3D bioprinted models. Finally, temperature sweep analyses were carried out on both photo-crosslinked and not photo-crosslinked 3D bioprinted constructs with the aim to evaluate the mechanical stability in incubation environment during time by applying an angular frequency (ω) and a strain amplitude (ɣ) of 1 rad/s and of 0.1%, respectively, at 37 °C and for 20 min, to mimic the static conditions of the models inside the incubator.

2.7.3. Thermal characterization

In order to evaluate the thermal stability of the samples and the thermal transitions of the hydrogels, thermogravimetric analysis (TGA) and differential scanning calorimetric analysis (DSC) were carried out using a TGA Q500 (TA Instruments) and DSC Q2000 (TA Instruments) instruments. TGA analyses were performed on 7-10 mg samples, from RT to 600 °C, with a heating rate of 10 °C/min, under nitrogen atmosphere, while DSC analyses were performed on 3-5 mg samples by performing two heating scans (from -90 °C to 200 °C, 20 °C/min) separated by a controlled cooling ramp (from 200 °C to -90 °C, 10 °C/min).

2.8. Biological assays

2.8.1. Materials

Hoechst 33342, Propinium Iodide and Calcein-AM were purchased from Sigma-Aldrich. Pure (99,9 %), high quality and anhydrous DMSO was used to reconstitute Live/Dead reagents and to prepare the corresponding stock solutions. Dilutions at the final working concentrations were performed in PBS (1X). Alamar blue TM cell viability reagent, Green cell tracker and red deep cell tracker were provided by Fisher Scientific. Monoclonal ZO-1 or ZO-1 (R40.76) AleaFluor 488 antibody (host: rat; target: mouse, human, rat) and E-cadherin or E-cad. (G-10) (host: mouse; target: mouse, human, rat) were purchased from Santa Cruz Biotechnology. AlexaFluor 594-conjugated AffiniPure anti-Mouse (host: goat; target: mouse) was provided by Jackson ImmunoResearch). Di-Sodium 4-nitrophenyl phosphate Hezahydrate reagent (Fluka), buffer pH 5.5 (sodium acetate anhydrous (PM:82.03 g/mol) 0.1 M; acetic acid 10% (0,1 M); triton (100X); Milli-Q water), NaOH 3 M and HBSS (1X) were employed for the acid phosphatase assay. Paraformaldehyde PFA (Sigma-Aldrch) was prepared at a concentration of 4 % in PBS (1X), pH 7.4. PBS (1X) Ca/Mg was purchased from Gibco.

2.8.2. Live/dead assay

Live/dead assay was performed to evaluate cell viability through confocal imaging from 1 h after the experiment up to 21 days. All the 3D cell cultures, excepted those ones with the Caco-2 cell line, have been treated by following the protocol below. 6 µl of 1 mM Calcein-AM (1mg/mL), 1 µl of 1,5 mM PI (1 mg/mL,1:300 dilution), 2 µl of 10 mg/ml Hoechst 33342 reagent (1:1500 dilution) and 2991 mL of PBS (1X) was used to prepare Live/Dead staining solution. Firstly, 3D cell cultures were washed three times with 1 ml of PBS (1X) before the staining. Then, 3D cell cultures were completely covered with 500 µl of Live/Dead solution and incubated at 37°C with 5% of CO_2 for 30 min. Finally, the staining solution was removed and the 3D cell cultures were rinsed three times with warm 1 ml of PBS (1X).

2.8.3. Cell proliferation

Alamar blue test was carried out to estimate the cell proliferation activities after the 3D bioprinting process from 1h after the experiment up to 21 days. In particular, cell proliferation activities of collagen, GelMa and IPN-based cultures, with HIFs and HCTs-8, cell lines were evaluated by following this protocol. 1 mL of Alamar solution at 10 % w/v in RPMI-based complete cell culture media (used for the HCTs-8 cell line) was prepared and warmed at 37 °C, protected from the light, prior the use. 500 uL of the Alamar solution was introduced in the 24-multiwell to entirely cover the 3D cell cultures. Then, the cultures were incubated for 4 hours at 37°C in a cell culture incubator, protected from direct light. 500 uL of each Alamar solutions were picked up and aliquoted in 100 uL inside a 96 multi-well, in order to have a good statistic and replica. Outputs were recorded by using an UV-vis spectrophotometer equipped with a 96-well plate reader and by setting the fluorescence excitation wavelength at 560 nm and the emission one at 590 nm. Finally, the absorbance was registered considering 600 nm as a reference wavelength (normalized to the 600-nm value).

2.8.4. Immunofluorescence

Immunofluorescence analyses were carried out on collagen and GelMa-based 3D cell cultures, displaying HCTs-8 epithelial monolayers, from 7 days to 21 days, in order to assess the presence of intermembranes proteins and tight-junctions, as typically found in the intestinal human tissue. All the samples were rinsed with pre-warmed PBS 1(1X) two times in order to remove any traces of cell culture medium. After this, the samples were fixed with PFA (paraformaldehyde at 4 % in PBS 1X pH 7.4) for 30 min at RT. Then, the samples were washed three times with PBS 1X Ca/Mg. Blocking Buffer (Triton) was added to each sample, that were incubated for 45 min at RT. The incubation with the primary antibody was carried out by adding separately ZO-1 (1:50 dilution) and E-cad (1:100 dilution) for each type of 3D cell culture. The samples were incubated in a humidified chamber overnight at 4 °C. Then, the secondary antibody incubation was performed after washing the sample for three times with PBS (1X) Ca/Mg by adding AlexaFluor 594 secondary antibody (1:150 dilution) to each sample, which were incubated for 60 min at RT in dark. Finally, in order to visualize the nuclei, a staining with Hoestch solution (1:1500 dilution) was performed for all the samples.

2.8.5. Confocal Laser Scanning Microscopy

Confocal laser scanning microscopy analysis was carried out on the 3D bioprinted samples placed in 35 mm diameter glass bottom microwell dishes (Mattek). Samples stained for viability assay were observed using a Nikon A1R confocal laser scanning microscope employing two laser lines (489 nm and 561 nm) and two detection GASP channels (525/20 and 595/20nm) for the green and red false colour channels, employed to measure the fluorescence intensity of Calcein-AM and Propidium Iodide, respectively. Viability percentages were estimated with a semi-quantitative analysis using Fiji software: live cells (stained green by calcein-AM) and dead cells (stained red by propidium iodide) were manually counted and live cell fraction calculated by dividing the number of live cells by the total number of cells.

2.8.6. Immunoistochemistry

3D bioprinted samples, containing Caco-2 as epithelial monolayer, were treated to carry out histological analysis after 48 h of incubation. Cell culture media was aspirated and all the sample was washed three time with PBS (1X). Then, 2 mL of paraformaldehyde (PFA) at 4 % were add to each well containing sample. Two different fixation protocols were tested. In the first one, after 1 h of treatment in PFA, the samples experienced several dehydration steps in alcohol and xylol which included 5 minutes in alcohol 75 %, 5 minutes in alcohol 90 %, 3 minutes in alcohol 100 %, 3 minutes in alcohol 100 % and two passages in xylol of 3 minutes each one. In the second one, after 2 h of fixation in PFA, the samples experienced several dehydration steps in alcohol and xylol which include 10 minutes in alcohol 75 %, 10 minutes in alcohol 90 %, 10 minutes in alcohol 100 %, 10 minutes in alcohol 100 % and two passages in xylol of 10 minutes each one. After fixation, all the samples were included in paraffin and 5 µm of thickness specimens were obtained by using the microtome. In order to stain the specimens with haematoxylin and eosin, paraffin was removed through three passages of 3 minutes in xylol and, then, were rehydrated through three immersion in alcohol 100 % for 3 minutes, one immersion in alcohol 95 % for 3 minutes and one immersion in alcohol 70 % for 3 minutes. Finally, the samples were immersed for 5 minutes in water. After rehydration, the samples were immersed in hematoxylin and eosin for 5 min, respectively. Before the analysis, the specimens were dehydrated again by following one passage in alcohol 70 % for 3 minutes, one passage in alcohol 95 % for 3 minutes, three passages in alcohol 100 % for 3 minutes and three passages in xylol for 3 minutes. Finally, samples were observed by using an optical microscope.

2.8.7. Statistical analysis

Cell counts are represented as mean ± standard deviation. Statistical analyses were performed using OriginPro 9.1 software. Statistical significance was determined by two sample t-test. Differences were considered to be statistically significant at $p < 0.05$. Different levels of statistical significance are indicated as follow: *, $p < 0.05$; **, $p < 0.01$; ***, $p < 0.001$; ****, $p < 0.0001$

3. Results and discussion

3.1. Alginate and Gelatin methacrylation

3.1.1. Alginate methacrylate

Alginate is the most employed polysaccharide as hydrogel among the natural polymers for the fabrication of 3D tissue models through 3D bioprinting, since it is capable to retain high amount of water, it supports cell growth and cell proliferation, it displays high cell viability and it is able to undergone extrusion-based bioprinting process if used in the appropriate concentration. However, its well-known cross-linking process, based on instantaneous and uncontrollable ionic interactions which produce egg-box structures defined by hydrogen bonds between alginate chains, makes its mechanical properties not tunable in the desired range of stiffness and produces crosslinks in an heterogenous manner inside the polymer matrix even when the crosslinker is employed at low concentration. For this reason, photo-crosslinking process might be a valid alternative to overcome all the limitations related to the ionic cross-linking one, since it provides a progressive increment of the mechanical properties by simply changing the photo-initiator concentration, the UV time exposure and the UV light intensity.

Alginate methacrylate was prepared by grafting the methacrylic group of the methacrylic anhydride (MAA) into the alginate backbone chains, as represented in the scheme reaction in Figure 13. Although this mechanism of reaction is well-known and widely reported in the literature to produce photocrosslinkable natural-based hydrogels, such as gelatine-methacrylate [156] collagen-methacrylate [228] hyaluronic acid-methacrylate [230] and chitosan-methacrylate [231], it is usually based on a laborious practice, which involve numerous pH adjustments during the whole reaction time, to maintain the suitable pH necessary to promote the substitution of the methacrylic group on the hydroxyl group of the alginate carboxylic functionalities [236]. Furthermore, the high molar excess of MAA usually required to achieve a good degree of substitution, makes this traditional approach not affordable and not easy to handle.

In this work, an affordable alginate methacrylation process was accomplished by adapting for the first time the new gelatin methacryloyl synthesis proposed by Shirahama et al. [156] to the alginate polymer chains, in order to make the AlgMa production easier and more manageable and to reduce the excess of MAA used in the reaction. In particular, 2 % w/v of pristine alginate was dissolved in a basic aqueous carbonate buffer (CB) which serves as solvent capable of autonomously maintain pH around 8 during the whole reaction time, with the aim to encourage the deprotonation of the carboxylic group making them available for the substitution with the methacrylic moieties. 2 % w/v was selected as the best concentration of alginate to obtain a low viscous solution which can be homogenously stirred at high rpm (600 rpm) to ensure a collision between the methacrylic anhydride and alginate chains. CB buffer at 0,325 of molarity (pH=9) was selected as aqueous solvent to carry out the reaction by considering its proven better buffering capacity [156] with respect to the common phosphate-based buffer solution, usually employed for the alginate methacrylation, which is not able to sustain pH around 8 and requires several pH adjustments with NaOH. Thanks to this enhanced buffer ability, a reduced molar excess of MAA was employed in this synthesis with respect to the molar excess normally used in the traditional AlgMa production, which usually ranging from 15 mL to 20 mL [236]. In fact, 1 mL of MAA per gram of alginate (1 mL of MAA/g of alginate) results as the suitable amount of anhydride to get an AlgMa product with a detectable and clear proton peak obtain through ^{1}H-NMR analysis. In this condition, only one pH adjustment is needed after the solubilization of alginate powder in the CB buffer, in order to stabilize the pH between 8 and 9. Finally, two different reaction times were evaluated (24 h and 72 h) with the aim to understand which is the best reaction time duration, taking into account that in the traditional synthesis of AlgMa, 24 h and 72 h are usually reported as the optimized time to get methacrylation [236].

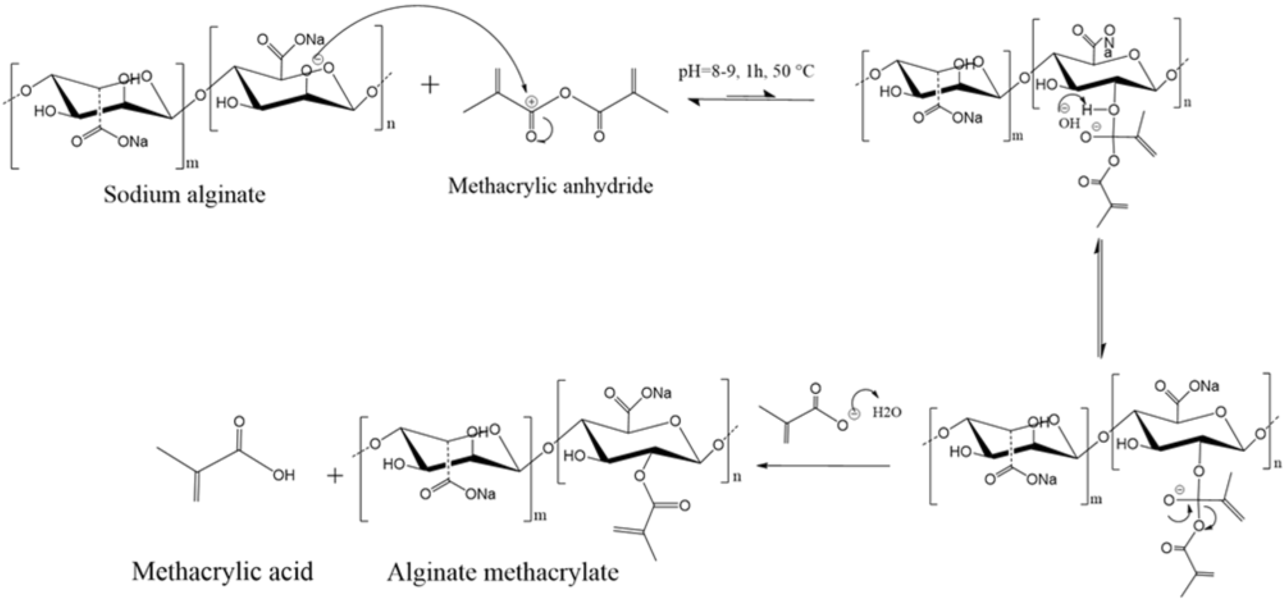

Figure 13. Schematic steps of alginate methacrylation by grafting methacrylate groups into sodium alginate chain.

Pristine alginate (Alg) and alginate methacrylate (AlgMa) were characterized by Proton Nuclear Magnetic Resonance (^{1}H-NMR), Fourier Transform Infrared Spectroscopy (FT-IR) and Matrix

Assisted Laser Desorption Ionization - Time of Flight (MALDI-TOF) to assess the presence of methacrylate groups and the degree of substitution.

^{1}H-NMR spectra reported in Figure 14 (a,b,c) show the comparison between Alg and AlgMa after 24 h (labelled AlgMa 24 h) and 72 h (labelled AlgMa 72 h) of methacrylation reaction. All the spectra display characteristic peaks between 3.50 and 5.20 ppm typical of the saccharide units of the alginate backbone chains [237]. In addition, both AlgMa spectra exhibit two distinctive signals of the vinyl in the region ranging from 6.5 ppm to 5.6 ppm and methyl hydrogens peaks of the methacrylate groups at ca. 2.00 ppm, which vary in location depending on the resulting chemical environment. In particular, the AlgMa spectrum obtained after 24 h of reaction time (Figure 14 b), shows the vinyl protons signals at 5.6 ppm (singlet) and 6.0 ppm (singlet) and the methyl hydrogens peak at 2.0 ppm (triplet), while the AlgMa obtained after 72 h of reaction time (Figure 14 c) shows more intense peaks shifted at 6.0 ppm (doublet) and 6.5 ppm (singlet) for the vinyl hydrogens and 2.23 ppm (triplet) for the methyl ones which integrate for three with respect to the vinyl protons. It is clear that the signals associated to the AlgMa 24 h are weaker and wider with respect to the AlgMa 72 h proton signals which display more intense and defined peaks.

Furthermore, Figure 14 c highlights that the block of peaks associated to the saccharide units of the alginate backbone chain slightly shift at higher ppm values. This deshielding in the downfield region of the spectrum could be ascribable to the presence of the new formed ester group, directly linked with the vinyl functionalization, which has a moderately deactivation effect due to its withdrawing nature. Because the protons experience higher external magnetic field, they need a higher frequency to achieve resonance, and therefore, the chemical shift appears at higher frequency.

Furthermore, ^{1}H-NMR could be useful to evaluate the degree of substitution (DS) on the alginate methacrylate backbone chains by integrating the peak of the protons of the mannuronic and guluronic units with respect to the proton peaks of the vinyl and methyl group of the methacrylate moieties [237]. However, an accurate quantification of the DS using only ^{1}H-NMR remains challenging. In particular, the peaks assignment and their consequent integration remains highly ambiguous due to the possible peak shifting, caused by the presence of the new introduced functionalities, and the high number of protons contained in the chains. Furthermore, the protons signal of the mannuronic and guluronic units are not fully separated, thus resulting in an overestimation or underestimation of the DS if the integration is not considered properly.

Alg and AlgMa were also characterized by FT-IR spectroscopy to further verify the substitution after 72 h of reaction time, which was selected through ^{1}H-NMR as the best duration time to obtain the methacrylation. As observed from Figure 14 (d,e), both spectra display wide bands in the region ranging from 3600 cm^{-1} to 3000 cm^{-1} and from 2980 cm^{-1} to 2850 cm^{-1}, ascribable to the stretching of –OH and –CH groups, respectively, typically of the polysaccharides [238]. The others bands might be more representative of the alginate chains since the bands at ca. 1595 cm^{-1} can be assigned to the stretching of carboxylate anions –COO^{-} [238][239], the bands at ca. 1403 cm^{-1} can be assigned to the C–OH deformation along with the symmetric stretching of O–C–O of the carboxylate groups [239][240] while the bands at ca. 1083 cm^{-1} and at ca. 1026 cm^{-1} are related to the vibrations of C–O and C–C, respectively, of the pyranose rings [238]. Furthermore, all the bands at low frequency ca. 946 cm^{-1}, ca. 883 cm^{-1} and ca. 812 cm^{-1} might be assigned to to the C–O stretching of uronic acid [238], to the C1–H deformation of β-mannuronic acid [238], and to the C–H bending vibrations of mannuronic acid residues [241]. In addition to these bands, the spectrum related to the AlgMa product exhibits a more intense peaks at 2980 cm^{-1}-2850 cm^{-1}and the presence of a “shoulder” at 1711 cm^{-1} (both highlighted with the red arrows in Figure 14 (e)), not observed in the pristine alginate spectrum (Figure 14 (d)). These marked bands along with the “shoulders” can be respectively assigned to the stretching of the –CH of the alkane and alkene bond contained in the methacrylate functionalization and to the stretching of the C=O group of the esters, both resulting from the grafting of the methacrylate units, as represented in the AlgMa chemical structure in Figure 14 (b,c). Furthermore, the broad band at ca. 3268 cm^{-1} (Figure 14 (e)) displays a more intense area with respect to the corresponding band in the pristine alginate spectrum (Figure 14 (d)), which might be ascribable to the increased number of –CH introduced with the methacrylic functionalization. Accordingly, these bands provide evidence of the desired alginate functionalization with the methacrylic group, which might occur on the -OH functional group since the characteristic peaks of the COO- groups are still present after the reaction and the new band at 1711 cm^{-1} highlight the formation of ester bond.

In order to better clarify whether and where the methacrylation occurs and to quantify the degree of substitution or DS (%) of the reaction, Matrix Assisted Laser Desorption Ionization - Time of Flight (MALDI-TOF) analysis was carried out.

Figure 14 f shows a representative (+) MALDI-TOF-MS spectra of the products solution obtained from hydrolyzing AlgMa under acid and thermic conditions (90°C, 5h, TFA 2M). High intensity readings were observed for several peaks in the mass range 300-1500 Da leading to the identification of Hexuronic acid (Glucuronic/Mannuronic acid) chains from two to eight units, both methacrylated and underivatized. These results confirm that different oligosaccharides were formed during the experimental treatment. The spectrum complexity is due to the formation of a number of decomposed products under acid/hydrothermal conditions. Moreover, is possible observe even and odd species that indicate the presence of protonated species and radical cation species. All the identified oligosaccharide chains are reported in table 3, while figure 14 g shows the theoretical distribution of the isotope cluster ions of an exemplificative signal. The composite signal (panel A, figure 14g) is derived from the overlapping of the isotope cluster ions of four different species of m/z 838, 840, 842 and 844. The comparison of measured experimental isotopic distribution with the theoretically calculated distribution of the expected summary formula, suggest that the ion clusters result from the combination of four radical cation species generated as degradation products under the adopted experimental conditions. The same elaboration was performed for all signals in order to confirm identity of the observed ion species (table 3).

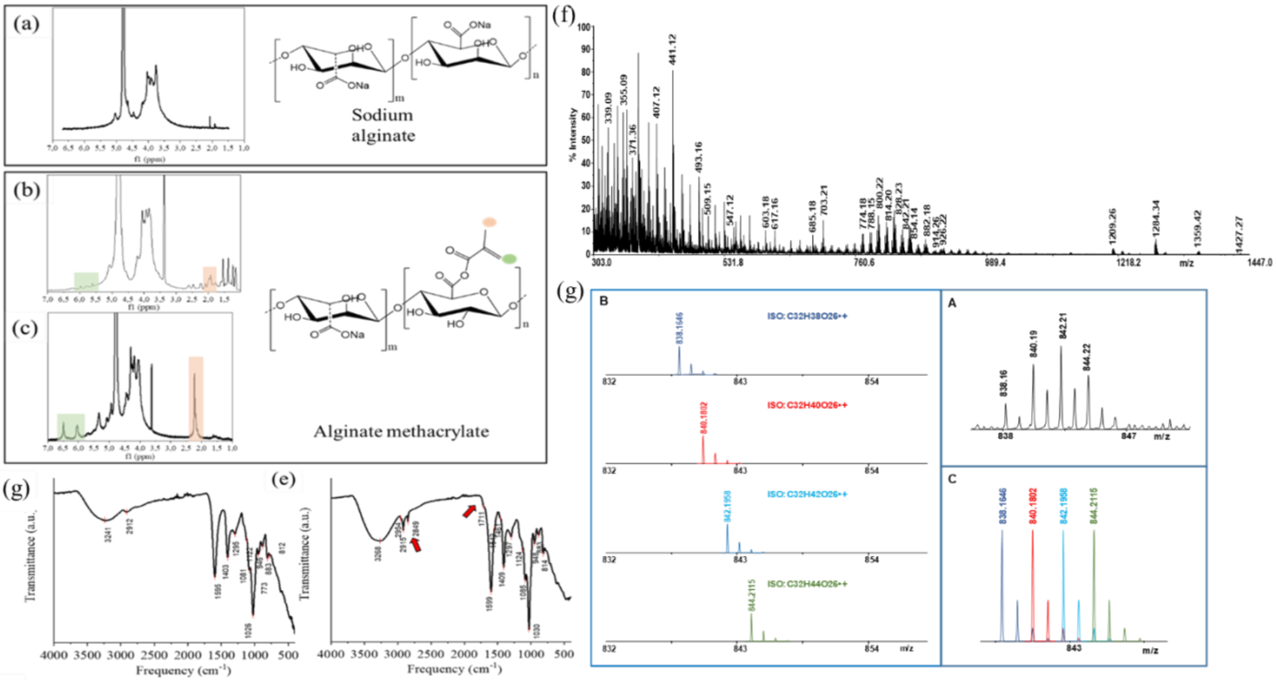

Figure 14. ^{1}H-NMR of pristine alginate (a), AlgMa after 24 h (b) and 72 h (c) of reaction time. FT-IR of pristine alginate (d) and AlgMa after 72 of reaction time (e). (+) MALDI MS of hydrolyzed AlgMa sample (f). (+) MALDI MS spectrum enlargement of AlgMa (A); (B) and (C) theoretical distribution of the isotope cluster ions (g).

Table 3. Mass spectrometry data of AlgMa products after hydrolysis, reported as observed m/z values, error in ppm and formula assignments; (Δ) -COC3H5 (methacrylation); Hexuronic acid: Glucuronic acid/Mannuronic acid.

Observed mass (m/z)	Error (ppm)	Formula	Structure
371.08	**5.0**	**$[C_{12}H_{19}O_{13}]^+$**	**Hexuronic acid$_2$**
339.09	5.0	$[C_{12}H_{19}O_{11}]^+$	Hexuronic acid$_2$
353.07	7.0	$[C_{12}H_{17}O_{12}]^+$	Hexuronic acid$_2$
355.09	6.0	$[C_{12}H_{19}O_{12}]^+$	Hexuronic acid$_2$
407.12	4.5	$[C_{16}H_{23}O_{12}]^+$	Hexuronic acid$_2$ +Δ
441.12	5.5	$[C_{16}H_{25}O_{14}]^+$	Hexuronic acid$_2$ +Δ
493.16	7.0	$[C_{20}H_{29}O_{14}]^+$	Hexuronic acid$_2$ +2Δ
509.15	6.0	$[C_{20}H_{29}O_{15}]^+$	Hexuronic acid$_2$ +2Δ
547.12	**5.8**	**$[C_{18}H_{27}O_{19}]^+$**	**Hexuronic acid$_3$**
603.18	8.0	$[C_{22}H_{35}O_{19}]^+$	Hexuronic acid$_3$ +Δ
617.16	5.7	$[C_{22}H_{33}O_{20}]^+$	Hexuronic acid$_3$ +Δ
685.18	5.0	$[C_{26}H_{37}O_{21}]^+$	Hexuronic acid$_3$ +2Δ
703.21	6.3	$[C_{30}H_{39}O_{19}]^+$	Hexuronic acid$_3$ +3Δ
719.20	5.7	$[C_{30}H_{39}O_{20}]^+$	Hexuronic acid$_3$ +3Δ
753.22	7.0	$[C_{30}H_{41}O_{22}]^+$	Hexuronic acid$_3$ +3Δ
723.14	6.1	**$[C_{24}H_{35}O_{25}]^+$**	**Hexuronic acid$_4$**
756.16	6.0	$[C_{28}H_{36}O_{24}]^{\bullet+}$	Hexuronic acid$_4$ +Δ
758.17	6.0	$[C_{28}H_{38}O_{24}]^{\bullet+}$	Hexuronic acid$_4$ +Δ
760.19	5.5	$[C_{28}H_{40}O_{24}]^{\bullet+}$	Hexuronic acid$_4$ +Δ
770.14	5.5	$[C_{28}H_{34}O_{25}]^{\bullet+}$	Hexuronic acid$_4$ +Δ
772.15	4.9	$[C_{28}H_{36}O_{25}]^{\bullet+}$	Hexuronic acid$_4$ +Δ
774.18	7.2	$[C_{28}H_{38}O_{25}]^{\bullet+}$	Hexuronic acid$_4$ +Δ
776.20	7.1	$[C_{28}H_{40}O_{25}]^{\bullet+}$	Hexuronic acid$_4$ +Δ
784.12	6.0	$[C_{28}H_{32}O_{26}]^{\bullet+}$	Hexuronic acid$_4$ +Δ
786.13	6.0	$[C_{28}H_{34}O_{26}]^{\bullet+}$	Hexuronic acid$_4$ +Δ
788.15	5.0	$[C_{28}H_{36}O_{26}]^{\bullet+}$	Hexuronic acid$_4$ +Δ
790.16	5.6	$[C_{28}H_{38}O_{26}]^{\bullet+}$	Hexuronic acid$_4$ +Δ
796.20	7.1	$[C_{31}H_{40}O_{24}]^{\bullet+}$	Hexuronic acid$_4$ +2Δ
798.21	5.0	$[C_{31}H_{42}O_{24}]^{\bullet+}$	Hexuronic acid$_4$ +2Δ
800.22	6.0	$[C_{31}H_{44}O_{24}]^{\bullet+}$	Hexuronic acid$_4$ +2Δ
802.24	5.3	$[C_{31}H_{46}O_{24}]^{\bullet+}$	Hexuronic acid$_4$ +2Δ
812.19	5.0	$[C_{31}H_{40}O_{25}]^{\bullet+}$	Hexuronic acid$_4$ +2Δ
814.20	4.5	$[C_{31}H_{42}O_{25}]^{\bullet+}$	Hexuronic acid$_4$ +2Δ
816.22	5.5	$[C_{31}H_{44}O_{25}]^{\bullet+}$	Hexuronic acid$_4$ +2Δ
826.20	6.0	$[C_{32}H_{42}O_{25}]^{\bullet+}$	Hexuronic acid$_4$ +2Δ
828.23	7.0	$[C_{32}H_{44}O_{25}]^{\bullet+}$	Hexuronic acid$_4$ +2Δ
830.23	5.0	$[C_{32}H_{46}O_{25}]^{\bullet+}$	Hexuronic acid$_4$ +2Δ
838.16	5.7	$[C_{32}H_{38}O_{26}]^{\bullet+}$	Hexuronic acid$_4$ +2Δ
840.19	6.0	$[C_{32}H_{40}O_{26}]^{\bullet+}$	Hexuronic acid$_4$ +2Δ
842.21	7.1	$[C_{32}H_{42}O_{26}]^{\bullet+}$	Hexuronic acid$_4$ +2Δ
844.22	8.0	$[C_{32}H_{44}O_{26}]^{\bullet+}$	Hexuronic acid$_4$ +2Δ
852.14	5.7	$[C_{32}H_{36}O_{27}]^{\bullet+}$	Hexuronic acid$_4$ +2Δ
854.17	6.3	$[C_{32}H_{38}O_{27}]^{\bullet+}$	Hexuronic acid$_4$ +2Δ
856.19	6.1	$[C_{32}H_{40}O_{27}]^{\bullet+}$	Hexuronic acid$_4$ +2Δ
858.20	6.0	$[C_{32}H_{42}O_{27}]^{\bullet+}$	Hexuronic acid$_4$ +2Δ
906.20	6.0	$[C_{36}H_{42}O_{27}]^{\bullet+}$	Hexuronic acid$_4$ +3Δ

908.21	5.5	$[C_{36}H_{44}O_{27}]^{\bullet +}$	Hexuronic acid$_4$ +3Δ
910.23	5.6	$[C_{36}H_{46}O_{27}]^{\bullet +}$	Hexuronic acid$_4$ +3Δ
912.24	4.9	$[C_{36}H_{48}O_{27}]^{\bullet +}$	Hexuronic acid$_4$ +3Δ
914.26	7.2	$[C_{36}H_{50}O_{27}]^{\bullet +}$	Hexuronic acid$_4$ +3Δ
924.20	5.0	$[C_{36}H_{44}O_{28}]^{\bullet +}$	Hexuronic acid$_4$ +3Δ
926.22	5.1	$[C_{36}H_{46}O_{28}]^{\bullet +}$	Hexuronic acid$_4$ +3Δ
928.24	6.0	$[C_{36}H_{48}O_{28}]^{\bullet +}$	Hexuronic acid$_4$ +3Δ
899.17	**4.3**	$\mathbf{[C_{30}H_{43}O_{31}]^{+}}$	**Hexuronic acid$_5$**
864.16	5.6	$[C_{30}H_{40}O_{29}]^{\bullet +}$	Hexuronic acid$_5$
866.19	7.1	$[C_{30}H_{42}O_{29}]^{\bullet +}$	Hexuronic acid$_5$
868.21	5.9	$[C_{30}H_{44}O_{29}]^{\bullet +}$	Hexuronic acid$_5$
870.22	7.2	$[C_{30}H_{46}O_{29}]^{\bullet +}$	Hexuronic acid$_5$
872.24	6.0	$[C_{30}H_{48}O_{29}]^{\bullet +}$	Hexuronic acid$_5$
878.14	5.1	$[C_{30}H_{38}O_{30}]^{\bullet +}$	Hexuronic acid$_5$
880.17	6.0	$[C_{30}H_{40}O_{30}]^{\bullet +}$	Hexuronic acid$_5$
882.18	4.3	$[C_{30}H_{42}O_{30}]^{\bullet +}$	Hexuronic acid$_5$
884.19	5.6	$[C_{30}H_{44}O_{30}]^{\bullet +}$	Hexuronic acid$_5$
886.22	7.1	$[C_{30}H_{46}O_{30}]^{\bullet +}$	Hexuronic acid$_5$
1075.21	**8.0**	$\mathbf{[C_{36}H_{51}O_{37}]^{+}}$	**Hexuronic acid$_6$**
1209.26	8.2	$[C_{44}H_{57}O_{39}]^{+}$	Hexuronic acid$_6$ +2Δ
1284.34	7.5	$[C_{48}H_{68}O_{40}]^{\bullet +}$	Hexuronic acid$_6$ +3Δ
1359.42	7.2	$[C_{52}H_{79}O_{41}]^{+}$	Hexuronic acid$_6$+4Δ
1427.27	**6.0**	$\mathbf{[C_{48}H_{67}O_{49}]^{+}}$	**Hexuronic acid$_8$**

Matrix-assisted laser desorption ionization mass spectrometry (MALDI-MS) has usually been considered for the analysis of carbohydrates. It can be successfully used to perform advanced structural investigation of complex polysaccharides and natural complex molecules, developing adequate experimental conditions [242-244]. MALDI-MS major advantages include high sensitivity and accuracy, applicability to a dynamic mass range [245] fast generation of results [246] and little or no fragmentation of the analytes. However, literature data reports MALDI analysis of carbohydrates is affected by salts, so that oligo- and polysaccharides often give rise to MALDI spectra of poor quality in the presence of contaminating salts [232,247]. In these experiments, the choice to perform partial hydrolysis of polysaccharides by acid and thermic conditions ensure the removal of sodium, as confirmed by high resolution mass measurements (table 3). Moreover, ammonium hydroxide solution was used to favour the formation of carboxylate/ammonium ion pairs, thus promote the desorption of oligosaccharides in MALDI MS experiments [248]. The experiments were planned in order to determine the methacrylation degree of the alginate (AlgMa) and spectra were handled using Data Explorer version 4.11 (AB Sciex). All signals of interest were detected as singly charged cation adduct or radical cation, and were used for data analysis. The degree of methacrylation

(MD%) was calculated as percentage ratio between derivatized oligomers vis total oligomers. Therefore, (MD%) was determined as average of three different experiments performed in triplicate (nine data points) and calculated as $(M_D\%)=[\Sigma ICA_M/\Sigma ICA]*100$, where ICA_M are the isotope cluster areas of only ion signals of methacrylated species (table 4) and ICA are isotope cluster areas of all identified oligosaccharides species. $(M_D\%)$ calculated was 63.4 ± 3.2.

Table 4. Isotope cluster area (ICA) of all identified species are reported. Three set of experiments (**1**, **2**, **3**) were performed. The listed ICA values are calculated as media from three consecutive acquisitions, in order to obtain a total of 9 subset data. In black are reported the oligosaccharides chains with no derivatization sites, in red are reported methacrylated species.

	1	**2**	**3**
Observed (m/z)	**ICA**	**ICA**	**ICA**
339.09	100663.7	189102.5	226460.7
353.07	113900.4	106517.5	141293.1
355.09	252417.8	169726.3	206883.1
371.08	233331.1	165196.7	233408.6
407.12	93049.0	107333.8	91277.5
441.12	208892.6	170514.3	393901.9
493.16	44751.0	42209.8	87516.0
509.15	12283.0	13228.4	29695.9
547.12	65984.4	43626.6	50261.5
603.18	37072.6	32687.0	46770.4
617.16	15552.1	6474.2	26693.8
685.18	21694.3	21486.8	38624.6
703.21	72892.7	48356.2	86437.2
719.20	29531.0	16025.6	32745.9
723.14	4821.6	3449.0	3528.0
753.22	10883.0	4031.4	4213.5
756.16	13470.5	9399.8	15550.4
758.17	23191.7	11464.4	26539.4
760.19	25181.2	14430.2	23780.2
770.14	19105.0	12010.6	19778.9
772.15	38201.5	25629.0	43505.2
774.18	28048.2	20738.0	33132.2
776.20	9166.3	5072.1	5351.9
784.12	19005.4	12605.7	22092.7
786.13	39395.7	26348.5	41325.6
788.15	34343.9	22897.5	42779.1
790.16	15481.3	11303.4	9516.7
796.20	15567.2	8677.0	17946.5
798.21	39132.4	33379.9	47264.3
800.22	66395.1	47332.3	76686.6
802.24	40989.8	27666.7	49429.7
812.19	35587.5	22448.1	43324.2
814.20	57817.3	43087.9	66495.1

816.22	42240.2	28973.0	52247.2
826.20	64070.3	46933.7	83361.4
828.23	70726.1	54696.5	84982.5
830.23	39595.3	28972.3	48588.3
838.16	11631.8	10461.0	16842.9
840.19	38195.3	25191.9	40558.9
842.21	50207.0	33149.4	49625.6
844.22	28572.5	20474.1	31849.2
852.14	27912.9	16100.6	29160.1
854.17	51601.1	33108.4	58315.9
856.19	37175.3	27464.8	45381.6
858.20	18045.7	10290.9	17363.3
864.16	3557.4	1705.7	2783.3
866.19	12136.6	7233.6	11353.5
868.21	16930.3	14585.7	22188.2
870.22	22118.8	14651.3	21759.8
872.24	11291.5	8303.2	9653.6
878.14	8669.2	6093.8	7717.9
880.17	17297.4	9036.9	18124.8
882.18	28955.5	17305.7	30367.3
884.19	17388.3	11255.4	18712.5
886.22	10599.5	5365.2	9911.5
899.17	7141.0	1607.0	2309.4
906.20	4836.3	2867.8	5360.1
908.21	8385.3	5470.8	7984.2
910.23	6526.8	4863.0	9536.1
912.24	10817.6	6828.9	10106.4
914.26	9350.9	4712.0	12423.4
924.20	5411.9	2689.9	6073.1
926.22	9824.6	4994.3	8697.4
928.24	7242.2	2893.5	7944.9
1075.21	519.3	746.0	2826.2
1209.26	2024.2	1433.5	7225.0
1284.34	2462.6	1739.8	9076.7
1359.42	1137.4	410.5	1022.9
1427.27	376.9	262.6	670.6
	Σ (ICA 1) 2542776.0	**Σ (ICA 2)** 1967331.7	**Σ (ICA 3)** 3086318.7
	Σ (ICA$_M$ 1) 1603791.4	**Σ (ICA$_M$ 2)** 1187527.7	**Σ (ICA$_M$ 3)** 2061888.6
	$\frac{\sum ICA_M 1}{\sum \mathrm{ICA1}} * 100$ **63.07**	$\frac{\sum ICA_M 2}{\sum \mathrm{ICA2}} * 100$ **60.36**	$\frac{\sum ICA_M 3}{\sum \mathrm{ICA3}} * 100$ **66.81**
		AVERAGE	***63.41***
		Standard Deviation	***3.24***

Thermal behaviour of the alginate, AlgMa, photo-crosslinked AlgMa and Irgacure 2959 (the photoinitiator used to trigger the photo-crosslinking process in the presence of UV light) was evaluate by thermogravimetric analyses, in order to verify (i) whether the methacrylation reaction affects the polymer's thermal stability and (ii) how the photo-crosslinking process influences the thermal stability with respect to the corresponding uncrosslinked polymer. All the measurements were carried out in inert environment, under nitrogen gas flow. Alginate was evaluated by directly weighting the pristine gelatine supplied by Carlo Erba, while GelMa and crosslinked GelMa (GelMa after UV) were both analysed by weighting the lyophilized form after the synthesis and after the photo-crosslinking process (1 min of UV light, 50 % of intensity, 3 cm of distance), respectively. As shown from Figure 15, Irgacure 2959 (I2959), represented by the green curve, displays one weight loss showing a weight residue of 8 % at 600 °C and a maximum degradation rate at 261 °C (degradation temperature). Alginate (Alg), represented in Figure 15 by the pink curve, shows a rapid decrease of the weight starting from low temperature up to 100 °C, which is ascribable to the loss of water from the hygroscopic sample. Then, at 240 °C (degradation temperature), it displays the highest rate of degradation until to reach the 32 % of weight residue at 600 °C. Both AlgMa and cross-linked AlgMa (AlgMa after UV), represented in Figure 15 by the blue and red thermograms, respectively, show a rapid weight decrease at low temperature, similarly to what observed for the alginate sample, suggesting, even in this case, the evaporation of the water which could be still entrapped in the AlgMa-based polymers structure after the lyophilization process. Furthermore, AlgMa sample displays the maximum degradation rate at 239 °C and a weight residue of 34 % at 600 °C while cross-linked AlgMa (photo-crosslinked with UV light 1 min, 50 % of light intensity, 3 cm of distance in the presence of Irgacure 2959 as photo-initiator) reaches the maximum degradation rate at 241 °C and shows a weight residue of 30 % at 600 °C. However, the presence of cross-links formed between the acrylate moieties after the UV photo-crosslinking are not detectable in the case of alginate by TGA analysis thus, as a general consideration, it is possible to assess that (i) all the thermograms are characterized by one single step of weight change, suggesting that the degradation processes of the polymers are based on one single degradation kinetic, (ii) the chemical methacrylation does not significantly affect the thermal stability of the GelMa polymer and (iii) the effect of the photo-crosslinking process on the AlgMa polymer are not detectable with this characterization technique.

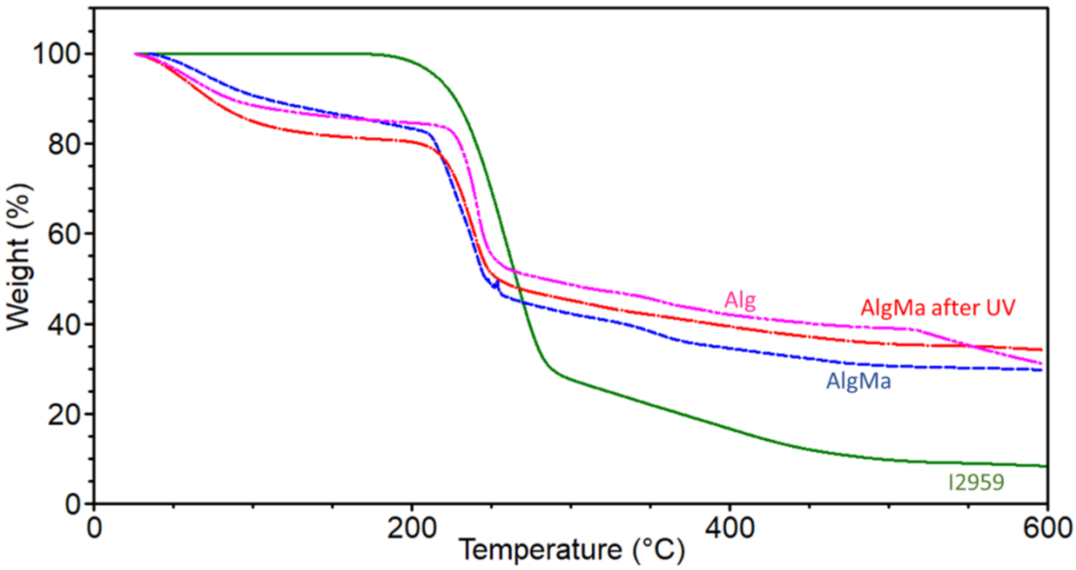

Figure 15. Thermogravimetric analyses of photo-initiator Irgacure 2959 (green solid line), unmodified alginate (Alg; pink broken double dash line), modified Alginate (AlgMa; blue short dash line) and cross-linked AlgMa (AlgMa after UV; red dash dot line).

3.1.2. Gelatin methacrylate

Similarly to the alginate and alginate-methacrylate, gelatin is one of the most used hydrogel for 3D bioprinting application thanks to its biocompatibility, ability to support cell growth and proliferation, transparency, printability and ability to preserve complex 3D bioprinted structures at low temperature (e.g. ranging from 20 °C to 25 °C). However, due to its high thermo-responsiveness, which makes it liquid over 32 °C and "gelly" below 32 °C, it cannot be used as such to reproduce ECM-like structure for 3D *in vitro* models fabrication because, at incubation conditions (37 °C), it losts all the mechanical properties and ability to support cell growth and proliferation. For this reason, photo-crosslinkable gelatine methacrylate might be a good alternative to overcome these limitations, because the methacrylate moieties, branched to the gelatin backbone chains, forms covalent crosslinks when irradiated with UV light in the presence of photo-initiator, which triggers the crosslinking process based on a radical reaction. In this way, once the photo-crosslinking process occurs, the hydrogel is able to maintain the imparted shape, stiffness and complexity even at 37 °C (incubation conditions). In this Thesis, gelatin methacrylate was obtained through a methacrylation reaction between the hydroxyl groups and primary amino groups of the biopolymer chains, and the methacrylate anhydride (MAA), under suitable conditions of pH, temperature, and initial concentration of reagents, as reported in Figure 16. The traditional preparation method of GelMa was originally developed by Van Den Bulcke et al. [249], in which, an important excess of MAA (> 10 mL/g of gelatin) reacted with the primary amino groups and hydroxyl groups of the gelatin dissolved in phosphate buffer (pH = 8) solution at 50°C for at least 2 days. However, because of the poor buffer capacity of the phosphate solution, this approach involved laborious lab practice and several pH adjustments by using concentrated NaOH (5 M) in order to maintain the pH over the gelatin isoelectric point (which is around 8) and to make the gelatin amino groups available for the substitution. For this reason, over the years, the synthesis of GelMa has been optimized in order to reduce the complexity and the time of the synthesis by changing the formulation of the buffer solution to increase its buffer capacity. Carbonate Bicarbonate (CB) buffer 0,25 M pH = 9 was selected as the best solvent to carry out the reaction since it has demonstrated to autonomously sustain the pH over the gelatin isoelectric point thus increasing the reaction efficiency in a short period of time. In particular, the use if CB buffer reduces the reaction time from 3 days to 1 hour and the excess of MAA from 10 mL/ g of gelatin to 1 mL/g of gelatin. Moreover, 10 % w/v of gelatin was selected as the best concentration to start the reaction because it ensures the suitable collision between gelatin chains and MAA monomers that lead to the desired substitution of the MAA to the amino groups by following the schematic reaction represented in Figure 16. For this reason, by changing the buffer solution it is possible to reach better degree of substitution by using a reduced amount of MAA and decreasing of two order of magnitude the reaction time.

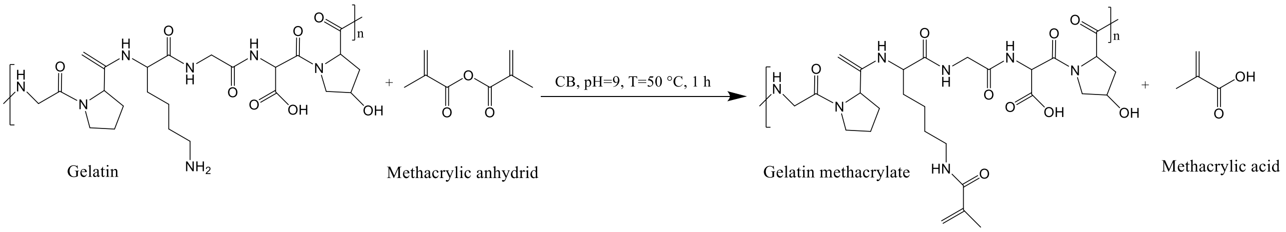

Figure 16. Schematic representation of GelMa synthesis.

The conjugation of methacryloyl groups to gelatin chains was confirmed by ^{1}H-NMR. Samples of GelMA and gelatin were dissolved in deuterium oxide (D_2O) at a concentration of 40 mg/1 mL. The spectra were collected at 50 °C, to avoid gel formation of gelatin and GelMa, as explained in the experimental section. The direct comparison between the GelMa (Figure 17a) and pristine gelatin ^{1}H-NMR spectra (GelMa spectrum not shown, spectrum provided from the literature [156], reveals the appearance of two proton signals at $\delta = 5.25$ and $\delta = 5.48$ ppm, which are related to the proton of methylene groups of the methacrylic unit, as well as a peak at $\delta = 1.8$ ppm, due to the methyl group of the same functional unit. This result confirms the efficiency of the functionalization. Furthermore, the decrease of the signal at $\delta = 3.02$ ppm, which is referred to the methylene lysine protons, indicates the conjugation of the lysine group with the MAA. However, it is worth pointing out that the evaluation of the degree of substitution (DS) cannot be evaluated through this analysis due to the presence of a high numbers of proton which makes the peak integration laborious. For this reason, the DS was evaluated through a titration with TNBS (2,4,6-Trinitrobenzenesulfonic acid), which is a colorimetric analysis in which the molecule links free amino groups of the gelatin backbone chains, as explained in the next section.

2,4,6-Trinitrobenzenesulfonic acid or TNBS is a rapid and sensitive assay reagent for the determination of free amino groups and it can be employed to quantitatively assess the degree of substitution of the gelatin amino groups with the acrylate moieties, using the procedure described in the experimental section. Briefly, primary amines, upon reaction with TNBS, form a highly chromogenic derivative (yellow-coloured), which absorbance can be measured at 335 nm.

Firstly, a standard calibration curve with glycine (standard model) was built by registering the absorbance values of the solutions containing several concentrations of glycine (0, 8, 20, 32, 70 µL/mL) reacted with the same concentration of TNBS 0.01% (w/v). Each absorbance value (Table 5) was reported in a graph against glycine concentration (µL/mL), as represented in Figure 17 b. Then, modified gelatin (GelMa) DS was obtained by detecting the absorbance values of pristine gelatin and GelMa after the reaction with TNBS and by using the following equations (equation 1 and 2):

$$\frac{\text{moles amino groups}}{\text{g (gelatin or GelMA)}} = \frac{2\text{x Abs (gelatin or GelMa) x } 0.0075}{1.46 \text{ x } 10^4 \text{ x } 1\text{x } 0.0158} \qquad \textit{equation (1)}$$

where:

- Abs (gelatin or GelMa): is the absorbance value of the solution obtained after the reaction with gelatin and TNBS or GelMa and TNBS;
- 0.0075: is the volume of the solution;
- $1.46 \text{ x } 10^4$: is the molar absorptivity of the TNBS;
- 1: cell path length in cm;
- 0.0158: sample weight in grams.

$$DS = \frac{M\ gelatin - M\ GelMa}{\text{M gelatin}} \qquad \textit{equation (2)}$$

where:

- $\frac{moles\ amino\ groups}{g\ (gelatin)} = M\ gelatin;$
- $\frac{moles\ amino\ groups}{g\ (GelMA)} = M\ GelMa.$

Finally, the DS of GelMa obtained from the methacrylation reaction and detected through the TNBS titration results to be 80 %.

Table 5. Absorbance values of glycine standard molecule at different concentrations, pristine gelatine and modified gelatine after reaction with TNBS.

	$[NH_2]$	Abs 1	Abs 2	Abs 3	ABS*	DVS**
Glycine	0	0.295	0.2384	0.1808	0.24	0.06
	8	0.5947	0.6892	0.5835	0.62	0.06
	20	0.9045	1.0988	0.9196	0.97	0.11
	32	0.9226	0.9984	0.992	1.04	0.04
	70	1.1801	1.2955	1.216	1.16	0.06
	Gel	1.025	1.001	1.036	1.02	0.02
	GelMa	0.291	0.1887	0.2768	0.25	0.06

*average value
**standard deviation

Pristine gelatin (Gel), gelatin methacrylate (GelMa) and photo-crosslinked gelatin methacrylate (p-GelMa) were characterized by FT-IR spectroscopy to (i) further verify the substitution after the methacrylation and (ii) and to evaluate the crosslinking reaction between acrylate moieties in the presence of photo-initiator and after UV irradiation. As observed from Figure 17 c, all the spectra display the characteristic peaks of gelatin polymer. The typical absorption band around 3340 cm^{-1} is attributed to the O–H and N–H stretching vibrations. The peaks in the region 2800 cm^{-1} - 3100 cm^{-1} are ascribed to the stretching vibration of C–H groups. The backbone structure of gelatin is associated in both spectra with the absorption bands at around 1650 cm^{-1} (C–O stretching, amide I), 1540 cm^{-1} (N–H bending coupled to C–H stretching, amide II), and 1250 cm^{-1} (C–N stretching and N–H bending, amide III). Regarding the GelMa spectrum, it is noteworthy that the typical peak at around 1640 cm^{-1} corresponds to the C–C stretching of the methacrylate groups, is too close to the amide I C–O stretching peak, therefore, it is difficult to detect and to verify its disappearance after the photo-crosslinking process.

Thermal behaviour of the gelatin, GelMa, photo-crosslinked GelMa and Irgacure 2959 was evaluated by thermogravimetric analysis, in order to verify (i) whether the methacrylation reaction affects the polymer's thermal stability and (ii) how the photo-crosslinking process influences the thermal stability with respect to the corresponding uncrosslinked polymer. All the measurements were carried out in inert environment, under nitrogen gas flow. As described for the alginate-based polymers, Gelatin was evaluated by directly weighting the pristine gelatine supplied Sigma Aldrich, while GelMa and crosslinkined GelMa were both analysed by weighting the lyophilized form after the synthesis and after the photo-crosslinking process (1 min of UV light, 50 % of intensity, 3 cm of distance), respectively. As shown from Figure 17 d, Irgacure 2959 (I2959), represented by the red curve, displays one weight loss showing a weight residue of 8 % at 600 °C and a maximum degradation rate at 261 °C (degradation temperature). Pristine gelatin (Gel), represented in Figure 17 d by the pink curve, shows a rapid decrease of the weight starting from the lowest temperature up to 100 °C, which is ascribable to the loss of water from the hygroscopic sample. Then, at 329 °C (degradation temperature), gelatin displays the highest rate of degradation until to reach the 22 % of weight residue at 600 °C. After methacrylation, gelatin metharylate (GelMa) product was obtained and the lyophilized product undergone the same thermogravimetric scan of the other polymer, resulting in the blue curve reported in Figure 17 d. As observed from the thermogram, GelMa (blue curve) shows a rapid weight decrease at low temperature, similarly to what observed for the gelatin sample, suggesting, even in this case, the evaporation of the water which could be still entrapped in the GelMa structure after the lyophilization process. Furthermore, GelMa sample displays the maximum degradation rate at 311 °C and a weight residue of 24 % at 600 °C. Finally, cross-linked GelMa (GelMa after UV) reported in Figure 17 d with the green curve, shows the same thermogram of the uncrosslinked GelMa (blue curve) in which the initial temperature of the degradation process and then maximum degradation temperature are shifted at higher temperature (321 °C), meaning that the cross-links formed between the acrylate moieties after the UV photo-crosslinking slightly increase the thermal stability of the polymer. As a general observation, (i) all the thermograms are characterized by one single step of weight change, suggesting that the degradation processes of the polymers are based on one single degradation kinetic, (ii) the chemical methacrylation does not significantly affect the thermal stability of the GelMa polymer and (iii) the photo-crosslinking process slightly induce an increase of the thermal stability.

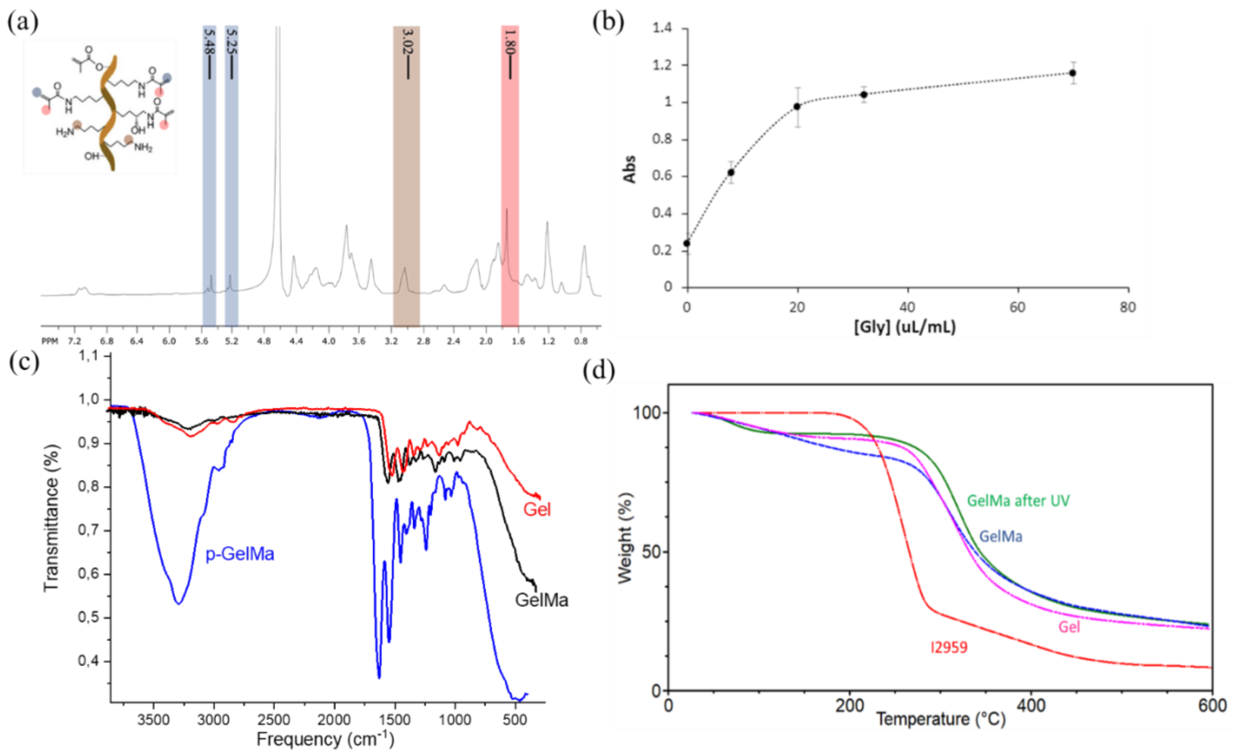

Figure 17. (a) ^{1}H-NMR of gelatin after methacrylation registrered at 50 °C. (b) Calibration curve obtained by reacting glycine and TNBSA. (8) FT-IR spectra of pristine gelatin (black curve), GelMa (blue curve) and p-GelMa (red curve). (d)Thermogravimetric analyses of photo-initiator Irgacure 2959 (red dash dot red line), unmodified gelatin (Gel; pink broken double dash line), modified gelatine (GelMa; blue short dash line) and cross-linked GelMa (GelMa after UV; green solid line).

3.1.3. Collagen

Collagen formulation was directly provided by the company Typeone Biomaterials s.r.l. (Lecce, Italy) ready-to-use, in a sterile condition and with a neutral pH.

In brief, as already mentioned in the introduction section, collagen is the most abundant protein of the ECM and play a key role in the cell pathway. The fabrication of 3D models through 3D bioprinting which are made by pure collagen hydrogel has gained great attention in order to simulate and replicate the main physiological constituent of the tissue [250]. However, the development and the use of plain collagen hydrogel is still challenging since collagen has poor mechanical properties, needed to provide mechanical stability during time. Furthermore, its uncontrollable gelation reflects in poorly controllable mechanical properties making it not suitable for the replication of a wide range of tissues stiffness. Most of the time, in order to overcome this limitation, collagen is used in blend with other synthetic or natural polymers which act as supporting materials and confer mechanical stability to the models but, at the same time, reduce the native-like composition of the matrix [250]. In addition, the latest plain collagen hydrogel formulations, display tricky and complex manual neutralization process to carry out before the bioprinting that reduce the reliability and reproducibility of the collagen batches, since the collagen hydrogel preparation involves the use of strong acid solvent which can affect its printability and cell viability, if any traces remain in the syringe [250].

For this reason, in order to produce collagen-based 3D *in vitro* model by overcoming the limitations related to the current collagen formulation, a printable plain collagen hydrogel with controlled gelation reaction was developed in cooperation with Typeone Biomaterials s.r.l. The chemical composition, characterization and process production of the collagen were optimized and developed by the company.

3.2. Evaluation of 3D printability through rheological characterization

3.2.1. Hydrogels and bioinks formulation

AlgMa, GelMa, collagen and collagen/gelatin IPN were employed to produce hydrogels and the corresponding bioinks containing cells for the fabrication of 3D bioprinted tissue models. Hydrogels and bioinks formulations were optimized with the aim to obtain printable materials (through extrusion-based mechanism) able to undergone the bioprinting process by maintaining, at the same time, the suitable mechanical properties after printing and to support cell growth from a biological side. In particular, when bioinks or hydrogels have to be prepared for the fabrication of 3D structures, it is fundamental to consider which steps they have to experience in order to prepare the suitable formulation able to withstand all the requirements. During a bioprinting process, the hydrogel or bioink is initially contained inside a syringe in which it is in a "rest" state, then it undergoes a transition to a high shear condition while passing through the nozzle, and finally it reaches a new "rest" state when it is deposited onto the bioprinter bed, which must preserve the designed shape and structure without collapse during the time (Figure 18 a). Basically, it is possible to resume that the materials experienced three different forces or shear during the whole process: (i) static force, (ii) high shear rate or high force and (iii) static force again, in which polymer chains has to reform all the physical entaglements in order to provide mechanical stability (Figure 18 b). To be able to address this, a material must display several mechanical and rheological requirements which can be evaluated and predicted before the bioprinting through a rheological characterization such as, for instance, characterization of storage (G') and loss (G'') moduli and viscosity function. In this way, it is possible to optimize the formulation of the hydrogels or bioinks as a function of its printability, ability to recover its initial mechanical properties and behaviour in static condition, by avoiding waste of time with laborious "trials and errors" using the bioprinter.

More in detail, in the first step, before the printing process, the elastic modulus (G') must be higher than the loss one (G''); in the second step, represented by the bioink flowing through the nozzle, the material must display a shear thinning behaviour, in which the macromolecular chains change their organization flowing under the applied shear (viscosity decreases with the increase of the shear rate); in the last stage, after the bioprinting process, the hydrogel must be able to retains its initial shape, thus the macromolecular chains should rapidly reform internal interactions in order to recover the initial mechanical properties and maintain the shape of the filament once deposited onto the bed (shape-fidelity property), as reported in the schematic representation below (Figure 18 b).

In this section, the hydrogels and bioinks formulation will be discussed in correlation with their rheological properties and printability behaviour.

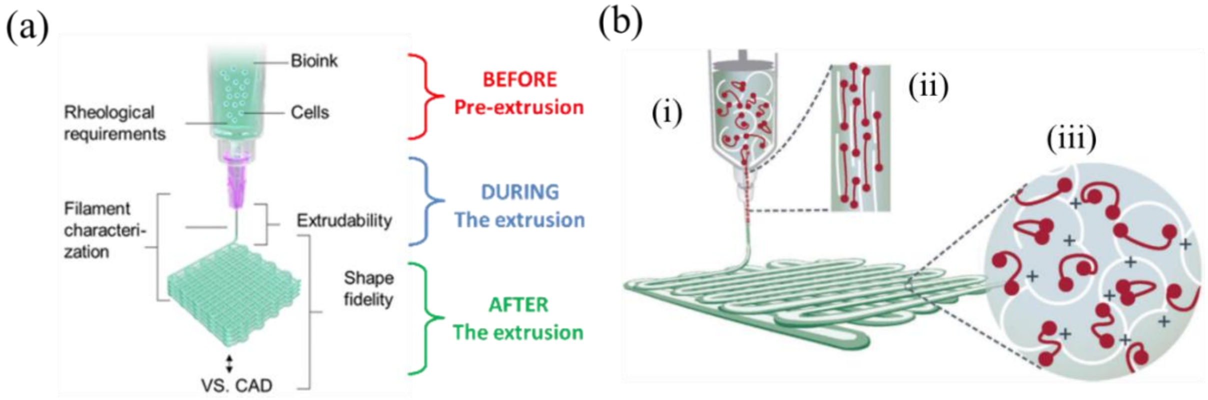

Figure 18. Schematic representation of (a) bioprinting steps before, during and after the extrusion; (b) schematic representation of the chains conformation (i) before, (ii) during and (iii)after the bioprinting process.

3.2.2. Alginate methacrylate-based hydrogel and bioink

AlgMa 72 h was selected as the best modified product to produce AlgMa-based hydrogels and bioinks, thanks to the proven substitution obtained through our affordable synthesis approach, as demonstrated by the chemical characterization previously described. The bioinks formulation used for the production of the final living 3D tissue models, involves different preparation stages which start from the development of (i) the alginate solution, (ii) follow with the actual hydrogel and ink, which in some cases can have the same composition, and ends (iii) with the final bionks form that contain ink intimately mixed with cells.

The first step regards the formulation of the pre-starting ink, which basically consists in the formulation of a biocompatible and photo-crosslinkable hydrogel with tunable mechanical properties able to undergone the 3D bioprinting process. To achieve this, AlgMa solution was first prepared prior to hydrogel formation by dissolving purified and lyophilized AlgMa in a phosphate-based buffer solution (pH = 7.4), in order to provide the suitable osmotic concentration to the cells once embedded in the final bioink and to avoid cell dehydration along with cell membrane breakage. Several concentrations of AlgMa, such as 2 % w/v, 3 % w/v, 4 % w/v and 10 % w/v, have been tested before the selection of the final one. In particular, lower AlgMa concentration (2 % w/v and 3 % w/v) leads to too liquid solutions, not suitable for the preparation of 3D printable hydrogel, while higher concentration (10 % w/v) requires long time of solubilization (more than overnight at 37 °C) and provides straw yellow colour to the final solution, which makes it not useful for 3D cell culture, in which transparent materials are required to carry out 3D imaging and biological assays. Finally, 4 % w/v of AlgMa solution was selected as the best concentration to obtain a homogenous “gelly-like” solution with a fast solubilization rate at 37 °C and optical transparency.

Rheological properties of AlgMa solution at 4 % w/v were analysed in order to predict and verify its behaviour by simulating the 3D bioprinting process. For this purpose, both oscillation and rotational measurements, such as amplitude sweep, flow curve and recovery tests, were carried out at 25 °C in a plate-plate geometry, as described in the experimental section. 4 % w/v of pristine alginate solution, solubilized in the same phosphate-based buffer, were also evaluated through the same rheological tests and compared with the AlgMa solution ones, in order to assess any effect of the methacrylation on the rheological properties. Amplitude sweep analysis was performed as first “screening” to identify the rheological moduli of the solutions and to correlate the resulting behaviour with the printability. Amplitude sweep analysis (oscillatory analyses), reported in Figure 19 a, was reported in logarithmic scale by plotting storage (G’) and loss (G’’) moduli against a deformation range (strain) from 0.01 % to 1000 %. In particular, pristine Alg and AlgMa solutions display a loss modulus G’’, of 61 Pa and 52 Pa, respectively, higher than the storage modulus G’, of 19 Pa and 15 Pa, respectively, up to 100 % of deformation. Then, over 100 % of strain, both moduli drop down without displaying any resistance to the higher deformation. This behaviour is typically ascribable to “liquid-like” gel in which the viscous behaviour, represented by the loss modulus G’’, dominates the elastic one, represented by the storage modulus G’. As it is possible to observe from the amplitude sweep graph (Figure 19 a), both Alg and AlgMa solutions show a similar trend and values of G’ and G’’ moduli, meaning that no differences before and after methacrylation are detected from a rheological point of view.

In order to verify the shear-thinning behaviour of the materials, which is the parameter related to the actual printability, flow curves (rotational analyses) where performed on both Alg and AlgMa solutions from 0.01 s^{-1} to 1000 s^{-1} and the results are reported in Figure 19 (b,c) by plotting the viscosity curve (η) (Figure 19 b) and the shear stress (τ) (Figure 19 c) as a function of the shear rate in both logarithmic and linear scales, respectively. As shown from Figure 19 b, Alg and AlgMa solution display a similar behaviour characterized by an initial and small pronounced viscosity plateau, also called zero-shear viscosity (η_0) or Newtonian plateau, followed by a linear decrease of the viscosity with the increase of the shear-rate (shear-rate dependent viscosity function $\eta = f(\dot{\gamma})$. In particular, Alg solution show 11 Pa×S of viscosity at 0.1 s^{-1} and 0.9 Pa×S at 1000 s^{-1} shear rate, while AlgMa solution display 13 Pa×S of viscosity at 0.1 s^{-1} and 0.8 Pa×S at 1000 s^{-1} shear rate.

From a macromolecular point of view, this behaviour might be explained by using the entanglement model, in which a volume element containing many entangled and randomly distributed polymer chains occupy a certain physical space. When shearing, a certain number of macromolecules are oriented into shear direction and, for some of them, this results in partial disentanglements. As a consequence, viscosity decreases in these parts of the volume element. Simultaneously, however, some other macromolecules which were already oriented and disentangled in the previous time interval are now recoiling and re-entangling again. This is a consequence of the viscoelastic behaviour which the polymer molecules still are able to show even under low-shear conditions. In the observed period of time, the sum of the partial orientations and re-coilings of the macromolecules results in no significant change of the flow resistance related to the behaviour of the whole volume element. Therefore here, the constant entanglement density results in a constant viscosity value. Thus, the total η-value in this shear rate range is still measured as a constant value, which is referred to as the zero-shear viscosity η_0. Moreover, from Figure 19 b it is possible to observe that AlgMa solution, represented with the red viscosity curve, displays a less pronounced zero-shear viscosity range or Newtonian plateau. This difference might be dependent to the polymer molar mass and spatial organization since polymers with smaller chains, could not show strong entanglements between the individual molecule chains, thus displaying ideally viscous flow behaviour, while polymer with higher molar mass or a more complex spatial organization, which might form entanglements between polymer chains, show zero-shear viscosity at a lower shear value and at higher viscosity value. Moreover, in order to better visualize the viscosity behaviour of the solutions, the flow curves were also reported by referring to the shear-stress (τ) as a function of the shear-rate in a linear scale, as shown in Figure 19 c. In this case, it is evident that the materials do not show a yield point. Finally, because of the "liquid-like" nature of these solutions, the lack of a flow point which define their printability, and their poor recovery behaviour resulting from the rheological characterization, 3D bioprinting tests were carried out to confirm the hypothesis of the impossibility to obtain printable materials with the suitable rheological properties and mechanical stability. The bioprinting test, which involves the formation of a circle grid structure with 3 cm of diameter and 5x5 mm of pore size, demonstrates that the AlgMa filament produced after the extrusion of the AlgMa solution, completely losts its shape and spread onto the bioprinter bed. The poor shape-fidelity of AlgMa solution was also confirmed by the recovery test results shown in Figure 19, which simulate the entire bioprinting process from the pre-printing stage to the material deposition onto the bioprinter bed, by reproducing through a rotational movement of the rheometer's plates, the same shear rate that the material experiences in the three printing stages: (i) a static shear (before the printing), (ii) an high shear (during the extrusion) and (ii) a static shear (after the extrusion). To reproduce the shear value as much as possible similar to that one experienced from the material during the extrusion, low shear (0,1 s^{-1}), simulating static condition were applied in the first and last stages, while high shear of 150 s^{-1} was applied in the second one for 6 min, reproducing the real shear applied onto the material while passing through the nozzle. This value was obtained through the mathematical equations (equation 3, equation 4, equation 5) reported below, which consider (i) the real bioprinting speed rate, (ii) the geometry of the needle and (iii) the volumetric flow rate:

$$\gamma = \frac{4Q}{\pi r^3} \qquad \textit{equation (3)}$$

where Q is the volumetric flow rate and r is the value of the nozzle radius. The value of the volumetric flow rate for a nozzle that has the shape of a cylinder was determined using the equation 4:

$$Q = A_l V \qquad \textit{equation (4)}$$

where A_l is the lateral area of the section and V represents the flow velocity. The lateral area of the cylinder section was calculated through the equation:

$$A_l = 2\pi r h \qquad \textit{equation (5)}$$

where r is the value of the nozzle radius and h is the height of the nozzle.

By approximation, the flow rate has been set at 10 mm/s, the nozzle 22 Gauge, which are equivalent to 0.4 mm in diameter, while the height of the nozzle is equal to 10 mm. Therefore, the value of shear strain was found to be equal to 150 s^{-1}. As resulted from the recovery test (Figure 19 d), AlgMa solution displays 13 Pa×s as viscosity value at low shear rate (0.1 s^{-1}), when the pre-printing stage is simulated, and the recovery behaviour after the high shear rate, simulating the extrusion step, is evaluated as the ability of the hydrogel to reach the same viscosity value displayed in the first step before the extrusion. As shown from the graph in Figure 19 d), AlgMa solution reaches 3 Pa×s as viscosity at low shear rate after the printing process, meaning that the recovery is 23%.

For this reason, the AlgMa hydrogel formation is required to create physical entanglements and weak chemical interactions between polymers chains, which should provide the suitable mechanical properties to fulfil all the requirements to get both printability and shape-fidelity properties that are the main characteristics of an ink.

AlgMa hydrogel was produced by mixing in a ratio of 25:10 v/v, 4 % w/v of AlgMa solution with calcium chloride 60 mM, as explained in the experimental section. This specific ratio was obtained after several optimization and by taking inspiration from Freeman et al. [251] work, with the aim to only provide the initial required mechanical properties to the material by avoiding any instantaneous and not homogenous permanently crosslinks between chains, typical of this ionic interaction. In fact, calcium ions are usually employed to ionically crosslink alginate or alginate-based hydrogel by exploiting the “egg-box” structure which is formed between alginate -OH groups and ions. This ability to produce ionic interactions, is preserved after the methacrylation reaction and it can be exploit to create the physical entanglements and the weak chemical interactions between polymers chains required for the formulation of the final ink.

Once the starting hydrogel is formed, AlgMa inks are produced by separately mixing two different concentrations of Irgacure 2959, 0.2 % w/v and 0.25 % w/v, to the AlgMa hydrogel formulation already optimized, in order to produce ink A and ink B, respectively. These concentrations of Irgacure were selected to obtain tunable mechanical properties, by considering the fact that different stiffnesses can be reached both by changing (i) the UV irradiation time after the printing process, maintaining fixed the photo-initiator concentration, and (ii) the concentration of Irgacure 2959, maintaining fixed the UV irradiation time. Several tests were carried out before to establish the right photo-initiator concentrations and UV irradiation parameters, by evaluating the mechanical stability tests and the cell viability, after photo-crosslinking. In brief, different AlgMa inks containing different concentration of both polymer and photo-initiator, were irradiated with different UV time, with the aim to maximize the mechanical stability in the culture media and preserve cell functionalities. To assess the efficiency and the effects of the photo-initiator and UV irradiation time on the cells, stability tests in phosphate buffer solution and cell viability evaluation through cell counting with tripam blue, were evaluated. Table 6 summarizes all the tests carried out and the corresponding results.

Table 6. Summary of the stability tests and cell viability of different AlgMa ink formulations.

Sample	I2959 concentration	UV time	Stability test	Cell viability
AlgMa 4% (w/v)	0.05 % (w/v)	1 min	Solubilized after 5 min	/
AlgMa 4% (w/v)	0.05 % (w/v)	5 min	Solubilized after 15 min	/
AlgMa 4% (w/v)	0.05 % (w/v)	10 min	Solubilized after 20 min	/
AlgMa 4% (w/v)	0.1 % (w/v)	1 min	Solubilized after 20 min	/
AlgMa 4% (w/v)	0.1 % (w/v)	5 min	Solubilized after 2 h	/
AlgMa 4% (w/v)	0.1 % (w/v)	10 min	Solubilized after 1 day	100% dead
AlgMa 4% (w/v)	0.2 % (w/v)	5 min	Stable until 3 days	100% dead
AlgMa 4% (w/v)	0.2 % (w/v)	1 min 1,5 min 2 min	Stable until 3 days but lost its shape[*]	Live/dead
AlgMa 4% (w/v)	0.25 % (w/v)	1 min 1,5 min 2 min	Stable until 3 days	Live/dead

[1] stability tests were performed in phosphate buffer solution by observing structural modification and the dissolution of the material during time.

[2] cell viability was assessed by counting live cells previously stained with tripam blue reagent. HeLa were used as cell type.

[*] shape of the scaffolds after the bioprinting process.

After this quick evaluation of mechanical stability and live/dead assay, 0.2 and 0.25 % (w/v) was selected as the best Irgacure concentration to produce ink A and ink B, respectively.

In order to evaluate the printability and the shape fidelity of both ink A and ink B, rheological characterization was carried out only on the AlgMa hydrogel formulation since the presence of Irgacure 2959 in the small percentage used does not affect the rheological parameters. Rheological behaviour of AlgMa hydrogel (or AlgMa ink) is reported in Figure 19 as a black curve. From the amplitude sweep measure (Figure 19 a), AlgMa hydrogel shows a clear different behaviour with respect to both Alg and AlgMa solutions by displaying higher storage modulus (G’) of 90 Pa than loss modulus (G’’) of 8 Pa. Moreover, an LVE (linear viscoelastic region) can be identified from 0.01 % of strain up to 3 % of strain, which determines the region in which the polymer maintain is elastic behaviour and, here, the elastic behaviour dominates the viscous one (“gel-like” behaviour). Furthermore, when exceeding the limit of the LVE range, with many gels, highly concentrated dispersions showing a network of forces, chemically cross-linked materials and solids, the curves of G’ and G’’ often do not slope downwards with increasing deformation. G’’ peak basically indicates a portion of deformation energy which is already used before the final breakdown of the internal superstructure occurs, to irreversibly deform at first only parts of the latter. This may occur due to relative motion between the molecules, flexible end-pieces of chains and side chains, long network bridges, or superstructures which are not linked or otherwise fixed in the network.

When a G’’ peak appears, it can be assumed that initially there was a network structure when at rest, independent of whether this structure was built up via primary or secondary bonds. In this case, it can also be interpreted that this network does not suddenly collapse in the whole shear gap if the LVE range has been exceeded, since here at the beginning, micro-cracks are forming which grow into macro-cracks until the G’’ peak is exceeded, until finally a large crack divides the entire shear gap. This event is displayed by the crossover point G’ = G’’, which in this case occurs at 46 %, and it means that the sample is flowing now as a whole. The maximum of the G’’ curve and the crossover point of the curves of G’ and G’’ are mostly occurring very close together.

By further analysing the viscosity function and the printability of the AlgMa hydrogel formulation through rotational tests, it is possible to observe that this material decreases his viscosity with the increase of the applied shear rate (Figure 19 b), meaning that it is able to flow under an applied shear rate without showing any constant η-value in the low-shear range, which is the plateau value of the zero-shear viscosity η_0, typical of the unfilled or uncrosslinked materials, as displayed for Alg and AlgMa solutions. In particular, at low shear rate AlgMa hydrogel displays 681 Pa×s of viscosity while at high shear rate this value decreases to reach a value of 0.4 Pa×s. Furthermore, Figure 19 c reporting shear stress against shear rate in a linear scale, clearly shows that AlgMa hydrogel display a well-defined and pronounced yield point around 100 s^{-1}, which defines the point at which a material is able to flow after the application of external forces and that typically characterize ink and bioink for 3D bioprinting application.

Finally, from the recovery test (Figure 19 d), carried out by applying the same strategy used for AlgMa solution, AlgMa hydrogel shows higher viscosity value of 720 Pa×s and 300 Pa×s at low shear rate (0.1 s^{-1}) in the first and last step of the measure, respectively, with respect to the AlgMa solution, and a compared viscosity value at high shear rate with a recovery percentage of 41 %. This result demonstrates that (i) AlgMa hydrogel formulation can be easily extruded as AlgMa solution, even the presence of entanglements and ionic interactions, and that (ii) the recovery behaviour is predominant after the high shear.

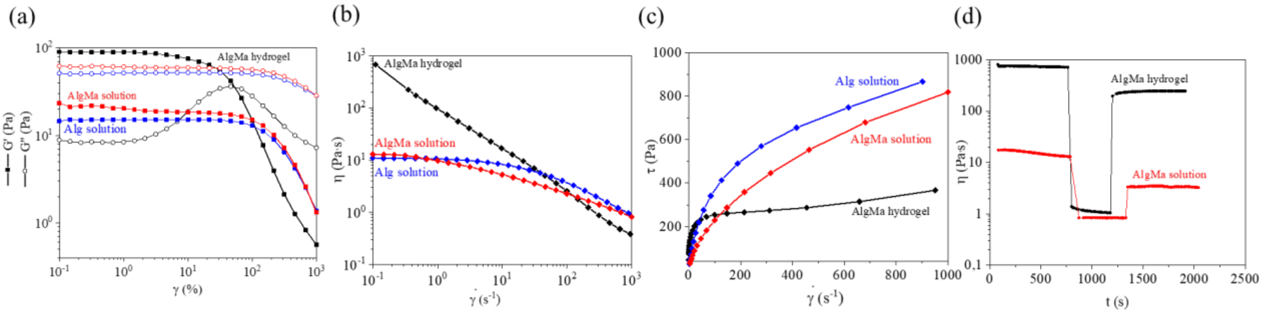

Figure 19. Rheological characterization of pristine alginate solution (blue curves), alginate methacrylate solution (red curve) and alginate methacrylate hydrogel (black curve) by amplitude sweep tests (a), flow curves in logarithmic (b) and linear (c) scale and recovery tests (d). Storage and loss moduli are represented as filled squares and empty circles, respectively.

Finally, once the inks formulations have been identified through the rheological characterization, two different AlgMa-based bioinks were developed, named as bioink A and bioink B. Both bioinks were prepared by gently mixing 100 µL of HeLa cells (10^6 cells/100 µL) with 1 mL of each ink formulation to form bioink A (BA) and bioink B (BB), respectively.

3.2.3. Gelatin methacrylate hydrogel and bioink

As already explained for the preparation of AlgMa hydrogel and bionks, the GelMa hydrogel, ink and bioink formulation involves a deep rheological characterization in order to predict its printability, mechanical and dimensional stability during time by evaluating both storage (G') and loss (G'') moduli and viscosity (η) as a function of a deformation (%) and shear rate ($\dot{\gamma}$), respectively. GelMa hydrogel and bioink preparation, firstly involves the preparation of GelMa solution. As described in the experimental section, GelMa hydrogel 5 % (w/v) was prepared by dissolving lyophilized GelMa in phosphate-buffer solution and by adding 0.1 % (w/v) of Irgacure 2959 (I2959), as photo-initiator. Both concentrations of GelMa and I2959 were selected as the best concentration to produce the GelMa ink and bioink by evaluating the mechanical stability tests and the cell viability, after photo-crosslinking. In brief, several tests were carried out on different GelMa inks containing different percentage of both polymer and photo-initiator, were irradiated with different UV time, with the aim to maximize the mechanical stability in the culture media and preserve cell functionalities. To assess the efficiency and the effects of the photo-initiator and UV irradiation time on the cells, stability tests in phosphate buffer solution and cell viability evaluation through cell counting with tripam blue, were evaluated. Table 7 summarizes all the tests carried out and the corresponding results.

Table 7. Summary of the stability tests and cell viability of different GelMa ink formulations.

Sample	I2959 concentration	UV intensity	UV time	Stability test[1]	Cell viability[2]
GelMa 5% (w/v)	0.1 % (w/v)	4 %	1 min	Solubilized after 1 h	100 %
		4 %	2 min	Solubilized after 1 h	100 %
		4 %	3 min	Solubilized after 1 h	100 %
GelMa 5% (w/v)	0.5 % (w/v)	4 %	1 min	Solubilized after 1 h	dead
		4 %	2 min	Solubilized after 1 h	
		4 %	3 min	Solubilized after 1 h	
		20 %	3 min	Solubilized after 3 d	
GelMa 10% (w/v)	0.1 % (w/v)	4 %	1 min	Solubilized after 12 h	100 %
		4 %	2 min	Solubilized after 12 h	100 %
		4 %	3 min	Solubilized after 12 h	100 %
GelMa 10% (w/v)	0.2 % (w/v)	4 %	1 min	Solubilized after 12 h	> 80 %
		4 %	2 min	Solubilized after 24 h	
		4 %	3 min	Solubilized after 24 h	
GelMa 5% (w/v)	0.5 % (w/v)	4 %	3 min	>7 d	dead
GelMa 5% (w/v)	0.1 % (w/v)	50 %	1 min	21 d	100 %

[1] stability tests were performed in phosphate buffer solution by observing structural modification and the dissolution of the material during time.

[2] cell viability was assessed by counting live cells previously stained with tripam blue reagent. HIFs, HCFs and HCTs-8 were used as cell types.

After the quick evaluation of mechanical stability and cell viability, 5 % (w/v) of GelMa and 0.1 % (w/v) of I2959, were selected as the best concentrations to produce the final GelMa ink formulation. Since the presence of I2959 does not affect the mechanical properties of the material, GelMa hydrogel and GelMa ink are considered equal.

Differently from AlgMa, in the case of GelMa, hydrogel formation is ensured by the presence of physically cross-links formed between chains when the temperature decreases below the gelling point at 32 °C. Over the gelling point temperature, GelMa becomes liquid since it still preserves the thermo-responsiveness characteristics of the gelatin polymer. For this reason, in order to get a printable and processable GelMa, physical gelling must be achieved by reducing the temperature below 32 °C before and during the bioprinting process. However, a deep rheological characterization is necessary to establish the right bioprinting temperature process in order to get a continuous filament extrusion and well-defined 3D structures by avoiding nozzle clogging issues.

For this reason, an intense rheological study was performed on GelMa ink with the aim to simulate the entire printing process through oscillatory and rotational tests at different temperatures and to find the right set up and printing parameters.

Firstly, the temperature dependent mechanical properties of the GelMa were characterized by evaluating how the G' and G" moduli change as a function of the temperature, in order to identify the best temperature to print GelMa hydrogel. Amplitude sweep oscillatory tests were performed on the GelMa 5% (w/v) hydrogel at 15°C, 20°C and 25°C, which represent the range of safely printing temperature of hydrogels and cells, once embedded in the final bioink formulation. As shown in figure 20 a, the hydrogel displays a well-defined gel-like behavior for each temperature, since the storage moduli (G’), represented by the filled squared curves, are always higher with respect to the loss moduli, along the applied strain (%). Furthermore, both moduli are largely independent of frequency for a certain range of strain %, thus defining a specific LVE for each curve. The specific values of G’ and G’’, along with the LVE range and the crossover point (c. pt.) are reported in Table 8.

Table 8. G’ and G’’ moduli, LVE range and crossover points of GelMa hydrogel obtained through amplitude sweep tests.

T(°C)	LVE (%)	G’ (Pa)	G’’ (Pa)	c. pt. (%)
15	0.1 - 60	845	8.40	320
20	0.1 - 70	131	3.41	480
25	0.1 - 100	0.46	0.23	463

Comparing all the curves reported in Figure 20 a, it is pointed out that at 25°C, the values of G’ and of G’, are similar, indicating a weak gel, whereas the difference between G’ and G’’ values at 20°C and 15°C increases, with the two moduli that differs for a hundred of P, typical of strong gels. Therefore, it was deduced that as the temperature increases, GelMa assumes a predominant viscous behavior. Moreover, the G’’ peak, which defines the presence of a well-defined substructure in the hydrogels, is very marked at 15°C and 20°C, but almost absent at 25°C. For this reason, due to the poor mechanical properties and interaction between chains in GelMa 5% (w/v) hydrogel at 25°C, this temperature was not further investigated. At the crossover point, G’ is equals to G’’, and the gel-like behavior of hydrogels switches into a liquid-like behavior, meaning that the materials is unable to rebuild its internal interaction responsible of the elastic behavior. GelMa at 15°C shows the lower crossover point at 320%, while GelMa at 20 °C and 25 °C displays a similar percentage of crossover point at 480 % and 470 %. This means that at 15 °C the physical entanglements formed are stronger with respect to the ones at 20 °C and 25 °C. At 15°C the gel, show a more rigid and fragile mechanical behavior with a narrower linear viscoelastic range. GelMa 20 °C and 15 °C shows better mechanical properties for 3D bioprinting application, since it has higher G' and G'' values with a great separation up to around 400 % of strain (see table 8), a well-defined substructure, and a suitable value of G' modulus to support cells once embedded in the gels, which are optimal properties to have good mechanical resistance in the 3D-bioprinted constructs. Through this first rheological scanning and qualitative evaluation, it was possible to select the optimal printing temperature at 15 °C or 20 °C.

Considering the excellent printability properties of the GelMa hydrogels at 15°C and 20 °C, the mechanical properties of the material were evaluated as a function of the temperature, in order to understand how the GelMa behaves by increasing the temperature at around 37 °C, which simulate the change of temperature from the printing process (15 °C or 20 °C) to the physiological/incubation temperature (37 °C). Temperature Sweep measurement was carried out at a constant value of angular frequency and at a constant value of strain, in order to understand how mechanical properties of the hydrogel could be influenced by a rage of temperature, that can simulate different temperature from the storage temperature to the printing and incubation one. In particular, (i) the storage temperature (4°C) of the hydrogel in the fridge, (ii) the printing temperature (15°C or 20°C) and (iii) the incubation temperature (37°C, physiological temperature) after printing process have been evaluated.
As it is shown in Figure 20 b, mechanical properties of the sample show two different trends depending on the temperature range: (i) from 4 °C to 20 °C, G' and G'' decrease quickly, but always maintaining a solid-like behavior, (ii) from 20 °C to 40 °C G' and G'' abruptly decrease until reached a cross point at 38°C with a value of G' and G'' around 0,200 Pa, so the material has a liquid-like behavior. This result highlights that at 37°C the hydrogel shows poor mechanical properties without a post-printing crosslinking process since it displays a clearly liquid-like behavior. By evaluating the rheological results as a function of the temperature, it is evident that GelMa 5 % (w/v) shows a good printability at both 15 °C and 20 °C but still maintain water-like characteristic over the gelling point (> 32 °C), indicating that the recovery behavior after printing process and the mechanical stability over time would be not suitable to accomplish all the requirements needed.

The second important parameter which characterizes a printable hydrogel, is the shear-thinning behavior, as previously explained. Viscosity test was performed on GelMa 5% (w/v) hydrogel in rotational mode applying a shear rate from 0,1 s^{-1} to 1000 s^{-1}, with controlled shear stress, at both 15 °C and 20 °C, and the resulted flow curves are reported in Figure 20 (c,d) both in terms of viscosity against the shear applied and as a function of shear stress vs shear rate, to better visualize and evaluate the yield point. In particular, the initial value of viscosity for GelMa hydrogel at 15°C, is around 4,190 Pa×s, while at 20°C is around 330 Pa×s. The final value of viscosity for GelMa at 15°C, at a shear rate of 1000 s^{-1}, is about 0,551 Pa s, while the final value of viscosity of GelMa at 20°C, at high shear rate, is about 0,563 Pa s. It is evident that GelMa displays shear thinning behavior at both 15°C and 20°C, since the viscosity decreases as the shear rate increases. Shear thinning behavior depends on the internal structure of the polymer, in fact, at low shear rates the material is able to resist to the applied shear forces since the material displays a strong physical interaction, as demonstrated from the amplitude sweep tests. On the contrary, at higher shear rate, the 'layers' which represent the internal network start to slide each other, meaning that the resistance to the flow decreases with the increase of the shear rate. Furthermore, by plotting the shear stress against shear rate (Figure 20 d) GelMa 5% (w/v) shows a particular trend at 15°C, which results in an increase of the shear stress at low shear rate. This behavior is due to the presence of strong intermolecular physical interaction controlled by the temperature. In fact, as demonstrated from the amplitude sweep measurements, GelMa hydrogels show higher moduli at 15 °C. Shear stress against the shear rate graph (Figure 20 c) further confirms the shear thinning behaviour, thanks to the presence of the yield point at 200 s^{-1}, which is more distinguishable than in the graph viscosity vs. shear rate reported in Figure 20 b, and it also allows to understand which is the shear stress corresponding to the shear rate (or printing rate) selected to carry out the bioprinting process, which will be experienced from the cells once embedded in the hydrogel. In fact, by considering both flow curves (Figure 20 (b,c)) it is possible to observe that at 80 s^{-1} shear rate (which correspond more or less at 3 mm/s of printing rate) the viscosity overcome the flow point and start to decreases enough to be extruded by miniating a low value of shear stress, 350 Pa, which is a value that can be safely experienced by the cells once embedded in the hydrogel. In order to evaluate if this value can be really used to produce a continuous filament once converted in a real extrusion rate, a bioprinting test was carried out by testing different extrusion rates from 3 mm/s until 10 mm/s. From the bioprinting tests, 5 mm/s (which is around 150 s^{-1}shear rate) revealed as the suitable printing rate (or extrusion rate) to get a continuous filament extrusion during the printing process. From this evidence, it is possible to confirm that (i) the value of the flow point corresponds to the leakage of the material outside the needle and (ii) that in order to produce a continuous flowing of material during time the overcoming of the flow point value (150 s^{-1}) is fundamental.

In conclusion, the viscosity curve pointed out that GelMa at 15°C and 20°C, can be defined as a printable ink, since it displays both shear thinning behavior and yield point which makes it an optimal material for the 3D Bioprinting. However, the strong yield point displayed by GelMa at 15 °C indicates that the extrusion process involves high pressure to trigger the flow process and generates the filament formation at the end of the needle, which could affect cell viability due to the high shear experienced from the cells itself. For this reason, 20 °C was selected as the suitable bioprinting temperature to fabricate the 3D models, by considering that to obtain stable structure a post-printing photo-crosslinking process is required. In order to quantitively identified the shear thinning behavior, the flow index "p" where identified through the interpolation of the Tscheuschner regression which can be represented with the following expression $\tau = \tau_0 + c_1 \cdot \dot{\gamma}^p + c_2 \cdot \dot{\gamma}$, where τ_0 is the yield point in Pa, c_1 is the coefficient for the low and medium shear range to describe the shear-induced structure change, c_2 is the coefficient that indicates the slope of the flow curve at high shear rate and the exponent p represents the flow index and quantitatively identify shear-thinning behaviour of gel. In particular, when $p > 1$, material displays shear-tickening behaviour, when $p < 1$ material displays shear-thinning behaviour, while $p = 1$ represents ideally viscous flow behaviour. In the case of GelMa 5 % w/v, after the interpolation of the Tscheuschner regression with the viscosity curve (correlation coefficient R^2=0.99) in Figure 20 d at 20 °C, p shows a value of 0.01, which further prove its shear-thinning characteristic.

Before moving on with the bioprinting process, a simulation of the entire bioprinting process was carried out by a rheological measure called recovery test, through which it is possible to predict how the hydrogel behaves before, during, and after the extrusion. In particular, low shear rate (0.01 s^{-1}), simulating static condition of the hydrogel, was used to describe the steady static situation of the hydrogel inside the syringe before the bioprinting and after the extrusion process (filament deposition onto the bioprinter bed), while high shear rate (300 s^{-1}) was used to simulate the extrusion process. This value was selected by using the equations mentioned in section 3.2.1. As reported in Figure 20 e, results highlight that before the bioprinting, the viscosity shows a time dependency behaviour at a constant shear rate (0.1 s^{-1}) in which the value decreases from 3570 Pa×s to 2110 Pa×s, and, after the extrusion, it still maintains the same trend even if it is less pronounced, by showing an initial viscosity of 945 Pa×s and a final one of 783 Pa×s, with a recovery percentage of 83 %. Instead, during the extrusion the viscosity reaches zero Pa×s. This behaviour demonstrates that (i) GelMa hydrogel formulation can be easily extruded at 20 °C, (ii) GelMa displays a time dependent behaviour since the viscosity change during time at fixed shear rate set at 0.1 s^{-1} and (ii) after the extrusion, GelMa does not completely recover its initial mechanical properties, probably because the physical entanglements established at 20 °C are partially broken during the extrusion.

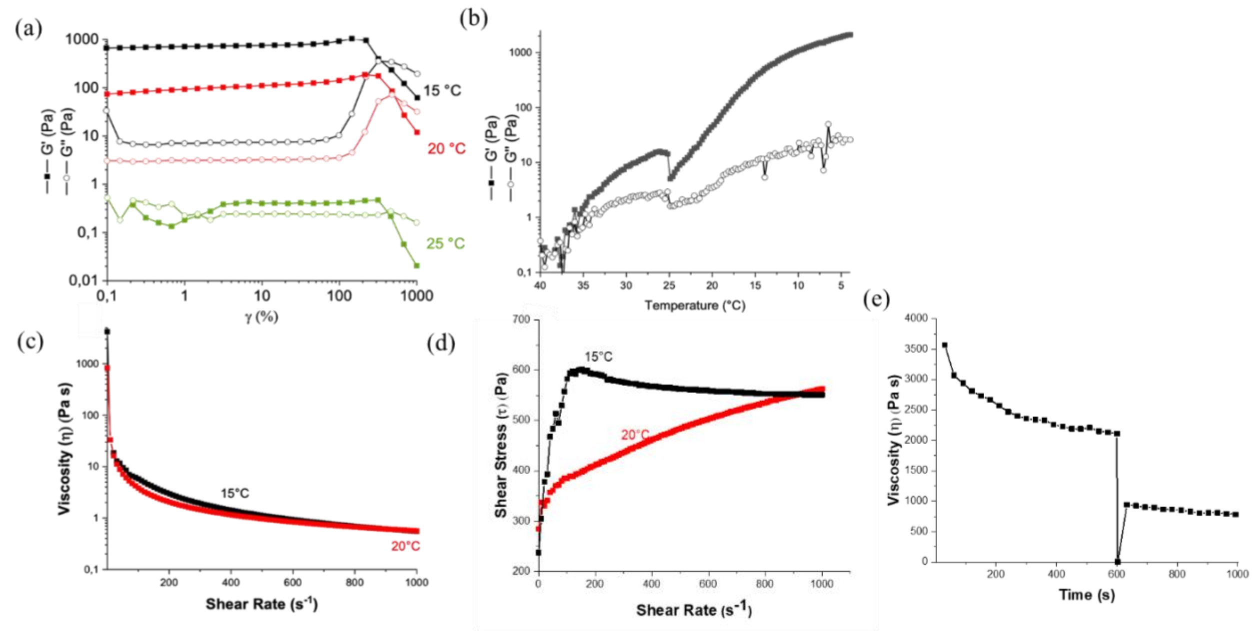

Figure 20. (a) Amplitude sweep of GelMa 5% (w/v) hydrogel at different temperature 15 °C (black curve), 20 °C (red curve) and 25 °C (green curve). The elastic and loss modulus are reported as single line with filled squares and empty circles, respectively. (b) Storage and loss moduli in a temperature range from 40 °C to 4 °C, at 1 °C/min of heating rate, at a constant angular frequency value of 5 rad/s and a constant strain of 0,5 %. (c) Controlled shear rate (CSR) of GelMa 5% (w/v) hydrogel in which the viscosity values are reported as a function of shear rate applied (0,1-1000 s^{-1}) at 15°C and 20°C plotted in a logarithmic scale. (d) Shear stress values as a function of the shear rate (0,1-1000 s^{-1}) at 15°C and 20 °C plotted in a linear scale. (e) Recovery test of GelMa 5 % performed at 20 °C by applying three different shears: low shear of 0.1 s^{-1} applied from 0 sec to around 500 sec and from around 600 sec to 1000 sec, and high shear rate of 300 s^{-1} for 3 sec after the first low shear rate applied.

Once the hydrogel formulation has been identified through the rheological characterization, GelMa ink was produced by mixing 0.1 % w/v of Irgacure 2959, which was selected as safely photo-initiator concentration for cells thanks to a quick cell viability evaluation carried out by placing in direct contact Irgacure 2959 with the cell, before and after UV irradiation. Finally, GelMa bioink was prepared by gently mixing 100 µL of human skin fibroblast (HSFs) (10^6 cells/100 µL) with 1 mL of GelMa ink formulation.

3.3.4. Collagen hydrogel and bioink

As explained above, collagen hydrogel was developed in cooperation with Typeone Biomaterials s.r.l. by signing an NDA and MTA agreements. The chemical composition, characterization and process production of the collagen hydrogel were optimized and developed by the company, while the rheological characterization to assess the printability and recovery properties was developed and carried out during this Thesis. 2.5 % of collagen hydrogel at neutral pH was employed for this study.

Firstly, amplitude sweep measurements were carried out to evaluate the viscoelastic properties of the collagen hydrogel formulation, which refer in particular to the assessment of G’ and G’’ moduli, as already explained for AlgMa and GelMa hydrogels. The measure was carried out by applying 1 Hz of frequency and an increasing deformation strain from 0.01 % to 1000 %. 20 °C was selected as temperature to carry out the measurements since the rheological properties of this collagen formulation are not affected by the temperature because of its chemical composition and nature. Furthermore, since collagen is also used in combination with GelMa, as explained in the next section, 20 °C can be used as reference temperature to compare all the rheological results with that one obtained with the pure GelMa. As shown in Figure 21 a, collagen shows a gel-like behavior since storage modulus (G’), represented as a black curve with filled squares, is higher (425 Pa) with respect to the loss one (G’’) (70 Pa). Furthermore, the LVE range is maintained up to 4 % of strain and the crossover point occurs at 69 %, after which the material starts to behave as a liquid.

In order to verify the shear-thinning behaviour of the material, which is the parameter related to the actual printability property, viscosity curve was obtained through rotational measurement by applying a shear rate from 0.01 s^{-1} to 1000 s^{-1} and the results are reported in Figure 21 (b,c) by plotting both the viscosity curve (η) (Figure 21 b) and the shear stress (τ) (Figure 21 c) as a function of the shear rate ($\dot{\gamma}$) in a logarithmic and linear scales, respectively. As shown in Figure 21 b, the typical shear thinning behaviour of printable material is well defined since the viscosity decrease with the increase of the applied shear rate by following the Tscheuschner regression which can be represented with the following expression $\tau = \tau_0 + c_1 \cdot \dot{\gamma}^p + c_2 \cdot \dot{\gamma}$, where τ_0 is the yield point in Pa, c_1 is the coefficient for the low and medium shear range to describe the shear-induced structure change, c_2 is the coefficient that indicates the slope of the flow curve at high shear rate and the exponent p represents the flow index and quantitatively identify shear-thinning behaviour of gel. In this case, collagen shows a p value of 0.22, which further proves its shear-thinning characteristic. Furthermore, by plotting the shear stress against the shear rate (Figure 21 c) it is possible to confirm the shear thinning behaviour, thanks to the presence of the yield point at 200 s^{-1}, which is more distinguishable than in the graph viscosity vs. shear rate reported in Figure 21 b, and it also allows to understand which is the shear stress corresponding to the shear rate (or printing rate) selected to carry out the bioprinting process, which will be experienced from the cells once embedded in the hydrogel. In fact, by considering both flow curves (Figure 21 (b,c)) it possible to observed that at 100 s^{-1} shear rate (which correspond more or less at 3 mm/s of printing rate) the viscosity overcome the flow point and start to decreases enough to be extruded by maintaining a low value of shear stress, 135 Pa, which is a value that can be safely experienced by the cells once embedded in the hydrogel. In order to evaluate if this value can be really used to produce a continuous filament once converted in a real extrusion rate, a bioprinting test was carried out by testing different extrusion rates from 3 mm/s until 10 mm/s. From the bioprinting tests, 7 mm/s (which is around 300 s^{-1}shear rate) was revealed as the suitable printing rate (or extrusion rate) to get a continuous filament extrusion during the printing process. From this evidence, it is possible to confirm that (i) the value of the flow point corresponds to the leakage of the material outside the needle and (ii) that in order to produce a continuous flowing of material during time the overcoming of the flow point value (100 s^{-1}) is fundamental.

Finally, the simulation of the entire bioprinting process was carried out by a rheological measure called recovery test, through which it is possible to predict how the hydrogel behaves before, during and after the extrusion, as already explained for the previous materials. In particular, low shear rate (0.01 s^{-1}), simulating static condition of the hydrogel, was used to describe the steady static situation of the hydrogel inside the syringe before the bioprinting after the extrusion process (filament deposition onto the bioprinter bed), while high shear rate (300 s^{-1}) was used to ideally simulate the extrusion process. This value was selected by using the equations mentioned in section 3.2.1. As reported in Figure 21 d, results show that collagen in both static conditions, before and after bioprinting, show 400 Pa s and 390 Pa s, respectively, while during the extrusion displays almost zero viscosity. This behaviour demonstrates that collagen hydrogel formulation (i) can be easily extruded at 20 °C, (ii) displays a short duration time dependency behaviour during small time since the viscosity change during time at fixed shear rate set at 0.1 s^{-1} and (ii) after the extrusion, it almost recovers its initial mechanical properties (97.5 % of recovery after extrusion).

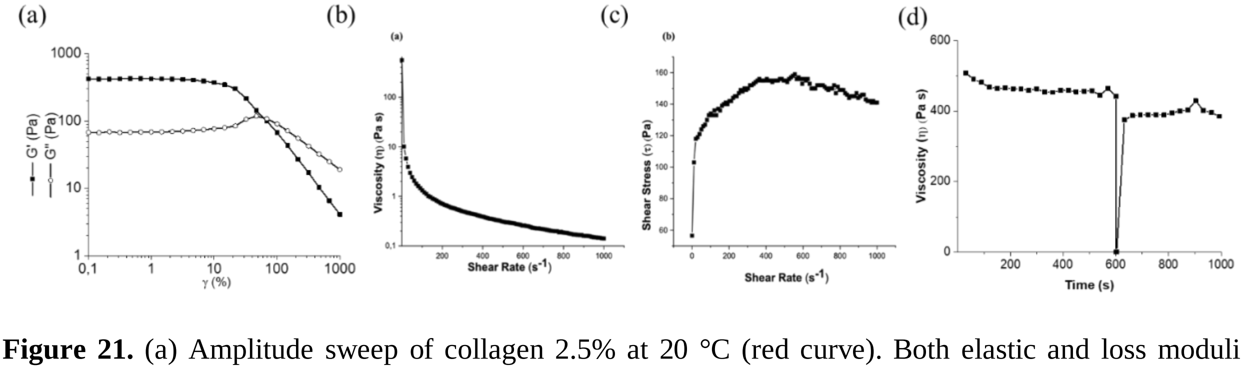

Figure 21. (a) Amplitude sweep of collagen 2.5% at 20 °C (red curve). Both elastic and loss moduli are reported as single line with filled squares and empty circles, respectively. (b) Controlled shear rate (CSR) of collagen 2.5 % which reports the viscosity values are reported as a function of shear rate applied (0,1-1000 s^{-1}) at 20°C plotted in a logarithmic scale. (d) Controlled shear rate (CSR) of collagen 2.5 % which reports shear stress values as a function of the shear rate (0,1-1000 s^{-1}) at 20 °C plotted in a linear scale. (e) Recovery test

of collagen 2.5 % performed at 20 °C by applying three different shears: low shear of 0.1 s^{-1} applied from 0 sec to around 500 sec and from around 600 sec to 1000 sec, and high shear rate of 300 s^{-1} for 3 sec after the first low shear rate applied.

Once the hydrogel formulation has been identified through the rheological characterization, collagen ink was produced by mixing 0.1 % (w/v) of Irgacure 2959, which was selected as safely photo-initiator concentration for cells thanks to a quick cell viability evaluation carried out by placing in direct contact Irgacure 2959 with the cell, before and after UV irradiation. Finally, collagen bioink was prepared by gently mixing 100 µL of both human intestinal fibroblast (HIFs) (10^6 cells/100 µL) and human skin fibroblast (HSFs) with 1 mL of collagen ink formulation.

3.2.4. Interpenetrating polymer network hydrogel and bioink

Interpenetrating polymer network was developed by mixing GelMa 5 % (w/v) and collagen 2.5 % in a ratio of 50:50, with the aim to obtain a new hydrogel formulation that can incorporate both the thermo-responsiveness properties of the GelMa and the biomimicry of the collagen, since it is the most abundant protein of the ECM. The hydrogel formulation, as explained in detail in the experimental section, involves the (i) the mixing of GelMa 5 % (w/v) and collagen 2.5 % and (ii) the photo-crosslinking process to establish covalent cross-links only between collagen chains. As already mentioned, IPN formation is ensured after the bioprinting process, in particular, during the photo-crosslinking process, which triggers the cross-links between GelMa chains to further stabilize the structure and create a fully cross-linked network, in which each polymer is crosslinked with itself in the presence of the other component. For this reason, the hydrogel and bioink formulation, should be properly called as semi-IPN in this section, because only the collagen is photo-crosslinked.
In order to print this formulation by ensuring the suitable filament without nozzle clogging issues, 20 °C was selected as temperature to carry out the bioprinting process since both collagen and GelMa show good rheological performances in this condition. Furthermore, in this way, at 20 °C, GelMa can form physical entanglements in the presence of cross-linked collagen, making the two materials intimately connected to form a semi-IPN structure.

To evaluate the rheological moduli (G' and G'') of the semi-IPN, amplitude sweep measurements were carried at 20 °C by applying 1 Hz of frequency and an increasing deformation strain from 0.01 % to 1000 %. As shown in Figure 22 a, IPN shows a gel-like behavior since storage modulus (G'), represented by the black curve with filled squares, is higher (300 Pa) with respect to the loss one (G'')

(30 Pa), with the LVE range ranging from 0.1 % up to 31 % of strain and the crossover point occurring at 150 %, after which the material starts to behave as a liquid.

As already explained in the previous sections, in order to verify the shear-thinning behaviour of the material, which is the parameter related to the actual printability property, rotational test was performed by applying a shear rate from 0.01 s^{-1} to 1000 s^{-1} and the results are reported in Figure 22 (b,c), by plotting both the viscosity curve (η) (Figure 22 b) and the shear stress (τ) (Figure 22 c) as a function of the shear rate ($\dot{\gamma}$) in a logarithmic and linear scales, respectively. As shown in Figure 22 b, the typical shear thinning behaviour of printable material is well defined since the viscosity decrease with the increase of the applied shear rate, from 700 Pa×s at 0.1 s^{-1} to 0.4 Pa×s at 1000 s^{-1}, by following the Tscheuschner regression which can be represented with the following expression $\tau = \tau_0 + c_1 \cdot \dot{\gamma}^p + c_2 \cdot \dot{\gamma}$, where τ_0 is the yield point in Pa, c_1 is the coefficient for the low and medium shear range to describe the shear-induced structure change, c_2 is the coefficient that indicates the slope of the flow curve at high shear rate and the exponent p represents the flow index and quantitatively identify shear-thinning behaviour of gel. In this case, collagen shows a p value of 0.18, which further proves its shear-thinning characteristic. Furthermore, by plotting the shear stress against the shear rate (Figure 22 c) it is possible to confirm the shear thinning behaviour, thanks to the presence of the yield point at 100 s^{-1}, which is more distinguishable than in the graph viscosity vs. shear rate reported in Figure 22 b, and it also allows to understand which is the shear stress corresponding to the shear rate (or printing rate) selected to carry out the bioprinting process, which will be experienced from the cells once embedded in the hydrogel.

In fact, by considering both flow curves (Figure 22 (b,c)) it possible to observe that at 100 s^{-1} shear rate (which correspond more or less at 3 mm/s of printing rate) the viscosity overcome the flow point and start to decreases enough to be extruded by miniating a low value of shear stress, 125 Pa, which is a value that can be safely experienced by the cells once embedded in the hydrogel. To evaluate if this value can be used to produce a continuous filament once converted in a real extrusion rate, a bioprinting test was carried out by testing different extrusion rates from 3 mm/s until 10 mm/s. From the bioprinting tests, 7 mm/s (which is around 300 s^{-1}shear rate) was revealed as the suitable printing rate (or extrusion rate) to get a continuous filament extrusion during the printing process. From this evidence, it is possible to confirm what already stated for the previous materials, that (i) the value of the flow point corresponds to the leakage of the material outside the needle and (ii) that to produce a continuous flowing of material during time the overcoming of the flow point value (100 s^{-1}) is, even in this case, fundamental.

Finally, the simulation of the entire bioprinting process was carried out by a rheological measurement called recovery test, through which it is possible to predict how the hydrogel behaves before, during and after the extrusion, as already explained for the previous materials. The measurement was performed at 20 °C, as explained above. In particular, low shear rate (0.01 s^{-1}), simulating the static condition of the hydrogel, was used to describe the steady static situation of the hydrogel experienced both inside the syringe, before the bioprinting, and after the extrusion process (filament deposition onto the bioprinter bed), while high shear rate (300 s^{-1}) was used to ideally simulate the extrusion process. This value was selected by using the equations mentioned in section 3.2.1. As reported in Figure 22 d, results show that IPN in both static conditions, before and after bioprinting, the viscosity increases with the increasing time. In particular, in the first trait (0 s – 600 s), representing the step before the printing process, the viscosity increases from 1150 Pa×s to 1500 Pa×s while in the last trait (630 s – 1000 s), representing the step after the extrusion, the viscosity increases from 1100 Pa×s to 1450 Pa×s. Differently, during the extrusion, the viscosity reaches the zero value. This behaviour demonstrates that collagen hydrogel formulation (i) can be easily extruded at 20 °C, since the viscosity abruptly decreases when the shear rate increases, (ii) displays a time dependency behaviour in both static steps, since the viscosity slightly increases during time at fixed shear rate set at 0.1 s^{-1} and (ii) after the extrusion, it recovers the 71 % of the viscosity and, at the end of the measure, the recovery percentage increase up to 94 %, by following the same trend found for the viscosity in the pre-printing stage.

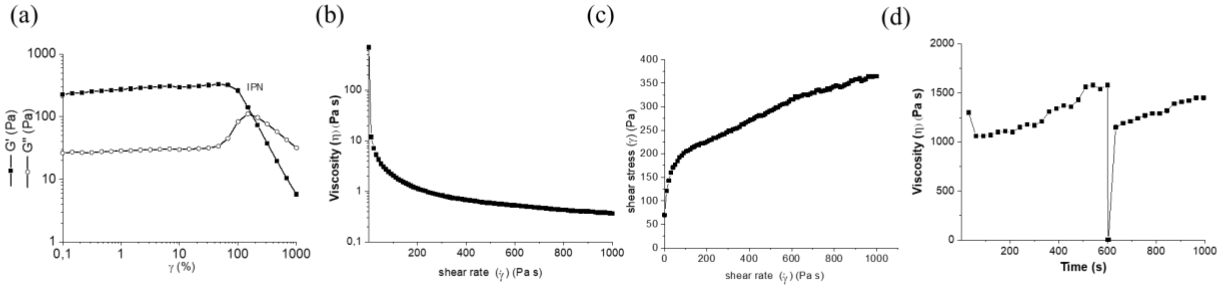

Figure 22. (a) Amplitude sweep of semi-IPN at 20 °C (red curve). Both elastic and loss moduli are reported as single line with filled squares and empty circles, respectively. (b) Controlled shear rate (CSR) of semi-IPN which reports the viscosity values are reported as a function of shear rate applied (0,1-1000 s^{-1}) at 20°C plotted in a logarithmic scale. (d) Controlled shear rate (CSR) of semi-IPN which reports shear stress values as a function of the shear rate (0,1-1000 s^{-1}) at 20 °C plotted in a linear scale. (e) Recovery test of semi-IPN performed at 20 °C by applying three different shears: low shear of 0.1 s^{-1} applied from 0 sec to around 500 sec and from around 600 sec to 1000 sec, and high shear rate of 300 s^{-1} for 3 sec after the first low shear rate applied.

Once the hydrogel formulation has been identified through the rheological characterization, semi-IPN ink was produced by mixing 0.1 % (w/v) of Irgacure 2959, which was selected as safely photo-initiator concentration for cells thanks to a quick cell viability evaluation carried out by placing in direct contact Irgacure 2959 with the cell, before and after UV irradiation. Finally, semi-IPN bioink was prepared by gently mixing 100 µL of both human intestinal fibroblast (HIFs) (10^6 cells/100 µL) and human skin fibroblast (HSFs) with 1 mL of collagen ink formulation.

3.2.5. Cross-linking procedures

After the bioprinting process, which will be explained in the next sections for each bioinks/hydrogels application, different post-printing crosslinking processes were carried out, in order to stabilize the 3D bioprinted scaffolds against water hydrolysis and to obtain stable mechanical properties during the incubation conditions. Furthermore, crosslinking process has the important aim to provide wider range of tunable mechanical properties, in the desired range stiffness, in order to replicate both healthy and altered states or pathological tissues. In fact, it is stated that the main alteration of tumor of inflammatory tissues regards the microenvironment surrounding cells, which changes in terms of mechanical properties that typically display higher stiffness with the disease progression [207].
This remodeling process of the extracellular matrix (ECM) strictly influences the morphology and the protein expression of the cells. For this reason, when a reliable and physiologically-like artificial *in vitro* models must be replicated, it is fundamental to provide the suitable mechanical properties to the artificial ECM, by preserving cell viability and providing stability of the living construct.

In this section, rheological evaluation of the cross-linked scaffolds will be discussed in order to understand how crosslinking affect the mechanical properties of the hydrogel and which are the best conditions to obtain stable scaffolds during time in the desired range of stiffness. Notice that AlgMa-based scaffolds will be discussed separately with respect to GelMa, collagen and IPN-based one, since they were employed for different applications.

Crosslinking of alginate methacrylate-based bioink

AlgMa-based scaffolds were produced through 3D bioprinting process as described in the experimental section, starting from both inks and bioinks formulations, with the aim to both (i) evaluate how the presence of the cells in the scaffolds might affect the rheological properties of the native inks and (ii) ensure a tunable mechanical property in the desired range of stiffness to reproduce the tissue-like stiffness conditions.

Ink A (IA) and ink B (IB), containing 0.2 % (w/v) and 0.25 % (w/v) of Irgacure 2959, respectively, were further crosslinked through different methods after the bioprinting process in order to have a stable structure during time. Ink A, which is that one containing less percentage of Irgacure, experiences a double crosslinking process, as detailed explained in the experimental section, involving (i) a first ionic cross-linking, by dipping the scaffold in a calcium chloride solution 60 mM for 5 min, and (ii) a photo-crosslinking process through UV irradiation. In the first case, AlgMa forms "egg-box" structure which links AlgMa -OH groups and calcium ions, while the second cross-linking event, creates covalent bonds between methacrylic group. This double crosslinking process was aimed to increase the mechanical resistance and stability of the scaffolds without increase the UV time irradiation, which strongly affect the cell viability in relation to the percentage of Irgacure involved in this experiment. On the contrary, ink B underwent both double and single crosslinking processes, in order to (i) obtain a more stable cell-laden structure during time, (ii) have a comparison with the double crosslinked BA scaffolds, and (ii) obtain a wider spectrum of stiffness.

Three different times of UV irradiation (120 s, 90 s, and 60 s) were tested on both ink A and ink B scaffolds, in order to improve tunable mechanical properties to the structures. In particular, three scaffolds of ink A were irradiated with UV light for 120 s, 90 s, and 60 s following the immersion in calcium chloride solution. The resulting crosslinked structures are labeled as IA120Ca, IA90Ca, and IA60Ca, respectively. Otherwise, three scaffolds of ink B were irradiated with UV light for 120 s, 90 s, and 60 s, as well, without following the immersion in calcium chloride solution, and other three scaffolds of ink B were also irradiated with UV light for 120 s, 90 s, and 60 s, as well, following a second crosslinking process in calcium chloride solution. The resulting crosslinked structures which follow one single crosslinking process are labeled as IB120, IB90, and IB60, respectively, while the other three scaffolds which experienced a double crosslinking process are labeled IB120Ca, IB90Ca, and IB60Ca, respectively.

To assess the stiffness of these 3D structures and their tunable mechanical properties, amplitude sweep analysis was carried out by applying a strain deformation (%) from 0.1 % until 1000 %, maintaining fixed the frequency of the oscillation at 1 Hz. As shown in Figure 23 a, IB120 shows the highest storage (33 kPa) and loss (10 kPa) moduli with respect to IB90 (21 kPa for G' and 6 kPa for G'') and IB60 (20 kPa for G' and 4 kPa for G''). All the curve show 'gel-like' behavior and a crossover point in which G' is equal to G'' (G'=G''). At this point, 'liquid-like' behavior dominates the elastic one and the materials do not preserve their internal structure and interaction. In particular, IB120, IB90 and IB60 crossover points are 45 %, 98 % and 31 %, respectively. Figure 23 b reports the storage and loss moduli for IA120Ca, IA90Ca, and IA60Ca 3D bioprinted constructs post dual crosslinking process. As it is clear from the graph in Figure 23 b, IA120Ca, IA90Ca, and IA60Ca display ‘gel-like’ behavior since G’ is always higher than the G’’. In particular, IA120Ca shows 21 kPa and 7 kPa for G’ and G’’, respectively, IA90Ca shows 17 kPa and 7 kPa for G’ and G’’, respectively, while IA60Ca displays 5 kPa and 2 kPa for G’ and G’’, respectively. Crossover points, or strain value at which ‘liquid-like’ characteristics overcome the ‘gel-like’ one, occurs at 70 %, 50 %, and 120 % for IA120Ca, IA90Ca, and IA60Ca, respectively. These results, summarized in Table 9, demonstrated that both inks are suitable to produce scaffolds with tunable mechanical properties, whose stiffness can be tuned by changing (i) the concentration of photo-initiator, (ii) the time of UV irradiation, and (iii) the cross-linking methods.

Table 9. Summary of the storage (G’) and loss (G’’) moduli values of all the 3D bioprinting scaffolds produced by using ink A and ink B, after the crosslinking processes.

	Crosslinking post-printing			
3D bioprinted scaffold	UV irradiation time	Time of immersion in $CaCl_2$	G’ (kPa)	G’’ (kPa)
IB120	120 s	/	33	10
IB90	90 s	/	21	6
IB60	60 s	/	20	4
IA120Ca	120 s	5 min	21	7
IA90Ca	90 s	5 min	17	7
IA60Ca	60 s	5 min	5	2

In particular, in this case, it is clear that by decreasing the photo-initiator concentration from ink B to ink A and by introducing a second step of crosslinking process it is possible to reach comparable value of G’ and G’’, in terms of order of magnitude, by providing at the same time a wide and complete range of stiffness from 33 up to 5 kPa (see table 8).

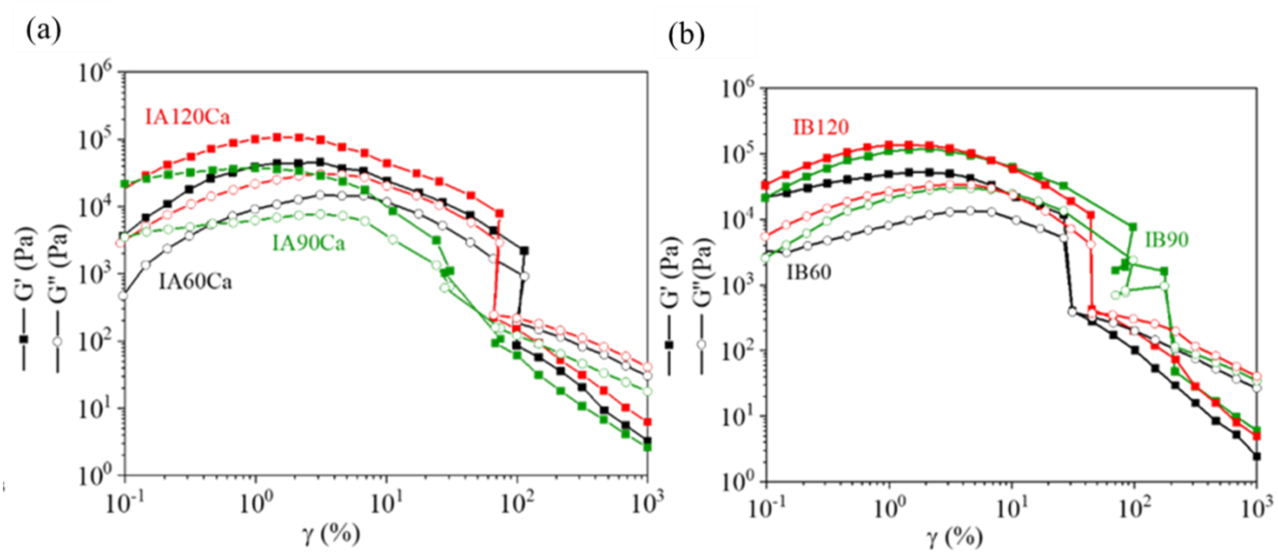

Figure 23. Rheological evaluation of 3D bioprinted ink A (IA) and ink B (IB) after (a) dual cross-linking process with $CaCl_2$ and UV light at 60 sec (IA60Ca, black curve), 90 sec (IA90Ca, green curve), 120 sec (IA120Ca, red curve) and (b) only photo-crosslinking at 60 sec (IB60, black curve), 90 sec (IB90, green curve) and 120 sec (IB 120, red curve) of UV light. Storage modulus (G’) loss modulus (G’’) are represented by filled squares and empty circles, respectively, and they are reported as a function of the strain (%) in logarithmic scale.

Same post-printing crosslinking processes carried out for IA and IB were performed on the corresponding bioinks containing cells. Bioink A (BA) and bioink B (BB), containing HeLa cells, were analysed through amplitude sweep measurements to evaluate the storage (G’) and loss (G’’) moduli and whether the presence of the cells might affect these parameters. Figure 24 reports the trend of both storage (G’) and loss (G’’) moduli of the scaffolds obtained with the printing of BA and BB after dual (Figure 24 (a,c)) and single crosslinking (Figure 24 b) process, respectively. Furthermore, Figure 24 (d,e,f) shows a comparison of the amplitude sweep measurements between BA and BB scaffolds with the same UV irradiation treatment.

Crosslinked BA scaffolds (Figure 24 a), obtained after dual crosslinking process with UV light and calcium ions, show ‘gel-like behaviour’, since storage modulus (G’) is always higher than the loss one (G’’), and a crossover point, in which G’=G’’ and the materials starts to behave as liquid. In particular, BA120Ca shows 200 Pa and 2 Pa for G’ and G’’, respectively, with an LVE range of 3 % and a crossover point of 100 %, BA90Ca displays 40 Pa and 7 Pa for G’ and G’’, respectively, respectively, with an LVE range of 2 % and a crossover point of 70 %, while BA60Ca shows the lowest G’ and G’’ moduli of 30 Pa and 2 Pa, respectively, which is consistent with the time of UV irradiation, with an LVE range of 2 % and a crossover point of 100 %. As summarized in Table 9, the LVE range increases at higher strain percentage values with the increase of the UV time irradiation. This trend can be ascribable to the fact that the higher is the number of crosslinks formed between polymers chains after UV treatment, the higher the LVE range, which defines the ability of the materials to withstand deformation without impairing its mechanical properties and maintain a ‘gel-like’ property.

For what concern the scaffolds obtained from bioink B (BB), which underwent a single photo-crosslinking process, results are shown in Figure 24 b. All the scaffolds display ‘gel-like’ characteristics, as in the case of crosslinked BA scaffolds, with higher values of G’ and G’’ moduli. In fact, BB120 displays 1000 Pa and 90 Pa for G’ and G’’, respectively, with an LVE of 14 % and a crossover point of 150 %, BB90 shows 120 Pa and 13 Pa for G’ and G’’, respectively, with an LVE of 10% and a crossover point of 135 %, while BB60 shows the lowest moduli of 75 Pa and 13 Pa for G’ and G’’, respectively, since it experienced the shortest UV duration treatment, and a crossover point of 140 %. As summarized in Table 9, the LVE shows higher strain percentage values with the increase of the UV time irradiation. As explained above, this trend can be ascribable to the fact that the higher is the number of crosslinks formed between polymers chains after UV treatment, the higher is the LVE range, which defines the ability of the materials to withstand deformation without impairing its mechanical properties and maintain a ‘gel-like’ property.

A dual crosslinking process, involving UV light treatment and ionic crosslinking, were also performed on 3D bioprinted bioink B (BB) scaffolds in order to (i) have a comparison with the double crosslinked BA scaffolds, (ii) to obtain a wider spectrum of stiffness and to (iii) obtain a stable cell-laden construct while keeping low the concentration of the photoinitiator, to reduce possible effects on the cell viability. Similarly to what obtained with BA and BB scaffolds reported in Figure 23 (a,b), double crosslinked BB scaffolds display ‘gel-like’ behavior in which G’ is always higher than G’’ and BB120Ca shows the highest moduli (2000 Pa for G’ and 200 Pa for G’’), as shown in Figure 24 c. As the time of UV decreases, both G’ and G’’ decreases as demonstrated by BB90Ca and BB60Ca which display 310 Pa (G’) and 40 Pa (G’’), and 120 Pa (G’) and 20 Pa (G’’), respectively. On the contrary, while BA and single crosslinked BB scaffolds show a clear trend of the LVE range and crossover points, in the case of the double crosslinked BB scaffolds, only BB60Ca highlights both LVE and crossover point, corresponding at 3 % and 150 % of strain, as summarized in Table 10. BB90Ca G’ and BB120Ca G’ do not show any plateau in the range of the applied deformation, probably due to the fact that the double crosslinking processes increase the number and the entity of the crosslinks between chains, which tends to agglomerate with the increase of the applied deformation. Then, once the deformation reaches high value, all the entanglements abruptly flow and possible inter-chains breakages occur.

Table 10. Summary of the storage (G’) and loss (G’’) moduli values of all the 3D bioprinting scaffolds produced by using bioink A and bioink B, after the crosslinking processes.

	Crosslinking post-printing				
3D bioprinted scaffold	UV irradiation time	Time of immersion in $CaCl_2$	G’ (kPa)	G’’ (kPa)	LVE (%)
BB120	120 s	/	0.900	0.390	14
BB90	90 s	/	0.120	0.013	10
BB60	60 s	/	0.075	0.013	10
BB120Ca	120 s	5 min	2	0.20	n.d.*
BB90Ca	90 s	5 min	0.310	0.040	n.d.*
BB60Ca	60 s	5 min	0.120	0.020	n.d.*
BA120Ca	120 s	5 min	0.200	0.020	3
BA90Ca	90 s	5 min	0.041	0.007	2
BA60Ca	60 s	5 min	0.030	0.002	2

*n.d.: not detectable

From the comparison curves, reported in Figure 24 (d,e,f), it is clear that the double crosslinked BB scaffolds always show higher G’ and G’’ moduli with respect to BA and the single crosslinked BB ones, thanks to the presence of both ionic crosslinks and the highest number of covalent interchains bonds formed in the presence of the highest concentration of photo-initiator. Moreover, it is possible to identify a correlation between the LVE ranges and the crossover points (G’ = G’’) parameters of BA and single crosslinked BB scaffolds, since the latter, displays a shifting of both parameters at higher values of strain with respect to BA scaffolds. These results might be explained considering that bioink B contains a higher concentration of Irgacure 2959 (0.25 % (w/v)), than bioink A (0.2 % (w/v)) and that, consequently, the formation of covalent crosslinks between acrylate moieties are higher than that one formed in the bioink A. In addition, despite BA scaffolds underwent a second crosslinking process, they always display lower mechanical properties than BB scaffolds, probably because the bond strengths related to the ionic crosslinks formed between AlgMa -OH groups and Ca^{++} ions are weaker than those one provided by covalent crosslinks. For these reasons, a higher number of covalent crosslinks in BB scaffolds dominates the sum of both ionic and covalent crosslinks in BA scaffolds, ensuring higher viscoelastic properties of the scaffolds, thus higher LVE ranges, and higher resistance at deformation before to flow and behave as liquid materials, thus higher crossover points. This correlation is not found for the double crosslinked BB scaffolds probably because the strong mechanical properties lead to fragile materials at high deformation applied.

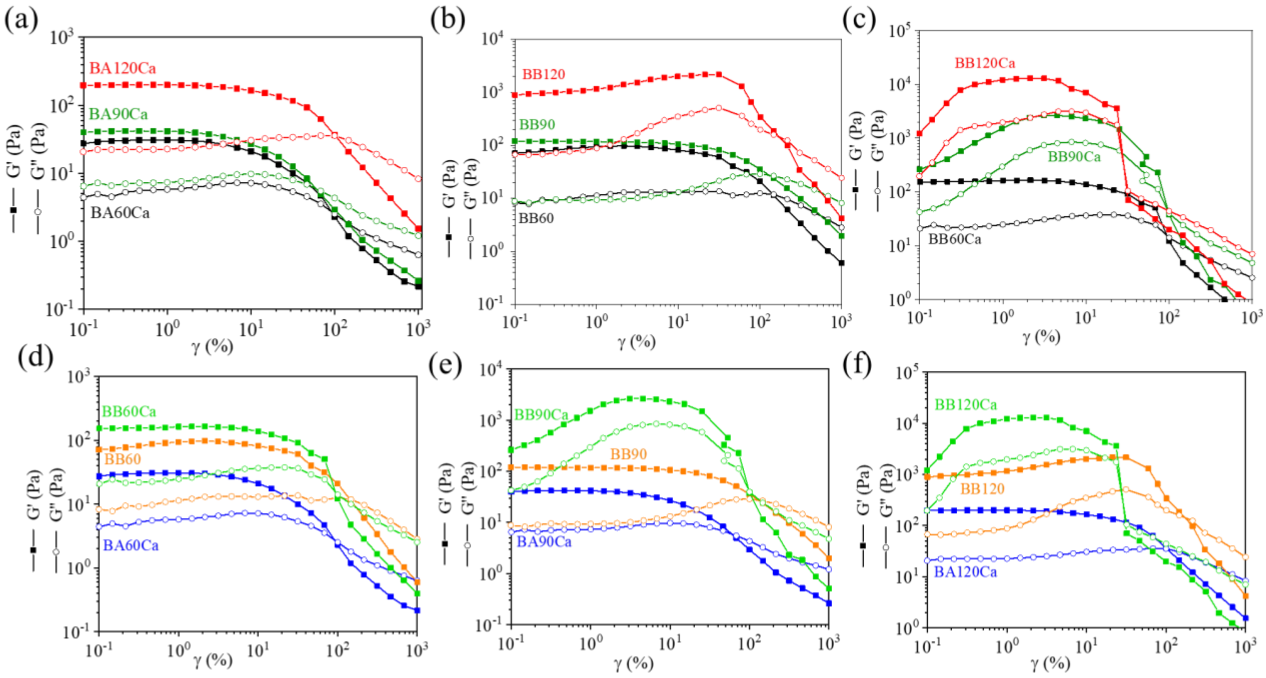

Figure 24. Rheological evaluation of 3D bioprinted bioink A (BA) and bioink B (BB) after (a) dual cross-linking process with $CaCl_2$ and UV light at 60 sec (BA60Ca, black curve), 90 sec (BA90Ca, green curve), 120 sec (BA120Ca, red curve) and (b) only photo-crosslinking at 60 sec (BB60, black curve), 90 sec (BB90, green curve) and 120 sec (BB 120, red curve) of UV light. Comparison between bioink A and B with different crosslinking methods at 60 sec (c), 90 sec (d) and 120 sec (e) of UV light. Storage and loss moduli are represented as filled and empty circles, respectively.

Finally, by comparing the double crosslinked scaffolds with and without cells obtained from bioink A, ink A, bioink B and ink B (Figure 25 (a,b,c,d,e,f)), it is possible to observe that the presence of the cells strongly affects the mechanical properties of both AlgMa ink A and ink B. In particular, by considering only the G' moduli, double crosslinked ink A scaffolds (Figure 25 (a,b,c)) decrease the G' moduli from, from 5 kPa to 0.030 kPa for BA60Ca (Figure 25 a), 17 kPa to 0.041 kPa (Figure 25 a) for BA90Ca and from 21 kPa to 0.2 kPa for BA120Ca (Figure 25 a). The same trend can be observed for G' values of double crosslinked ink B scaffolds. In fact, the G' decreases from 14 kPa to 0.15 kPa for BB60Ca, from 23 kPa to 0.27 kPa for BB90Ca, and from 99 kPa to 1.2 kPa for BA120Ca. Table 11 summarizes all the G' and G'' of the scaffolds obtained from bioink A/ink A and bioink B7ink B, after dual crosslinking process. As a general consideration, after cell loading, all the moduli decrease of ca. two orders of magnitude.

The decreasing of both G’ and G’’ moduli after cells loading can be explained by considering the steric hindrance of the cells themselves, which usually have dimensions around hundred of microns, thus several orders of magnitude higher than the ionic or covalent crosslinks established between polymer chains. In this way, cells might distance AlgMa chains by reducing the statistical probability to interact each other to form crosslinks when in presence of calcium ions or when triggered by UV light and photo-initiator. As a consequence, if the number of interactions reduces, the number of crosslinks follows the same trend, by leading to a proportional decreasing of the mechanical properties.

Table 11. Summary of the storage (G’) and loss (G’’) moduli values of the 3D bioprinting scaffolds produced by using bioink A and bioink B (colored in yellow), and the corresponding scaffolds not containing cells (colored in green), after dual crosslinking processes.

	Crosslinking post-printing			
3D bioprinted scaffold	UV irradiation time	Time of immersion in $CaCl_2$	G’ (kPa)	G’’ (kPa)
IB120Ca	120 s	5 min	99	16
IB90Ca	90 s	5 min	23	5
IB60Ca	60 s	5 min	14	2.8
BB120Ca	120 s	5 min	2	0.20
BB90Ca	90 s	5 min	0.310	0.040
BB60Ca	60 s	5 min	0.120	0.020
IA120Ca	120 s	5 min	21	7
IA90Ca	90 s	5 min	17	7
IA60Ca	60 s	5 min	5	2
BA120Ca	120 s	5 min	0.200	0.020
BA90Ca	90 s	5 min	0.041	0.007
BA60Ca	60 s	5 min	0.030	0.002

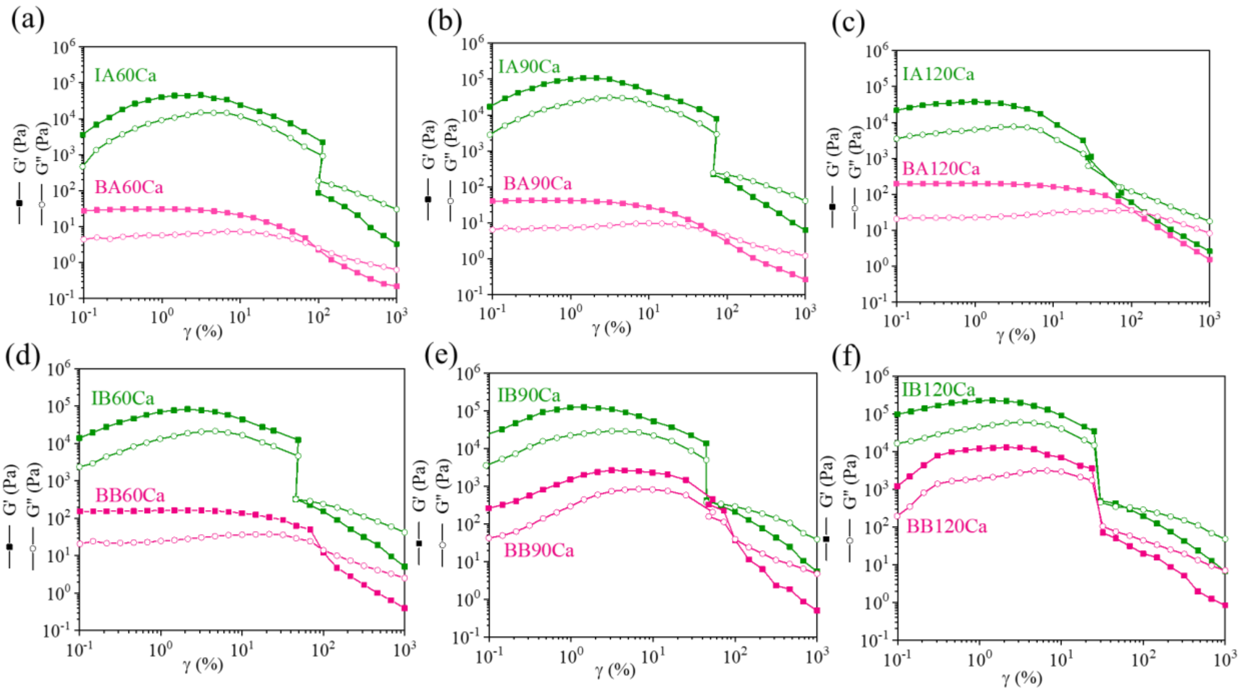

Figure 25. Comparison of rheological curves of 3D bioprinted ink A not containing cells (IA) and bioink A containing cells (BA) after dual crosslinking process with $CaCl_2$ and UV light at (a) 60 sec (IA60Ca green curve and BA60Ca pink curve), 90 sec (IA90Ca green curve and BA90Ca pink curve), 120 sec (IA120Ca green curve and BA120Ca pink curve). Comparison of rheological curves of 3D bioprinted ink B not containing cells (IB) and bioink B containing cells (BB) after dual crosslinking process with $CaCl_2$ and UV light at (a) 60 sec (IB60Ca green curve and BB60Ca pink curve), 90 sec (IB90Ca green curve and BB90Ca pink curve), 120 sec (IB120Ca green curve and BB120Ca pink curve). Storage and loss moduli are represented as filled and empty circles, respectively.

In conclusion, from the rheological characterization it is clear that both bioink A and bioink B lead to a variety of scaffolds displaying a wide range of stiffness, after single and double crosslinking processes. In the case of dual crosslinking, the process was optimized to obtain a stable cell-laden construct, by keeping low the concentration of the photoinitiator to avoid adverse effects on cell viability. The tuneable mechanical properties obtained, summarized in table 10, can be exploited to reproduce pathological, inflammatory or tumor tissues. For this purpose, it is difficult to define a univocal value of rigidity of a tissue, whether it is physiological or pathological, due to the intra-heterogeneity of the real tissues. However, AFM measurements carried out on cancer biopsy demonstrated that stiffness of such tissue is described by a bimodal distribution [252]. Breast cancer tissue stiffness shows two prominent peaks at 0.57 + 0.16 kPa and 1.99 + 0.73 kPa while healthy specimen reveals a unimodal stiffness distribution of 1.13 + 0.78 kPa. In the same study, Plodinec et al. [252] showed that the core part of the breast cancer varies from 0 to 20 kPa in only 20µm of distance with a well-defined boundary, whether periphery shows a non-homogeneous area.

Crosslinking of gelatin methacrylate and collagen-based bioinks

Gelatin methacrylate (GelMa), collagen, and IPN of GelMa and collagen were further crosslinked after 3D bioprinting process, to stabilize the structures at incubation condition and to avoid fast hydrolysis once in direct contact with cell culture media.

Rheological analyses provide the best information about the mechanical properties the stiffness, the structures, and the general mechanical properties of the scaffolds, which help to monitor the crosslinking process and how the mechanical properties change as a function of the crosslinking parameters.

Gelatin methacrylate

GelMa ink and bioink were bioprinted, as explained in detail in the next section, and then were crosslinked through a photo-crosslinking process, which involves 1 min of UV irradiation at 50 % of UV intensity and 3 cm of distance. This crosslinking condition was optimized after several stability tests and evaluation of cell viability, in order to ensure high mechanical performance during time at incubation condition by avoiding cell damages, as explained in section 3.2.1.2.

Amplitude Sweep measurements were carried out on GelMa bioprinted scaffolds not containing cells to evaluate how elastic and loss moduli are affected by the crosslinking process. The curves were obtained by applying a constant oscillation frequency of 5 Hz as a function of the strain (0,1 % - 1000 %) at 20 °C, since it was chosen as the best printing temperature after many printing tests that were conducted simultaneously. Figure 26 a, shows the comparison between uncrosslinked (u-GelMa) and crosslinked (c-GelMa) GelMa 5% (w/v) at 20°C. As expected, the mechanical properties increase after the crosslinking process and the G’’ peak of c-GelMa appears at lower strain with respect to that one of the u-GelMa, which indicates a highly inner connected network provided by the co-presence of (i) a substructure formed by the physical crosslinked at 20 °C, and (ii) covalent crosslinks formed between acrylate moieties after UV treatment. In table 12, the value of G’ and G’’ moduli along with the LVE range are reported, in both u-GelMa and crosslinked c-GelMa at 20°C. As it is evident from Figure 26 a, since the value of G’ increased from 80 Pa, for u-GelMa, to 200 Pa, for c-GelMa, while G’’ increased from 3.4 Pa to 6 Pa, after crosslinking, it has been proved that the crosslinking with the selected conditions successfully provide higher stability during time at 37 °C. On the contrary, LVE range displays almost same range from 0.1 % to 50 %. Moreover, the shift of the crossover point at lower strain value, from 500% for u-GelMa to 320% for c-GelMa, means that the material displays higher rigidity and fragility.

Table 12. G’ and G’’ moduli, LVE range and crossover points of c-GelMa and u-GelMa obtained through amplitude sweep tests at 20 °C.

sample	LVE (%)	G’ (Pa)	G’’ (Pa)	c. pt. (%)
c-GelMa	0.1 - 60	200	6	320
u-GelMa	0.1 - 60	80	3.4	500

To assess if the crosslinking process stabilize the structure during time in incubation condition, a temperature sweep measurement was performed in static conditions, with a low and constant value of shear rate (0.1 s^{-1}) and of strain (0,1%) from 15 °C to 40 °C, in order to simulate (i) the printing temperature (20 °C) and (ii) the incubation temperature (37°C) on the printed scaffolds and crosslinked scaffolds. As shown in Figure 25 b, G’ and G'’ moduli display constant trend among the overall range of temperature. In particular, G’ maintains the same value of 150 Pa with respect to that one obtained from the amplitude sweep test (Figure 26 a) while G’’ shows a decrease from 80 Pa to 5 Pa. From this result, it is possible to assume that the crosslinking process strongly stabilizes the scaffolds at incubation condition and that the mechanical properties do not change during the temperature, meaning that the covalent crosslinks dominate the physical interactions. The strong ‘gel-like’ behavior displayed by c-GelMa at high temperature (37 – 40 °C), means that it is able to support cell growth and physical manipulation without dissolving in the culture media. Notice that no comparison between u-GelMa and c-GelMa was introduced in Figure 25 b, since u-GelMa at 37 °C completely dissolve and spread away from the plate-plate set up of the rheometer, thus making the recording of the moduli not relevant.

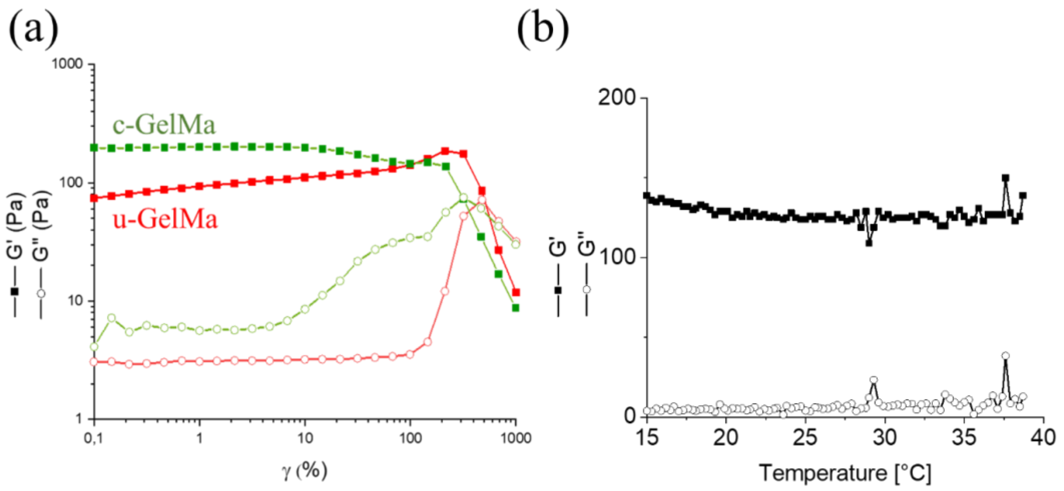

Figure 26. (a) Comparison of G’ and G’’ moduli, obtained through amplitude sweep tests at a constant angular frequency of 5 Hz, between u-GelMa (red curve) and c-GelMa (green curve) at 20°C. Both moduli are plotted

as a function of the applied strain from 0,1% to 1000%. (b) G’ and G’’ moduli of c-GelMa obtained through temperature sweep from 15 °C to 40 °C (5 °C/min), with angular frequency of 0,1 s^{-1} and a strain of 0,1%. Both moduli are plotted as a function of the duration time (13 min). G’ and G’’ moduli are reported as filled squares and empty circles, respectively.

Collagen

Collagen ink and bioink were bioprinted, as explained in detail in the next section, and then were crosslinked through a photo-crosslinking process, by using the same crosslinking procedure used for GelMa (1 min of UV irradiation at 50 % of UV intensity and 3 cm of distance), which were defined safe for cell growth. Furthermore, this crosslinking condition was replicate for collagen-based scaffolds with the aim to maintain fixed the crosslinking parameters among GelMa and collagen materials, to only compare cells response and biological activity as a function of the material stiffness or chemical nature. Finally, stability tests previously performed (not shown in this Thesis) demonstrate that u-coll structures are stable in DMEM based culture media only for 3 days. For this reason, in order to more stabilize collagen structures, crosslinking process was performed on collagen material without the presence of photo-initiator, by exploiting its inherent ability to self-response to UV light.

In order to evaluate how the crosslinking process, affects the mechanical properties of the collagen, rheological characterizations were carried out by comparing both uncrosslinked (u-coll) and crosslinked (c-coll) collagen behavior.

Amplitude sweep measurements were carried out to evaluate the viscoelastic properties of c-coll with respect to the u-coll one, by applying an increasing strain from 0.1% to 1000%, at a temperature of 20 ° C. As shown in Figure 27 a, both elastic (G’) and loss (G'') moduli of c-coll slightly increases after the crosslinking process, from 0.4 kPa to 0.6 kPa for G’, and from 0.060 kPa to 0.080 kPa for G’’ (Table 12), indicating a growth of the internal substructure due to the higher number of crosslinks provided by the UV irradiation. Moreover, c-coll shows a more pronounced G’’ peak, thus confirming the presence of crosslinks between polymer chains, while maintaining the crossover point at 50 % and the LVE range from 0.1 % to 7 % (see Table 13).

Table 13. G’ and G’’ moduli, LVE range and crossover points of c-GelMa and u-GelMa obtained through amplitude sweep tests at 20 °C.

sample	LVE (%)	G’ (Pa)	G’’ (Pa)	c. pt. (%)
c-coll	0.1 - 7	600	80	50
u-coll	0.1 - 7	400	60	50

In order to assess whether the crosslinking process stabilizes the structure during time in incubation condition, temperature sweep measurement was carried out to investigate the viscoelastic behavior of collagen as a function of increasing temperature (5 °C/min), at a constant value of angular frequency (1 Hz) and strain (0.1 %), simulating static condition. In particular, a ramp of temperature from 15 °C to 40 °C was applied, to simulate (i) the printing temperature (20 °C) and (ii) the incubation temperature (37°C), after the printing process. From Figure 27 b it is possible to observe that, despite an initial decrease of both moduli with increasing temperature, they still remain fairly high, with G' modulus of 550 Pa and G'' modulus of 80 Pa, at 37°C. This result demonstrates that even the weak dependency of the G' and G'' moduli on the temperature, the crosslinking process is able to provide enough crosslinks to stabilize the structure at 37 °C, over than 1 week. The slight decrease of G' and G'' at lower temperature might be due to a possible physical interaction and hydrogel bond formation between chains that dominate only at very low temperature. On the contrary, at incubation temperature, the chemical crosslinks totally determine the 'gel-like' behavior of the scaffolds, displaying the desired mechanical property.

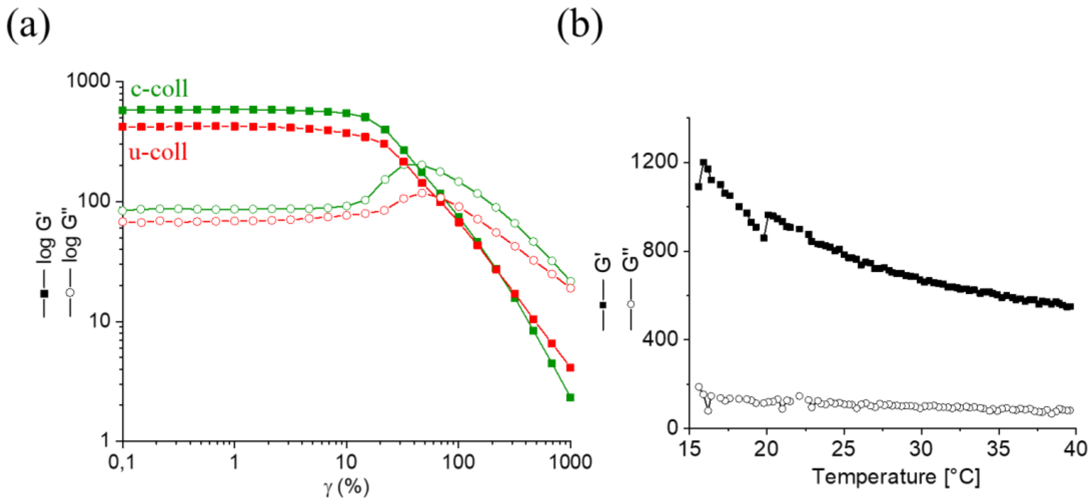

Figure 27. (a) Comparison of G' and G'' moduli, obtained through amplitude sweep tests at a constant angular frequency of 1 Hz, between u-coll (red curve) and c-coll (green curve) at 20°C. Both moduli are plotted as a function of the applied strain from 0,1 % to 1000 %. (b) G' and G'' moduli of c-GelMa obtained through temperature sweep, from 15 °C to 40 °C, with angular frequency of 0,1 s^{-1} and a strain of 0,1 %. G' and G'' moduli are reported as filled squares and empty circles, respectively.

Interpenetrating polymer network

Interpenetrating polymer network of GelMa 5 % (w/v) and collagen 2.5 % (50:50) was produced in order to provide a new artificial ECM, which conjugates both the mechanical stability of the crosslinked GelMa and the high biomimicry of the collagen and that displays intermediate rheological properties between GelMa and collagen.

By definition, an Interpenetrating Polymer Network (IPN) is a polymer comprising two or more networks that are at least partially interlaced on a polymer scale but not covalently bonded to each other and cannot be separated unless chemical bonds are broken [253]. The two or more networks can be envisioned to be entangled in such a way that they are concatenated and cannot be pulled apart, but not bonded to each other by any chemical bond. It is important to highlight that simply mixing two or more polymers does not create an interpenetrating polymer network, nor does create a polymer network out of more than one kind of monomers which are bonded to each other to form one network (heteropolymer or copolymer). For this reason, in order to ensure the formation of an IPN, after the semi-IPN formulation, which is well explained in the experimental section and in paragraph 3.2.1., a post-printing crosslinking process was carried out through UV irradiation.

In particular, in the semi-IPN matrix, collagen is covalently crosslinked in the presence of GelMa without the presence of the photo-initiator, to avoid as much as possible secondary crosslinking reaction between collagen and GelMa; then, once the covalent bonds between collagen chains intercalated on GelMa ones are formed, a second photo-crosslinking process must be performed, in the presence of the photo-initiator Irgacure 2959, to ensure chemical linkages between the acrylate moieties of the GelMa chains, which can be established only if triggered by a radical photo-initiator. At this purpose, with the aim to quickly assess the formation of the IPN, thus the crosslinks between collagen chains and not between collagen and GelMa, GelMa was firstly crosslinked in the presence of c-coll with UV light but without the presence of photo-initiator and the sample was incubated at 37 °C to qualitatively observed the result. After 3 min of incubation, it is clear that GelMa starts to dissolve in the phosphate buffer solution, which was employed to immerge the scaffold and carry out the experiment, while collagen still maintains its structure by displaying highly porosity in the zones where GelMa was intercalated. However, further rheological and morphological characterizations are needed to assess the IPN formation and to exclude the formation of GelMa-collagen covalent bonds.

Amplitude sweep measurements were carried out to evaluate the viscoelastic properties of IPN with respect to the semi-IPN one, by applying an increasing strain from 0.1% to 1000%, at a temperature of 20 ° C. As shown in figure 28 a, both elastic (G’) and loss (G'') moduli of IPN increases after the crosslinking process, from 0.3 kPa to 4 kPa for G’, and from 0.026 kPa to 0.26 kPa for G’’ (Table 13), indicating a growth of the internal substructure due to the higher number of crosslinks provided by the UV irradiation. Moreover, IPN shows a shorter range of LVE, from 0.1 % to 3 %, and shifted crossover point at lower strain value (70 %), while semi-IPN displays an LVE range from 0.1 % to

30 % (see Table 14). These trends can be ascribable to the fact that IPN after crosslinking process display higher fragility, thus less viscoelastic property. Finally, in the IPN sample, G'' peak start to appears at lower strain deformation, by following the same trend displayed by c-GelMa (Figure 28 b), thus meaning that the photo-crosslinking process after the bioprinting, forms covalent bonds between the acrylate groups branched on the GelMa chains.

Table 14. G' and G'' moduli, LVE range and crossover points of semi-IPN and IPN obtained through amplitude sweep tests at 20 °C.

sample	LVE (%)	G' (Pa)	G'' (Pa)	c. pt. (%)
IPN	0.1 - 4	4000	260	70
semi-IPN	0.1 - 60	300	26	100

In order to assess whether the crosslinking process stabilizes the structure during time in incubation condition, temperature sweep measurement was carried out to investigate the viscoelastic behavior of collagen as a function of increasing temperature (5 °C/min), at a constant value of angular frequency (1 Hz) and strain (0.1 %), simulating static condition. In particular, a ramp of temperature from 15 °C to 40 °C was applied, in order to simulate (i) the printing temperature (20 °C) and (ii) the incubation temperature (37°C), after the printing process. From Figure 28 c it is possible to observe that, both G' and G'' display constant values of 3600 Pa and 300 Pa, respectively, during the whole temperature ramp and show slightly decrease mechanical properties with respect to the amplitude sweep analysis acquired at 20 °C (Figure 28 a), meaning that, even in this case, the crosslinking process provides enough crosslinks to stabilize the structure at 37 °C.

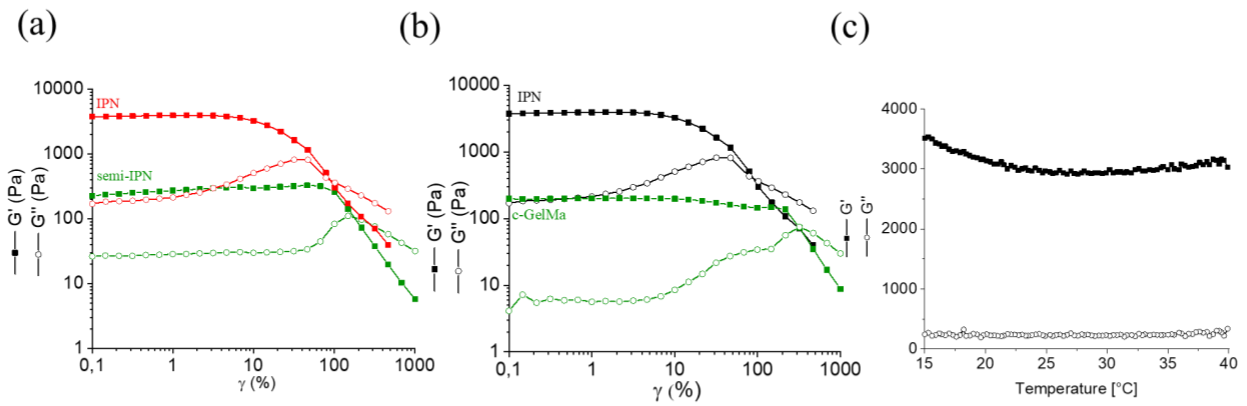

Figure 28. (a) Comparison of G’ and G’’ moduli, obtained through amplitude sweep tests at a constant angular frequency of 1 Hz, between IPN (red curve) and semi-IPN (green curve) at 20°C. Both moduli are plotted as a function of the applied strain from 0,1 % to 1000 %. (b) Comparison between IPN (black curve) and c-GelMa (green curve) G’ and G’’ moduli obtained through temperature sweep at 20 °C. (c) IPN G’ and G’’ moduli plotted against a ramp temperature from 15 °C to 40 °C (5 °C/min), obtained with a temperature sweep test with angular frequency of 0,1 s^{-1} and a strain of 0,1 %. G’ and G’’ moduli are reported as filled squares and empty circles, respectively.

3.3. DEVELOPMENT OF 3D BIOPRINTED PLATFORM WITH STIFFNESS GRADIENT

In this Thesis, AlgMa-based bioinks were employed to produce a cell-laden polymeric platform with tailored mechanical properties and gradient stiffness, which aims to replicate physiologically-like gradient of both healthy and pathological tissues useful for studying the correlation between extracellular matrix (ECM) mechanical/chemical properties and cell spheroids behaviour (mechanobiology). In order to create the cell-laden platform, HeLa cells were used as model cell line and were loaded into the modified alginate-based bioink.

The importance of a gradient is mainly related to structural and dynamical properties, which influence molecular diffusion, generate concentration gradients of the soluble factors, and mediate cell response to external mechanical inputs [254,255]. The fabrication of well-defined 3D architectures is a big challenge and requires not only a precise formulation of the components that constitute cell microenvironment, but also the control of several physico-chemical properties such as stiffness and nano-porosity, of grow-factor binding and matrix degradation properties [58]. The stiffness of extracellular matrix is recognized to play a key role in the regulation of cell behaviour; the external mechanical inputs are transduced in cellular systems into molecular outputs (i.e., transcriptional programs, differential spatial organisation of cell molecular determinants) that drive tumour progression [22], epithelial mesenchymal transition/aggressiveness [256], genomic variation [257], invasion [258], metastatization [259] and chemoresistance [23]. A reduction in the stiffness of the cancer cell niche promotes reversible cellular quiescence (dormancy), while increases in environmental stiffness might facilitate reactivation of dormant cell [23]. Tumorigenic tissues are considerably stiffer and have a Young's modulus of one or two orders of magnitude greater than normal tissue, depending on the type of tissue and lesion size [24,25]. Furthermore, cancer tissues are not homogeneous but present an intratumor heterogeneity, stiffness increase from the periphery to the core of the solid tumours [26,27]. This enhanced stiffness and its heterogeneity make complex to study the mechanism of carcinogenicity in standard in vitro models that do not recapitulate the reality of human physiologic and pathologic tissues. Therefore, the development of smart biomaterials that recapitulate the physico-chemical characteristics found in the microenvironment of the tumor, will enable more realistic in vitro studies and a better comprehension of cancer mechanisms, which is fundamental to develop new strategies to fight tumor onset, development, and relapse.

In several studies, alginate methacrylate was chosen as a good candidate to support cell growth in 3D constructs, thanks to its high biocompatibility, ability to form hydrogel under mild conditions, and the possibility to modify and tune its biological and mechanical proprieties [19,20]. Furthermore, the absence of ECM proteins, makes easier the detection of ECM produced by cells themselves.

3.3.1. 3D bioprinting

To evaluate the biocompatibility of AlgMa BA and BB bionks, circular cell-laden scaffolds were obtained through 3D bioprinting, with 5 mm and 1 mm of diameter (Ø) and height (h), respectively. After bioprinting, both single and double crosslinking processes were carried out on the sample, to obtain stable construct with tailored mechanical properties in the desired range of stiffness. The bioprinting speed and the conical needle were selected thanks to the deep rheological characterization carried out, which enabled to correlate rheological parameters with bioprinting process. In particular, 10 mm s^{-1} and 0.4 mm (22 G) were chosen as the final bioprinting speed and nozzle diameter, respectively, to get a continuous and well-defined filament extrusion. In this context, flow curves represent a powerful tool to predict and suggest the best bioprinting condition to use, since they can exactly simulate what happens to a material during the extrusion moment and provide, at the same time, viscosity vs. shear rate outcomes, that contains the information needed. In fact, from the flow curve, shear stress vs. shear rate, it is possible to evaluate the flow point of a material, which corresponds to the point where the change of the slope occurs. After this point, the chains (represented as layers of randomly packed macromolecules) are not able to contrast the rotational movements, thus start to flow [197]. In the practice, this situation indicatively corresponds to the moment of materials extrusion outside the needle. In the specific case of AlgMa inks, by analyzing the rheological results of AlgMa inks, explained in the previous section and reported in Figure 22, it is possible to detect the flow point at around 150 s^{-1}, thus corresponding at a bioprinting speed of 10 mm/s, calculated by using the equation 1, 2, 3, 4 and 5. Furthermore, even the selection of the nozzle can be evaluated through these equations, since it is directly proportional to the flow speed which is indicated as V in equation 1.

Finally, BA bioink was employed to produce the gradient stiffness platform, by using the same bioprinting parameters explained above and a “fortune cookie”-like shape was chosen as model, to promptly distinguish the different regions during all the experimental phases (Figure 29 b). The fortune cookie shape also enabled to determine the boundaries of the regions characterized by different stiffness and to easily examine cells in a specific area. After the bioprinting, post crosslinking process was performed on three different areas by using a UV-shielding mask that allowed UV light to pass only throughout a selected portion of the fortune cookie, in order to get differential stiffness (Figure 29 (a-d)). Thanks to this strategy the stiffness is tailored by exposing the construct to different times of UV treatment, which can be spatially controlled.

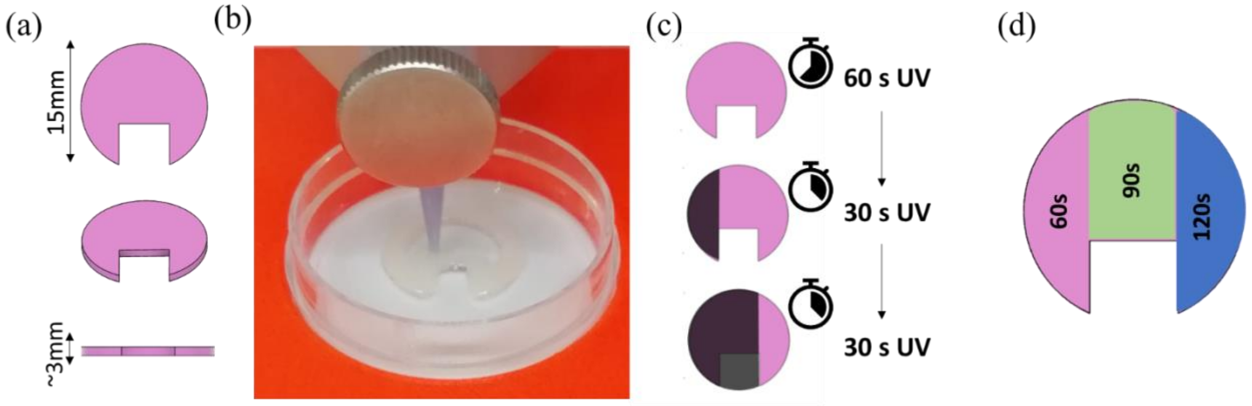

Figure 29. CAD model of cell-laden 'fortune-cookie'; (b) Bioprinting process of the cell-laden 'fortune-cookie' platform; (c) UV irradiation processes to obtain a gradient stiffness platform; (d) Schematic representation of the gradient stiffness platform.

3.3.2. Biological results

HeLa cells survival was first evaluated after 3 days (T3) of culture by using a live/dead assay with calcein-AM and propidium iodide (see experimental section for more details). Double crosslinked BA scaffolds and both single and double crosslinked BB scaffolds were considered for this analysis. In particular, 90 s of UV exposure time was considered and discussed in this section to quickly evaluate how the stiffness of the matrix can affect cell behavior, by maintaining fixed the UV irradiation time. The results, reported in Figure 29 d, show different viability ranges as a function of bioink and scaffold characteristics. In particular, BA90Ca (Figure 30 a), which is characterized by the lowest stiffness of 41 Pa, shows 79 ± 8 % of viability, BB90 (Figure 30 b), which display an intermediate value of stiffness (120 Pa), display 52 ± 7 % of viability, while BB90Ca (Figure 30 c) scaffolds display the highest stiffness of 270 Pa and the lowest cell viability of 27 ± 11 % (Table 15 summarize all the results). From these results, it is possible to assess that cell viability strongly depends on matrix stiffness, as reported by BB90 and BB90Ca, in which the concentration of I2959 and the UV irradiation time are constant. The increase of the mechanical properties is only related to the second step of post printing crosslinking process, in the case of BB90Ca, which should not affect cell viability since it is widely used as crosslinking method with alginate-based scaffolds and HeLa cells [260]. Similarly, the decreases of viability from BA90Ca to BB90Ca scaffolds, might be caused by (i) the strong increase of the stiffness of one order of magnitude, from 41 Pa for BA90Ca to 270 Pa for BB90Ca, and (ii) the increase of I2959 concentration contained in the corresponding bioinks formulation, from 0.2 %, for BA90Ca, to 0.25 %, for BB90Ca. However, since many works report the use of similar concentration of I2959 in the presence of HeLa cells [261-264], the significant decreases of cell viability registered for BA90Ca and BB90Ca might be ascribable mainly to the strong increase of the mechanical properties.

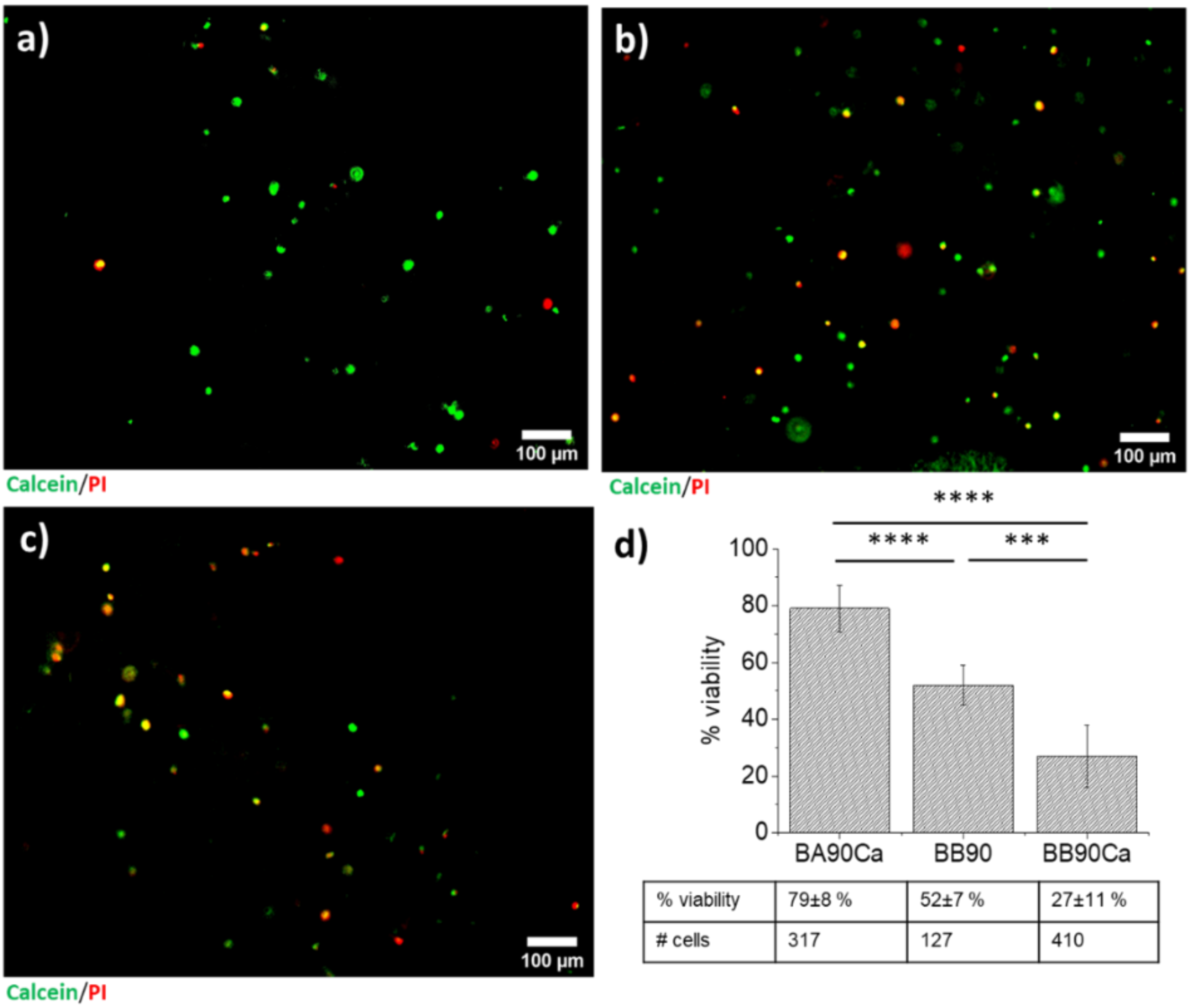

% viability	79±8 %	52±7 %	27±11 %
# cells	317	127	410

Figure 30. Live/dead analysis on 3D bioprinted constructs obtained by using (**a**) bioink A (BA) followed by dual-crosslinking process with $CaCl_2$ and 90 sec of UV treatment (BA90Ca), (**b**) bioink B (BB) followed by only 90 s of UV treatment (BB90) and (**c**) bioink B (BB) followed by dual-crosslinking process with $CaCl_2$ and 90 sec of UV treatment (BB90Ca). Live cells (green) and dead cells (red) are stained with calcein and PI respectively. Cell viability was measured after 72h in incubation. **d**) Percentages of cell viability in BA90Ca (left column), BB90 (center column) and BB90Ca (right column) 3D bioprinted scaffolds.

Table 15. Comparison between cell viability and storage modulus G'of BA90Ca, BB90 and BB90Ca bioprinted models.

Bioprinted model	Cell viability %[*]	G' (Pa)
BA90Ca	79 ± 8	41
BB90	52 ± 7	120
BB90Ca	27 ± 11	270

[*] cell viability evaluated at day 3.

Thanks to the higher cell viability displayed by BA90Ca scaffold, bioink A was selected as the final bioink to fabricate the gradient stiffness platform with tailored mechanical properties. Firstly, cell viability tests were also performed on BA60Ca and BA120Ca, after dual crosslinking process, in order to assess cell survival in three different matrices stiffness. As reported in Table 16 and in Figure 31, HeLa cells embedded in BA60Ca, BA90Ca, and BA120Ca scaffolds show 79 ± 8 %, 79 ± 8 %, and 60 ± 12 % of viability, respectively. By comparing these results, it is possible to observe that viability decreases when the stiffness increases of one order of magnitude from BA60/90Ca to BA120Ca, as also reported in the previous Table 16 between BB90 and BB90Ca in which the time of UV irradiation and the I2959 concentration are constant. For this reason, it is reasonable to think that the cell viability strongly depends on the mechanical properties of the matrix and that, only in part, UV irradiation time might affect cell survival.

Table 16. Comparison between cell viability and storage modulus G' of BA60Ca, BA90Ca and BA120Ca bioprinted models.

Bioprinted model	Cell viability %[*]	G' (Pa)
BA60Ca	79 ± 8	200
BA900Ca	79 ± 8	41
BA120Ca	52 ± 7	30

[*] cell viability evaluated at day 3.

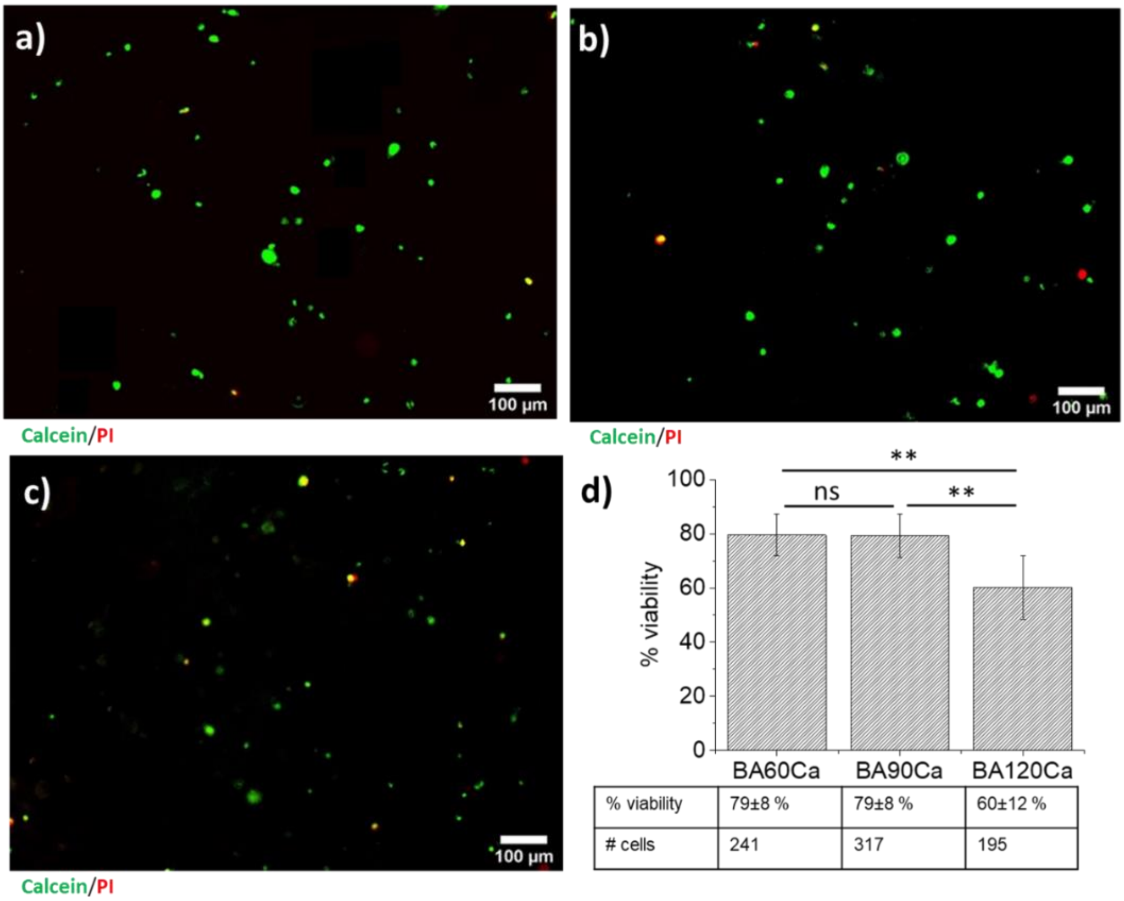

% viability	79±8 %	79±8 %	60±12 %
# cells	241	317	195

Figure 31. Live cells (green) and dead cells (red) stained in bioink A cell-laden scaffolds after dual cross-linking procedure with CaCl2 and (a) 60 sec (BA60Ca), (b) 90sec (BA90Ca) and (c) 120 sec (BA120Ca) of UV light. (d) Percentages of cell viability in BA60Ca (left column), BA90Ca (centre column) and BA120Ca (right column) 3D bioprinted scaffolds.

To have a complete screening of the correlation between I2959 concentration, matrix stiffness, UV irradiation time and cell behavior, live/dead assays were also performed on the remaining BA and BB scaffolds as summarized in Table 17. Data show that scaffolds realized using Bioink A, which experienced a double crosslinking process and contain less percentage of I2959 (0.2 %), display higher cell viability than samples obtained from Bioink B, which display higher mechanical properties and concentration of I2959. In particular, BB60Ca, BB90Ca, and BB120Ca scaffolds, which have experienced both UV curing and calcium chloride crosslinking, show higher mortality in comparison with samples made using the same bioink but crosslinked only via UV curing. As a general consideration, it is possible to assess that cell viability decreases (i) with the increasing of the mechanical properties and UV irradiation time, at fixed concentration of I2959 (as in the case of BB120, BB90, BB60, BB120Ca, BB90Ca, and BB60Ca), (ii) with the increasing of the stiffness after ionic crosslinking, at fixed concentration of I2959 and UV time (as in the case of the comparison between BB120-BB120Ca, BB90-BB90Ca and BB60-BB60Ca) and (iii) with the increasing of both I2959 concentration and mechanical properties, at fixed UV time and ionic crosslinking process (as in the case of the comparison between BA120Ca-BB120Ca, BA90Ca-BB90Ca and BA60Ca-BB60Ca), thus meaning that the stiffness of the matrix, thus the high compression experienced from the cells, has the most significant effect on the cell behavior and proliferation, even if the mechanical moduli match the stiffness of the native-tissues [252].

Table 17. Cell viability percentage and the stiffness (storage modulus, Pa) of all the scaffolds obtained from BA and BB after (i) printing process and after (ii) single and dual crosslinking.

	Crosslinking post-printing			
3D bioprinted scaffold	UV irradiation time	Time of immersion in $CaCl_2$	G' (kPa)	Cell viability*
BB120	120 s	/	0.900	43 ± 7
BB90	90 s	/	0.120	52 ± 7
BB60	60 s	/	0.075	58 ± 7
BB120Ca	120 s	5 min	2	28 ± 17
BB90Ca	90 s	5 min	0.310	27 ± 11
BB60Ca	60 s	5 min	0.120	60 ± 5
BA120Ca	120 s	5 min	0.200	52 ± 7
BA90Ca	90 s	5 min	0.041	79 ± 8
BA60Ca	60 s	5 min	0.030	79 ± 8

*evaluated after 3 days of incubation

Finally, HeLa cell-laden bioprinted platform with ‘fortune-cookie’-like shape was successfully fabricated, as reported in Figure 32 e, by using bioink A, due to its higher bioactivity reported. Thanks to the optimized dual crosslinking post-printing process, the platform displayed high mechanical stability up to 14 days. HeLa cells embedded in the structure experienced different external forces provided by the different mechanical properties of the matrix. In particular, as reported in Figure 32 (a-e), the stiffness increases from the left side to the right side from 200 Pa (120 s of UV) to 30 Pa (60 s of UV), and cell viability follow the same trend after 3 days of incubation, as summarized in Table 17. Live-dead assays directly performed on the platform after 14 days of incubation (Figure 32), show a decrease of cell viabilities with respect to those one obtained after 3 days of incubation, displaying 69 ± 12 %, 59 ± 18 % and 30 ± 10 % percentage of cell viability in the regions treated at

60 s, 90 s and 120 s of UV, respectively. These results demonstrate that matrices stiffness strongly influence cell behaviour during incubation and that this platform can be useful to examine cell behaviour in correlation to the mechanical properties. Many papers demonstrate the effects of the matrix stiffness on the cell pathway [15,34,265-256], which are consistent with the results obtained in these experiments, but only few works deeply analyse also the effect of the photo-initiator concentration and the crosslinking parameters on cell behaviour [266-268].

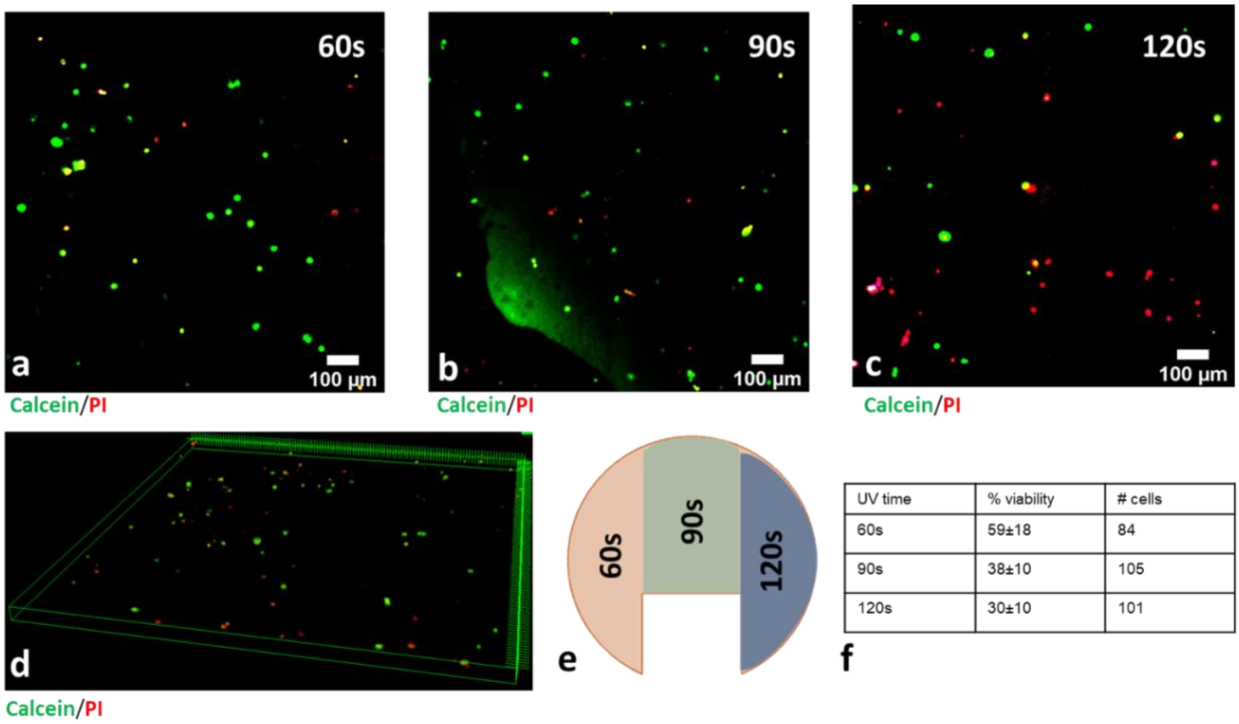

UV time	% viability	# cells
60s	59±18	84
90s	38±10	105
120s	30±10	101

Figure 32. Live cells (green) and dead cells (red) stained in the fortune cookie construct cultured up to 14 days. Crosslinking was obtained with (a) 60 sec (BA60Ca), (b) 90sec (BA90Ca) and (c) 120 sec (BA120Ca) of irradiation with UV light. (d) 3D plot of a portion of the fortune cookie. (e) Schematic representation of the differential stiffness area and their boundaries within the overall 3D structure. (f) Percentage of viability of cells in each area.

3.3.3. Conclusions

In conclusion, a cell-laden stiffness gradient platform was successfully obtained by 3D bioprinting, thanks to a post-printing dual crosslinking process. This method was developed to overcome limitations related to the low cells viabilities induced by extended UV irradiation or weak mechanical proprieties inherent to constructs fabrication [269,270]. In this case, dual crosslinking processes were optimized to obtain a stable cell-laden construct while keeping low the concentration of the photoinitiator and therefore without adversely affecting cell viability. Since HeLa cells viability could be very high, by reaching percentage around 95% in a gelatin/alginate/fibrinogen bioink [48], Bioink

A formulation was selected to fabricate the entire platform thanks to its better bioactivity with respect to Bioink B. Furthermore, by employing the strategy illustrated in this Thesis, it is possible to replicate in one printing process, a well-defined structure with the desired mechanical properties reproducing the native stiffness of certain tissues, their variability, and even the characteristics of the boundaries between different regions. Furthermore, by tuning the duration of UV irradiation is possible to obtain a differential stiffness platform recapitulating the stiffness heterogeneity of the tissue from the periphery to the core. In general, physiological and pathological situations can be easily mimicked: e.g. bioink B dual crosslinked shows a stiffness that range from physiological to pathological tissue (according to the UV curing times), while bioink A dual crosslinked shows a stiffness able to mimic softer tissue areas. Finally, this platform represents a model which aims to provide a useful, practical and easy to manage *in vitro* tool that enables important studies on cancer mechanisms, which are strictly correlated with their mechanical properties and intratumor heterogeneity. Moreover, the possibility to introduce growth factor, bioactive molecules, and other types of cells, depending on the targeted tissue, make this model versatile and adaptable at different systems.

3.4. PROOF OF CONCEPT OF 3D BIOPRINTED INTESTINAL BARRIER

The intestinal barrier is one of the most studied tissue, especially to evaluate some nutrients and drugs absorption. 2D intestinal barrier cannot replicate the main biological function of the native tissue, thus 3D bioprinted models might provide a great improvement on the replication of the 3D environment and the stratification of this tissue, which are fundamental characteristics to take into account during drug testing. Many efforts were performed to create a 3D bioprinted intestinal barrier with physiologically-like hierarchical architecture and cells composition, however, the recapitulation of this tissue still remains challenging due to the highly complex structure of intestinal villus and cellular composition. The models reported in the literature, usually involve only a single cell type, the use of material that is not found in the ECM of the tissue, and therefore they do not reproduce the real stiffness of the tissue.

Collagen is the main constituent of the intestinal barrier and typically is located below the epithelial layer. It acts as supporting layer of the epithelial cells and provides mechanical stability regulating also cell signaling. For this reason, the collagen bioink formulation developed during this Thesis was employed to achieve a ‘proof of concept’ of intestinal barrier with the aim to reproduce the native collagen layer and evaluate its performance during time and in contact with living components, which usually modify the characteristic of the materials. Furthermore, GelMa-based bioinks and semi-IPN-based bioink were additionally employed as matrices to create intestinal barrier, in order to compare cell behavior, growth, proliferation, and protein expression as a function of different mechanical properties and chemical composition of the external environment. GelMa bioink was selected since it is a ‘gold standard’ in this field, and its bioactivity and biocompatibility are deeply reported in the literature [167,271,272], while semi-IPN was employed thanks to its intermediate mechanical properties between collagen and GelMa bioinks and multiple chemical composition.

Finally, multiple cell types were employed to increase the complexity of the system and provide a more realistic model.

3.4.1. 3D bioprinting

3D bioprinting of intestinal barrier model consists of multiple steps in which GelMa, collagen, and semi-IPN based bioinks, and the corresponding inks not containing cells, were printed in a multilayered structure to simulate the physiologically-like conditions.

In particular, a good replication of the intestinal structure should include the fundamental layers of the tissue which are (i) the submucosa, mainly composed of fibroblast and human umbilical vascularized endothelial (HUVEC), (ii) the lamina propria, mainly composed of macrophages and white cells, (iii) the epithelial layers, which is the outermost external layer and it both drives and regulate the absorption of substances. For this reason, to obtain a full representation of the main components of the intestinal tissue, submucosa, lamina propria, and epithelial monolayer were printed, by including in the submucosa layer fibroblasts cells and in the external layer intestinal epithelial cells.

Firstly, GelMa bioink containing human intestinal fibroblast, labeled as **GelMa bioink HIF (GB_{HIF}),** collagen bioink containing human intestinal fibroblast, labeled as **Collagen bioink HIF (CB_{HIF}),** and semi-IPN bioink containing human intestinal fibroblast, labeled as **semi-IPN bioink HIF (SB_{HIF})**, were separately printed inside 24-multiwell to form circular shape geometry (1.5 mm of thickness and 1 cm of width), schematically represented in Figure 33. The dimension of the model was deeply evaluated by also considering the native thickness of the intestinal layers which range from 2 to 3 mm [77]. In fact, the advantage of using 3D bioprinting is also the possibility to simulate the physiologic dimension of the tissue structure which strongly influences drug absorption. Then, in the same printing process, a second layer of 0.4 mm, representing the lamina propria, was printed by the second cartridge onto the previous basal layer with the corresponding inks not containing cell, thus **GelMa ink (GI), Collagen ink (CI),** and **semi-IPN bioink (SI).** This layer remains empty within all the structure, in order to reduce the number of living components in the scaffolds and decrease the number of uncontrollable variables. Finally, the third layer, reproducing the epithelial monolayer, has been fabricated through a manual seeding of human intestinal epithelial cells (HTCs-8), onto the surface of the printed scaffolds. This layer was introduced manually in the *in vitro* system, since in the native intestinal structure epithelial cells are not embedded inside ECM and form a thin epithelial coat that assumes villi-like shape. A schematic representation of the bioprinting process is reported in Figure 33 (a,b).

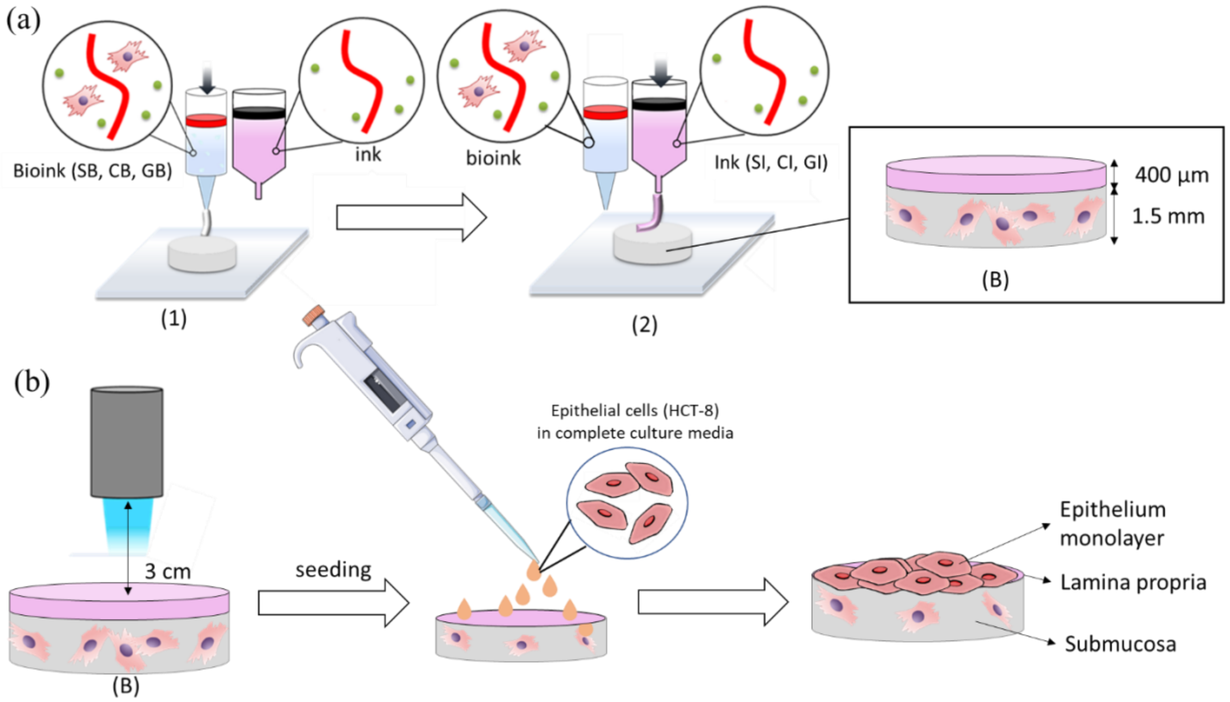

Figure 33. (a) Schematic representation of bioprinting process of semi-IPN, collagen and GelMa-based models, containing HIFs and HSFs, with shape (B) by using REG4LIFE bioprinter. (b) Schematic representation of HCTs-8 manual seeding onto GelMa, collagen and IPN-based 3D models.

After the printing and photo-crosslinking processes, cell viability, cell proliferation, immunofluorescence, and immunohistochemistry were evaluated to assess the model functionalities and performance.

3.4.2. Biological results

Firstly, cell viabilities of human intestinal fibroblasts both embedded in GelMa, collagen, and semi-IPN based bioinks and in 2D cell cultures were evaluated to define cell culture media, matrix biocompatibility, and cell proliferation. Live/dead of HIFs were evaluated in 3D conditions through the staining with calcein/propinium iodide, as explained in detail in the experimental section. Figure 34 a shows confocal images of HIFs embedded in c-coll (crosslinked collagen) matrix, as example, during time after 1 h until 21 days of incubation time. As it is clear from the images, cells perfectly survive to the bioprinting process and few dead cells are reported at 21 days of incubation, thus the viability decrease from 100 % to 95 % during the whole experiment. Furthermore, from day 1 to day 21, fibroblasts maintain a rounded shape, mostly occupied from the nucleus of the cell but, at day 21, the formation of short filaments occurs at the periphery of the cells nuclei. However, from the confocal images, cell proliferation seems to decrease, since the images reported in Figure X are representative of the number of cells found in the entire 3D bioprinted scaffold. By comparing the behavior of HIFs in 3D condition with that one in 2D cell culture reported in Figure 34 b, it is clear that even in 2D multiwell cells slowly proliferate and do not reach the confluences expected, meaning that the collagen matrix only influences the cells morphology and that cell proliferation is strongly altered and slow even in 2D condition, because of inherent characteristics of this kind of cell line (CCD-18 cell line).

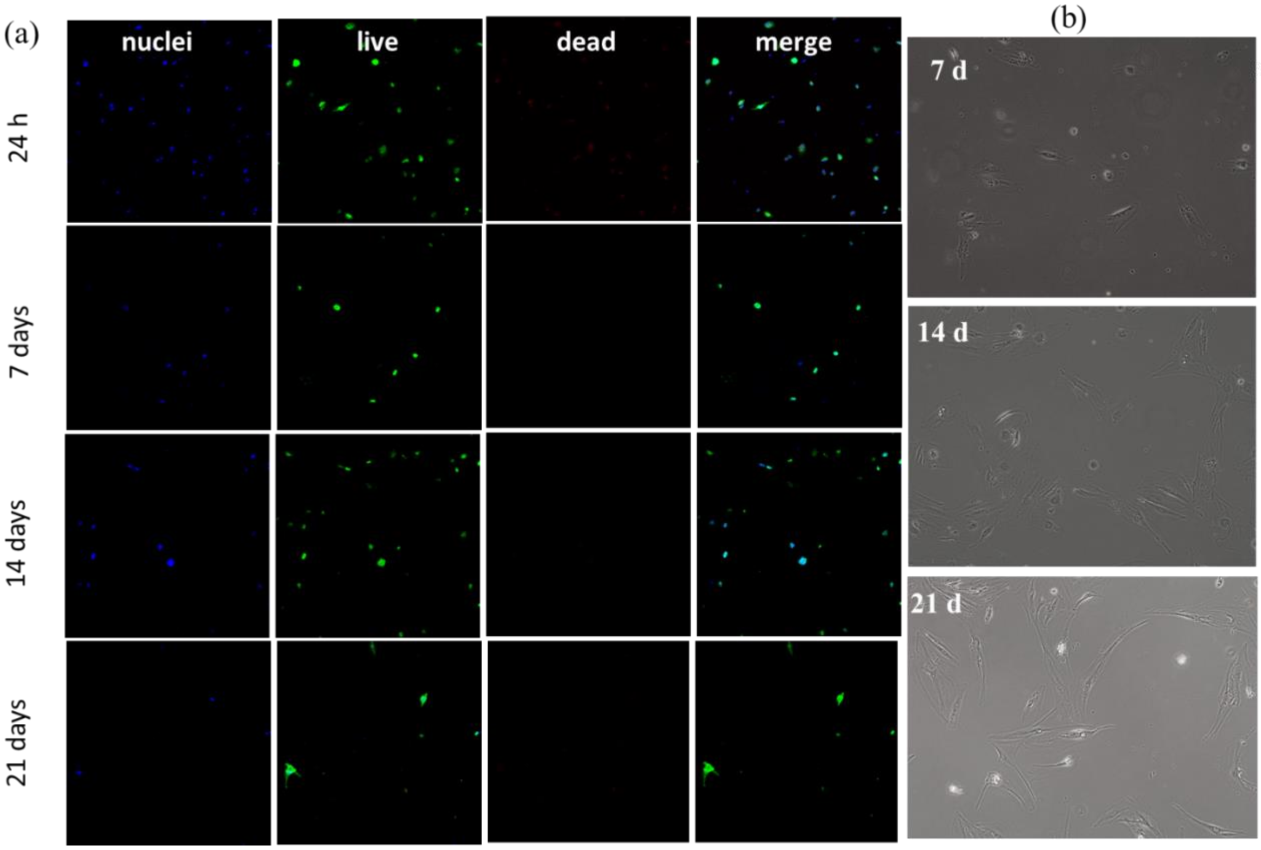

Figure 34. (a) Confocal images of HIFs embedded in c-coll obtained through live/dead staining, after 1day, 7days, 14 days and 21 days of incubation. (b) Optical images of HIFs in 2D conditions at 7 days, 14 days and 21 days.

Cell proliferation assays through alamar blue were also performed to quantitively evaluate HIFs growth in DMEM-based cell culture medium and in 2D conditions. From Figure 35, which reports the normalized cell proliferation (RFU) against the duration time of the experiment, it is evident that the cell proliferation does not increase during time, as expected, but show a random behavior, thus confirming what observed in the optical images in Figure 34 b. Moreover, on day 1, HIFs show less than 3.5 RFU while on day 21 the RFU decrease until 1.5 RFU, which are low value of RFU to carry out statistically and relevant experiments. For this reason, the use of HIFs was excluded for the fabrication of the 'proof of concept' intestinal barrier model, since they require long time of cell cultivation in both 2D and 3D conditions.

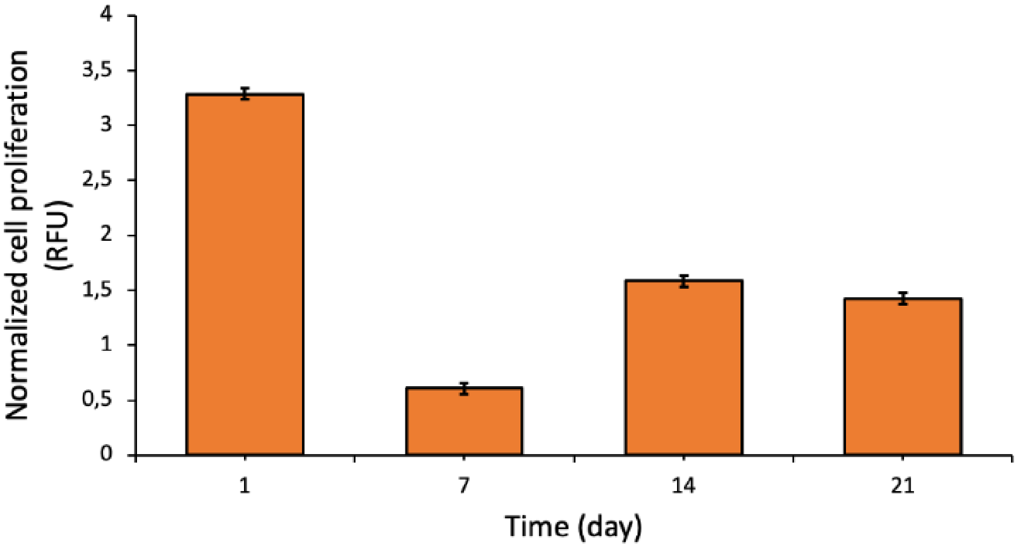

Figure 35. Cell proliferation of HIFs in 2D conditions carried out by Alamar blue assay after 1 day, 7 days, 14 days and 21 days of incubation.

For this reason, Human skin fibroblasts (HSFs) patient-derived were employed to create the cell-laden submucosa layer by separately printing GelMa bioink containing human skin fibroblast, labeled as **GelMa bioink HSF (GB$_{HSF}$),** collagen bioink containing human skin fibroblast, labeled as **Collagen bioink HSF (CB$_{HSF}$),** and semi-IPN bioink containing human skin fibroblast, labeled as **semi-IPN bioink HSF (SB$_{HSF}$)**, inside 24-multiwell to form circular shape geometry as already described above and represented in Figure 33 a. Then, in the second step of printing, the corresponding inks not containing cells, were deposited onto the submucosa layer to form the so-called lamina propria. UV treatment (50 % of UV intensity, 3 cm of distance, 1 min of irradiation time) was performed on the scaffolds in order to provide the covalent crosslinks and the optimal mechanical stability (Figure 33 b). Finally, human epithelial cells (HTC-8) tumor-derived were manually seeded onto the surfaces of the models to build the outermost epithelial monolayer (Figure 34 b).

Before the fabrication of the complete structured 3D intestinal models, different cell culture media and UV irradiation time were tested to assess (i) the best condition to cultivate two different types of cells, which usually grow in different culture media, in the same cell medium and (ii) the possible effects of UV treatment on HSFs, which are the only ones the experienced contact with UV light. In particular, 1 min (green bars) and 2 min (yellow bars) of UV light treatment (50 % of intensity and 3 cm of distance) were tested on 2D HSFs, in the presence of 0.1 % of I2959, in order to evaluate possible effects on cell culture. As shown in Figure 36 a, 2 min of UV light strongly decreases cell proliferation with respect to 1 min. In fact, on day 1 and day 21, for instance, HSFs show 2 and 13 RFU, after 2 min of UV treatment, and 4 and 39 RFU after 1 min only. For this reason, 1 min of UV treatment was selected as the best UV duration time to both (i) provide the suitable mechanical properties to support cell growth, as already explained and demonstrated in section 3.2.2., and (ii) preserve as much as possible cell health. Once the UV irradiation time was optimized, the second important aspect to evaluate is the selection of the suitable cell culture media to cultivate both epithelial and fibroblast cells in the same structure. Epithelial cells perfectly grow in RPMI 1640-based medium supplemented with horse serum (HS), while fibroblasts mainly grow in DMEM-based medium supplemented with fetal bovine serum (FBS). For this reason, several cell culture media mixtures were produced to evaluate the right components of the final formulation and, from qualitative observation at the confocal microscope and cell proliferation assay, it was evident that HTCs-8 can grow only in RPMI-based medium in the presence of HS, while fibroblast better support the change of the primary component, from DMEM to RPMI 1640, and the presence of HS in addition to FBS. In fact, as reported in Figure 36 b, 2D fibroblasts after 1 min of UV treatment better grow in the original DMEM-based media (orange bars) even when HS is added to the medium, displaying an increased proliferation rate from 1 RFU at day 1 to 13 RFU at day 21, while when the medium formulation is changed with RPMI 1640 (blue bars) and supplemented with both 5 % of HA and 5 % of FBS, cell proliferation slightly decreases from 1 RFU at day 1 to 7 RFU at day 21. RPMI 1640 in the co-presence of 5 % of FBS and 5 % of HS was the final optimal formulation to grow both HSFs and HTCs-8, which show greater cell proliferation rate with respect to HSFs thanks to the presence of the RPMI (Figure 36 c). In fact, cell proliferation rate of HTCs-8 increases from 8 at day 1 until 22 RFU at day 21.

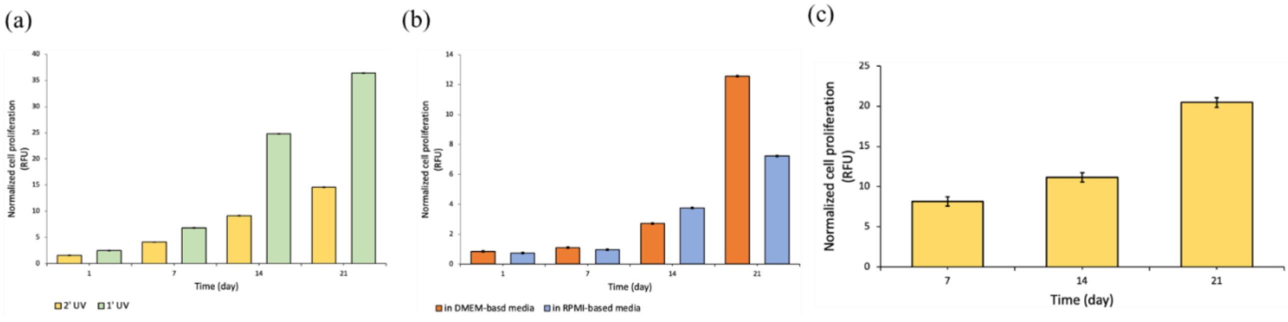

Figure 36. (a) Cell proliferation of 2D human skin fibroblasts (HSFs) after 2 min (yellow bars) and 1 min (green bars) of UV treatments at days 1, 7, 14 and 21 of incubation. (b) Cell proliferation of 2D human skin fibroblasts (HSFs) in DMEM (orange bars) and RPMI-based (blue bars) cell culture media at days 1, 7, 14 and

21 of incubation after 1 min of UV treatment. (c) Cell proliferation of 2D human intestinal epithelial cells (HCTs-8) in RPMI-based media at day 7, 14 and 21 of incubation.

At this point, once both UV irradiation time and cell culture media were optimized, 3D bioprinting of multi-layered intestinal barriers were carried out as described above and schematically represented in Figure 33 (a,b).

HSFs cell viabilities embedded in **GelMa bioink (GB$_{HSF}$), Collagen bioink (CB$_{HsF}$),** and **semi-IPN bioink (SB$_{HSF}$)**, were evaluated after the printing process and photo-crosslinking through live/dead assays. Figure 37 a reports a comparison of the confocal images of HSFs inside all the bioinks at day 1, 7, 14 and 21 of incubation. From the results, HSFs show a clear change of morphology from day 1 to day 21 of incubation in all the matrixes and high cell viability percentage (98 %) during the whole experiments. As highlighted from Figure 37 a and Figure 37 b, HSFs display more elongated shape at 21 days in GelMa matrix with respect to collagen and IPN one. This behavior might be a consequence of the different mechanical properties experienced from the cells inside the matrixes. In fact, as reported in section 3.2.2., GelMa (c-GelMa) displays the lowest stiffness (0.2 kPa), collagen (c-coll) shows an intermediate value between GelMa and IPN (0.6 kPa), while IPN shows the highest modulus (4 kPa) after photo-crosslinking process. For this reason, HSFs recognize weaker external forces in GelMa-based scaffolds, thus they retain the ability to form elongations and spiral orientation through the matrix as in 2D condition (Figure 37 c), where cells appear flatter with pronounced filaments. On the contrary, HSFs inside crosslinked collagen and IPN display rounder shape with minor formation of peripherical filaments. Furthermore, HSFs in c-coll and IPN do not assume spiral orientation as observed in GelMa environment. This change of morphology and spatial organization might be due, even in this case, to the different external forces experienced from the cells and provided by the different stiffness of the matrix. In fact, it is reasonable to think that inside a stiffer matrix, the degree of crosslinking and the number of covalent linkages is significant and higher with respect to matrices with lower mechanical properties, thus, as a consequence, porosity and the inter-chains space decrease, making more difficult for HSFs to making their way among polymer chains to form elongations. Different works confirm that fibroblasts elongations and shape are strictly influenced by the matrix stiffness, and that the higher is the matrix stiffness the more elongated is the cell morphology [14,273,274].

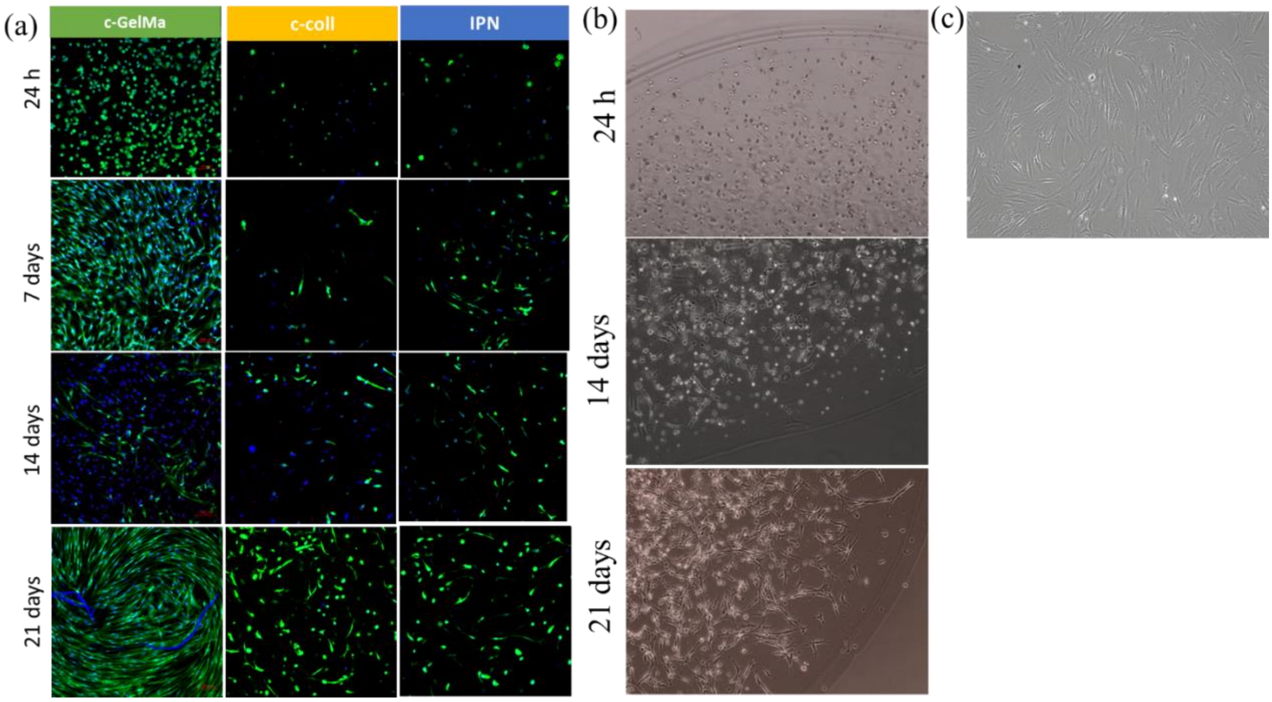

Figure 37. (a) Merge of live, dead and nuclei confocal images of HSFs embedded in c-GelMa (green panel), c-coll (orange panel) and IPN-based (blue panel) scaffolds obtained through live/dead staining, after 1day, 7days, 14 days and 21 days of incubation. (b) Optical images of HSFs in c-GelMa matrix at 7 days, 14 days and 21 days of incubation. Only HSFs in GelMa are reported since GelMa is the only transparent matrix which enable the observation of cell growth at confocal microscope. (c) Optical images of HSFs in 2D conditions at 7 days of incubation.

Cell viabilities of human intestinal epithelial cells (HCTs-8) were also evaluated through live/dead assay at days 7, 14, and 21 of incubation and the corresponding confocal images were reported in Figure 38 a directly as the merge between live cells, dead cells, and nuclei, previously stained with calcein-AM, propidium iodide, and DAPI, respectively. HCTs-8 cell morphology and growth onto 3D models was also compared with that in 2D condition, reported in Figure 38 b.

Confocal images demonstrate that HCTs-8 grow onto the surface of 3D models, starting from isolated rounded cells until to spontaneously form packed columns that resemble villi-like shape as shown at 21 days both in 3D that in 2D (Figure 38 (a,b)). Furthermore, 100 % of cell viability is preserved from day 1 to day 14, while at day 21 of incubation, cell viability decreases until 95 %, probably because of the high number of cells that reach confluences onto the scaffold’s surfaces.

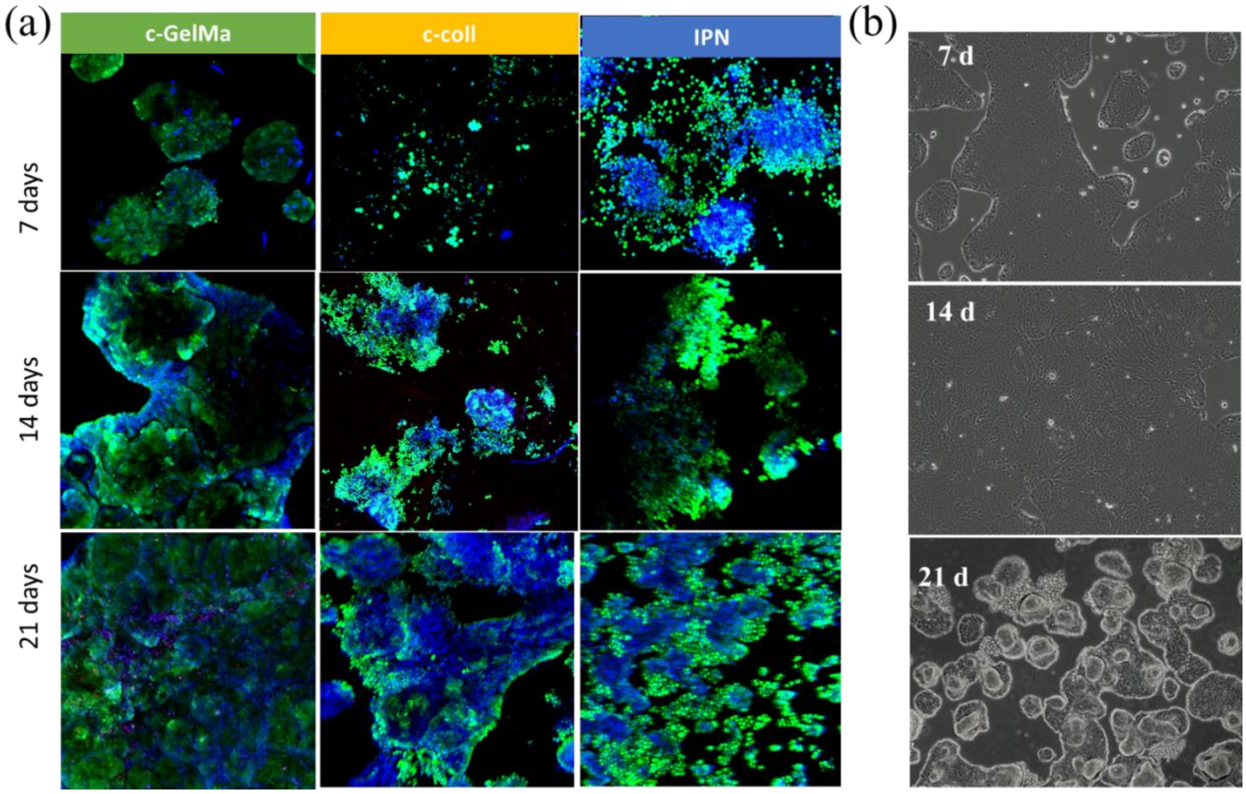

Figure 38. (a) Merge of live, dead and nuclei confocal images HCTs-8 seeded onto c-GelMa (green panel), c-coll (orange panel) and IPN-based (blue panel) scaffolds obtained through live/dead staining, after 7days, 14 days and 21 days of incubation. (b) Optical images of HCTs in 2D conditions at 7 days, 14 days and 21 days of incubation.

Cell proliferation of both HSFs and HCTs-8 in 3D conditions, were quantitatively evaluated through alamar blue assay, as explained in the experimental section. HSFs proliferation inside c-GelMa, c-coll and IPN matrixes, after bioprinting and UV photo-crosslinking, were reported in the Figure 39 a. Graph shows that HSFs in IPN display the highest RFU at 14 and 21 days of incubation, 11 and 19 RFU, respectively, while HSFs in c-GelMa and c-coll show similar cell proliferation rate from day 1 to day 21. Furthermore, the cell proliferation for HSFs in IPN scaffolds abruptly increases at day 14, as in an exponential way, while in c-GelMa and c-coll the increase of cell proliferation is slower and linear.

A similar trend can be observed for HTCs-8 proliferation when seeded onto c-GelMa, c-coll and IPN-based scaffolds (Figure 39 b). In fact, HCTs-8 onto IPN models display higher RFU since day 7 of incubation, with respect to HCTs-8 growth onto c-coll and c-GelMa scaffolds. In particular, HCTs-8 show 33, 42, and 47 RFU at days 7, 14, and 21 of incubation, respectively, onto IPN scaffolds, 23, 24, and 25 RFU at days 7, 14, and 21 of incubation, respectively, onto c-coll scaffolds, and 7, 10 and 19 RFU at day 7, 14 and 21 of incubation, respectively, onto c-GelMa scaffolds.

From these alamar blue assays it is possible to deduce that IPN matrix shows the most bioactive properties with respect to c-coll and c-GelMa, probably thanks to the enhanced biomimicry provided by the combined action of GelMa and collagen.

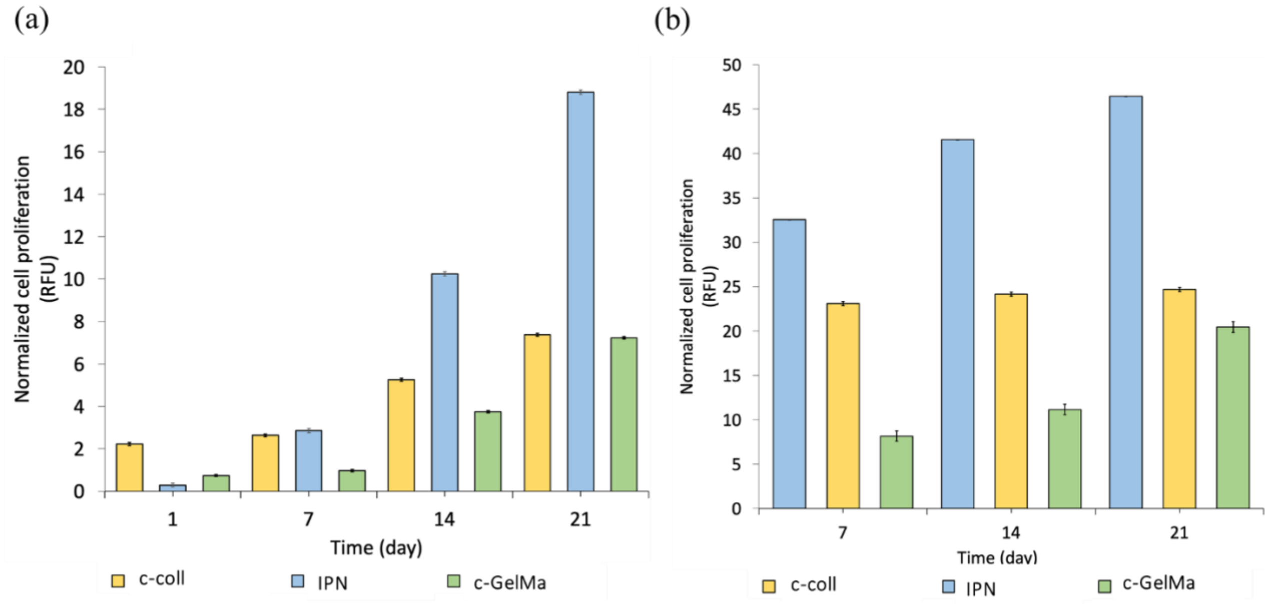

Figure 39. (a) Cell proliferation of human skin fibroblasts embedded in c-coll (yellow bars), IPN (blue bars) and c-GelMa (green bars), after bioprinting and photo-crosslinking. at day 1, 7, 14 and 21 of incubation. (b) Cell proliferation of human intestinal epithelial cells growth onto c-coll (yellow bars), IPN (blue bars) and c-GelMa (green bars) scaffolds, at day 1, 7, 14 and 21 of incubation.

Finally, HCTs-8 protein expressions were evaluated through confocal microscope after immunostaining with E-cadherin and tight-junctions primary and secondary antibodies. As a general consideration, cadherins are a type of cell adhesion molecule that play a key role in the formation of adherens junctions to allow cells to adhere to each other, while tight junctions, also known as occluding junctions are multiprotein junctional complexes whose canonical function is to prevent leakage of solutes and water and seals the paracellular pathway. Both proteins are typical of the epithelial monolayer and their presence is fundamental for the replication of a physiologically-like intestinal barrier tissue, since they strictly influence substances regulation and are responsible of active/passive ions transport [275,276].

Confocal images (Figure 40) report the E-cadherin expression in red and the tight junction (ZO-1) in green of HCTs-8 seeded onto c-GelMa and c-coll scaffolds at day 14 and day 21 of incubation. Notice that, proteins expression of HCTs-8 seeded onto IPN is not reported in this Thesis. As it is clear from the images, both E-cadherin and tight junctions are produced from the epithelial layer and they are localized in the periphery of the cells, in the cell intermembrane space. In fact, it is stated that in physiological conditions, E-cadherins behave as both receptors and ligands for other molecules, thus are present in the plasma membrane space generated between two or more cells, while tight junctions, which consist of the three major transmembrane proteins such as occludin, claudins, and junction adhesion molecule (JAM) proteins, are associate with different peripheral membrane proteins such as ZO-1 located on the intracellular side of plasma membrane, which anchor the strands to the actin component of the cytoskeleton [275,276].

Furthermore, E-cadherins display a strong correlation with cancer, since the loss of the cell adhesion molecules is involved in the formation of epithelial types of cancers such as carcinomas. The changes in any type of cadherin expression may not only control tumor cell adhesion but also may affect signal transduction leading to the cancer cells growing uncontrollable [275,276]. For this reason, the replication of these proteins is fundamental when 3D intestinal barrier models must be replicated to evaluate any pathology, inflammation or tumor disease.

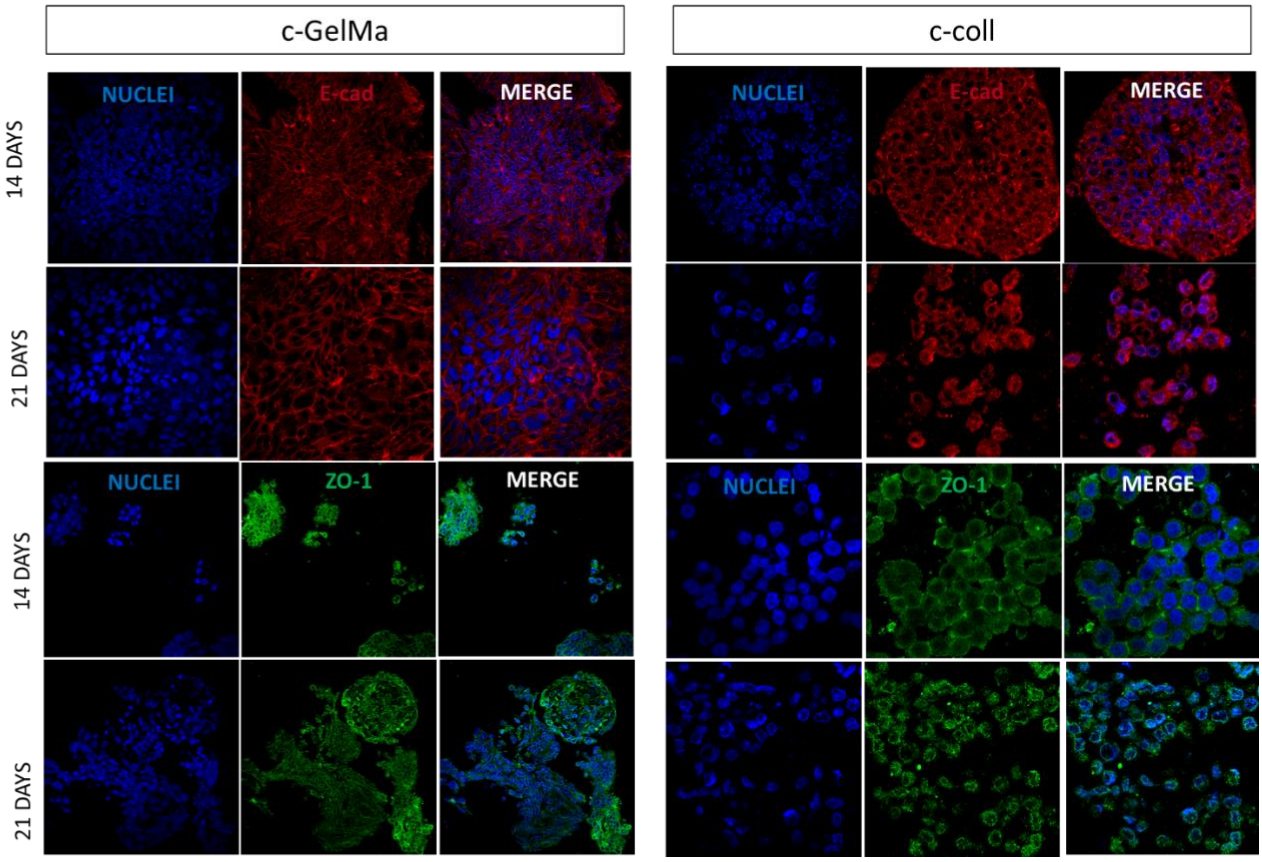

Figure 40. Confocal images of HCTs-8 E-cadherin (in red) and ZO-1 (in green) protein expression after immunostaining with primary and secondary antibodies at day 14 and 21 of incubation. Left side shows HCTs-8 protein expression when seeded onto c-GelMa scaffold, while right side of the image show HCTs-8 protein expression when seeded onto c-coll scaffold.

Moreover, in order to carry out immunohistochemistry and compare both 3D model architecture and structure to the native hierarchical organization of intestinal barrier, a new biological protocol to include, stain (haematoxylin and eosin staining), and cut with the microtome the 3D bioprinted models is under development. Usually, the immunohistochemistry protocols used for the human and animal tissues are employed for the treatment of *in vitro* models. However, when soft materials are involved, such as hydrogel or polymer matrices, all the steps traditionally involved in the immunohistochemistry procedure, confer to the artificial ECM fragility and dryness. This limitation leads to get samples not being easy to handle and with high breakages points in the internal structure, which can cause cells detachments. Furthermore, no procedures are available in the literature which detailed described all the passages to include and treat 3D bioprinted *in vitro* models.

For these reasons, in order to optimize a new inclusion procedure which aims to preserve the structure of the *in vitro* models after the treatments, a simple bilayer models of c-coll and IPN were produced though 3D bioprinting process. GelMa was not considered at this stage of the experiment. Then, to introduce the living component to the system and easily evaluate how cells behave in contact with soft materials after the optimized inclusion procedure, Caco-2 cells line were manually seeded onto UV photo-crosslinked scaffolds, as explained in the experimental section and schematically reported in Figure 41. Caco-2 cell line were employed since they are widely used for the replication of intestinal barrier and they well adhere on GelMa/collagen-based materials [277,278].

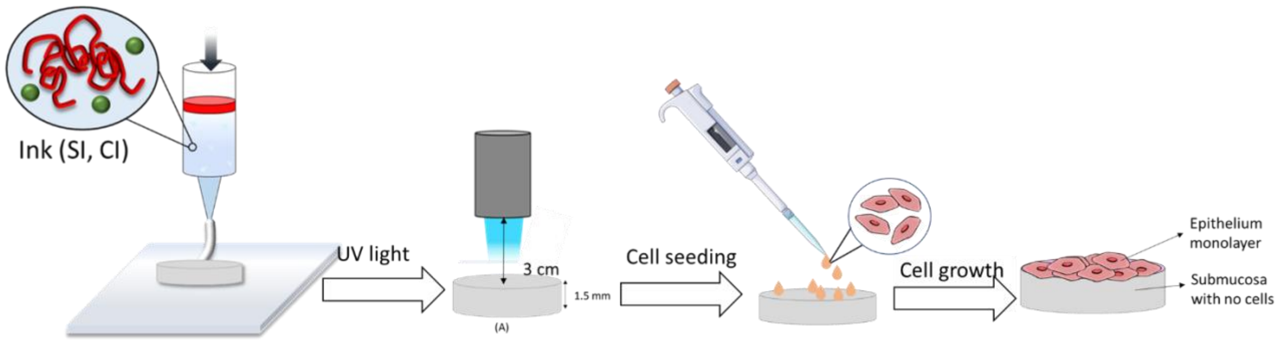

Figure 41. Schematic representation of 3D printing of coll, GelMa and semi-IPN ink, not containing cells, UV photo-crosslinking and Caco-2 manual cell seeding onto the scaffolds surfaces.

Several inclusion procedures were tested before to define that one that enable a safety inclusion of the models that provide, at the same time, the highest structural stability after the cut. Usually, different passages in xylol must be performed on the sample to dehydrate it from the aqueous components and thus allow the permeation of PFA inside the whole structure. However, xylol seems to strongly affect structural stability of the soft materials. For this reason, several timing of each step of dehydration through xylol were tested on both c-coll and IPN scaffolds starting from 10 min up to 3 min. Figure 42, show three different samples of (a) c-coll, (b) IPN and (c) IPN after 10 min and 3 min, repeated for three times, of immersion in xylol. Figure 42 a, reports only pure collagen reported since IPN was completely destroyed after 10 min of xylol treatment. As it is clear from the image, c-coll does not retain its structure because of its high fragility. Furthermore, cell monolayer was completely detached from the scaffold surface. By decreasing the time of xylol treatment, from 10 min to 3 min, while maintaining the number of passages constant, both c-coll (Figure 42 b) and IPN (Figure 42 c) appear less fragile and easier to handle, able to withstand the whole inclusion process. Furthermore, Figure 42 c demonstrate that c-blend better support the xylol treatment thanks to the presence of an intact structure in the bottom part of the sample and the presence of a continuous cell monolayer in the right side of the images (highlighted with the black arrows), which is almost destroyed in the c-coll sample.

Further improvements are ongoing to preserve and retain the structure of the sample after the inclusion process and to avoid cell detachments.

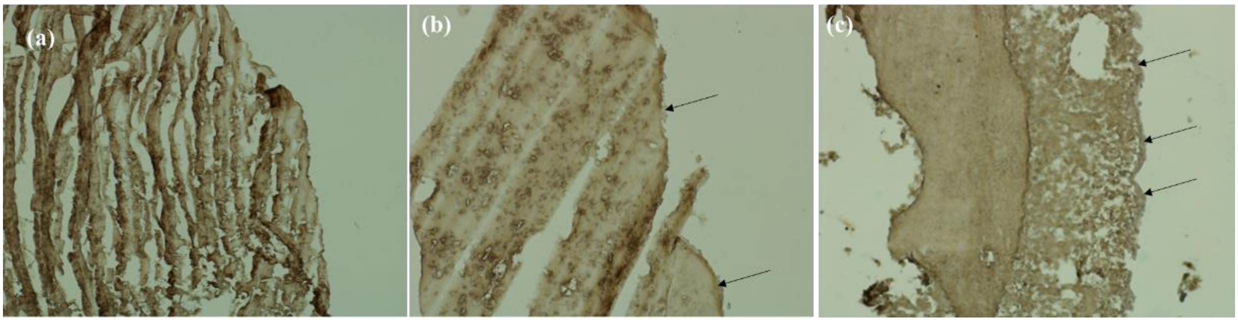

Figure 42. Histological images of (a) c-coll after 10 min of xylol treatments, (b) c-coll sample after 3 min of xylol treatments and (c) IPN after 3 min of xylol treatments.

3.4.3. Conclusions

In conclusion, a ‘proof of concept’ of 3D intestinal barrier, fully representing the three main important layers of the tissue (submucosa, lamina propria, and epithelial monolayer), and the two main living cell components (intestinal epithelial cells and fibroblasts), was successfully obtained in this Thesis through a dual printing process, by using GelMa, coll and semi-IPN bioinks. All the bioprinted models displayed good cell viability (> 90 %) and proliferation, meaning that the models can support cell growth and are suitable for this application. Biological results demonstrate that all the matrixes are suitable to support cell growth and proliferation and provide, at the same time, suitable mechanical stability up to 21 days. The different mechanical properties displayed by c-coll, c-GelMa, and IPN strongly influence cell morphology, proliferation, and orientation. In fact, fibroblasts inside c-coll and IPN-based scaffolds (which show higher mechanical properties) show rounder cell morphologies with less pronounced filaments, while inside c-GelMa (which display the lowest stiffness) cells are more elongated with a pronounced presence of filament extensions.

Furthermore, cell proliferation evaluation demonstrates that, in general, all the matrixes well support cell proliferation and that cells onto and inside IPN-based scaffold present the highest proliferation rate. These results might be ascribable to the fact that the combination of GelMa and collagen in the IPN formulation strongly enhance the bioactivity with respect to the single material. Moreover, proteins expressions successfully demonstrate the production of E-cadherin and ZO-1 junction at the epithelial monolayer level.

In conclusion, these models represent a ‘proof of concept’ of intestinal barrier easy to reproduce in all the labs equipped with a basic 3D bioprinter. The models can be easily adapted to the traditional biological assays and can be used for drug screening applications. Moreover, to further simulate *in vivo* conditions, the models can be incorporated inside dynamic bioreactors which can reproduce physiological flux. Finally, a standardized biological procedure is under optimization to process this type of soft tissue-based *in vitro* models for immunohistochemistry analysis, since a strong stiffening of the hydrogel matrix usually occurs during all the passages necessary to prepare the sample, and the resulting rapture of the specimen does not allow the correct analysis of the tissue. Since no standard biological procedures yet exist in the literature, a deep investigation was carried out in order to develop a new customized biological procedure that might be used for 3D bioprinted systems.

4. Conclusions

The culture of cells on two-dimensional (2D) surfaces has provided groundbreaking insights into basic cell biology. However, cells naturally grow in three-dimensional (3D) environment and the extracellular matrix (ECM) plays a central role on controlling cell pathways through biological and mechanical stimuli. The development of 3D bioprinted *in vitro* models has become increasingly attractive, enabling to artificially reproduce ECM of the tissues by using cell-embedded hydrogels (bioinks) with tailored physical and chemical properties. In this context, the hydrogel not only provides mechanical support and stability to the cells but also allows to tailor protein composition, nutrition, chemical and spatial gradients to match the native extracellular matrix. Moreover, considering that in several diseases and inflammatory states the ECM shows different stiffness with respect to the corresponding healthy conditions, the possibility to tailor hydrogels mechanical properties by modifying the polymer chemical structures, while maintaining their biocompatibility and biomimicry, make their use versatile and suitable to simulate a broad spectrum of physiological features. Finally, since 3D bioprinting allows to produce complex structures by using different bioinks in the same printing process, multi-components tissues containing different type of cells, proteins, matrices and gradients, in the z-axis, can be produced.

The employment of these advanced models during drug screening pipeline might reduce the number of failures encountered in the pre-clinical stages since they should resume all the essential characteristics of the native tissues. However, 3D bioprinted models for drug testing must overcome several technological, regulatory and ethical challenges prior to inclusion in the drug screening pipeline. Currently, these models lack of key physiologically features which, at the moment, are fully recognized only by the animal models, such as the reproduction of tissue vasculature and incorporation of multi-cellular components which cooperate each other's in a synergic way during drug-tissue interaction. Spheroids, cell aggregates and organ on a chip have been extensively used as 3D models to represent the *in vivo* condition since they well spontaneously reproduce cell morphology or the hierarchical structure of cell arrangement in some complex tissue, such as the intestine. However, spheroids or cell aggregates can be formed in limited and expensive matrices which do not replicate the features of the tissue external environment, that has been demonstrate to strictly influence cell functionalities and drug response, while organ-on-a-chip models usually involve the use of seeded cells onto complex and stiff structure, made by soft-lithography, that provide dynamic flux, as in physiological system, but do not replicate the suitable mechanical stimuli. Despite the limitations related to the 3D bioprinted models, they have the potential to fill the gap between 2D cultures and animal models thanks to their ability to include both living components and mechanical characteristics in the models, paving the way towards more accuracy methods to carry out drug screening.

For this reason, in this Thesis 3D bioprinting has been used to produce practical and useful 3D models which might find space in the drug screening field. In particular, a photo-crosslinkable alginate-based 3D gradient stiffness platform and 3D intestinal barrier have been produced, because of the great interesting they acquired in the research field, by focusing the attention both in the replication of the suitable mechanical properties of the tissue's ECM to be reproduced and in the preservation of cell viabilities and functionalities. The synthesis and formulation of natural-based hydrogels and bioinks were also explained and proposed. In addition, this Thesis provides valid instructions on the use of rheology for the characterization, selection and understanding of bioinks for the fabrication of 3D bioprinted constructs. In fact, the deep rheological characterization carried out on the bioinks formulation and on the final 3D bioprinted models has been demonstrated as powerful predictive tool to assess the bioprinting process and to fully characterize the stiffness of the matrices. In this context, one of the most important aspect to consider before to cultivate 3D models is the ability of the hydrogels to represent, from a mechanical point of view, the desired range of stiffness as in human environments.

Here, an innovative and affordable synthetic approach for the production of alginate methacrylate is proposed. This hydrogel has been selected as natural-based ECM since it is widely used in this field and it does not contain ECM-derived components, making it useful for the evaluation of protein secreted by the cells themselves. Moreover, in this Thesis, the fabrication of 3D bioprinted construct with gradient stiffness based on HeLa cells embedded in alginate methacrylate hydrogel is fully reported. This model aims to represent a platform which acts as powerful biological tool to study, at the same moment, cell behavior and pathways at the interfaces of regions or inside different portions representing healthy (region of the platform with lower stiffness) or pathologic tissues (region of the platform with higher stiffness). In this PhD work, the evaluation of the effect of the photo-initiator, photo-crosslinking process, necessary to stabilize the models, and mechanical properties on the cell behavior was also reported, since the use of photo-crosslinkable ECM-free derived polymeric matrices (such as alginate methacrylate) has increased great attention. The obtained 3D bioprinted platform displays mechanical stability up to 14 days of incubation. HeLa were used only to easy fabricate the platform since they represent the 'gold-standard' cell model in 2D conditions but the concept of the gradient stiffness platform might be applied to other living systems.

At the same time, a proof-of-concept for the fabrication of 3D intestinal barrier was proposed in this Thesis. In native condition, intestinal tissue displays hierarchical structure with a complex architecture and cell arrangement, because of the presence of different cell types, macrophages, white cells and villi-like epithelial monolayer. New pure collagen formulation was optimized in cooperation with Typeone Biomaterials s.r.l. which completely avoid manual neutralization process from the operators by proving a fluent filament extrusion and, at the same time, mechanical stability during time after crosslinking. In order to simplify the 3D system to the most easy but representative model, both human fibroblasts and epithelial colonic cells were used to produce natural-based bionks formulation and the multilayered structure which spatially resemble the native condition. The use of human colonic epithelial cells to make the epithelial monolayer, lead to the spontaneous formation of villi-like structure while intestinal fibroblasts were located at the basal layer of the model representing the submucosa. In the middle of monolayer and submucosa, lamina propria is located and represented by a hydrogel-based layer not containing living components. Here, a multilayered and bioprinted intestinal barrier composed by two different cell types which are able to live in the same system, was successfully achieved. Bioinks formulation was carried out by considering the bioprinting process, the long-term sustainment of the model, and the stiffness through rheological analysis. Mechanical characterization highlights that the models display tunable and tailored mechanical properties, that represent physiologic conditions. The expression of both tight-junctions and inter-membrane proteins demonstrate that the fabricated models possess the biological characteristics to be used for drug screening, because they are directly involved in drug absorption and regulation. Furthermore, the high mechanical stability displayed up to 21 days suggest the possible use of these models in dynamic condition. Finally, the ability of the 3D bioprinting to fine control the thickness of the layers makes the final models suitable for histological analysis, which could provide a significant comparison with the i*n vivo* situation. Rheological analysis also demonstrates that rheological parameters, bioprinting process, mechanical stability and shape-fidelity of the models are strongly correlated and this might provide a predictive tool to researchers for the fabrication of reliable models with tissue-like condition.

Future work will regard the introduction of these models inside bioreactors or microfluidic systems consisting of hosting chamber and microtubing connection to simulate the dynamic flow condition might provide a further step toward the *in vivo* systems and a valid tool for the prediction of drug effects. Here the proposal for the validation and assessment of the models from a practical fabrication and biological point of view is proposed, and, to further demonstrate the potentiality of the models for drug screening application, they might be combined with the bioreactor proposed by the Italian company IVtech s.r.l. This bioreactor is designed for inter-connected dynamic cell cultures and is equipped with a dual-chamber system interconnected with two flow inlets and outlets, and a holder to house a porous membrane, in which is possible to directly print the desired models. The system is designed to reproduce the typical surface of a 12 transwell, thus making the analysis easy to be adaptable to the traditional biological instruments. Live imaging during static/dynamic culture, i.e. in situ imaging of the three-dimensional culture environment using optical microscopy, or post culture imaging including staining procedures can be carried out thanks to the easily removable holder system.

References

[1] C. Jensen and Y. Teng, “Is It Time to Start Transitioning From 2D to 3D Cell Culture?,” *Frontiers in Molecular Biosciences*, vol. 7. 2020, doi: 10.3389/fmolb.2020.00033.

[2] M. Kapałczyńska *et al.*, “2D and 3D cell cultures – a comparison of different types of cancer cell cultures,” *Arch. Med. Sci.*, vol. 14, no. 4, 2018, doi: 10.5114/aoms.2016.63743.

[3] K. Duval *et al.*, “Modeling physiological events in 2D vs. 3D cell culture,” *Physiology*, vol. 32, no. 4. 2017, doi: 10.1152/physiol.00036.2016.

[4] *Drug Discovery and Evaluation: Methods in Clinical Pharmacology*. 2020.

[5] F. J. Hock, *Drug discovery and evaluation: Pharmacological assays, fourth edition*. 2015.

[6] E. D’Arcangelo and A. P. McGuigan, “Micropatterning strategies to engineer controlled cell and tissue architecture in vitro,” *Biotechniques*, vol. 58, no. 1, 2015, doi: 10.2144/000114245.

[7] J. Robertus, W. R. Browne, and B. L. Feringa, “Dynamic control over cell adhesive properties using molecular-based surface engineering strategies,” *Chemical Society Reviews*, vol. 39, no. 1. 2010, doi: 10.1039/b906608j.

[8] H. Shin, “Fabrication methods of an engineered microenvironment for analysis of cell-biomaterial interactions,” *Biomaterials*, vol. 28, no. 2. 2007, doi: 10.1016/j.biomaterials.2006.08.007.

[9] A. A. Manzoor, L. Romita, and D. K. Hwang, “A review on microwell and microfluidic geometric array fabrication techniques and its potential applications in cellular studies,” *Can. J. Chem. Eng.*, vol. 99, no. 1, 2021, doi: 10.1002/cjce.23875.

[10] A. M. Ross, Z. Jiang, M. Bastmeyer, and J. Lahann, “Physical aspects of cell culture substrates: Topography, roughness, and elasticity,” *Small*, vol. 8, no. 3. 2012, doi: 10.1002/smll.201100934.

[11] A. Kajzar, C. M. Cesa, N. Kirchgeßner, B. Hoffmann, and R. Merkel, “Toward physiological conditions for cell analyses: Forces of heart muscle cells suspended between elastic micropillars,” *Biophys. J.*, vol. 94, no. 5, 2008, doi: 10.1529/biophysj.107.115766.

[12] Z. Wang and B. Yu, “Chapter 15 - Metabolomics, Proteomics, and Genomics: An Introduction to a Clinician,” in *Biomarkers in Cardiovascular Disease*, 2019.

[13] F. R. Pinu *et al.*, “Systems biology and multi-omics integration: Viewpoints from the metabolomics research community,” *Metabolites*, vol. 9, no. 4, 2019, doi: 10.3390/metabo9040076.

[14] R. G. Wells, “The role of matrix stiffness in regulating cell behavior,” *Hepatology*, vol. 47, no. 4. 2008, doi: 10.1002/hep.22193.

[15] P. A. Janmey, D. A. Fletcher, and C. A. Reinhart-King, “Stiffness sensing by cells,” *Physiol. Rev.*, vol. 100, no. 2, 2020, doi: 10.1152/physrev.00013.2019.

[16] Y. A. Brito Barrera, C. Husteden, J. Alherz, B. Fuhrmann, C. Wölk, and T. Groth, “Extracellular matrix-inspired surface coatings functionalized with dexamethasone-loaded liposomes to induce osteo- and chondrogenic differentiation of multipotent stem cells,” *Mater. Sci. Eng. C*, vol. 131, 2021, doi: 10.1016/j.msec.2021.112516.

[17] C. Tao, M. Jin, H. Yao, and D. A. Wang, “Dopamine based adhesive nano-coatings on extracellular matrix (ECM) based grafts for enhanced host-graft interfacing affinity,” *Nanoscale*, vol. 13, no. 43, 2021, doi: 10.1039/d1nr06284k.

[18] M. J. Lydon, T. W. Minett, and B. J. Tighe, “Cellular interactions with synthetic polymer surfaces in culture,” *Biomaterials*, vol. 6, no. 6, 1985, doi: 10.1016/0142-9612(85)90100-0.

[19] J. D. Krutty, S. K. Schmitt, P. Gopalan, and W. L. Murphy, “Surface functionalization and dynamics of polymeric cell culture substrates,” *Current Opinion in Biotechnology*, vol. 40. 2016, doi: 10.1016/j.copbio.2016.05.006.

[20] A. I. Khoruzhenko, “2D- and 3D-cell culture,” *Biopolym. Cell*, vol. 27, no. 1, 2011, doi: 10.7124/bc.00007D.

[21] S. A. Langhans, “Three-dimensional in vitro cell culture models in drug discovery and drug repositioning,” *Frontiers in Pharmacology*, vol. 9, no. JAN. 2018, doi: 10.3389/fphar.2018.00006.

[22] R. S. Stowers *et al.*, “Matrix stiffness induces a tumorigenic phenotype in mammary epithelium through changes in chromatin accessibility,” *Nat. Biomed. Eng.*, vol. 3, no. 12, 2019, doi: 10.1038/s41551-019-0420-5.

[23] J. Schrader *et al.*, “Matrix stiffness modulates proliferation, chemotherapeutic response, and dormancy in hepatocellular carcinoma cells,” *Hepatology*, vol. 53, no. 4, 2011, doi: 10.1002/hep.24108.

[24] E. Azzalini *et al.*, “Cell-stiffness and morphological architectural patterns in clinical samples of high grade serous ovarian cancers,” *Nanomedicine Nanotechnology, Biol. Med.*, vol. 37, 2021, doi: 10.1016/j.nano.2021.102452.

[25] J. M. Chang *et al.*, “Clinical application of shear wave elastography (SWE) in the diagnosis of benign and malignant breast diseases,” *Breast Cancer Res. Treat.*, vol. 129, no. 1, 2011, doi: 10.1007/s10549-011-1627-7.

[26] L. J. W. Tang *et al.*, “Engineering stromal heterogeneity in cancer,” *Advanced Drug Delivery Reviews*, vol. 175. 2021, doi: 10.1016/j.addr.2021.05.027.

[27] C. Liu *et al.*, “Heterogeneous microenvironmental stiffness regulates pro-metastatic functions of breast cancer cells,” *Acta Biomater.*, vol. 131, 2021, doi: 10.1016/j.actbio.2021.07.009.

[28] R. Akhtar, M. J. Sherratt, J. K. Cruickshank, and B. Derby, “Characterizing the elastic properties of tissues,” *Materials Today*, vol. 14, no. 3. 2011, doi: 10.1016/S1369-7021(11)70059-1.

[29] G. Singh and A. Chanda, “Mechanical properties of whole-body soft human tissues: A review,” *Biomedical Materials (Bristol)*, vol. 16, no. 6. 2021, doi: 10.1088/1748-605X/ac2b7a.

[30] A. B., S. Rao, and H. J. Pandya, “Engineering approaches for characterizing soft tissue mechanical properties: A review,” *Clinical Biomechanics*, vol. 69. 2019, doi: 10.1016/j.clinbiomech.2019.07.016.

[31] C. F. Guimarães, L. Gasperini, A. P. Marques, and R. L. Reis, “The stiffness of living tissues and its implications for tissue engineering,” *Nature Reviews Materials*, vol. 5, no. 5. 2020, doi: 10.1038/s41578-019-0169-1.

[32] D. J. Webb, C. M. Brown, and K. A. DeMali, “Signals Regulating Adhesion Dynamics,” *J. Signal Transduct.*, vol. 2012, 2012, doi: 10.1155/2012/785196.

[33] H. Bachman, J. Nicosia, M. Dysart, and T. H. Barker, “Utilizing Fibronectin Integrin-Binding Specificity to Control Cellular Responses,” *Adv. Wound Care*, vol. 4, no. 8, 2015, doi: 10.1089/wound.2014.0621.

[34] K. H. Vining and D. J. Mooney, “Mechanical forces direct stem cell behaviour in development and regeneration,” *Nature Reviews Molecular Cell Biology*, vol. 18, no. 12. 2017, doi: 10.1038/nrm.2017.108.

[35] M. Urbanczyk, S. L. Layland, and K. Schenke-Layland, “The role of extracellular matrix in biomechanics and its impact on bioengineering of cells and 3D tissues,” *Matrix Biology*, vol. 85–86. 2020, doi: 10.1016/j.matbio.2019.11.005.

[36] D. Anton, H. Burckel, E. Josset, and G. Noel, “Three-dimensional cell culture: A breakthrough in vivo,” *International Journal of Molecular Sciences*, vol. 16, no. 3. 2015, doi: 10.3390/ijms16035517.

[37] L. P. Ferreira, V. M. Gaspar, and J. F. Mano, “Design of spherically structured 3D in vitro tumor models -Advances and prospects,” *Acta Biomaterialia*, vol. 75. 2018, doi: 10.1016/j.actbio.2018.05.034.

[38] E. C. Costa, A. F. Moreira, D. de Melo-Diogo, V. M. Gaspar, M. P. Carvalho, and I. J. Correia, “3D tumor spheroids: an overview on the tools and techniques used for their analysis,” *Biotechnology Advances*, vol. 34, no. 8. 2016, doi: 10.1016/j.biotechadv.2016.11.002.

[39] B. Djordjevic and C. Lange, “Cell-cell interactions in spheroids maintained in suspension,” *Acta Oncol. (Madr).*, vol. 45, no. 4, 2006, doi: 10.1080/02841860500520743.

[40] J. Alcaraz, C. M. Nelson, and M. J. Bissell, “Biomechanical approaches for studying integration of tissue structure and function in mammary epithelia,” *Journal of Mammary Gland Biology and Neoplasia*, vol. 9, no. 4. 2004, doi: 10.1007/s10911-004-1406-8.

[41] J. Costa and A. Ahluwalia, “Advances and Current Challenges in Intestinal in vitro Model Engineering: A Digest,” *Frontiers in Bioengineering and Biotechnology*, vol. 7, no. JUN. 2019, doi: 10.3389/fbioe.2019.00144.

[42] M. W. Carlson, A. Alt-Holland, C. Egles, and J. A. Garlick, “Three-dimensional tissue models of normal and diseased skin,” *Current Protocols in Cell Biology*, no. SUPPL. 41. 2008, doi: 10.1002/0471143030.cb1909s41.

[43] T. Weng *et al.*, “3D bioprinting for skin tissue engineering: Current status and perspectives,” *Journal of Tissue Engineering*, vol. 12. 2021, doi: 10.1177/20417314211028574.

[44] V. Perez-Puyana, M. Jiménez-Rosado, A. Romero, and A. Guerrero, “Polymer-based scaffolds for soft-tissue engineering,” *Polymers*, vol. 12, no. 7. 2020, doi: 10.3390/polym12071566.

[45] R. Edmondson, A. F. Adcock, and L. Yang, “Influence of matrices on 3D-cultured prostate cancer cells’ drug response and expression of drug-action associated proteins,” *PLoS One*, vol. 11, no. 6, 2016, doi: 10.1371/journal.pone.0158116.

[46] C. Godugu, A. R. Patel, U. Desai, T. Andey, A. Sams, and M. Singh, “AlgiMatrix^{TM} Based 3D Cell Culture System as an In-Vitro Tumor Model for Anticancer Studies,” *PLoS One*, vol. 8, no. 1, 2013, doi: 10.1371/journal.pone.0053708.

[47] M. Rimann and U. Graf-Hausner, “Synthetic 3D multicellular systems for drug development,” *Current Opinion in Biotechnology*, vol. 23, no. 5. 2012, doi: 10.1016/j.copbio.2012.01.011.

[48] Y. Zhao *et al.*, “Three-dimensional printing of Hela cells for cervical tumor model in vitro,”

Biofabrication, vol. 6, no. 3, 2014, doi: 10.1088/1758-5082/6/3/035001.

[49] Z. F. Bielecka, K. Maliszewska-Olejniczak, I. J. Safir, C. Szczylik, and A. M. Czarnecka, “Three-dimensional cell culture model utilization in cancer stem cell research,” *Biol. Rev.*, vol. 92, no. 3, 2017, doi: 10.1111/brv.12293.

[50] C. N. Salinas and K. S. Anseth, “The influence of the RGD peptide motif and its contextual presentation in PEG gels on human mesenchymal stem cell viability,” *J. Tissue Eng. Regen. Med.*, vol. 2, no. 5, 2008, doi: 10.1002/term.95.

[51] J. D. Clapper, M. E. Pearce, C. A. Guymon, and A. K. Salem, “Biotinylated biodegradable nanotemplated hydrogel networks for cell interactive applications,” *Biomacromolecules*, vol. 9, no. 4, 2008, doi: 10.1021/bm701176j.

[52] L. Shor *et al.*, “Precision extruding deposition (PED) fabrication of polycaprolactone (PCL) scaffolds for bone tissue engineering,” *Biofabrication*, vol. 1, no. 1, 2009, doi: 10.1088/1758-5082/1/1/015003.

[53] R. Dwivedi *et al.*, “Polycaprolactone as biomaterial for bone scaffolds: Review of literature,” *Journal of Oral Biology and Craniofacial Research*, vol. 10, no. 1. 2020, doi: 10.1016/j.jobcr.2019.10.003.

[54] R. Scaffaro, F. Lopresti, L. Botta, S. Rigogliuso, and G. Ghersi, “Integration of PCL and PLA in a monolithic porous scaffold for interface tissue engineering,” *J. Mech. Behav. Biomed. Mater.*, vol. 63, 2016, doi: 10.1016/j.jmbbm.2016.06.021.

[55] T. Wang, X. Yang, X. Qi, and C. Jiang, “Osteoinduction and proliferation of bone-marrow stromal cells in three-dimensional poly (ε-caprolactone)/ hydroxyapatite/collagen scaffolds,” *J. Transl. Med.*, vol. 13, no. 1, 2015, doi: 10.1186/s12967-015-0499-8.

[56] M. P. Nikolova and M. S. Chavali, “Recent advances in biomaterials for 3D scaffolds: A review,” *Bioact. Mater.*, vol. 4, 2019, doi: 10.1016/j.bioactmat.2019.10.005.

[57] F. Pampaloni, E. G. Reynaud, and E. H. K. Stelzer, “The third dimension bridges the gap between cell culture and live tissue,” *Nature Reviews Molecular Cell Biology*, vol. 8, no. 10. 2007, doi: 10.1038/nrm2236.

[58] L. G. Griffith and M. A. Swartz, “Capturing complex 3D tissue physiology in vitro,” *Nature Reviews Molecular Cell Biology*, vol. 7, no. 3. 2006, doi: 10.1038/nrm1858.

[59] S. Khanna, A. N. Bhatt, and B. S. Dwarakanath, “Multicellular Spheroid: 3-D Tissue Culture Model for Cancer Research,” in *Animal Biotechnology: Models in Discovery and Translation*, 2013.

[60] S. Khanna, A. Chauhan, A. N. Bhatt, and B. S. R. Dwarakanath, “Multicellular tumor spheroids as in vitro models for studying tumor responses to anticancer therapies,” in *Animal Biotechnology*, 2020.

[61] S. Gunti, A. T. K. Hoke, K. P. Vu, and N. R. London, “Organoid and spheroid tumor models: Techniques and applications,” *Cancers*, vol. 13, no. 4. 2021, doi: 10.3390/cancers13040874.

[62] Z. Gilazieva, A. Ponomarev, C. Rutland, A. Rizvanov, and V. Solovyeva, “Promising applications of tumor spheroids and organoids for personalized medicine,” *Cancers*, vol. 12, no. 10. 2020, doi: 10.3390/cancers12102727.

[63] H. C. K. Angus, A. G. Butt, M. Schultz, and R. A. Kemp, “Intestinal Organoids as a Tool for Inflammatory Bowel Disease Research,” *Frontiers in Medicine*, vol. 6. 2020, doi:

10.3389/fmed.2019.00334.

[64] N. Mise *et al.*, “Differences and similarities in the developmental status of embryo-derived stem cells and primordial germ cells revealed by global expression profiling,” *Genes to Cells*, vol. 13, no. 8, 2008, doi: 10.1111/j.1365-2443.2008.01211.x.

[65] S. Malijauskaite, J. J. E. Mulvihill, A. M. Grabrucker, and K. McGourty, “IPSC-derived intestinal organoids and current 3D intestinal scaffolds,” in *iPSCs in Tissue Engineering*, 2021.

[66] Z. Jin *et al.*, “3D Printing of Physical Organ Models: Recent Developments and Challenges,” *Advanced Science*, vol. 8, no. 17. 2021, doi: 10.1002/advs.202101394.

[67] S. Agarwal, S. Saha, V. K. Balla, A. Pal, A. Barui, and S. Bodhak, “Current Developments in 3D Bioprinting for Tissue and Organ Regeneration–A Review,” *Front. Mech. Eng.*, vol. 6, 2020, doi: 10.3389/fmech.2020.589171.

[68] S. Ostrovidov *et al.*, “3D Bioprinting in Skeletal Muscle Tissue Engineering,” *Small*, vol. 15, no. 24. 2019, doi: 10.1002/smll.201805530.

[69] P. Zhuang, J. An, C. K. Chua, and L. P. Tan, “Bioprinting of 3D in vitro skeletal muscle models: A review,” *Materials and Design*, vol. 193. 2020, doi: 10.1016/j.matdes.2020.108794.

[70] H. J. Jeong, H. Nam, J. Jang, and S. J. Lee, “3D bioprinting strategies for the regeneration of functional tubular tissues and organs,” *Bioengineering*, vol. 7, no. 2. 2020, doi: 10.3390/bioengineering7020032.

[71] S. Vijayavenkataraman, W. C. Yan, W. F. Lu, C. H. Wang, and J. Y. H. Fuh, “3D bioprinting of tissues and organs for regenerative medicine,” *Advanced Drug Delivery Reviews*, vol. 132. 2018, doi: 10.1016/j.addr.2018.07.004.

[72] B. Wang *et al.*, “Affinity-bound growth factor within sulfated interpenetrating network bioinks for bioprinting cartilaginous tissues,” *Acta Biomater.*, vol. 128, 2021, doi: 10.1016/j.actbio.2021.04.016.

[73] J. Groll *et al.*, “Biofabrication: Reappraising the definition of an evolving field,” *Biofabrication*, vol. 8, no. 1. 2016, doi: 10.1088/1758-5090/8/1/013001.

[74] N. H. Nicol, “Anatomy and physiology of the skin.,” *Dermatol. Nurs.*, vol. 17, no. 1, 2005, doi: 10.4324/9780203450505_chapter_1.

[75] T. Klouda *et al.*, “From 2D to 3D: Promising Advances in Imaging Lung Structure,” *Front. Med.*, vol. 7, 2020, doi: 10.3389/fmed.2020.00343.

[76] G. S. Zamay *et al.*, “DNA Aptamers for the Characterization of Histological Structure of Lung Adenocarcinoma,” *Mol. Ther. - Nucleic Acids*, vol. 6, 2017, doi: 10.1016/j.omtn.2016.12.004.

[77] M. Vancamelbeke and S. Vermeire, “The intestinal barrier: a fundamental role in health and disease,” *Expert Review of Gastroenterology and Hepatology*, vol. 11, no. 9. 2017, doi: 10.1080/17474124.2017.1343143.

[78] X. Ma *et al.*, “3D bioprinting of functional tissue models for personalized drug screening and in vitro disease modeling,” *Adv. Drug Deliv. Rev.*, vol. 132, 2018, doi: 10.1016/j.addr.2018.06.011.

[79] B. Sebastian and P. S. Dittrich, “Microfluidics to Mimic Blood Flow in Health and Disease,” *Annual Review of Fluid Mechanics*, vol. 50. 2018, doi: 10.1146/annurev-fluid-010816-060246.

[80] A. Shakeri, S. Khan, and T. F. Didar, “Conventional and emerging strategies for the fabrication

and functionalization of PDMS-based microfluidic devices," *Lab on a Chip*, vol. 21, no. 16. 2021, doi: 10.1039/d1lc00288k.

[81] K. Ziółkowska, A. Stelmachowska, R. Kwapiszewski, M. Chudy, A. Dybko, and Z. Brzózka, "Long-term three-dimensional cell culture and anticancer drug activity evaluation in a microfluidic chip," *Biosens. Bioelectron.*, vol. 40, no. 1, 2013, doi: 10.1016/j.bios.2012.06.017.

[82] X. Li, A. V. Valadez, P. Zuo, and Z. Nie, "Microfluidic 3D cell culture: Potential application for tissue-based bioassays," *Bioanalysis*, vol. 4, no. 12. 2012, doi: 10.4155/bio.12.133.

[83] U. A. Gurkan *et al.*, "Engineering anisotropic biomimetic fibrocartilage microenvironment by bioprinting mesenchymal stem cells in nanoliter gel droplets," *Mol. Pharm.*, vol. 11, no. 7, 2014, doi: 10.1021/mp400573g.

[84] M. S. Kim, J. H. Yeon, and J. K. Park, "A microfluidic platform for 3-dimensional cell culture and cell-based assays," *Biomed. Microdevices*, vol. 9, no. 1, 2007, doi: 10.1007/s10544-006-9016-4.

[85] G. S. Jeong *et al.*, "Microfluidic assay of endothelial cell migration in 3D interpenetrating polymer semi-network HA-Collagen hydrogel," *Biomed. Microdevices*, vol. 13, no. 4, 2011, doi: 10.1007/s10544-011-9541-7.

[86] M. C. W. Chen, M. Gupta, and K. C. Cheung, "Alginate-based microfluidic system for tumor spheroid formation and anticancer agent screening," *Biomed. Microdevices*, vol. 12, no. 4, 2010, doi: 10.1007/s10544-010-9417-2.

[87] M. Kitsara, D. Kontziampasis, O. Agbulut, and Y. Chen, "Heart on a chip: Micro-nanofabrication and microfluidics steering the future of cardiac tissue engineering," *Microelectronic Engineering*, vol. 203–204. 2019, doi: 10.1016/j.mee.2018.11.001.

[88] F. Zhang *et al.*, "Design and fabrication of an integrated heart-on-a-chip platform for construction of cardiac tissue from human iPSC-derived cardiomyocytes and in situ evaluation of physiological function," *Biosens. Bioelectron.*, vol. 179, 2021, doi: 10.1016/j.bios.2021.113080.

[89] J. Deng *et al.*, "Engineered liver-on-a-chip platform to mimic liver functions and its biomedical applications: A review," *Micromachines*, vol. 10, no. 10. 2019, doi: 10.3390/mi10100676.

[90] I. Dickson, "Multispecies liver-on-a-chip for improved drug toxicity testing," *Nature Reviews Gastroenterology and Hepatology*, vol. 17, no. 1. 2020, doi: 10.1038/s41575-019-0244-5.

[91] S. Bang, S. Jeong, N. Choi, and H. N. Kim, "Brain-on-a-chip: A history of development and future perspective," *Biomicrofluidics*, vol. 13, no. 5. 2019, doi: 10.1063/1.5120555.

[92] I. Raimondi, L. Izzo, M. Tunesi, M. Comar, D. Albani, and C. Giordano, "Organ-On-A-Chip in vitro Models of the Brain and the Blood-Brain Barrier and Their Value to Study the Microbiota-Gut-Brain Axis in Neurodegeneration," *Frontiers in Bioengineering and Biotechnology*, vol. 7. 2020, doi: 10.3389/fbioe.2019.00435.

[93] S. Sances *et al.*, "Human iPSC-Derived Endothelial Cells and Microengineered Organ-Chip Enhance Neuronal Development," *Stem Cell Reports*, vol. 10, no. 4, 2018, doi: 10.1016/j.stemcr.2018.02.012.

[94] N. Ashammakhi *et al.*, "Gut-on-a-chip: Current progress and future opportunities," *Biomaterials*, vol. 255. 2020, doi: 10.1016/j.biomaterials.2020.120196.

[95] M. A. Signore, C. De Pascali, L. Giampetruzzi, P. A. Siciliano, and L. Francioso, “Gut-on-Chip microphysiological systems: Latest advances in the integration of sensing strategies and adoption of mature detection mechanisms,” *Sensing and Bio-Sensing Research*, vol. 33. 2021, doi: 10.1016/j.sbsr.2021.100443.

[96] J. H. Tsui, W. Lee, S. H. Pun, J. Kim, and D. H. Kim, “Microfluidics-assisted in vitro drug screening and carrier production,” *Advanced Drug Delivery Reviews*, vol. 65, no. 11–12. 2013, doi: 10.1016/j.addr.2013.07.004.

[97] C. Schmitz, E. Potekhina, V. V. Belousov, and A. Lavrentieva, “Hypoxia Onset in Mesenchymal Stem Cell Spheroids: Monitoring With Hypoxia Reporter Cells,” *Front. Bioeng. Biotechnol.*, vol. 9, 2021, doi: 10.3389/fbioe.2021.611837.

[98] A. Ganguli *et al.*, “Three-dimensional microscale hanging drop arrays with geometric control for drug screening and live tissue imaging,” *Sci. Adv.*, vol. 7, no. 17, 2021, doi: 10.1126/sciadv.abc1323.

[99] S. J. Han, S. Kwon, and K. S. Kim, “Challenges of applying multicellular tumor spheroids in preclinical phase,” *Cancer Cell International*, vol. 21, no. 1. 2021, doi: 10.1186/s12935-021-01853-8.

[100] M. Shri, H. Agrawal, P. Rani, D. Singh, and S. K. Onteru, “Hanging drop, a best three-dimensional (3D) culture method for primary buffalo and sheep hepatocytes,” *Sci. Rep.*, vol. 7, no. 1, 2017, doi: 10.1038/s41598-017-01355-6.

[101] L. Polonchuk *et al.*, “Cardiac spheroids as promising in vitro models to study the human heart microenvironment,” *Sci. Rep.*, vol. 7, no. 1, 2017, doi: 10.1038/s41598-017-06385-8.

[102] Y. Park, K. M. Huh, and S. W. Kang, “Applications of biomaterials in 3d cell culture and contributions of 3d cell culture to drug development and basic biomedical research,” *International Journal of Molecular Sciences*, vol. 22, no. 5. 2021, doi: 10.3390/ijms22052491.

[103] I. Gaitán-Salvatella, E. O. López-Villegas, P. González-Alva, F. Susate-Olmos, and M. A. Álvarez-Pérez, “Case Report: Formation of 3D Osteoblast Spheroid Under Magnetic Levitation for Bone Tissue Engineering,” *Front. Mol. Biosci.*, vol. 8, 2021, doi: 10.3389/fmolb.2021.672518.

[104] L. Labusca *et al.*, “Magnetic nanoparticle loaded human adipose derived mesenchymal cells spheroids in levitated culture,” *J. Biomed. Mater. Res. - Part B Appl. Biomater.*, vol. 109, no. 5, 2021, doi: 10.1002/jbm.b.34727.

[105] I. A. Khawar, T. Ghosh, J. K. Park, and H. J. Kuh, “Tumor spheroid-based microtumor models for preclinical evaluation of anticancer nanomedicines,” *Journal of Pharmaceutical Investigation*, vol. 51, no. 5. 2021, doi: 10.1007/s40005-021-00534-y.

[106] L. A. Kotze *et al.*, “Establishment of a Patient-Derived, Magnetic Levitation-Based, Three-Dimensional Spheroid Granuloma Model for Human Tuberculosis,” *mSphere*, vol. 6, no. 4, 2021, doi: 10.1128/msphere.00552-21.

[107] I. Martin, D. Wendt, and M. Heberer, “The role of bioreactors in tissue engineering,” *Trends in Biotechnology*, vol. 22, no. 2. 2004, doi: 10.1016/j.tibtech.2003.12.001.

[108] T. G. Hammond and J. M. Hammond, “Optimized suspension culture: The rotating-wall vessel,” *American Journal of Physiology - Renal Physiology*, vol. 281, no. 1 50-1. 2001, doi: 10.1152/ajprenal.2001.281.1.f12.

[109] M. Cipriano *et al.*, “Self-assembled 3D spheroids and hollow-fibre bioreactors improve MSC-

derived hepatocyte-like cell maturation in vitro," *Arch. Toxicol.,* vol. 91, no. 4, 2017, doi: 10.1007/s00204-016-1838-0.

[110] V. I. Sikavitsas, G. N. Bancroft, and A. G. Mikos, "Formation of three-dimensional cell/polymer constructs for bone tissue engineering in a spinner flask and a rotating wall vessel bioreactor," *J. Biomed. Mater. Res.,* vol. 62, no. 1, 2002, doi: 10.1002/jbm.10150.

[111] M. Z. Ismadi *et al.*, "Flow characterization of a spinner flask for induced pluripotent stem cell culture application," *PLoS One,* vol. 9, no. 10, 2014, doi: 10.1371/journal.pone.0106493.

[112] S. Stich *et al.*, "Continuous cultivation of human hamstring tenocytes on microcarriers in a spinner flask bioreactor system," *Biotechnol. Prog.,* vol. 30, no. 1, 2014, doi: 10.1002/btpr.1815.

[113] M. P. Yavropoulou and J. G. Yovos, "The molecular basis of bone mechanotransduction," *J. Musculoskelet. Neuronal Interact.,* vol. 16, no. 3, 2016.

[114] J. Schmid *et al.*, "A perfusion bioreactor system for cell seeding and oxygen-controlled cultivation of three-dimensional cell cultures," *Tissue Eng. - Part C Methods,* vol. 24, no. 10, 2018, doi: 10.1089/ten.tec.2018.0204.

[115] M. Radisic, A. Marsano, R. Maidhof, Y. Wang, and G. Vunjak-Novakovic, "Cardiac tissue engineering using perfusion bioreactor systems," *Nat. Protoc.,* vol. 3, no. 4, 2008, doi: 10.1038/nprot.2008.40.

[116] A. Braccini *et al.*, "Three-Dimensional Perfusion Culture of Human Bone Marrow Cells and Generation of Osteoinductive Grafts," *Stem Cells,* vol. 23, no. 8, 2005, doi: 10.1634/stemcells.2005-0002.

[117] O. Nur and M. Willander, "Conventional nanofabrication methods," in *Low Temperature Chemical Nanofabrication,* 2020.

[118] F. Pati, J. Gantelius, and H. A. Svahn, "3D Bioprinting of Tissue/Organ Models," *Angew. Chemie - Int. Ed.,* vol. 55, no. 15, 2016, doi: 10.1002/anie.201505062.

[119] T. Xu, H. Kincaid, A. Atala, and J. J. Yoo, "High-throughput production of single-cell microparticles using an inkjet printing technology," *J. Manuf. Sci. Eng. Trans. ASME,* vol. 130, no. 2, 2008, doi: 10.1115/1.2903064.

[120] S. Yoon, J. A. Park, H. R. Lee, W. H. Yoon, D. S. Hwang, and S. Jung, "Inkjet–Spray Hybrid Printing for 3D Freeform Fabrication of Multilayered Hydrogel Structures," *Adv. Healthc. Mater.,* vol. 7, no. 14, 2018, doi: 10.1002/adhm.201800050.

[121] X. Cui, T. Boland, D. D.D'Lima, and M. K. Lotz, "Thermal Inkjet Printing in Tissue Engineering and Regenerative Medicine," *Recent Pat. Drug Deliv. Formul.,* vol. 6, no. 2, 2012, doi: 10.2174/187221112800672949.

[122] H. Gudapati, M. Dey, and I. Ozbolat, "A comprehensive review on droplet-based bioprinting: Past, present and future," *Biomaterials,* vol. 102. 2016, doi: 10.1016/j.biomaterials.2016.06.012.

[123] B. Hopp *et al.*, "Survival and proliferative ability of various living cell types after laser-induced forward transfer," *Tissue Eng.,* vol. 11, no. 11–12, 2005, doi: 10.1089/ten.2005.11.1817.

[124] P. Delaporte and A. P. Alloncle, "[INVITED] Laser-induced forward transfer: A high resolution additive manufacturing technology," *Opt. Laser Technol.,* vol. 78, 2016, doi: 10.1016/j.optlastec.2015.09.022.

[125] H. Gudapati, J. Yan, Y. Huang, and D. B. Chrisey, “Alginate gelation-induced cell death during laser-assisted cell printing,” *Biofabrication*, vol. 6, no. 3, 2014, doi: 10.1088/1758-5082/6/3/035022.

[126] A. Sorkio *et al.*, “Human stem cell based corneal tissue mimicking structures using laser-assisted 3D bioprinting and functional bioinks,” *Biomaterials*, vol. 171, 2018, doi: 10.1016/j.biomaterials.2018.04.034.

[127] C. Dou, V. Perez, J. Qu, A. Tsin, B. Xu, and J. Li, “A State-of-the-Art Review of Laser-Assisted Bioprinting and its Future Research Trends,” *ChemBioEng Reviews*, vol. 8, no. 5. 2021, doi: 10.1002/cben.202000037.

[128] S. Catros *et al.*, “Laser-assisted bioprinting for creating on-demand patterns of human osteoprogenitor cells and nano-hydroxyapatite,” *Biofabrication*, vol. 3, no. 2, 2011, doi: 10.1088/1758-5082/3/2/025001.

[129] M. Askari, M. Afzali Naniz, M. Kouhi, A. Saberi, A. Zolfagharian, and M. Bodaghi, “Recent progress in extrusion 3D bioprinting of hydrogel biomaterials for tissue regeneration: A comprehensive review with focus on advanced fabrication techniques,” *Biomaterials Science*, vol. 9, no. 3. 2021, doi: 10.1039/d0bm00973c.

[130] N. Jones, “Science in three dimensions: The print revolution,” *Nature*, vol. 487, no. 7405, 2012, doi: 10.1038/487022a.

[131] M. Chopin-Doroteo, E. A. Mandujano-Tinoco, and E. Krötzsch, “Tailoring of the rheological properties of bioinks to improve bioprinting and bioassembly for tissue replacement,” *Biochimica et Biophysica Acta - General Subjects*, vol. 1865, no. 2. 2021, doi: 10.1016/j.bbagen.2020.129782.

[132] J. H. Kim *et al.*, “3D Bioprinted Human Skeletal Muscle Constructs for Muscle Function Restoration,” *Sci. Rep.*, vol. 8, no. 1, 2018, doi: 10.1038/s41598-018-29968-5.

[133] M. Tavafoghi *et al.*, “Multimaterial bioprinting and combination of processing techniques towards the fabrication of biomimetic tissues and organs,” *Biofabrication*, vol. 13, no. 4. 2021, doi: 10.1088/1758-5090/ac0b9a.

[134] D. B. Kolesky, R. L. Truby, A. S. Gladman, T. A. Busbee, K. A. Homan, and J. A. Lewis, “3D bioprinting of vascularized, heterogeneous cell-laden tissue constructs,” *Adv. Mater.*, vol. 26, no. 19, 2014, doi: 10.1002/adma.201305506.

[135] B. Kaczmarek, K. Nadolna, and A. Owczarek, “The physical and chemical properties of hydrogels based on natural polymers,” in *Hydrogels Based on Natural Polymers*, 2019.

[136] E. Axpe and M. L. Oyen, “Applications of alginate-based bioinks in 3D bioprinting,” *International Journal of Molecular Sciences*, vol. 17, no. 12. 2016, doi: 10.3390/ijms17121976.

[137] X. Zhang *et al.*, “Polyethylene glycol diacrylate scaffold filled with cell-laden methacrylamide gelatin/alginate hydrogels used for cartilage repair,” *J. Biomater. Appl.*, vol. 36, no. 6, 2022, doi: 10.1177/08853282211044853.

[138] D. Das, H. T. T. Pham, S. Lee, and I. Noh, “Fabrication of alginate-based stimuli-responsive, non-cytotoxic, terpolymric semi-IPN hydrogel as a carrier for controlled release of bovine albumin serum and 5-amino salicylic acid,” *Mater. Sci. Eng. C*, vol. 98, 2019, doi: 10.1016/j.msec.2018.12.127.

[139] A. Khavari, M. Nydén, D. A. Weitz, and A. J. Ehrlicher, “Composite alginate gels for tunable

cellular microenvironment mechanics," *Sci. Rep.*, vol. 6, 2016, doi: 10.1038/srep30854.

[140] S. J. Bidarra, C. C. Barrias, K. B. Fonseca, M. A. Barbosa, R. A. Soares, and P. L. Granja, "Injectable in situ crosslinkable RGD-modified alginate matrix for endothelial cells delivery," *Biomaterials*, vol. 32, no. 31, 2011, doi: 10.1016/j.biomaterials.2011.07.013.

[141] J. A. Rowley, G. Madlambayan, and D. J. Mooney, "Alginate hydrogels as synthetic extracellular matrix materials," *Biomaterials*, vol. 20, no. 1, 1999, doi: 10.1016/S0142-9612(98)00107-0.

[142] J. M. Unagolla and A. C. Jayasuriya, "Hydrogel-based 3D bioprinting: A comprehensive review on cell-laden hydrogels, bioink formulations, and future perspectives," *Applied Materials Today*, vol. 18. 2020, doi: 10.1016/j.apmt.2019.100479.

[143] Z. Wu, X. Su, Y. Xu, B. Kong, W. Sun, and S. Mi, "Bioprinting three-dimensional cell-laden tissue constructs with controllable degradation," *Sci. Rep.*, vol. 6, 2016, doi: 10.1038/srep24474.

[144] S. Rhee, J. L. Puetzer, B. N. Mason, C. A. Reinhart-King, and L. J. Bonassar, "3D Bioprinting of Spatially Heterogeneous Collagen Constructs for Cartilage Tissue Engineering," *ACS Biomater. Sci. Eng.*, vol. 2, no. 10, 2016, doi: 10.1021/acsbiomaterials.6b00288.

[145] W. W. Chan, D. C. L. Yeo, V. Tan, S. Singh, D. Choudhury, and M. W. Naing, "Additive biomanufacturing with collagen inks," *Bioengineering*, vol. 7, no. 3. 2020, doi: 10.3390/bioengineering7030066.

[146] X. Wang *et al.*, "Gelatin-based hydrogels for organ 3D bioprinting," *Polymers*, vol. 9, no. 9. 2017, doi: 10.3390/polym9090401.

[147] M. Djabourov, "Gelation—A review," *Polym. Int.*, vol. 25, no. 3, 1991, doi: 10.1002/pi.4990250302.

[148] A. J. Kuijpers *et al.*, "Characterization of the network structure of carbodiimide cross-linked gelatin gels," *Macromolecules*, vol. 32, no. 10, 1999, doi: 10.1021/ma981929v.

[149] W. G. Liu, K. De Yao, G. C. Wang, and H. X. Li, "Intrinsic fluorescence investigation on the change in conformation of cross-linked gelatin gel during volume phase transition," *Polymer (Guildf).*, vol. 41, no. 20, 2000, doi: 10.1016/S0032-3861(00)00015-X.

[150] E. Leo, M. A. Vandelli, R. Cameroni, and F. Forni, "Doxorubicin-loaded gelatin nanoparticles stabilized by glutaraldehyde: Involvement of the drug in the cross-linking process," *Int. J. Pharm.*, vol. 155, no. 1, 1997, doi: 10.1016/S0378-5173(97)00149-X.

[151] C. M. Ofner, Y. E. Zhang, V. C. Jobeck, and B. J. Bowman, "Crosslinking studies in gelatin capsules treated with formaldehyde and in capsules exposed to elevated temperature and humidity," *J. Pharm. Sci.*, vol. 90, no. 1, 2001, doi: 10.1002/1520-6017(200101)90:1<79::AID-JPS9>3.0.CO;2-L.

[152] L. Guo, R. H. Colby, C. P. Lusignan, and A. M. Howe, "Physical gelation of gelatin studied with rheo-optics," *Macromolecules*, vol. 36, no. 26, 2003, doi: 10.1021/ma034266c.

[153] F. Bode, M. A. Da Silva, A. F. Drake, S. B. Ross-Murphy, and C. A. Dreiss, "Enzymatically cross-linked tilapia gelatin hydrogels: Physical, chemical, and hybrid networks," *Biomacromolecules*, vol. 12, no. 10, 2011, doi: 10.1021/bm2009894.

[154] C. Peña, K. de la Caba, A. Eceiza, R. Ruseckaite, and I. Mondragon, "Enhancing water repellence and mechanical properties of gelatin films by tannin addition," *Bioresour. Technol.*,

vol. 101, no. 17, 2010, doi: 10.1016/j.biortech.2010.03.112.

[155] B. Mohanty and H. B. Bohidar, “Systematic of alcohol-induced simple coacervation in aqueous gelatin solutions,” *Biomacromolecules*, vol. 4, no. 4, 2003, doi: 10.1021/bm034080l.

[156] H. Shirahama, B. H. Lee, L. P. Tan, and N. J. Cho, “Precise tuning of facile one-pot gelatin methacryloyl (GelMA) synthesis,” *Sci. Rep.*, vol. 6, 2016, doi: 10.1038/srep31036.

[157] M. Aurora and J. R. Spence, “hPSC-derived lung and intestinal organoids as models of human fetal tissue,” *Developmental Biology*, vol. 420, no. 2. 2016, doi: 10.1016/j.ydbio.2016.06.006.

[158] S. W. Kang, B. H. Cha, H. Park, K. S. Park, K. Y. Lee, and S. H. Lee, “The Effect of Conjugating RGD into 3D Alginate Hydrogels on Adipogenic Differentiation of Human Adipose-Derived Stromal Cells,” *Macromol. Biosci.*, vol. 11, no. 5, 2011, doi: 10.1002/mabi.201000479.

[159] A. L. Rutz, K. E. Hyland, A. E. Jakus, W. R. Burghardt, and R. N. Shah, “A multimaterial bioink method for 3D printing tunable, cell-compatible hydrogels,” *Adv. Mater.*, vol. 27, no. 9, 2015, doi: 10.1002/adma.201405076.

[160] E. Mancha Sánchez *et al.*, “Hydrogels for Bioprinting: A Systematic Review of Hydrogels Synthesis, Bioprinting Parameters, and Bioprinted Structures Behavior,” *Front. Bioeng. Biotechnol.*, vol. 8, 2020, doi: 10.3389/fbioe.2020.00776.

[161] W. Hu, Z. Wang, Y. Xiao, S. Zhang, and J. Wang, “Advances in crosslinking strategies of biomedical hydrogels,” *Biomaterials Science*, vol. 7, no. 3. 2019, doi: 10.1039/c8bm01246f.

[162] D. F. D. Campos *et al.*, “Exploring cancer cell behavior in vitro in three-dimensional multicellular bioprintable collagen-based hydrogels,” *Cancers (Basel).*, vol. 11, no. 2, 2019, doi: 10.3390/cancers11020180.

[163] M. Szekalska, A. Puciłowska, E. Szymańska, P. Ciosek, and K. Winnicka, “Alginate: Current Use and Future Perspectives in Pharmaceutical and Biomedical Applications,” *International Journal of Polymer Science*, vol. 2016. 2016, doi: 10.1155/2016/7697031.

[164] A. I. Chou, S. O. Akintoye, and S. B. Nicoll, “Photo-crosslinked alginate hydrogels support enhanced matrix accumulation by nucleus pulposus cells in vivo,” *Osteoarthr. Cartil.*, vol. 17, no. 10, 2009, doi: 10.1016/j.joca.2009.04.012.

[165] P. S. Gungor-Ozkerim, I. Inci, Y. S. Zhang, A. Khademhosseini, and M. R. Dokmeci, “Bioinks for 3D bioprinting: An overview,” *Biomaterials Science*, vol. 6, no. 5. 2018, doi: 10.1039/c7bm00765e.

[166] C. O. Crosby and J. Zoldan, “Mimicking the physical cues of the ECM in angiogenic biomaterials,” *Regen. Biomater.*, vol. 6, no. 2, 2019, doi: 10.1093/rb/rbz003.

[167] C. McBeth, J. Lauer, M. Ottersbach, J. Campbell, A. Sharon, and A. F. Sauer-Budge, “3D bioprinting of GelMA scaffolds triggers mineral deposition by primary human osteoblasts,” *Biofabrication*, vol. 9, no. 1, 2017, doi: 10.1088/1758-5090/aa53bd.

[168] X. Chen, Z. Yue, P. C. Winberg, Y. R. Lou, S. Beirne, and G. G. Wallace, “3D bioprinting dermal-like structures using species-specific ulvan,” *Biomater. Sci.*, vol. 9, no. 7, 2021, doi: 10.1039/d0bm01784a.

[169] J. Yin, M. Yan, Y. Wang, J. Fu, and H. Suo, “3D Bioprinting of Low-Concentration Cell-Laden Gelatin Methacrylate (GelMA) Bioinks with a Two-Step Cross-linking Strategy,” *ACS Appl. Mater. Interfaces*, vol. 10, no. 8, 2018, doi: 10.1021/acsami.7b16059.

[170] J. Xu *et al.*, “Advances in the research of bioinks based on natural collagen, polysaccharide and their derivatives for skin 3D bioprinting,” *Polymers*, vol. 12, no. 6. 2020, doi: 10.3390/POLYM12061237.

[171] C. C. Piras and D. K. Smith, “Multicomponent polysaccharide alginate-based bioinks,” *Journal of Materials Chemistry B*, vol. 8, no. 36. 2020, doi: 10.1039/d0tb01005g.

[172] X. Yang, Z. Lu, H. Wu, W. Li, L. Zheng, and J. Zhao, “Collagen-alginate as bioink for three-dimensional (3D) cell printing based cartilage tissue engineering,” *Mater. Sci. Eng. C*, vol. 83, 2018, doi: 10.1016/j.msec.2017.09.002.

[173] R. Schipani, S. Scheurer, R. Florentin, S. E. Critchley, and D. J. Kelly, “Reinforcing interpenetrating network hydrogels with 3D printed polymer networks to engineer cartilage mimetic composites,” *Biofabrication*, vol. 12, no. 3, 2020, doi: 10.1088/1758-5090/ab8708.

[174] A. García-Lizarribar, X. Fernández-Garibay, F. Velasco-Mallorquí, A. G. Castaño, J. Samitier, and J. Ramon-Azcon, “Composite Biomaterials as Long-Lasting Scaffolds for 3D Bioprinting of Highly Aligned Muscle Tissue,” *Macromol. Biosci.*, vol. 18, no. 10, 2018, doi: 10.1002/mabi.201800167.

[175] A. Sigen *et al.*, “Instant Gelation System as Self-Healable and Printable 3D Cell Culture Bioink Based on Dynamic Covalent Chemistry,” *ACS Appl. Mater. Interfaces*, vol. 12, no. 35, 2020, doi: 10.1021/acsami.0c08567.

[176] J. Jin, L. Cai, Y. G. Jia, S. Liu, Y. Chen, and L. Ren, “Progress in self-healing hydrogels assembled by host-guest interactions: Preparation and biomedical applications,” *Journal of Materials Chemistry B*, vol. 7, no. 10. 2019, doi: 10.1039/c8tb02547a.

[177] I. Naassaoui and A. Aschi, “Evaluation of Properties and Structural Transitions of Poly-L-lysine: Effects of pH and Temperature,” *J. Macromol. Sci. Part B Phys.*, vol. 58, no. 10, 2019, doi: 10.1080/00222348.2019.1638593.

[178] S. Tamburic and D. Q. M. Craig, “An investigation into the rheological, dielectric and mucoadhesive properties of poly(acrylic acid) gel systems,” *J. Control. Release*, vol. 37, no. 1–2, 1995, doi: 10.1016/0168-3659(95)00064-F.

[179] I. Mironi-Harpaz, D. Y. Wang, S. Venkatraman, and D. Seliktar, “Photopolymerization of cell-encapsulating hydrogels: Crosslinking efficiency versus cytotoxicity,” *Acta Biomater.*, vol. 8, no. 5, 2012, doi: 10.1016/j.actbio.2011.12.034.

[180] H. Xu, J. Casillas, S. Krishnamoorthy, and C. Xu, “Effects of Irgacure 2959 and lithium phenyl-2,4,6-trimethylbenzoylphosphinate on cell viability, physical properties, and microstructure in 3D bioprinting of vascular-like constructs,” *Biomed. Mater.*, vol. 15, no. 5, 2020, doi: 10.1088/1748-605X/ab954e.

[181] D. Nieto, J. A. Marchal Corrales, A. Jorge De Mora, and L. Moroni, “Fundamentals of light-cell-polymer interactions in photo-cross-linking based bioprinting,” *APL Bioengineering*, vol. 4, no. 4. 2020, doi: 10.1063/5.0022693.

[182] J. H. Wen *et al.*, “Interplay of matrix stiffness and protein tethering in stem cell differentiation,” *Nat. Mater.*, vol. 13, no. 10, 2014, doi: 10.1038/nmat4051.

[183] B. Yang *et al.*, “Enhanced mechanosensing of cells in synthetic 3D matrix with controlled biophysical dynamics,” *Nat. Commun.*, vol. 12, no. 1, 2021, doi: 10.1038/s41467-021-23120-0.

[184] B. Bachmann *et al.*, “Stiffness Matters: Fine-Tuned Hydrogel Elasticity Alters Chondrogenic

Redifferentiation," *Front. Bioeng. Biotechnol.*, vol. 8, 2020, doi: 10.3389/fbioe.2020.00373.

[185] L. R. Smith, S. Cho, and D. E. Discher, "Stem cell differentiation is regulated by extracellular matrix mechanics," *Physiology*, vol. 33, no. 1. 2018, doi: 10.1152/physiol.00026.2017.

[186] A. J. Steward and D. J. Kelly, "Mechanical regulation of mesenchymal stem cell differentiation," *Journal of Anatomy*, vol. 227, no. 6. 2015, doi: 10.1111/joa.12243.

[187] Y. Piao *et al.*, "Biomedical applications of gelatin methacryloyl hydrogels," *Eng. Regen.*, vol. 2, 2021, doi: 10.1016/j.engreg.2021.03.002.

[188] M. Zaidi, F. Fu, D. Cojocari, T. D. McKee, and B. G. Wouters, "Quantitative Visualization of Hypoxia and Proliferation Gradients Within Histological Tissue Sections," *Front. Bioeng. Biotechnol.*, vol. 7, 2019, doi: 10.3389/fbioe.2019.00397.

[189] S. Sultan and A. P. Mathew, "3D printed scaffolds with gradient porosity based on a cellulose nanocrystal hydrogel," *Nanoscale*, vol. 10, no. 9, 2018, doi: 10.1039/c7nr08966j.

[190] M. Kuzucu *et al.*, "Extrusion-Based 3D Bioprinting of Gradients of Stiffness, Cell Density, and Immobilized Peptide Using Thermogelling Hydrogels," *ACS Biomater. Sci. Eng.*, vol. 7, no. 6, 2021, doi: 10.1021/acsbiomaterials.1c00183.

[191] J. A. Thomson, "Embryonic stem cell lines derived from human blastocysts," *Science (80-.).*, vol. 282, no. 5391, 1998, doi: 10.1126/science.282.5391.1145.

[192] L. Ouyang, R. Yao, S. Mao, X. Chen, J. Na, and W. Sun, "Three-dimensional bioprinting of embryonic stem cells directs highly uniform embryoid body formation," *Biofabrication*, vol. 7, no. 4, 2015, doi: 10.1088/1758-5090/7/4/044101.

[193] M. Du *et al.*, "3D bioprinting of BMSC-laden methacrylamide gelatin scaffolds with CBD-BMP2-collagen microfibers," *Biofabrication*, vol. 7, no. 4, 2015, doi: 10.1088/1758-5090/7/4/044104.

[194] K. Ye *et al.*, "Chondrogenesis of infrapatellar fat pad derived adipose stem cells in 3D printed chitosan scaffold," *PLoS One*, vol. 9, no. 6, 2014, doi: 10.1371/journal.pone.0099410.

[195] G. Gao *et al.*, "Improved properties of bone and cartilage tissue from 3D inkjet-bioprinted human mesenchymal stem cells by simultaneous deposition and photocrosslinking in PEG-GelMA," *Biotechnol. Lett.*, vol. 37, no. 11, 2015, doi: 10.1007/s10529-015-1921-2.

[196] S. M. Richardson *et al.*, "Mesenchymal stem cells in regenerative medicine: Focus on articular cartilage and intervertebral disc regeneration," *Methods*, vol. 99. 2016, doi: 10.1016/j.ymeth.2015.09.015.

[197] T. Mezger, *The Rheology Handbook*. 2020.

[198] A. Faulkner-Jones *et al.*, "Bioprinting of human pluripotent stem cells and their directed differentiation into hepatocyte-like cells for the generation of mini-livers in 3D," *Biofabrication*, vol. 7, no. 4, 2015, doi: 10.1088/1758-5090/7/4/044102.

[199] A. Mazzocchi, M. Devarasetty, R. Huntwork, S. Soker, and A. Skardal, "Optimization of collagen type I-hyaluronan hybrid bioink for 3D bioprinted liver microenvironments," *Biofabrication*, vol. 11, no. 1, 2019, doi: 10.1088/1758-5090/aae543.

[200] N. S. Bhise *et al.*, "A liver-on-a-chip platform with bioprinted hepatic spheroids," *Biofabrication*, vol. 8, no. 1, 2016, doi: 10.1088/1758-5090/8/1/014101.

[201] A. Dash *et al.*, "Hemodynamic flow improves rat hepatocyte morphology, function, and

metabolic activity in vitro," *Am. J. Physiol. - Cell Physiol.*, vol. 304, no. 11, 2013, doi: 10.1152/ajpcell.00331.2012.

[202] I. Wagner *et al.*, "A dynamic multi-organ-chip for long-term cultivation and substance testing proven by 3D human liver and skin tissue co-culture," *Lab Chip*, vol. 13, no. 18, 2013, doi: 10.1039/c3lc50234a.

[203] D. Liu, S. Chen, and M. Win Naing, "A review of manufacturing capabilities of cell spheroid generation technologies and future development," *Biotechnology and Bioengineering*, vol. 118, no. 2. 2021, doi: 10.1002/bit.27620.

[204] T. Mulholland *et al.*, "Drug screening of biopsy-derived spheroids using a self-generated microfluidic concentration gradient," *Sci. Rep.*, vol. 8, no. 1, 2018, doi: 10.1038/s41598-018-33055-0.

[205] S. J. Fey and K. Wrzesinski, "Determination of drug toxicity using 3D spheroids constructed from an immortal human hepatocyte cell line," *Toxicol. Sci.*, vol. 127, no. 2, 2012, doi: 10.1093/toxsci/kfs122.

[206] Y. Li, T. Zhang, Y. Pang, L. Li, Z. N. Chen, and W. Sun, "3D bioprinting of hepatoma cells and application with microfluidics for pharmacodynamic test of Metuzumab," *Biofabrication*, vol. 11, no. 3, 2019, doi: 10.1088/1758-5090/ab256c.

[207] B. Trappmann and C. S. Chen, "How cells sense extracellular matrix stiffness: A material's perspective," *Current Opinion in Biotechnology*, vol. 24, no. 5. 2013, doi: 10.1016/j.copbio.2013.03.020.

[208] Z. Zhang *et al.*, "Preclinical pharmacokinetics, tolerability, and pharmacodynamics of metuzumab, a novel CD147 human-mouse chimeric and glycoengineered antibody," *Mol. Cancer Ther.*, vol. 14, no. 1, 2015, doi: 10.1158/1535-7163.MCT-14-0104.

[209] Z. N. Chen *et al.*, "Targeting radioimmunotherapy of hepatocellular carcinoma with iodine (131I) metuximab injection: Clinical Phase I/II trials," *Int. J. Radiat. Oncol. Biol. Phys.*, vol. 65, no. 2, 2006, doi: 10.1016/j.ijrobp.2005.12.034.

[210] M. A. Heinrich, R. Bansal, T. Lammers, Y. S. Zhang, R. Michel Schiffelers, and J. Prakash, "3D-Bioprinted Mini-Brain: A Glioblastoma Model to Study Cellular Interactions and Therapeutics," *Adv. Mater.*, vol. 31, no. 14, 2019, doi: 10.1002/adma.201806590.

[211] N. Liu *et al.*, "Advances in 3D bioprinting technology for cardiac tissue engineering and regeneration," *Bioactive Materials*, vol. 6, no. 5. 2021, doi: 10.1016/j.bioactmat.2020.10.021.

[212] Y. Wang *et al.*, "3D Bioprinting of Breast Cancer Models for Drug Resistance Study," *ACS Biomater. Sci. Eng.*, vol. 4, no. 12, 2018, doi: 10.1021/acsbiomaterials.8b01277.

[213] B. Kato, G. Wisser, D. K. Agrawal, T. Wood, and F. G. Thankam, "3D bioprinting of cardiac tissue: current challenges and perspectives," *Journal of Materials Science: Materials in Medicine*, vol. 32, no. 5. 2021, doi: 10.1007/s10856-021-06520-y.

[214] M. Vinci *et al.*, "Advances in establishment and analysis of three-dimensional tumor spheroid-based functional assays for target validation and drug evaluation," *BMC Biol.*, vol. 10, 2012, doi: 10.1186/1741-7007-10-29.

[215] K. L. Miller *et al.*, "Rapid 3D BioPrinting of a human iPSC-derived cardiac micro-tissue for high-throughput drug testing," *Organs-on-a-Chip*, vol. 3, 2021, doi: 10.1016/j.ooc.2021.100007.

[216] Y. S. Zhang *et al.*, “Bioprinting 3D microfibrous scaffolds for engineering endothelialized myocardium and heart-on-a-chip,” *Biomaterials*, vol. 110, 2016, doi: 10.1016/j.biomaterials.2016.09.003.

[217] J. S. Dutton, S. S. Hinman, R. Kim, Y. Wang, and N. L. Allbritton, “Primary Cell-Derived Intestinal Models: Recapitulating Physiology,” *Trends in Biotechnology*, vol. 37, no. 7. 2019, doi: 10.1016/j.tibtech.2018.12.001.

[218] L. R. Madden *et al.*, “Bioprinted 3D Primary Human Intestinal Tissues Model Aspects of Native Physiology and ADME/Tox Functions,” *iScience*, vol. 2, 2018, doi: 10.1016/j.isci.2018.03.015.

[219] C. Schmidt, J. Markus, H. Kandarova, and J. Wiest, “Tissue-on-a-chip: Microphysiometry with human 3D models on Transwell inserts,” *Front. Bioeng. Biotechnol.*, vol. 8, 2020, doi: 10.3389/fbioe.2020.00760.

[220] N. P. Sykes, “Constipation during active cancer therapy: Diagnosis and management,” in *Supportive Oncology*, 2011.

[221] W. Tomisato, S. Tsutsumi, K. Rokutan, T. Tsuchiya, and T. Mizushima, “NSAIDs induce both necrosis and apoptosis in guinea pig gastric mucosal cells in primary culture,” *Am. J. Physiol. - Gastrointest. Liver Physiol.*, vol. 281, no. 4 44-4, 2001, doi: 10.1152/ajpgi.2001.281.4.g1092.

[222] U. A. Boelsterli, M. R. Redinbo, and K. S. Saitta, “Multiple NSAID-induced hits injure the small intestine: Underlying mechanisms and novel strategies,” *Toxicol. Sci.*, vol. 131, no. 2, 2013, doi: 10.1093/toxsci/kfs310.

[223] M. F. Neurath, “New targets for mucosal healing and therapy in inflammatory bowel diseases,” *Mucosal Immunology*, vol. 7, no. 1. 2014, doi: 10.1038/mi.2013.73.

[224] L. Peyrin-Biroulet, “Anti-TNF therapy in inflammatory bowel diseases: A huge review,” *Minerva Gastroenterologica e Dietologica*, vol. 56, no. 2. 2010.

[225] M. Zoetemelk, M. Rausch, D. J. Colin, O. Dormond, and P. Nowak-Sliwinska, “Short-term 3D culture systems of various complexity for treatment optimization of colorectal carcinoma,” *Sci. Rep.*, vol. 9, no. 1, 2019, doi: 10.1038/s41598-019-42836-0.

[226] S. V. Murphy and A. Atala, “3D bioprinting of tissues and organs,” *Nature Biotechnology*, vol. 32, no. 8. 2014, doi: 10.1038/nbt.2958.

[227] W. L. Ng and W. Y. Yeong, “The future of skin toxicology testing - Three-dimensional bioprinting meets microfluidics,” *Int. J. Bioprinting*, vol. 5, no. 2.1 Special Issue, 2019, doi: 10.18063/ijb.v5i2.1.237.

[228] R. Ravichandran *et al.*, “Functionalised type-I collagen as a hydrogel building block for bio-orthogonal tissue engineering applications,” *J. Mater. Chem. B*, vol. 4, no. 2, 2015, doi: 10.1039/c5tb02035b.

[229] W. T. Brinkman, K. Nagapudi, B. S. Thomas, and E. L. Chaikof, “Photo-cross-linking of type I collagen gels in the presence of smooth muscle cells: Mechanical properties, cell viability, and function,” *Biomacromolecules*, vol. 4, no. 4, 2003, doi: 10.1021/bm0257412.

[230] B. S. Spearman, N. K. Agrawal, A. Rubiano, C. S. Simmons, S. Mobini, and C. E. Schmidt, “Tunable methacrylated hyaluronic acid-based hydrogels as scaffolds for soft tissue engineering applications,” *J. Biomed. Mater. Res. - Part A*, vol. 108, no. 2, 2020, doi: 10.1002/jbm.a.36814.

[231] S. Jaiswal, P. K. Dutta, S. Kumar, J. Koh, and S. Pandey, "Methyl methacrylate modified chitosan: Synthesis, characterization and application in drug and gene delivery," *Carbohydr. Polym.*, vol. 211, 2019, doi: 10.1016/j.carbpol.2019.01.104.

[232] A. Jacobs and O. Dahlman, "Enhancement of the quality of MALDI mass spectra of highly acidic oligosaccharides by using a Nafion-coated probe," *Anal. Chem.*, vol. 73, no. 3, 2001, doi: 10.1021/ac001222i.

[233] M. Persike and M. Karas, "Rapid simultaneous quantitative determination of different small pharmaceutical drugs using a conventional matrix-assisted laser desorption/ionization time-of-flight mass spectrometry system," *Rapid Commun. Mass Spectrom.*, vol. 23, no. 22, 2009, doi: 10.1002/rcm.4283.

[234] D. Aiello *et al.*, "Analytical Strategy for MS-Based Thanatochemistry to Estimate Postmortem Interval," *J. Proteome Res.*, vol. 20, no. 5, 2021, doi: 10.1021/acs.jproteome.0c01038.

[235] M. Persike, M. Zimmermann, J. Klein, and M. Karas, "Quantitative determination of acetylcholine and choline in microdialysis samples by MALDI-TOF MS," *Anal. Chem.*, vol. 82, no. 3, 2010, doi: 10.1021/ac902130h.

[236] M. Hasany *et al.*, "Synthesis, properties, and biomedical applications of alginate methacrylate (ALMA)-based hydrogels: Current advances and challenges," *Appl. Mater. Today*, vol. 24, 2021, doi: 10.1016/j.apmt.2021.101150.

[237] B. Stubbe *et al.*, "A straightforward method for quantification of vinyl functionalized water soluble alginates via 13 C-NMR spectroscopy," *Int. J. Biol. Macromol.*, vol. 134, 2019, doi: 10.1016/j.ijbiomac.2019.05.015.

[238] E. Gómez-Ordóñez and P. Rupérez, "FTIR-ATR spectroscopy as a tool for polysaccharide identification in edible brown and red seaweeds," *Food Hydrocoll.*, vol. 25, no. 6, 2011, doi: 10.1016/j.foodhyd.2011.02.009.

[239] D. Leal, B. Matsuhiro, M. Rossi, and F. Caruso, "FT-IR spectra of alginic acid block fractions in three species of brown seaweeds," *Carbohydr. Res.*, vol. 343, no. 2, 2008, doi: 10.1016/j.carres.2007.10.016.

[240] M. Mathlouthi and J. L. Koenig, "Vibrational spectra of carbohydrates," *Adv. Carbohydr. Chem. Biochem.*, vol. 44, no. C, 1987, doi: 10.1016/S0065-2318(08)60077-3.

[241] N. P. Chandía, B. Matsuhiro, E. Mejías, and A. Moenne, "Alginic acids in Lessonia vadosa: Partial hydrolysis and elicitor properties of the polymannuronic acid fraction," *J. Appl. Phycol.*, vol. 16, no. 2, 2004, doi: 10.1023/B:JAPH.0000044778.44193.a8.

[242] Y. Lin, M. de Kreuk, M. C. M. van Loosdrecht, and A. Adin, "Characterization of alginate-like exopolysaccharides isolated from aerobic granular sludge in pilot-plant," *Water Res.*, vol. 44, no. 11, 2010, doi: 10.1016/j.watres.2010.03.019.

[243] D. Aiello, C. Siciliano, F. Mazzotti, L. Di Donna, C. M. Athanassopoulos, and A. Napoli, "Molecular species fingerprinting and quantitative analysis of saffron (Crocus sativus L.) for quality control by MALDI mass spectrometry†," *RSC Adv.*, vol. 8, no. 63, 2018, doi: 10.1039/C8RA07484D.

[244] T. M. Aida, T. Yamagata, M. Watanabe, and R. L. Smith, "Depolymerization of sodium alginate under hydrothermal conditions," *Carbohydr. Polym.*, vol. 80, no. 1, 2010, doi: 10.1016/j.carbpol.2009.11.032.

[245] D. Aiello, C. Siciliano, F. Mazzotti, L. Di Donna, R. Risoluti, and A. Napoli, "Protein

extraction, enrichment and MALDI MS and MS/MS analysis from bitter orange leaves (citrus aurantium)," *Molecules*, vol. 25, no. 7, 2020, doi: 10.3390/molecules25071485.

[246] D. Aiello, C. Siciliano, F. Mazzotti, L. Di Donna, C. M. Athanassopoulos, and A. Napoli, "A rapid MALDI MS/MS based method for assessing saffron (Crocus sativus L.) adulteration," *Food Chem.*, vol. 307, 2020, doi: 10.1016/j.foodchem.2019.125527.

[247] D. J. Harvey, "Analysis of carbohydrates and glycoconjugates by matrix-assisted laser desorption/ionization mass spectrometry: An update covering the period 1999-2000," *Mass Spectrometry Reviews*, vol. 25, no. 4. 2006, doi: 10.1002/mas.20080.

[248] J. Zaia, "Mass spectrometry of oligosaccharides," *Mass Spectrom. Rev.*, vol. 23, no. 3, 2004, doi: 10.1002/mas.10073.

[249] A. I. Van Den Bulcke, B. Bogdanov, N. De Rooze, E. H. Schacht, M. Cornelissen, and H. Berghmans, "Structural and rheological properties of methacrylamide modified gelatin hydrogels," *Biomacromolecules*, vol. 1, no. 1, 2000, doi: 10.1021/bm990017d.

[250] E. O. Osidak, V. I. Kozhukhov, M. S. Osidak, and S. P. Domogatsky, "Collagen as bioink for bioprinting: A comprehensive review," *International Journal of Bioprinting*, vol. 6, no. 3. 2020, doi: 10.18063/IJB.V6I3.270.

[251] F. E. Freeman and D. J. Kelly, "Tuning alginate bioink stiffness and composition for controlled growth factor delivery and to spatially direct MSC Fate within bioprinted tissues," *Sci. Rep.*, vol. 7, no. 1, 2017, doi: 10.1038/s41598-017-17286-1.

[252] M. Plodinec *et al.*, "The nanomechanical signature of breast cancer," *Nat. Nanotechnol.*, vol. 7, no. 11, 2012, doi: 10.1038/nnano.2012.167.

[253] D. Myung *et al.*, "Progress in the development of interpenetrating polymer network hydrogels," *Polym. Adv. Technol.*, vol. 19, no. 6, 2008, doi: 10.1002/pat.1134.

[254] M. Ravi, V. Paramesh, S. R. Kaviya, E. Anuradha, and F. D. Paul Solomon, "3D cell culture systems: Advantages and applications," *J. Cell. Physiol.*, vol. 230, no. 1, 2015, doi: 10.1002/jcp.24683.

[255] J. Myungjin Lee *et al.*, "A three-dimensional microenvironment alters protein expression and chemosensitivity of epithelial ovarian cancer cells in vitro," *Lab. Investig.*, vol. 93, no. 5, 2013, doi: 10.1038/labinvest.2013.41.

[256] S. C. Wei *et al.*, "Matrix stiffness drives epithelial-mesenchymal transition and tumour metastasis through a TWIST1-G3BP2 mechanotransduction pathway," *Nat. Cell Biol.*, vol. 17, no. 5, 2015, doi: 10.1038/ncb3157.

[257] C. R. Pfeifer, C. M. Alvey, J. Irianto, and D. E. Discher, "Genome variation across cancers scales with tissue stiffness - An invasion-mutation mechanism and implications for immune cell infiltration," *Current Opinion in Systems Biology*, vol. 2. 2017, doi: 10.1016/j.coisb.2017.04.005.

[258] I. Acerbi *et al.*, "Human breast cancer invasion and aggression correlates with ECM stiffening and immune cell infiltration," *Integr. Biol. (United Kingdom)*, vol. 7, no. 10, 2015, doi: 10.1039/c5ib00040h.

[259] S. E. Reid *et al.*, "Tumor matrix stiffness promotes metastatic cancer cell interaction with the endothelium," *EMBO J.*, vol. 36, no. 16, 2017, doi: 10.15252/embj.201694912.

[260] A. Dodero, L. Pianella, S. Vicini, M. Alloisio, M. Ottonelli, and M. Castellano, "Alginate-

based hydrogels prepared via ionic gelation: An experimental design approach to predict the crosslinking degree," *Eur. Polym. J.*, vol. 118, 2019, doi: 10.1016/j.eurpolymj.2019.06.028.

[261] J. P. Lata, F. Guo, J. Guo, P. H. Huang, J. Yang, and T. J. Huang, "Surface Acoustic Waves Grant Superior Spatial Control of Cells Embedded in Hydrogel Fibers," *Adv. Mater.*, vol. 28, no. 39, 2016, doi: 10.1002/adma.201602947.

[262] E. Hachet, H. Van Den Berghe, E. Bayma, M. R. Block, and R. Auzély-Velty, "Design of biomimetic cell-interactive substrates using hyaluronic acid hydrogels with tunable mechanical properties," *Biomacromolecules*, vol. 13, no. 6. 2012, doi: 10.1021/bm300324m.

[263] S. Zustiak, R. Nossal, and D. L. Sackett, "Multiwell stiffness assay for the study of cell responsiveness to cytotoxic drugs," *Biotechnol. Bioeng.*, vol. 111, no. 2, 2014, doi: 10.1002/bit.25097.

[264] K. Shim *et al.*, "Fabrication of micrometer-scale porous gelatin scaffolds for 3D cell culture," *J. Ind. Eng. Chem.*, vol. 50, 2017, doi: 10.1016/j.jiec.2017.02.012.

[265] J. Xu, S. N. Fu, and F. Hug, "Age-related increase in muscle stiffness is muscle length dependent and associated with muscle force in senior females," *BMC Musculoskelet. Disord.*, vol. 22, no. 1, 2021, doi: 10.1186/s12891-021-04519-8.

[266] J. Jung and J. Oh, "Influence of photo-initiator concentration on the viability of cells encapsulated in photo-crosslinked microgels fabricated by microfluidics," *Dig. J. Nanomater. Biostructures*, vol. 9, no. 2, 2014.

[267] T. Billiet, E. Gevaert, T. De Schryver, M. Cornelissen, and P. Dubruel, "The 3D printing of gelatin methacrylamide cell-laden tissue-engineered constructs with high cell viability," *Biomaterials*, vol. 35, no. 1, 2014, doi: 10.1016/j.biomaterials.2013.09.078.

[268] S. Piluso *et al.*, "Rapid and cytocompatible cell-laden silk hydrogel formation: Via riboflavin-mediated crosslinking," *J. Mater. Chem. B*, vol. 8, no. 41, 2020, doi: 10.1039/d0tb01731k.

[269] N. S. Kajave, T. Schmitt, T. U. Nguyen, and V. Kishore, "Dual crosslinking strategy to generate mechanically viable cell-laden printable constructs using methacrylated collagen bioinks," *Mater. Sci. Eng. C*, vol. 107, 2020, doi: 10.1016/j.msec.2019.110290.

[270] G. Basara, X. Yue, and P. Zorlutuna, "Dual crosslinked gelatin methacryloyl hydrogels for photolithography and 3D printing," *Gels*, vol. 5, no. 3, 2019, doi: 10.3390/gels5030034.

[271] P. Koti, N. Muselimyan, E. Mirdamadi, H. Asfour, and N. A. Sarvazyan, "Use of GelMA for 3D printing of cardiac myocytes and fibroblasts," *J. 3D Print. Med.*, vol. 3, no. 1, 2019, doi: 10.2217/3dp-2018-0017.

[272] G. Ying, N. Jiang, C. Yu, and Y. S. Zhang, "Three-dimensional bioprinting of gelatin methacryloyl (GelMA)," *Bio-Design and Manufacturing*, vol. 1, no. 4. 2018, doi: 10.1007/s42242-018-0028-8.

[273] E. Hadjipanayi, V. Mudera, and R. A. Brown, "Close dependence of fibroblast proliferation on collagen scaffold matrix stiffness," *J. Tissue Eng. Regen. Med.*, vol. 3, no. 2, 2009, doi: 10.1002/term.136.

[274] S. Rhee, "Fibroblasts in three dimensional matrices: Cell migration and matrix remodeling," *Experimental and Molecular Medicine*, vol. 41, no. 12. 2009, doi: 10.3858/emm.2009.41.12.096.

[275] M. R. Schneider *et al.*, "A key role for E-cadherin in intestinal homeostasis and paneth cell

maturation," *PLoS One,* vol. 5, no. 12, 2010, doi: 10.1371/journal.pone.0014325.

[276] M. Itoh, A. Nagafuchi, S. Moroi, and S. Tsukita, "Involvement of ZO-1 in cadherin-based cell adhesion through its direct binding to α catenin and actin filaments," *J. Cell Biol.*, vol. 138, no. 1, 1997, doi: 10.1083/jcb.138.1.181.

[277] Y. Sambuy, I. De Angelis, G. Ranaldi, M. L. Scarino, A. Stammati, and F. Zucco, "The Caco-2 cell line as a model of the intestinal barrier: Influence of cell and culture-related factors on Caco-2 cell functional characteristics," *Cell Biology and Toxicology*, vol. 21, no. 1. 2005, doi: 10.1007/s10565-005-0085-6.

[278] M. H. Macedo, E. Martínez, C. C. Barrias, and B. Sarmento, "Development of an Improved 3D in vitro Intestinal Model to Perform Permeability Studies of Paracellular Compounds," *Front. Bioeng. Biotechnol.*, vol. 8, 2020, doi: 10.3389/fbioe.2020.524018.

Acknowledgments

This PhD research activity was supported by Farmaindustria – Associazione delle imprese del farmaco. I would like to thank my supervisors and co-supervisors for their valuable guidance and advice that has helped me in completing this project. The Biomaterials and Polymer Science Research Group of the University of Bologna, Department of Chemistry "Giacomo Ciamician", is acknowledged for providing all lab facilities, instrument access, scientific know-how, consultation, conceptualization, support on scientific writing and support on research activities. The Functional Imaging and Cellular Chemistry research group of the University of Bologna, Department of Chemistry "Giacomo Ciamician", is acknowledged for the scientific contribution on the conceptualization, biological characterization and scientific support on the fabrication of 3D bioprinted platform with gradient stiffness. I would like to thank the translational physiology and nutrition group of the University of Bologna, Department of Biological, Geological, and Environmental Sciences, for supporting the activities related to the optimization on new biological procedure to carry out histological analysis on 3D bioprinted models. Regemat 3D company (Granada, Spain) and the "Diferenciación, Regeneración y Cáncer" research group of the University of Granada (Spain), are acknowledged for the scientific support in the development of the proof-of-concept of 3D intestinal barrier. I would like also to thank Typeone Biomaterials s.r.l. for the cooperation and support in the development of collagen bioinks and for providing the material, and Prof. Anna Napoli and Prof. Donatella Aiello, Department of Chemistry and Chemical Technologies, University of Calabria, for the scientific contribution regarding the quantification of AlgMa degree of substitution through MALDI-TOF analysis.